CHAPTER 3

SPIN-POLARIZED ATOMIC HYDROGEN

BY

Isaac F. SILVERA

Lyman Laboratory of Physics, Harvard University, Cambridge, MA 02138, USA

and

J.T.M. WALRAVEN

Natuurkundig Laboratorium, Universiteit van Amsterdam, 1018 XE Amsterdam, The Netherlands

Progress in Low Temperature Physics, Volume X
Edited by D.F. Brewer

Contents

Glossary of symbols

Many of the symbols used are listed here with an indication of the approximate location in the text [eq. number (between parentheses), Chapter or section number (bold)] where more complete definitions are given. Some of the symbols used have several different uses or definitions. This table will hopefully help lift some of this degeneracy.

Symbol	Definition	Location
a	Hyperfine constant	(2.1)
a	Hyperfine state of H; n_a	(2.2), **5.3**
$\hat{a}$	Fractional density	(6.17)
$B, B_0, B_1, B_\perp, B_z$	Magnetic field	(5.1)
b	Hyperfine state of H, n_b	(2.2) **5.3**
$\hat{b}$	Fractional density	(6.17)
c	Hyperfine state of H, n_c	(2.2) **5.3**
c_H, c_M	Compression	(5.5), (5.8)
d	Hyperfine state of H, n_d	(2.2) **5.3**
D	Atomic deuterium	
D↓	Spin-polarized deuterium	
D_0	Dissociation energy	**3, 1**
D_0	Spin diffusion constant	(8.18)
$D\downarrow_\nu$	Nuclear state of D↓	(7.7)
E_a, E_b, etc.	Hyperfine energies of H and T	(2.2)
E_α, E_β, etc.	Hyperfine energies of D	(2.3)
E_F	Fermi energy	(7.8)
F	Free energy	(7.5)
f, F	Total angular momentum	(2.1)
f_0, f_1	Recombination parameter	(6.15), (6.17)
F_c	Cut-off function	(3.7)
g	Nuclear-spin degeneracy	(1.1)
g	Magnetic g-factor	**2, 1**
g_0, g_1	Recombination parameter	(6.51)
g_B	Bose pair-distribution function	(7.14)
g_e	Electronic g-factor	**2, 1**

Symbol	Definition	Location
g_n	Nuclear g-factor	**2, 1**
$g_{3/2}$, $g_{5/2}$	Bose integrals	(1.9), (1.11)
G^{eff}	Effective spin-relaxation rate constant	(5.12)
G_+	See T-matrix	(6.10a)
$G^v_{h_ih_j}$, $G^s_{h_ih_j}$	Spin-relaxation rate constant	**5.2.2**
G_E	Spin-exchange rate constant	(5.15)
H	Atomic hydrogen	
H↓	Spin-polarized hydrogen	
H↓↕	Double-polarized hydrogen	
H_Z	Zeeman interaction	**2.1**
H_{hyp}	Hyperfine interaction	**2.1**
H_D	Direct interaction	(3.1)
H_{exch}	Exchange interaction	(3.1)
H_{dd}	Dipolar interaction	(3.1)
H_3	Three-body Hamiltonian	(6.10a)
$\boldsymbol{I}$	Nuclear spin of a composite system	
i	Single-atom nuclear spin	
J	Exchange constant	(3.5)
$\boldsymbol{J}$	Spin current	(8.10)
k	Boltzmann's constant	(1.1)
k_B	Boltzmann's constant	**4.6**
$\boldsymbol{k}$	Wave vector	
K	Kelvin unit of temperature	
K	Clausing factor	(5.6)
$K^{v,s}_{h_i,h_j}$, etc.	Recombination-rate constant	**5.2.2**
K^{eff}	Effective recombination-rate constant	(5.12)
L	Rotational angular momentum	**2, 1**
L^v	Three-body recombination constant	(5.25)
M, m	Mass	
m_i, m_s, etc.	Angular momentum projections of single atoms	**2, 1**
M_I, M_S, etc.	Angular momentum projections of composite systems	**2, 1**
n_n	Normal number density	(8.8)
n	Bulk number density	
n_0	Initial number density	(1.6)
n_0	Condensate density	

Symbol	Definition	Location
$n_h(n_a, n_b$, etc.)	Number density of state h	(2.8)
n_x	Third-body density	(1.3a)
N	Total number of atoms	(1.5)
N^s	Number of atoms on surface	(1.3a)
N^v	Number of atoms in volume	(1.3a)
N_i	Population of ith state	(1.8)
N_0	Population of ground state	(1.9)
p, p_i	Momentum, momentum of ith state	(1.8)
p, P	Pressure	
P	Spin-polarization	(8.10), (5.23)
P_c	Critical pressure	(1.11)
P_s, P_{st}	Polarization	(2.5), (2.6)
P_h	Probability-occupation of state h	(2.5)
$\dot{Q}$	Heating rate	**5.4**
$\boldsymbol{q}$	Two-dimensional wavevector	(4.5)
$\boldsymbol{q}$	Three-dimensional wavevector	(6.4)
$r_{s\,min}$, $r_{t\,min}$	Well minima	(3.7)
R_K	Kapitza resistance	(4.7)
$\boldsymbol{S}$, $\boldsymbol{s}$	Spin angular momentum	
S	Entropy	(7.6)
T	T-matrix	(6.10)
T	Temperature	
T	Kinetic energy operator	(3.2)
T	Atomic tritium	
T↓	Spin-polarized tritium	
T_{He}	Temperature of helium	(4.7)
T_w	Temperature of wall	(4.7)
T_c, T_c^{2D}	Critical temperature	(1.1), (9.7)
T_F	Fermi temperature	(1.2)
t_a	Adsorption time	(4.3)
V	Volume	
v	Vibrational quantum number	(6.4)
$\bar{v}$	Average thermal velocity	(4.3)
v_0, v_s	Effective range potential	(8.6), (9.3)
V^3	Scattering potential	(6.10)
V_i^{dd}, V_{dd}	Dipolar interaction	(6.55), (3.1)
V_D	Direct interaction	(3.5)
V_s, V^s	Singlet potential	**3, 1**
V_t, V^t	Triplet potential	**3, 1**

Symbol	Definition	Location
U_{ext}	External potential	(8.8)
z	Fugacity	(1.9)
z_0	Dimension	(5.1)
z_F	Boundary of Fermi surface	(8.5)
$\alpha, \hat{\alpha}$	Hyperfine state of D	(2.3), (6.17)
α_s	Sticking probability per collision	(4.3)
$\alpha(\nu)$	Absorption coefficient	(5.22)
$\beta, \hat{\beta}$	Hyperfine state of D	(2.3), (6.17)
$\gamma, \hat{\gamma}$	Hyperfine state of D	(2.3), (6.17)
γ	Surface tension	(4.6)
γ	Recombination ratio	(5.19)
γ_e	Electronic gyromagnetic ratio	**2, 1**
γ_n	Nuclear gyromagnetic ratio	**2, 1**
Γ	Transition rate	(6.3)
Γ_{hf}	Hyperfine transition rate	(2.10)
$\gamma_{orbital}$	Recombination rate	(6.74)
$\delta, \hat{\delta}$	Hyperfine state of D	(2.3), (6.17)
$\varepsilon, \hat{\varepsilon}$	Hyperfine state of D	(2.3), (6.17)
ε	L–J well minimum	(7.4)
ε	Mixing parameter of the spin-wavefunction	(2.4)
$\varepsilon_\pm$	Mixing parameter of the spin-wavefunction	(2.4)
ε_a	Surface adsorption energy	(1.7)
ε_i	Energy of ith state	(1.8)
$\varepsilon_s, \varepsilon_t$	Well minima singlet and triplet potentials	**3,1**
$\xi, \hat{\xi}$	Hyperfine state of D	(2.3), (6.17)
η	deBoer parameter	(7.4)
η	T-matrix parameter	(6.10a)
η	Mixing parameter of the spin-wavefunction	(2.4)
$\eta_\pm$	Mixing parameter of the spin-wavefunction	(2.4)
θ	Mixing parameter of the spin-wavefunction	(2.4)
$\theta_\mp$	Mixing parameter of the spin-wavefunction	(2.4)

Symbol	Definition	Location
θ_b^v	Recombination parameter	(5.26)
κ	Two-dimensional wavevector	(4.2)
λ_{th}	Thermal de Broglie wavelength	(1.7)
μ	Identical spin rotation parameter	(8.10)
μ	Reduced mass	(6.6)
μ	Chemical potential	(1.8)
μ_s	Chemical potential of surface	(1.12)
$\mu^{\mp}$	Magnetic moment	(2.2d)
μ_0	Free-space magnetic permeability	(5.23)
μ_B	Bohr magneton	
μ_e	Electronic magnetic moment	**2, 1**
μ_H	H magnetic moment	**2, 1**
μ_N	Nuclear magnetic moment	**2, 1**
μ_n	Nuclear magneton	**2, 1**
ν	Reduced mass	(6.6)
ξ	Recombination parameter	(5.15)
ρ	Mass density	(4.6)
σ	L–J parameter	(7.2)
σ	Surface number density	
$\sigma^{\pm}$	Spin-exchange cross section	(6.89)
σ_{sat}	Saturation surface density	(9.5)
$^1\Sigma_g^+$	V_s	**3, 1**
$^3\Sigma_u^+$	V_t	**3, 1**
τ_{es}	Time constant for escape	(5.7)
ϕ	Flux	(4.3)
ω	Angular frequency	

1. Introduction

The hydrogen atom with its single electron and proton, each bearing a spin of $\frac{1}{2}$ is the simplest and most abundant atom in the universe. This simplicity has made hydrogen one of the most fruitful substances of study for the physicist, yielding deep insights into the fundamental properties of nature. Although hydrogen is not naturally found in the atomic form here on earth, it can be produced in an electrical discharge of molecular H_2. The atomic species in such a discharge is usually short lived, rapidly recombining to form H_2. Nevertheless, such techniques can be used to study single-atom properties of hydrogen. Optical spectra of hydrogenic dis-

charges, studied near the turn of the century, consisting of discrete spectral lines led to the Bohr theory of the atom and the development of modern quantum mechanics. After the second World War a careful study of the underlying structure in the spectra of the hydrogen atom by Lamb and Retherford (1950) led to the Lamb shift and the experimental establishment of quantum electrodynamics. Advances concerning the preparation of inert teflon surfaces suppressed surface recombination of hydrogen to H_2 and enabled a low-density short-lived ($t \simeq 1$ s) gas of hydrogen to be used as the active medium of a maser. The hydrogen maser which operates on the zero-field hyperfine transitions of the hydrogen atom has become the most stable time and frequency source in existence (Kleppner et al. 1962). Recently, denser gases of hydrogen (H) and deuterium (D) have been successfully "stabilized" in a long-lived state at low temperatures and in high magnetic fields. These gases are called spin-polarized hydrogen (H↓) and deuterium (D↓). In this chapter we shall review the properties of these new quantum gases; we shall also discuss some of the properties of spin-polarized tritium (T↓).

These new quantum gases promise to have many new and exciting properties in the low-temperature, high-density regime of quantum degeneracy. Some of these properties shall be discussed in this introduction, without going into great detail. As of the writing of this review, it has been five years since hydrogen was first stabilized in the laboratory (Silvera and Walraven 1980a). Since that time the field has matured with a large number of publications concerning both theory and experiment. These can be classified as factual, promising, hopeful and speculative. It is our objective to emphasize the first classification, but not to ignore the others. A realistic assessment of the literature shows that most work and progress has been made in the area of understanding of the decay mechanisms of H and D. To meet our objective, in the first four sections we discuss single-atom properties and interatomic interactions. The two following sections (5 and 6) are devoted to an extensive review of the most important experiments and to the corresponding theory of decay, respectively. In particular, in section 6 we have tried to lay out the theory of decay with a unified approach (with some redundancy for emphasis) and then carefully relate this to experimentally observable quantities. In section 7 we discuss thermodynamic properties, in particular from the point of view of the quantum theory of corresponding states, as well at $T = 0$ K properties. Section 8 is devoted to magnetic properties of the many-body gas while section 9 concentrates on many-body phenomena on surfaces or in two-dimensions. The final section (section 10) is devoted to more speculative ideas, or how degenerate quantum systems might be produced in the laboratory.

1.1. General

In the condensed state, hydrogen and its isotope deuterium provide physics with the two fundamental many-body quantum systems of nature, boson- and fermion-fluids. Hydrogen, composed of two tightly bound fermions, should behave as a composite boson (Ehrenfest and Oppenheimer 1931, Freed 1980), and deuterium as a composite fermion (the deuteron is a spin 1 fermion). Tritium should behave as a heavy version of H (the triton is a spin $\frac{1}{2}$ fermion). Due to its very light mass and weak interactions, a many-particle system of electron spin-polarized hydrogen (later, we shall precisely define this state, which we refer to as H↓) is predicted to have the unique property that it will remain in the gaseous state at the absolute zero of temperature. Under pressure it should pass directly from the gaseous to the solid state at a pressure of about 80 bar (Danilowicz et al. 1976). We compare this to the boson fluid ^{4}He which condenses into the liquid state at a finite temperature. The equilibrium state of spin-polarized deuterium is more subtle to analyze and recent calculations (Panoff et al. 1982) indicate that it will liquefy at a low, but finite temperature.

One of the most exciting aspects of these quantum gases is their behavior as degenerate quantum gases. At low density ($n \lesssim 10^{21}$ atoms/cm^3) hydrogen can be treated as a weakly interacting boson gas and is expected to display Bose–Einstein condensation (BEC) at a critical temperature

$$T_c = 3.31 \frac{\hbar^2}{mk}\left(\frac{n}{g}\right)^{2/3}. \tag{1.1}$$

Here, k is Boltzmann's constant, m is the mass, n the density and g the spin degeneracy, $2I+1$. For hydrogen the degeneracy is the number of hyperfine states that are populated in the gas.

A real example of a weakly interacting Bose gas has never existed. However, the Bose liquid, ^{4}He, becomes a superfluid below a critical temperature of 2.17 K. London (1938) first suggested that ^{4}He was actually Bose condensed (the calculated value of T_c based on the theory of weakly interacting Bose fluids is 3.15 K) and superfluidity was a property of this phase. However, ^{4}He condenses into a (high-density) liquid state for $T > T_c$ and there is very little control over the density. As a consequence of the high density, the ideas and predictions of the weakly interacting Bose gas are not applicable. Hydrogen, on the other hand, does not liquefy, and the density can always be controlled so that it behaves as a weakly interacting gas. The experimental realization of BEC is therefore one of the major goals of spin-polarized hydrogen research and its achievement holds the promise of exciting new studies of macroscopic quantum phenomena.

Currently, the maximum density of spin-polarized hydrogen that has been achieved is approximately $4.5 \times 10^{18}/\text{cm}^3$ (Hess et al. 1984), however, at a temperature $T = 570\,\text{mK}$ which is much higher than the predicted critical temperature of 43 mK for this density. With current techniques it is conceivable that densities a factor 3 or 4 higher, corresponding to $T_c \simeq 100\,\text{mK}$, can be achieved, but with great difficulty. In particular the rapidly increasing recombination rate with increasing density will make it difficult to dissipate the heat generated by recombination, and thus difficult to attain temperatures of order T_c at high densities. Limitation to lower densities for the study of degenerate properties is not a serious restriction since it is this regime of the weakly interacting boson gas that enables the most detailed comparison with theory. Some suggestions for achieving BEC in a very low-density, low-temperature sample of hydrogen shall be discussed in section 10 of this review.

Hydrogen can be condensed on a liquid helium surface having a single, weakly bound state and two-dimensional translational motion (Miller and Nosanow 1978). The atoms do not penetrate the helium surface (Miller 1978) and have an effective mass of order one. As such it represents an almost ideal two-dimensional gas, which among other properties is expected to display two-dimensional superfluidity (Edwards and Mantz 1980).

The situation for deuterium is quite different. The maximum achieved density of order $10^{14}/\text{cm}^3$ (Silvera and Walraven 1980a) can probably be increased by at least an order of magnitude, although no other experimenters have succeeded in collecting a measurable quantity since the first report.

The Fermi temperature

$$T_F = \frac{\hbar^2}{2mk}\left(6\pi^2 \frac{n}{g}\right)^{2/3} \tag{1.2}$$

corresponding to a density of $10^{15}\,\text{cm}^{-3}$ is $1.828 \times 10^{-4}\,\text{K}$, with $g = 1$. However, the density requirements are even more severe, as in order to observe superfluidity due to fermion pairing, densities of order $10^{21}\,\text{cm}^{-3}$ ($T_c = 1\,\text{K}$) are required (Leggett 1980).

At lower densities, hydrogen and deuterium have already proven to be rich systems, and promise much more interesting physics in the future, both in fundamental and applied aspects. In the past few years our understanding and knowledge has been vastly increased in the area of recombination and relaxation; interactions between H atoms and with the He gas and surfaces have also been studied in detail. The interaction with the helium surface has turned out to be of fundamental importance and has presented a host of problems, both theoretical and experimental, ranging from the determination of the adsorption energy to the Kapitza thermal

boundary resistance between a gas of the H↓ and a helium film. A hydrogen maser operating at low temperatures with helium-covered walls may have a frequency precision enhanced by a factor of 300 compared to a room-temperature maser (Berlinsky and Hardy 1981). The spin-polarized gas of hydrogen is actually a mixture of two hyperfine states, one a pure (Zeeman) state with electron and nuclear spin projections $m_s = -\frac{1}{2}$, $m_i = -\frac{1}{2}$ and the other the ground state which is an admixture of electron and nuclear spin-up and down. A gas of hydrogen in the pure Zeeman state was first produced by Cline et al. (1981). This is called double-polarized hydrogen, or H↓↓, as both the electron and nuclear spins are polarized. In this pure state the recombination rate is greatly reduced and the decay of the gas is controlled by the much slower relaxation to the admixed ground state. Recently spin-waves have been observed in a low-density nondegenerate gas of H↓↓ (Johnson et al. 1984).

In high-energy physics experimental efforts are under way to use a low-temperature (high-density) gas of nuclear polarized hydrogen (H↓↓) as a polarized proton source or a scattering target at CERN and at Brookhaven (Niinikoski 1981, Niinikoski et al. 1984, Kleppner and Greytak 1983), while at Los Alamos an experiment is being developed with a source of atomic tritium to measure the rest mass of the neutrino. It is expected that by polarizing the nuclear spins in a fusion reactor, the fusion cross section and energy yield will be enhanced (Kulsrud et al. 1982).

At this point in the introduction it is useful to address the question of why atomic hydrogen is the most abundant material in the universe and yet does not naturally exist on earth. Atomic hydrogen is a highly reactive gas and can always enjoy a much more stable state by forming a covalent bond with another H atom or other elements (H_2O, etc.). Let us concentrate on recombination to form H_2. Jones et al. (1958) calculated the probability for recombination with the emission of radiation and found it to be extremely small as the radiative transitions are electric-dipole forbidden for the homonuclear diatomic molecule. As a consequence a third body is required for conservation of energy and momentum. The rate equation for the decay of the density n of a gas of H at constant volume is (at this point we omit the hyperfine-state labels on the density)

$$\frac{dn}{dt} = -K_x^v n^2 n_x \,. \tag{1.3a}$$

Here $n = N^v/V$ where N^v is the number of atoms in volume V, and n_x is the density of third bodies. For a gas of pure H, $K_x^v \to K^v$ and $n_x \to n$ and one obtains

$$\frac{dn}{dt} = -K^v n^3 \,. \tag{1.3b}$$

The rate constant K_x^v depends on the initial states of the gas, the temperature, magnetic field, etc..

A second place where atoms can recombine is on surfaces. For surface coverage $\sigma = N^s/A$ (N^s is the total number of atoms on the surface and A the surface area) the rate equation becomes

$$\frac{d\sigma}{dt} = -K_x^s \sigma^2 . \tag{1.4}$$

This process corresponds to a situation where hydrogen atoms are weakly bound to the surface and the collision of two atoms in the presence of the surface, which plays the role of the third body, can result in a recombination. Here we consider only the second-order process with the rate constant K_x^s for H physisorbed on surfaces such as helium, although there are examples of first- and third-order surface decay of H. If the surface is helium, we shall drop the subscript x, so $K_x^s \rightarrow K^s$.

In thermodynamic equilibrium there is a relationship between the surface coverage σ and the gas density n, and both n and σ can be large so that recombination of atoms in both phases can be important. Since the total number of atoms in a system with area A and volume V is $N = N^v + N^s = Vn + A\sigma$, combining (1.3b) and (1.4) we find

$$\frac{dN}{dt} = -VK^v n^3 - AK^s \sigma^2 , \tag{1.5}$$

and the decay of the atoms will depend critically on the details of the system.

Let us first consider outer space, in the absence of surfaces or other gases. Here the lowest densities are estimated to be of order 1 atom/cm^3. To characterize the lifetime of the gas we consider the time for the density to decrease by a factor of 2, or $\Delta n/n = \frac{1}{2}$. From eq. (1.3b) we find

$$t_{1/2} = (\tfrac{2}{3} K^v n_0^2)^{-1} , \tag{1.6}$$

where n_0 is the initial density. Using $K^v = 1.2 \times 10^{-32}$ cm^6 atom^{-1} s^{-1} for unpolarized hydrogen at room temperature (Mitchell and LeRoy 1977) we find, as a rough estimate, $t_{1/2} = 1.25 \times 10^{32}$ s, a lifetime much longer than that of the universe. A gas of H at the density of the earth's atmosphere at sea level would have a half-life of about 10^{-7} s.

In outer space H can condense on surfaces of interstellar grains and be catalyzed to H_2. Likewise, on earth, surfaces can control the decay rate of an assembly of hydrogen atoms. Metallic surfaces are extremely active with first-order decay as the dominant process (Wise and Wood 1967) so that the lifetime is determined by the diffusion of the gas to the surface. For a

container with metallic walls and with a mean dimension of 1 cm and a mean atomic velocity of 5×10^5 cm/s, the lifetime is a few μs. On the other hand, hydrogen has a very low probability of sticking to a teflon surface and an atom can strike the surface 10^4–10^5 times before recombining (this implies a first-order process), leading to a lifetime of order 0.1 s for the same container. The properties of various other surfaces have been reviewed by Wise and Wood (1967).

On a liquid-helium surface the adsorption energy of a hydrogen atom, ε_a, is quite small. As we shall see later in the low-density, high-temperature limit the adsorption isotherm takes a very simple form

$$\sigma = n\lambda_{th} \exp(\varepsilon_a/kT) , \tag{1.7}$$

where $\lambda_{th} = (2\pi\hbar^2/mkT)^{1/2}$ is the thermal de Broglie wavelength. For moderate temperatures and gas densities, the coverage will be quite low and the decay due to the surface term will be insignificant. We shall present numerical examples later.

The first production of a long-lived gas of atomic hydrogen (Silvera and Walraven 1980a) employed liquid-^{4}He covered surfaces. The gas was "stabilized" in a high magnetic field of order 7 T at low temperature, of order 300 mK. The high field is of extreme importance in extending the lifetime of the gas. It maintains the hydrogen in a highly polarized state which reduces the recombination rate constant by 5 orders of magnitude for a field of 10 T. In the first experiment the gas ($n \sim 10^{14}$ cm^{-3}) was observed to have no measurable decay in a period of 10 min. Later measurements with densities 2–4 orders of magnitude higher showed that the gas slowly decays.

A gas of atomic hydrogen is never absolutely stable. The word stabilization is used to imply that the lifetime of the gas has been increased by several orders of magnitude. These lifetimes are sufficiently long to allow the gas to come into quasi-thermodynamic equilibrium and its properties can be studied by both static and dynamic techniques. To date, this has always been the observed experimental situation at the highest densities with the shortest lifetimes. With each stage of increased density, new barriers to high densities appear. Gases of H↓↑ have recently been compressed to achieve densities in the 10^{18}/cm^3 region (Sprik et al. 1983, 1985, Hess et al. 1983, 1984). At these densities three-body volume and surface recombination becomes the dominant and limiting process.

1.2. Bose statistics

The phenomenon of Bose–Einstein condensation for the ideal gas is found

by a careful examination of the Bose distribution function

$$N_i = \frac{g}{\exp[(\varepsilon_i - \mu)/kT] - 1}\,, \tag{1.8}$$

where N_i is the average population of the ith state, g the spin degeneracy, μ the chemical potential and ε_i the energy. The volume (V) density, n, is found by summing (1.8). For the noninteracting gas with $\varepsilon_i = p_i^2/2m$, this is evaluated by converting the sum to an integral over p, after first separating out the $p = 0$ term. By the usual procedure (Huang 1963) one finds

$$n = \frac{\bar{N}_0}{V} + \frac{g}{\lambda_{\rm th}^3}\, g_{3/2}(z), \quad z = \exp\left(\frac{\mu}{kT}\right), \tag{1.9}$$

where $g_n(z) = \Sigma_{l=1}^{\infty} z^l/l^n$ is a Bose integral with $g_{3/2}(1) = 2.612$. $\bar{N}_0$ is the number of particles in the zero-momentum state, the condensate. The chemical potential is always negative and approaches zero as the temperature is reduced. Bose–Einstein condensation takes place at a finite temperature

$$T_{\rm c} = 3.31\, \frac{\hbar^2}{mk} \left(\frac{n}{g}\right)^{2/3} \tag{1.10}$$

when the argument of $g_{3/2}$ becomes 1, or $\mu \to 0$. $\bar{N}_0$, which is microscopic for $T > T_{\rm c}$, becomes macroscopically populated, of order N, the total number of atoms in the system. Expression (1.10) remains valid for a weakly interacting gas. However, in this case μ takes on a small positive value (the interaction energy) for $T \leqslant T_{\rm c}$.

The pressure of the gas at BEC is

$$P_{\rm c} = (kT/\lambda_{\rm th}^3) g_{5/2}(1)\,, \tag{1.11}$$

where $g_{5/2}(1) = 1.342$. For the weakly interacting gas, the critical pressure increases with the strength of the interaction (Huang 1963).

For a two-dimensional surface of area A the same procedure is carried out, only we now extend the energy of $\varepsilon_i = p_i^2/2m - \varepsilon_{\rm a}$, where $\varepsilon_{\rm a}$ (a positive number) is a single-particle surface adsorption energy and p_i is a two-dimensional momentum. The integral can be evaluated in closed form to find the surface coverage

$$\sigma = -(g/\lambda_{\rm th}^2)\ln\{1 - \exp[(\mu_s + \varepsilon_a g^{-1})/kT]\}\,, \tag{1.12}$$

where μ_s is the chemical potential of the atoms on the surface. In this case the $p = 0$ term plays no special role and the expression diverges for $\mu_s + \varepsilon_a g^{-1} = 0$. Bose–Einstein condensation does not take place (however, the two-dimensional system can have a normal–superfluid phase transition).

Let us now consider the case of a gas H↓ in contact with a surface. (For simplicity we shall take the degeneracy $g = 1$.) The total number of particles, $N = nV + \sigma A$, and the distribution of particles over V and A at equilibrium are found by setting $\mu = \mu_s$, in eqs. (1.9) and (1.12); this yields the adsorption isotherm. For the ideal gas an unphysical result is found! When $\mu_s = -\varepsilon_t$, the number of particles on the surface, eq. (1.12), diverges. The addition of further particles cannot increase μ to zero, so BEC cannot occur in the gas phase. Silvera and Goldman (1980) and Edwards and Mantz (1980) resolved this problem by taking into account the interaction energy of the two-dimensional gas of H↓; we shall discuss this is section 9. Expression (1.7) for the adsorption isotherm is easily found by setting $\mu = \mu_s$ in eqs. (1.9) and (1.12) in the high-temperature, low-density limit.

In the ensuing sections of this review, we shall first describe the single-particle properties and the interatomic interactions, before discussing the techniques of stabilization. We shall then deal with the theory of recombination and spin relaxation, thermodynamic properties, magnetic properties, and interactions with surfaces. This will be complemented with a presentation of the experimental determination of the physical properties in section 5. The emphasis will be placed on H with a number of complementary treatments of D; T will receive relatively little attention. In section 10 we present some of the speculations and difficulties to be encountered in attempts to achieve BEC.

An alternate means of stabilizing atomic hydrogen was studied some years ago: matrix isolation in a solid lattice (H in H_2, for example). These so-called free-radical studies (Bass and Broida 1960, Hess 1971) have many interesting properties, but because the atoms are immobile and isolated from each other, the aspects of Bose and Fermi gases are suppressed. The subject will not be treated in this review. A general review of atomic hydrogen has appeared about three years ago (Silvera 1982); recent reviews by Walraven (1984) and Greytak and Kleppner (1984) are more up-to-date. Hardy et al. (1982) have reviewed resonance techniques as applied to low-density hydrogen in low magnetic fields; Nosanow (1980) has reviewed some of the thermodynamic properties of spin-polarized quantum gases.

2. Single-atom properties

The atomic hydrogens (H, D and T) are one-electron atoms with $^2S_{1/2}$ electronic ground states. Higher excited electronic states fall outside the region of interest in this chapter; we shall confine our attention to the ground state spin multiplet. The proton and triton have spin $i = \frac{1}{2}$ whereas the deuteron has spin $i = 1$ with associated magnetic moments for the electron, $\boldsymbol{\mu}_e = -g_e\mu_B\boldsymbol{s}$ and the nucleon, $\boldsymbol{\mu}_N = g_n\mu_n\boldsymbol{i}$. Here μ_B and μ_n are the Bohr magneton and the nuclear magneton, respectively; g_e and g_n are the corresponding g factors. Values of the constants are given in table 2.1. We note that $\boldsymbol{\mu}_e$ is oriented antiparallel to $\boldsymbol{s}$ so that in a magnetic field the lowest energy state of the atoms will have the electronic magnetic moments parallel to the field but the electronic spins antiparallel. We also define the gyromagnetic ratios here: $\gamma_e = g_e\mu_B/\hbar$ and $\gamma_n = g_n\mu_n/\hbar$.

Throughout this article we use μ_n and μ_B for nuclear and electronic Bohr magnetons, respectively; μ_N, μ_H and μ_e refer to magnetic moments of the nucleus, H atoms and electrons, respectively. Similar notations are used for the g-factors or gyromagnetic ratios. Furthermore, we use lower case letters to denote spin or angular momentum of single particles and upper case to distinguish that of a molecule or a pair of atoms. $\boldsymbol{J}$ is used for the rotational angular momentum of an H_2 molecule, whereas $\boldsymbol{l}$ (or $\boldsymbol{L}$) is used for the angular momentum of unbound (scattering) pairs of atoms.

2.1. Hyperfine energies and states

There are two single-atom interactions which lift the spin degeneracy: the Zeeman and the Fermi contact hyperfine interactions given by

$$H = H_Z + H_{hyp} = -(-g_e\mu_B\boldsymbol{s} + g_n\mu_n\boldsymbol{i})\cdot\boldsymbol{B} + a\boldsymbol{i}\cdot\boldsymbol{s}\,. \tag{2.1}$$

Diagonalization of this Hamiltonian to find the hyperfine energies is straightforward. In zero field the total angular momentum $\boldsymbol{f} = \boldsymbol{s} + \boldsymbol{i}$ is a good quantum number, whereas in high field ($\mu_e B \gg a$), the spin projections m_s and m_i (thus, also m_f) are good quantum numbers. The energies of the states for hydrogen and tritium are:

$$E_a = -\tfrac{1}{4}a - \tfrac{1}{2}a[1 + (\mu^+ B/a)^2]^{1/2}\,, \tag{2.2a}$$

$$E_b = \tfrac{1}{4}a - \tfrac{1}{2}\mu^- B\,, \tag{2.2b}$$

$$E_c = -\tfrac{1}{4}a + \tfrac{1}{2}a[1 + (\mu^+ B/a)^2]^{1/2}\,, \tag{2.2c}$$

Table 2.1

Single-atoms constants of H, D and T in the ground electronic state. Values for the electronic and nuclear Bohr magnetons are $\mu_B = 9.274\,078(36) \times 10^{-24}$ J T^{-1} and $\mu_n = 5.050\,824(20) \times 10^{-27}$ J T^{-1}. The magnetic moment of the nucleon is $\boldsymbol{\mu}_N = g_n \mu_n \boldsymbol{I}$. The ratio of the deuteron magnetic moment to the proton magnetic moment is 0.307 012 192(15) [Wimmet 1953]. The ratio of electron to proton magnetic moment is 658.210 688 0(66), $\hbar \equiv h/2\pi = 1.0545887(57) \times 10^{-34}$ J s.

Quantity	Hydrogen	Tritium	Deuterium	Ref.
Electron spin	$\frac{1}{2}$	$\frac{1}{2}$	$\frac{1}{2}$	
g_e	2.002 319 313 4(70)	2.002 319 313 4(70)	2.002 319 313 4(70)	
$g_e\mu_B \equiv \hbar\gamma_e$	$1.856\,966\,4(72) \times 10^{-23}$ J T^{-1}	$1.856\,966\,4(72) \times 10^{-23}$ J T^{-1}	$1.856\,966\,4(72) \times 10^{-23}$ J T^{-1}	
Nuclear spin	$\frac{1}{2}$	$\frac{1}{2}$	1	[1]
g_n	5.585 691 2(22)	5.9577	0.857 419 2(60)	
$g_n\mu_n \equiv \hbar\gamma_n$	$2.821\,234(11) \times 10^{-26}$ J T^{-1}	3.0091×10^{-26} J T^{-1}	$4.330\,673 \times 10^{-26}$ J T^{-1}	
a/h	1420.405 751 773(1) MHz	1516.701 470 808 7(71) MHz	327.384 352 522 2(17) MHz	[2–5]

References:

[1] Ramsey (1956).
[2] Petit et al. (1980).
[3] Hellwig et al. (1970).
[4] Mathur et al. (1967).
[5] Wineland and Ramsey (1972).

$$E_d = \tfrac{1}{4}a + \tfrac{1}{2}\mu^- B\,, \tag{2.2d}$$

where $\mu^{\pm} = g_e\mu_B \pm g_n\mu_n$.

For deuterium we have 6 hyperfine states, with energies

$$E_\alpha = -\tfrac{1}{2}\Delta_n - \tfrac{1}{4}a - \tfrac{1}{2}aR^+\,, \tag{2.3a}$$

$$E_\beta = \tfrac{1}{2}\Delta_n - \tfrac{1}{4}a - \tfrac{1}{2}aR^-\,, \tag{2.3b}$$

$$E_\gamma = -\tfrac{1}{2}\Delta_e + \Delta_n + \tfrac{1}{2}a\,, \tag{2.3c}$$

$$E_\delta = \tfrac{1}{2}\Delta_n - \tfrac{1}{4}a + \tfrac{1}{2}aR^-\,, \tag{2.3d}$$

$$E_\varepsilon = -\tfrac{1}{2}\Delta_n - \tfrac{1}{4}a + \tfrac{1}{2}aR^+\,, \tag{2.3e}$$

$$E_\zeta = \tfrac{1}{2}\Delta_e - \Delta_n + \tfrac{1}{2}a\,, \tag{2.3f}$$

with $\Delta_e \equiv g_e\mu_B B$; $\Delta_n \equiv g_n\mu_n B$, and $R^{\pm} \equiv [(\mu^+ B/a \pm \tfrac{1}{2})^2 + 2]^{1/2}$. Note that in eqs. (2.2) and (2.3) the hyperfine constant a (which has not been given a subscript) actually has different values for D and H, given in table 2.1.

The energy levels are shown in fig. 2.1 along with the states in the low- and high-field limits. We note that in high field, the upper levels cross when the nuclear Zeeman energy is equal to half the hyperfine energy, or $B \simeq a/(2g_n\mu_n) \simeq 16.7$ T for H, D and T. The crossing field is the same for all three isotopes, since the hyperfine constant is proportional to the nuclear magnetic moment.

The high-field limit holds for $B \gg a/\mu^+$ which is 507 and 541 G for H and T, respectively, and $B \gg a/2\mu^+ = 58.5$ G for D. Hydrogen, tritium and deuterium all have two pure Zeeman states, b and d (for H and T) and γ and ζ (for D). All other states are mixed-spin states. The mixing parameters in the figures are

$$\text{for H and T:}\quad \varepsilon \equiv \sin\theta = \{1 + (\mu^+ B/a + [1 + (\mu^+ B/a)^2]^{1/2})^2\}^{-1/2}\,;$$

$$\eta = \cos\theta\,, \tag{2.4a}$$

$$\text{for D:}\quad \varepsilon_\pm \equiv \sin\theta_\pm = \{1 + \tfrac{1}{2}(Z^\pm + R^\pm)^2\}^{-1/2}\,;$$

$$\eta_\pm = \cos\theta_\pm\,, \tag{2.4b}$$

with $Z^\pm = (\mu^+ B/a) \pm \tfrac{1}{2}$. In the high-field limit ($\theta, \theta_\pm \to 0$), $\varepsilon \to a/(2\mu^+ B)$ and $\varepsilon_\pm \to a/(\sqrt{2}\mu^+ B)$. For a magnetic field of 10 T, ε and $\varepsilon_\pm$ are 2.54×10^{-3} (for H) and 8.26×10^{-4} (for D), respectively. The η and $\eta_\pm$ are defined here for later use.

$$\tan 2\theta = \frac{a}{\mu^+ B}$$

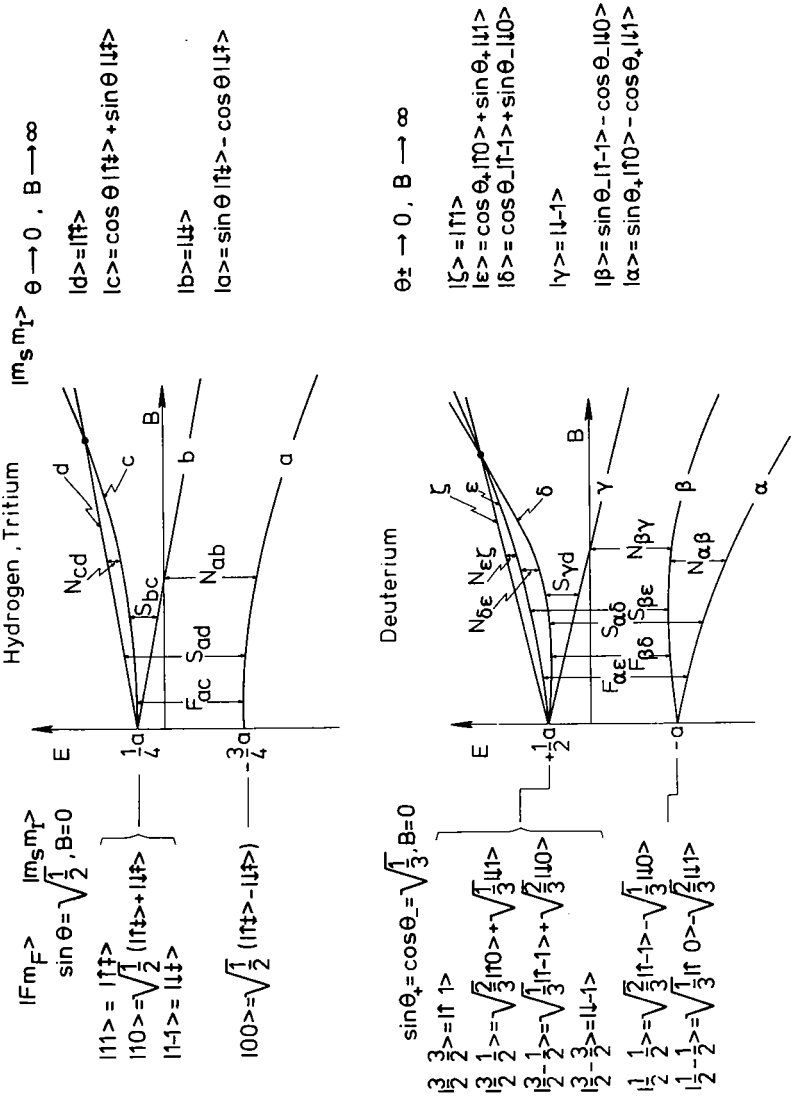

Fig. 2.1. The hyperfine energies and states of hydrogen, tritium and deuterium as a function of magnetic field B. Allowed magnetic-dipole transitions are indicated with vertical arrows. N_{if} and S_{if} are nuclear and electronic transitions, respectively; F_{if} are the longitudinal resonance transitions.

2.2. Electron spin polarization

In thermodynamic equilibrium at low temperatures and high fields the polarization of the electron spins is almost complete. From eqs. (2.1) we find that for a field $B = 10\,\mathrm{T}$, the splitting between the lowest and the highest pairs of hyperfine states amounts to $\Delta E/k \simeq 13\,\mathrm{K}$. For a temperature of 200 mK the thermal occupation of the $|c\rangle$ and $|d\rangle$-levels is suppressed by a factor 10^{28}. Unfortunately, this does not mean that the electronic spin "up" component is also suppressed by this amount, because the lowest hyperfine state (state $|a\rangle$ in fig. 2.1) has an admixture of spin "up" due to the hyperfine coupling between the nuclear and electronic spins.

To be quantitative, it is useful to introduce the concept of state polarization,

$$P_{\mathrm{st}} = (P_{\mathrm{ab}} - P_{\mathrm{cd}})/(P_{\mathrm{ab}} + P_{\mathrm{cd}})\,, \tag{2.5a}$$

and electron spin polarization,

$$P_{\mathrm{s}} = (P{\downarrow} - P{\uparrow})/(P{\downarrow} + P{\uparrow})\,, \tag{2.5b}$$

Here P_{ij} is the probability that an atom is in state i or j, $P_{ij} = P_i + P_j$, and one easily finds $P_{\mathrm{st}} = \tanh(\mu_{\mathrm{B}}B/kT) \simeq 1 - 2\exp(-\mu_{\mathrm{B}}B/kT)$ for the high-field, low-temperature limit. For $B = 10\,\mathrm{T}$, P_{st} is essentially temperature-independent for a temperature below 1 K.

To determine P_{s}, we evaluate $P{\downarrow} \equiv \Sigma_{\mathrm{h}} P_{\mathrm{h}} |\langle{\downarrow}|\mathrm{h}\rangle|^2$ and $P{\uparrow} \equiv \Sigma_{\mathrm{h}} P_{\mathrm{h}} |\langle{\uparrow}|\mathrm{h}\rangle|^2$, where $|\mathrm{h}\rangle$ is a hyperfine state and P_{h} the occupation probability. Let us examine the case in which $P_{\mathrm{st}} = 1$, i.e., only the hyperfine states a and b are occupied. For hydrogen we easily find $P_{\mathrm{s}} = 1 - \varepsilon^2 \simeq 1 - (a/4\mu_{\mathrm{B}}B)^2$ for high fields. We see that the electron spin polarization depends on the degree of admixture, which is controlled by the magnetic field. As shown by eq. (2.4a) it cannot be rendered negligible with currently accessible fields. For a field of 10 T, $(a/4\mu_{\mathrm{B}}B)^2 \simeq 6.4 \times 10^{-6}$, which is rather small, but by no means negligible. In sections 5 and 6, we shall see that for H↓, this small admixture of reversed electronic spin provides an open channel for recombination to the $^1\Sigma_{\mathrm{g}}^+$ bound molecular H_2 state, with rate proportional to ε^2; similar considerations hold for D↓ and T↓. Finally we note that if only the hyperfine state $|b\rangle$ is populated, then the sum has but one term and $P_{\mathrm{s}} = 1$.

2.3. Magnetization

For an assembly of hydrogen atoms, each with magnetic moment $\boldsymbol{\mu}_{\mathrm{H}}$,

the magnetization is

$$\boldsymbol{M} = \sum_i \boldsymbol{\mu}_{\mathrm{H}}(\boldsymbol{r}_i, \boldsymbol{B})\delta(\boldsymbol{r} - \boldsymbol{r}_i) \,. \tag{2.6}$$

The effective magnetic moment of the hydrogen atom depends on the hyperfine state, $|\mathrm{h}\rangle$, and is given by

$$\boldsymbol{\mu}_{\mathrm{H}}(\mathrm{h}) = -\boldsymbol{\nabla}_{\mathrm{B}} E_{\mathrm{h}} \,, \tag{2.7}$$

where E_{h} is the energy of the state, eqs. (2.2) and (2.3), and $\boldsymbol{\nabla}_{\mathrm{B}}$ is the gradient with respect to the magnetic field. The magnetic moments for the four hyperfine states of hydrogen are shown in fig. 2.2 (we ignore μ_{N} since $\mu_{\mathrm{e}} \gg \mu_{\mathrm{N}}$); a similar diagram exists for D. For later purposes it is useful to consider the magnetization in high field, where only hyperfine states $|\mathrm{a}\rangle$ and $|\mathrm{b}\rangle$ are populated. Then from eq. (2.6) we find

$$|\boldsymbol{M}| = g_{\mathrm{e}}\mu_{\mathrm{B}}\tfrac{1}{2}(n_{\mathrm{a}} + n_{\mathrm{b}}) + g_{\mathrm{n}}\mu_{\mathrm{n}}\tfrac{1}{2}(n_{\mathrm{a}} - n_{\mathrm{b}}) \,. \tag{2.8}$$

Here n_{a} and n_{b} are the number densities of atoms in states a and b. Since in the high-field regime a gas of a- and b-state atoms corresponds to electron spin-polarized hydrogen we see that in this case the magnetization is proportional to the atomic density n of the gas, to the approximation that the nuclear magnetization can be ignored.

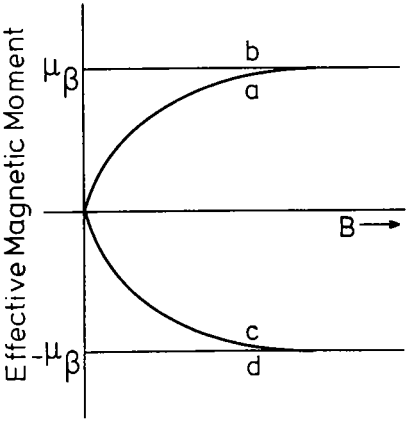

Fig. 2.2. The effective magnetic moments for the four hyperfine states of hydrogen, shown in fig. 2.1, as a function of applied magnetic field. States a and c reach their high-field values for $B \gg 507$ G (after Silvera and Walraven 1981a).

2.4. ESR AND NMR TRANSITIONS

The hyperfine energy level diagrams can be studied by means of magnetic resonance. The problem is analyzed in terms of the Hamiltonian eq. (2.1) in which $\boldsymbol{B} = \boldsymbol{B}_0 + 2\boldsymbol{B}_1 \cos \omega t$, $\boldsymbol{B}_1$ being a small polarized rf perturbation field and $\boldsymbol{B}_0$ the applied static field. The transition rate from an initial state $|\mathrm{h}\rangle = |sm_s, im_i\rangle$ to $|\mathrm{f}\rangle = |s'm_s', i'm_i'\rangle$ is given by

$$\Gamma_{\mathrm{hf}} = P_{\mathrm{h}} \frac{2\pi}{\hbar} |\langle\ |V|\ \rangle|^2 \delta(E_{\mathrm{h}} - E_{\mathrm{f}} - \hbar\omega)\,, \tag{2.9}$$

where P_{h} is the probability that an atom is in hyperfine state $|\mathrm{h}\rangle$ and V is the perturbation for magnetic dipole transitions, $V = -2\mu_{\mathrm{H}} B_1 \cos \omega t$. ESR transitions are allowed which only involve a change in the electron spin ($\Delta m_s = 1$, $\Delta m_i = 0$), or NMR transitions which only involve a change in the nuclear spin ($\Delta m_s = 0$, $\Delta m_i = 1$). Pure ESR and NMR transitions only occur in high magnetic fields, where the mixed nature of the hyperfine states $|\mathrm{a}\rangle$ and $|\mathrm{c}\rangle$ may be neglected. In addition, for low external fields, a longitudinal resonance ($\boldsymbol{B}_1 // \boldsymbol{B}$) with $|\mathrm{f}, m_{\mathrm{f}}\rangle \rightarrow |\mathrm{f} \pm 1, m_{\mathrm{f}}\rangle$ is allowed. The field dependence of the transition frequencies for hydrogen is shown in fig. 2.3.

We shall make a few general remarks about the line strengths, which are

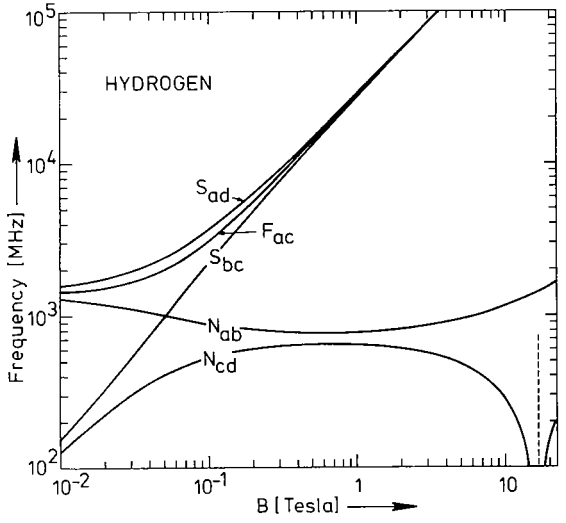

Fig. 2.3. Magnetic-field dependence of the hyperfine transitions in the hydrogen atom. The notation is given in fig. 2.1. F_{ac} is the transition used in the hydrogen maser; N_{ab}, S_{ad} and S_{bc} have also been observed experimentally in H↓ and H↓↕.

proportional to the square of the magnetic transition moment. ESR transitions are of order $(g_e\mu_B/g_n\mu_n)^2 = 4.4\times10^5$ stronger than NMR transitions. We note that the a→b and c→d transitions, which are pure NMR transitions in the high-field limit, are greatly enhanced at low field due to the spin state mixing caused by the hyperfine interaction. For longitudinal resonance the transition rate $\Gamma_{hf} \propto \sin 2\theta$ ($\sin\theta$ is given in eq. 2.4a). This rapidly weakens with increasing field, i.e.

$$\Gamma_{hf}(B \neq 0)/\Gamma_{hf}(B=0) = \sin 2\theta \simeq a/\mu^+ B = 2\varepsilon\,. \tag{2.10}$$

The hyperfine states have very long lifetimes and as a consequence the natural linewidths are extremely small. The observed linewidths are determined by radiation damping or inhomogeneities in the external field B. The latter is generally the most severe limitation. There are two field regimes where this problem can be minimized: for the a→c transition at approximately zero field and for the (a→b) or (c→d) transition at $B = 0.648$ T (at 765.48 MHz and 654.92 MHz response, respectively). For both fields, the derivative of the transition energy with respect to field is zero (see fig. 2.3). Due to this, field broadening is a second-order effect and less important.

The first resonance experiments on gaseous atomic hydrogen at low temperature were designed to optimize sensitivity for low-density gases, exploiting the considerations discussed above. Crampton et al. (1979) studied the a→c transition in a field of approximately 10^{-5} T, whereas Hardy et al. (1979) studied the a→b transition at $B \simeq 0.65$ T. At both fields the homogeneity requirements are quite modest and a field of 0.65 T is still low enough to assure a considerable hyperfine enhanced transition probability. Hardy et al. (1980a,b), Morrow et al. (1981) and Jochemsen et al. (1981) used zero-field resonance techniques to study H below 1 K. At the high magnetic fields ($B \geq 5$ T) required to study the spin-polarized gas, the homogeneity requirements are severe. Yurke et al. (1983) studied the build-up of nuclear polarization using NMR. van Yperen et al. (1983) succeeded in using ESR on the a→d and b→c transitions to study the time evolution of the hyperfine occupations n_a and n_b in a stabilized gas of hydrogen; Statt et al. (1985) have also used ESR to study properties of H in high fields. Recently, Johnson et al. (1984) have observed nuclear spin-waves in a low-density gas of hydrogen in high fields.

3. Interatomic interactions

One of the most attractive aspects of the hydrogen system is the high degree of precision to which the intraction between pairs and with external

fields is known. Unlike most larger atomic systems, these ab initio potentials have been confirmed by experiment. In addition, the pair approximation, i.e. the approximation that the interaction energy of the many-body system is the sum of the pair interactions, is a very good approximation for most properties of interest. The Hamiltonian of a gas of atomic hydrogen can be expressed as

$$H = T + H_Z + H_{hf} + H_D + H_{exch} + H_{dd} . \tag{3.1}$$

Here the kinetic energy is

$$T = \sum_j p_j^2/2m , \tag{3.2}$$

the Zeeman energy is

$$H_Z = -\boldsymbol{B} \cdot \sum_j (-g_e \mu_B \boldsymbol{s}_j + g_n \mu_n \boldsymbol{i}_j) , \tag{3.3}$$

and the hyperfine interaction is

$$H_{hf} = a \sum_j \boldsymbol{i}_j \cdot \boldsymbol{s}_j . \tag{3.4}$$

Terms (3.3) and (3.4) have already been discussed in the previous section and are responsible for the mixing of the spin states (fig. 2.1). In addition, during a collision there is a hyperfine interaction between an electron on one atom and a nucleus on another, which we shall ignore.

The most important pair interaction, which determines the binding of atoms into a stable molecular state, is $H_D + H_{exch}$ due to the Coulomb interaction. This interatomic potential has been calculated from first principles by Kolos and Wolniewicz (1965, 1974, 1975) and is the most accurately known pair potential of all atomic systems. In the ground electronic state, ignoring nuclear spin (i.e., the hyperfine interaction), there are two potential curves: the singlet, $S = 0$, and the triplet, $S = 1$, state, where $\boldsymbol{S} = \boldsymbol{s}_1 + \boldsymbol{s}_2$. In fig. 3.1 we see the singlet potential $^1\Sigma_g^+ \equiv V_s$ which has a well minimum $\varepsilon_s/k = 55\,100$ K at $r_{min} = 0.74$ Å. This potential supports bound states. Dabrowski (1984) has extensively analyzed the spectrum of H_2 and made comparisons between theory and experiment. The ground vibrational–rotational state of H_2 has an experimental dissociation energy of $D_0(H_2) = 36\,118.3(3)\,cm^{-1} \simeq 51\,967$ K (Herzberg 1970), $D_0(D_2) = 36\,748.88(30)\,cm^{-1} \simeq 52\,874$ K (LeRoy and Barwell 1975). The best value available for T_2 is probably the theoretical value of

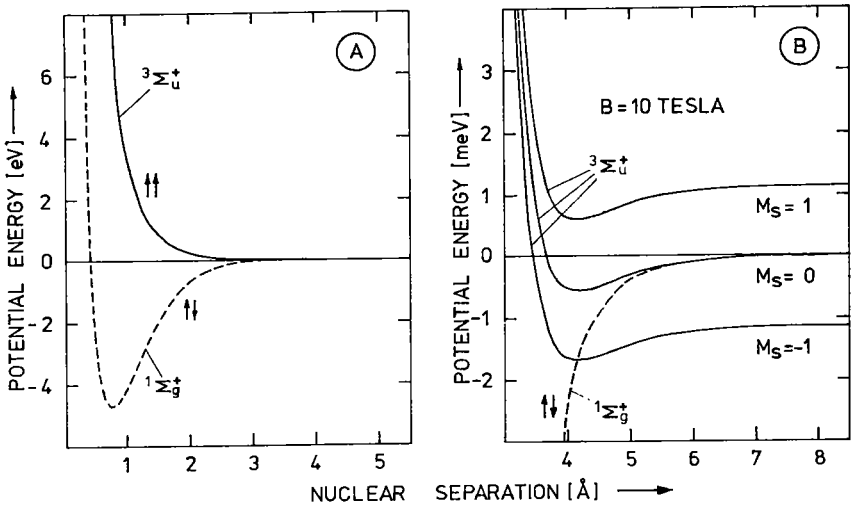

Fig. 3.1. (a) The singlet and triplet interatomic potentials of hydrogen according to calculations of Kolos and Wolniewicz (1965, 1968, 1974, 1975). (b) The potentials of (a) in a high magnetic field on a magnified vertical scale.

Kolos and Wolniewicz (1968): $D_0(T_2) = 37\,028.89\ \text{cm}^{-1} \simeq 53\,277$ K. LeRoy (1971) has made the most extensive study of the number of bound and quasi-bound states of the $^1\Sigma_g^+$ potential of H_2 using the Kolos–Wolniewicz potential and finds 301 bound levels and 47 quasi-bound states. The quasi-bound states are long-lived states with an energy in the continuum. These are resonance states of the effective potential, i.e., the singlet or triplet potential plus the (repulsive) rotational barriers. A few of these potentials are shown in fig. 3.2 for both the singlet and triplet potentials, and high-lying bound states near the continuum are shown for H in fig. 3.3. Potential parameters and energy levels will differ for D_2 and T_2 due to the dependence of zero-point energy on mass (table 7.1).

Due to the indistinguishability of the protons, the wavefunction of the H_2 molecule must be antisymmetric under proton exchange. This imposes a restriction on the molecular quantum numbers. Under nuclear exchange the rotational part of the wavefunction ψ_J is symmetric for even rotational quantum number J and antisymmetric for odd J. The allowed values of the nuclear spin states are $I = 1$, where $\boldsymbol{I} = \boldsymbol{i}_1 + \boldsymbol{i}_2$. The three $I = 1$ states correspond to symmetric wavefunctions; $I = 0$ to antisymmetric. As a consequence of this, molecules with even J have $I = 0$ and odd-J ones have $I = 1$. The former is called para-H_2, the latter ortho-H_2. The same combinations and notation exist for T_2, whereas D_2 must have a symmetric

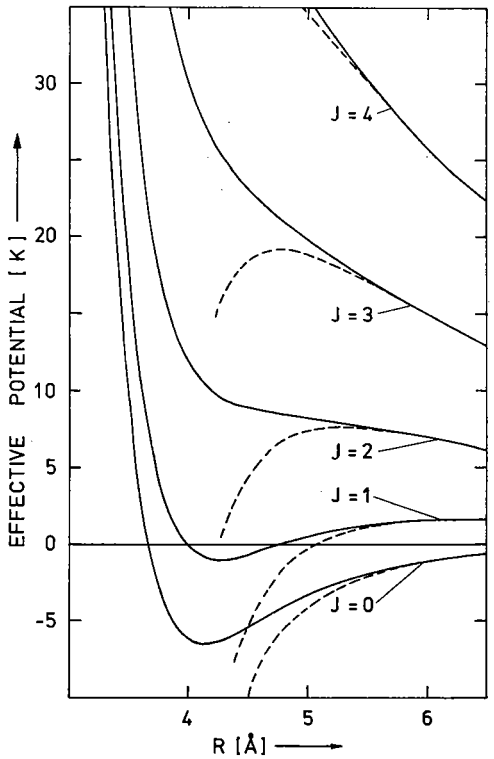

Fig. 3.2. The effective triplet interatomic potential of hydrogen, including the centripetal barrier, for a few of the lower rotational states. The angular momentum J is designated L in the text (after Walraven 1984).

wavefunction under nuclear exchange as the spin of the deuteron is 1. The designations and states are summed up in table 3.1.

In contrast to the singlet state, we see in fig. 3.1a that the triplet potential ${}^3\Sigma_u^+ \equiv V_t$ is essentially a repulsive interaction on the scale shown. Since the long-range Van der Waals interaction is always attractive and the repulsive electronic overlap forces are short-range, the atoms must have a negative potential well. The well can be seen on the expanded scale in fig. 3.1b (curve labeled $M_s = 0$). Its well depth of $\varepsilon_t/k = 6.46$ K at $r_{min} = 4.16$ Å is insufficient to support a bound diatomic-molecular state. In the same figure we show the effect of an applied magnetic field. Taking into consideration only the electronic magnetic moment, we see that the singlet potential is field-independent, whereas the degeneracy of the triplet potential is lifted by the field.

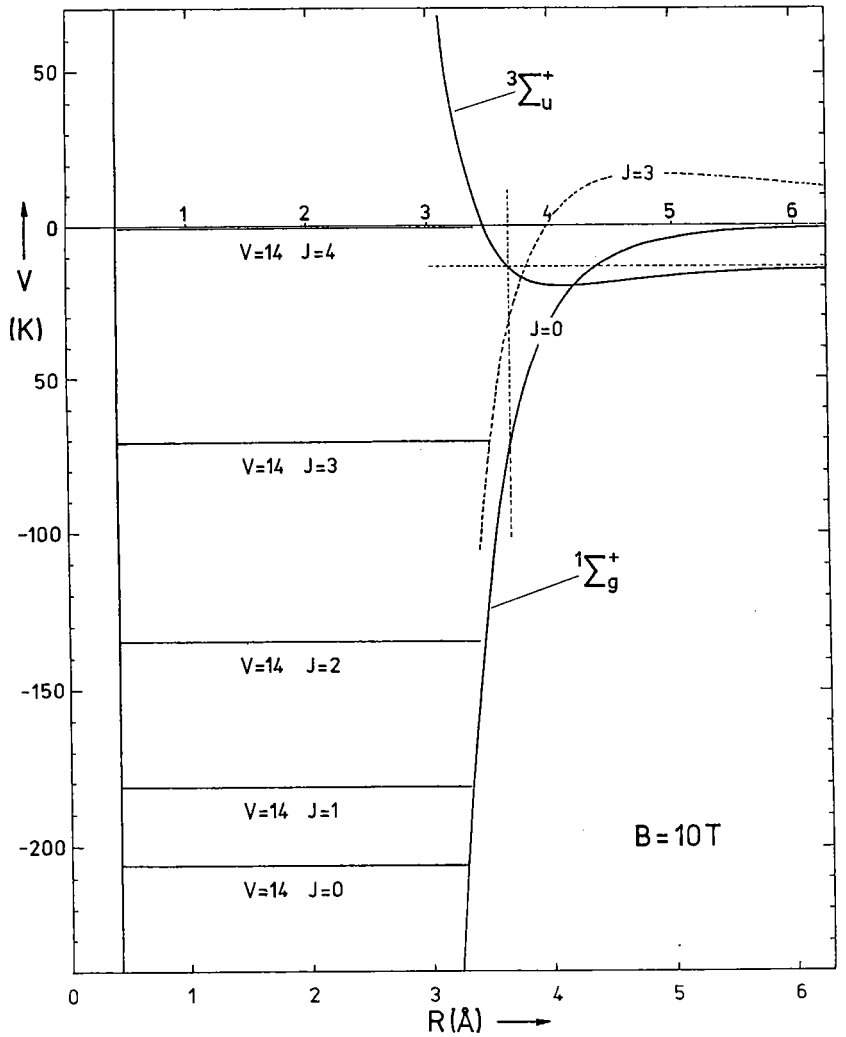

Fig. 3.3. High-lying bound states near the continuum of the singlet potential of hydrogen. (After Walraven 1984.)

It is noteworthy that the attractive part of the H–H triplet potential is the weakest of all interatomic potentials. For comparison, in fig. 3.4 we show a number of other potentials for weakly interacting species. It is believed that two ^{4}He atoms with a well depth of $\varepsilon/k \simeq 10.5$ K will just form a bound state with dissociation energy $D/k \ll 1$ K, although the bound dimer has never been observed.

Table 3.1

Allowed combination of nuclear-spin states and rotational states for hydrogen, deuterium, and tritium, and the ortho–para designations. Antisymmetric is abbreviated by AS and symmetric by S; I_{mol} is the total molecular nuclear spin and L the rotational quantum number.

Molecule and spin of nucleon		I_{mol}	L	$\psi(I_{mol})\psi(L)$	Nuclear weight g_I	Designation
Hydrogen,	State	0	Even			para
Tritium;	Symmetry	AS	S	AS	1	
$I_N = \frac{1}{2}$	State	1	Odd			ortho
	Symmetry	S	AS	AS	3	
Deuterium;	State	1	Odd			para
$I_N = 1$	Symmetry	AS	AS	S	3	
	State	0, 2	Even			ortho
	Symmetry	S	S	S	6	

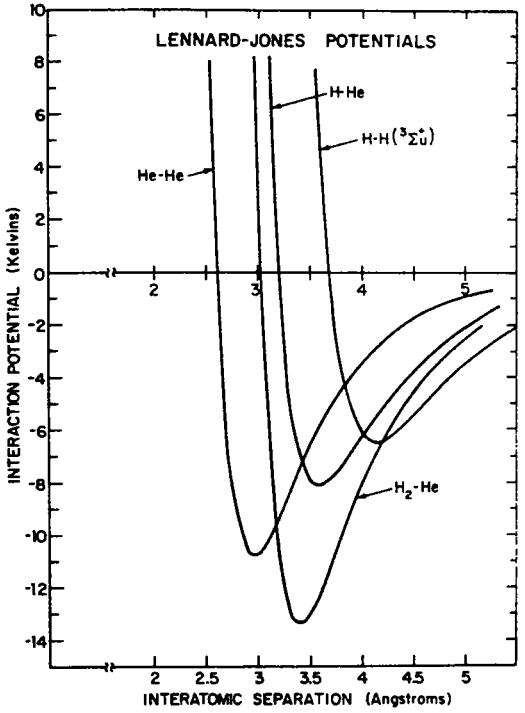

Fig. 3.4. Lennard–Jones potentials of some weakly interacting pairs (after Silvera 1984).

Later in this section, after a complete discussion of interactions, we shall return to discuss how spin polarization can be used to stabilize atomic hydrogen. We now express the direct and exchange term of eq. (3.1) in terms of V_t and V_s:

$$H_D + H_{exch} = \tfrac{1}{2}\sum_{i,j} V_D(r_{ij}) + \tfrac{1}{2}\sum_{i,j} J(r_{ij}) s_i \cdot s_j \,, \tag{3.5}$$

where $V_D \equiv \frac{1}{4}(V_s + 3V_t)$ and $J \equiv V_t - V_s$. A rather accurate fit to the tabulated potential values of Kolos and Wolniewicz (1974), useful for calculations, has been given by Silvera (1980):

$$V_t = \exp(0.096\,78 - 1.101\,73r - 0.039\,45r^2) + F_c(r)\left(-\frac{6.5}{r^6} - \frac{124}{r^8} - \frac{3285}{r^{10}}\right), \tag{3.6}$$

with the cut-off function

$$F_c(r) = \exp -\left(\frac{10.04}{r} - 1\right)^2, \quad r < 1.28 r_{t\,min},$$
$$= 1, \quad r > 1.28 r_{t\,min}, \tag{3.7}$$

where $r_{t\,min}$ is the minimum in the triplet potential curve. In eq. (3.6) atomic units are used (1 Hartree = 219 474.6 cm^{-1}, 1 Bohr = 0.529 177 Å). The fit is based on approximating the potential with an exponential repulsive part (first term) plus the long-range attractive part (second term) which is exponentially attenuated at short distances as proposed by Ahlrichs et al. (1976). The exchange energy can be fit over a range from 1 to 12 Bohr by

$$J(r) = \exp(-0.288 - 0.275r - 0.176r^2 + 0.0068r^3). \tag{3.8}$$

V_s can be obtained by combining eqs. (3.6) and (3.8), however, this is restricted to $r > 1$ Bohr since Kolos and Wolniewicz did not tabulate the potential for smaller values of r. For calculations with V_s in the region of its well, the tabulated values are recommended, with interpolation for intermediate points.

A word of caution is in order for using the Kolos and Wolniewicz (KW) potential curves for calculational purposes. The "best" tabulated values for the singlet- (1975) and triplet-potential (1974) energy curves (KW 1975 and KW 1974, respectively) are obtained within the Born–Oppenheimer approximation. To reproduce the experimental values for the vibrational and rotational levels this potential is not sufficient and one also has to apply adiabatic, nonadiabatic and relativistic corrections (for phenomena not included in eq. 3.1), which are incompatible with the simple potential concept (see Kolos and Wolniewicz 1975, Wolniewicz 1983). Bishop and Shih (1976) have proposed an effective Schrödinger equation to calculate nonadiabatic rovibronic energies, yielding improved agreement with experiment. For some properties (like spin exchange) at very low temperatures these small corrections may have a rather dramatic effect, depending on the exact location of the $H_2(v = 14, J = 4)$ vibrational–rotational level, which is close to the dissociation limit (see Dabrowski 1984).

The final set of important interactions for the hydrogens are the magnetic dipole–dipole interactions, which can involve electron–electron, electron–nucleon and nucleon–nucleon magnetic dipole interactions. All are of the same form and can be written as

$$H_{\mathrm{dd}} = \frac{\mu_0}{4\pi}\frac{\hbar^2}{2}\frac{1}{r_{ij}^3}\sum_{i,j}[\gamma_{\mathrm{e}}^2 f(s_i, s_j) - \gamma_{\mathrm{e}}\gamma_{\mathrm{n}}[f(s_i, i_j) + f(i_i, s_j)] + \gamma_{\mathrm{n}}^2 f(i_i, i_j)], \quad (3.9a)$$

where

$$f(s_i, i_j) = [\boldsymbol{s}_i \cdot \boldsymbol{i}_j - 3(\boldsymbol{s}_i \cdot \hat{\boldsymbol{r}}_{ij})(\boldsymbol{i}_i \cdot \hat{\boldsymbol{r}}_{ij})]. \quad (3.9b)$$

Here r_{ij} is the distance between spin $\boldsymbol{s}_i$ and $\boldsymbol{i}_j$ and $\hat{\boldsymbol{r}}_{ij}$ is a unit vector. As we shall see later, the term H_{dd} is the dominant cause of relaxation between the hyperfine levels in high magnetic fields and is responsible for three-body recombination of highly polarized atomic hydrogen at high densities. In general, the term $f(i_i, i_j)$ is negligible.

Until now we have only discussed the electronic singlet and triplet potentials of the H–H interaction. When nuclear spin is also taken into account, due to the spin multiplicity ($4 \times 4 = 16$ spin states), the number of interaction potentials is far greater, but it usually suffices just to consider the singlet and triplet. Nevertheless, it is useful to consider all the possible potential curves.

First, consider the interaction potentials between a pair of H atoms in zero magnetic field. In the absence of the hyperfine and dipolar interactions, we have the ground-state singlet and degenerate triplet potentials. Harriman et al. (1967) have analyzed the H–H hyperfine curves and Milleur et al. (1968) D–D curves; Uang et al. (1981) have treated H–D, D–T and H–T in an applied magnetic field. The H–H potentials are shown in fig. 3.5. There are 16 hyperfine states, but due to degeneracy, only 11 distinct potential curves exist for H–H (36 with 22 distinct potentials for D–D). H_{D}, H_{exch}, and H_{dd} depend strongly on the nuclear separation, whereas the hyperfine constant, a, is independent of range, except for very close approach. Comparing the magnitudes to a, we find $a = (\mu_0/4\pi)(\mu_{\mathrm{e}}^2/r^3)$ for $r \simeq 3.3$ Å (6.2 au); the hyperfine splitting is equal to the singlet–triplet splitting $[a = J(r)]$ for $r \simeq 5.8$ Å (11 au).

For the long-range region, $r \geq 6.75$ Å, the exchange can be ignored ($J/a < 0.1$) and $\boldsymbol{f}_i = \boldsymbol{s}_j + \boldsymbol{i}_j$, m_{fj} are good quantum numbers. For separated atoms (J, $\mu_i^2/r^3 \to 0$) in zero applied field, there are three curves with energies $-\frac{3}{2}a$, $-\frac{1}{2}a$, and $\frac{1}{2}a$ with 1-, 6- and 9-fold degeneracies, respectively. These correspond to both atoms singlet, singlet–triplet, and triplet–triplet, respectively. For intermediate ranges, $5 < r < 6.75$ Å, all terms in eq. (3.1) must be considered. For short ranges, $r < 5$ Å, H_{exch} is dominant and $\boldsymbol{S} = \boldsymbol{s}_1 + \boldsymbol{s}_2$, M_{s} and $\boldsymbol{I} = \boldsymbol{i}_1 + \boldsymbol{i}_2$, M_I are all good quantum numbers. For longer ranges, where I is no longer a good quantum number, the

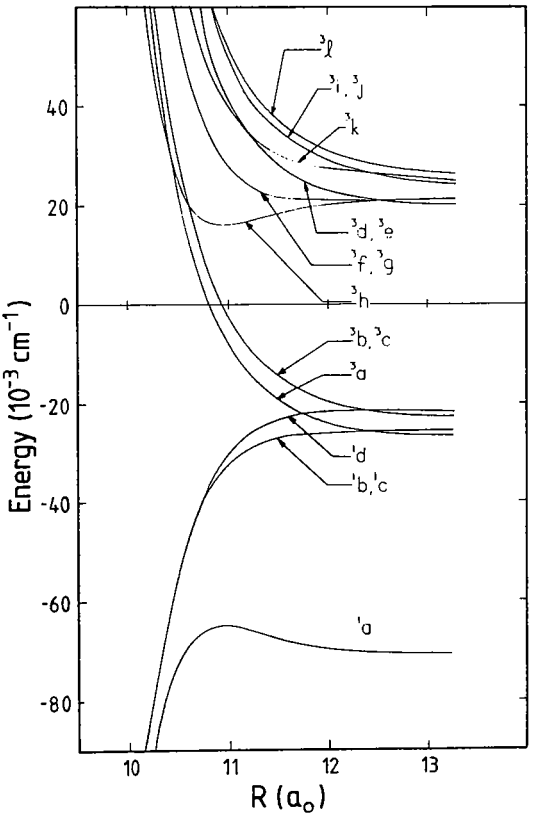

Fig. 3.5. Spin independent part of the 16 (5 are degenerate) interatomic potentials of H for the hyperfine states as a function of separation R given in Bohrs. For large separation there are three curves with degeneracies 1, 6 and 9 and energies $-3a/2$, $-a/2$, and $a/2$ depending only on the single atom hyperfine interactions (after Harriman et al. 1967, their notation is used).

ortho-para classification made for short ranges in terms of the quantum number I can still be made in terms of J. A simplified argument can be made by considering large distances, so that we are only concerned with atomic exchange. Since the Hamiltonian, eq. (3.1), is symmetric under permutation (P) of two atoms (see table 6.4a), the spin states can be separated into 10 symmetric ($P = +1$) and 6 antisymmetric ($P = -1$) states. Under atomic exchange the wavefunction must be symmetric for the composite particles. Thus, the six odd-spin states must couple with the odd-orbital (ortho) states, and the other 10 spin states must have even rotational quantum numbers (para). The restriction to atom exchange is

easily lifted, but the argument is longer. For deuterium one finds 15 symmetric and 21 antisymmetric spin states (see table 6.4b).

It is now clear that the spin character of a state depends on the range. In order to characterize a potential curve as triplet or singlet, it is useful to examine the fractional triplet character of a pair of interacting atoms which is given by

$$\tfrac{1}{2}\langle S^2\rangle = \tfrac{3}{4} + \langle s_1 \cdot s_2\rangle \,. \tag{3.10}$$

This has the value 1 for a pure triplet state and 0 for a pure singlet, and varies with separation for other states. Similarly $\frac{1}{2}\langle I^2\rangle$ gives the fractional triplet character of the nuclear spin.

Consider now the effect of an applied magnetic field. In the infinite-field limit m_{s_j} and m_{i_j} are good quantum numbers for individual atoms. For pairs of atoms the electronic singlet has $M_S = m_{s_1} + m_{s_2} = 0$ and the triplet has $M_S = 1, 0, -1$ as shown in fig. 3.1. Inclusion of nuclear spin increases the number of states to 4 and 12 for the singlet and triplet, respectively; these additional states and splittings are not shown in fig. 3.1.

For a high, but finite, field the triplet character of the states can be determined by evaluating eq. (3.10). Consider two hydrogen atoms at large separation in the $|\mathrm{b}\rangle$ state (fig. 2.1), then $\frac{1}{2}\langle S^2\rangle = 1$. However for two $|\mathrm{a}\rangle$-state atoms the amount of triplet character is $\frac{3}{4} + \frac{1}{4}(2\sin^2\theta - 1)^2 \simeq (1 - \sin^2\theta)$ for high fields; the atoms have a small but finite singlet character. For short range the exchange will dominate and S becomes a good quantum number; the interaction is then either singlet or triplet in nature.

Let us now discuss how spin polarization stabilizes a gas of atomic hydrogen. Since a pair of atoms interacting on the triplet potential cannot form a bound state, clearly, if an assembly of atoms could be maintained in the spin-polarized state such that all pairs mutually interact on the triplet potential, the gas will be stable against recombination to H_2. An assembly of atoms in electron spin-down states (high-field hyperfine states $|\mathrm{a}\rangle$ and $|\mathrm{b}\rangle$ of fig. 2.1) is called spin-polarized hydrogen and symbolized by H↓; an assembly in the electron spin-up states $|\mathrm{c}\rangle$ and $|\mathrm{d}\rangle$ is represented by H↑. If the assembly of atoms are all in the $|\mathrm{b}\rangle$ state, this is called doubly-polarized hydrogen, H↓‡. From the discussion of the previous paragraph we see that for H↓‡, all pair interactions are pure triplet and we expect this to be more stable than H↓. The wavefunction of a pair with at least one atom in the a-state will, in high field, have a small yet finite degree of singlet character, enabling recombination to the molecular state. Analogous definitions are used for deuterium (D) and tritium (T). Finally, we note that if an atom in the $|\mathrm{a}\rangle$ or $|\mathrm{b}\rangle$ state interacts with one in the $|\mathrm{c}\rangle$ or $|\mathrm{d}\rangle$ state, the interaction

contains a strong singlet component and recombination during a collision has a much greater probability.

From fig. 3.1 we see that in zero-field the singlet state is lower in energy than the triplet state for all separations. At $T = 0\,\mathrm{K}$ the singlet is the equilibrium state to which a triplet state will relax, followed by recombination into the bound molecular state. At elevated temperatures ($T \gg 2\mu_B B/k$) then the thermal occupation of singlet to triplet state is 1:3 (for H, D and T). If equilibrium is maintained, the gas will continue to rapidly recombine until no atoms remain. With an applied magnetic field, the triplet $M_s = -1$ state is lower in energy than the singlet. Outside of a certain range and for low temperatures ($T \ll 2\mu_B B/k$) where H$\downarrow$ is the equilibrium state, a great degree of stability is offered to the system. Again at high temperatures, population of singlet states enables recombination to rapidly proceed. However, even at low temperature, we note that since a gas of H$\downarrow$ is always in motion the region with $V_s < V_t$ is accessible and at best we can speak of metastability for magnetic fields that are available in the laboratory.

4. Single-atom interactions with helium surfaces

In the study of the lifetime enhancement of a gas of atomic hydrogen, the surface appears to play a dominant and controlling role for all densities, at low enough temperatures. As already mentioned in the introduction, at elevated temperatures the interaction with most surfaces, in particular metals, leads to very rapid recombination. Two types of recombination processes can be identified on surfaces with attractive potentials for atoms. In one, deep traps are rapidly filled with hydrogen atoms; mobile atoms recombine at these sites to form H_2 and the sites are then again rapidly filled by another atom. This leads to a first-order decay process of the surface number density σ, i.e. $\dot{\sigma} \propto -\sigma$. In the second type of process, mobile atoms on the surface interact with each other to recombine; this can be a second- or third-order process.

Early experiments by Crampton et al. (1979), Hardy et al. (1979) and Silvera and Walraven (1979) demonstrated that H could be observed for $T \geq 5\,\mathrm{K}$, although lifetimes were quite limited. In the initial stabilization experiments of H$\downarrow$ (Silvera and Walraven 1980a) at low temperatures ($T < 1\,\mathrm{K}$) and high fields, it was found that on ordinary surfaces H$\downarrow$ rapidly recombined and no detectable sample could be produced. However, when the surfaces were covered with a thin film of ^{4}He, H$\downarrow$ could be collected for long pèriods of time. The reason for this is that H has a very small adsorption energy, ε_a, on ^{4}He, and according to eq. (1.7), $\sigma =$

$n\lambda_{th}\exp(\varepsilon_a/kT)$, the surface coverage should be small. On ^{4}He, only second- and third-order decay processes are significant, and these become negligible for $T \geqslant \varepsilon_a/k$ due to the small value of σ. Because of its importance, we shall concentrate our attention on this surface.

The properties of free-helium surfaces have been reviewed by Edwards and Saam (1978) and more recently by Edwards (1982). The currently accepted picture is that ^{4}He presents a flat, translationally invariant impenetrable surface to hydrogen, with an adsorption energy, $\varepsilon_a/k \simeq 1$ K. The adsorption potential is believed to be about 5 K deep with a single bound state; ε_a is the energy required to remove an H atom from this surface state. The expectation value for the distance of the atom above the surface is about 6 Å. The atom moves on the surface as an almost free-particle in two-dimensional momentum states, with effective mass $m \simeq m_H$.

The helium surface itself is flat (but not rigid, as elementary excitations such as ripplons exist) and there is no evidence that the adsorbed hydrogen causes a significant puckering or dimpling of the underlying surface. The helium density does not reduce abruptly from its bulk value to zero at the surface, but has a more gradual fall-off similar to a Fermi function with a width of a few Å (Edwards and Fatouros 1978). Recent calculations (Pandharipande et al. 1983) indicate that this width may be as large as 7 Å.

The interesting question of whether hydrogen and its isotopes penetrate into bulk helium has been addressed by Miller (1978, 1980), Guyer and Miller (1979), and more recently, by Kürten and Ristig (1985). The latter, more rigorous calculation confirms the general trends of the earlier results. The quantity calculated is the change of the chemical potential, μ, when a He atom from the bulk is replaced with a foreign atom. For positive μ, the atom does not penetrate into the bulk (at $T = 0$ K) unless it has kinetic energy μ. At the saturation density of ^{4}He, Kürten and Ristig obtained values of $\mu \simeq 75$ K, 40 K, and 27 K for H, D and T, respectively, so that none of these atoms penetrate the surface (uncertainties of order 5–10 K exist due to uncertainties in the He–H pair potential). μ is strongly density dependent and in going over to ^{3}He surfaces with a molar volume of 36.8 cm^3/mol compared to 27.6 cm^3/mol for ^{4}He, these values could drop by more than a factor of two. In fact T on ^{3}He might be similar to ^{3}He on ^{4}He with the possibility of dissolving into the bulk.

Another problem of significance for the stability of H$\downarrow$ is the question of "what happens to the H_2 produced by recombination?". If it accumulates on the He surface it could seriously affect the environment of the H$\downarrow$ gas. Silvera (1984) has investigated this problem experimentally. While spraying a cold molecular beam of H_2 on the surface of superfluid liquid ^{4}He, he observed the formation of macroscopic clusters of H_2 within the bulk liquid

^{4}He. This provided evidence that H_2 penetrates the ^{4}He surface either in monomolecular or clustered form. Kürten and Ristig have also analyzed this system and found $\mu = -23$ K for H_2 with lower values for D_2 and T_2, implying that all of these molecules penetrate into the bulk liquid as single molecules.

4.1. The surface adsorption potential

An accurate calculation of the adsorption potential presented to a hydrogen atom by a He surface is a formidable task. At large distances, z, from the surface it is easily shown that the potential varies as z^{-3}. However, near the surface the calculation requires knowledge of the surface density profile, the two-particle (He–He) distribution function and the kinetic-energy density, none of which are precisely known. Calculations have been carried out by Mantz and Edwards (1979), Guyer and Miller (1979) and De Simone and Maraviglia (1979). Stwalley (1982) has provided a scaling model which yields nice predictions for the isotopes. Of the ab initio type calculations, only the Manz–Edwards result, which gives a lower bound for ε_a of 0.6 K, is reasonably close to the value which was experimentally determined afterwards (see section 5). Mantz and Edwards used an extension of the Feynman–Lekner variational principle. The Hamiltonian for the N particle ^{4}He liquid with a He atom replaced by an H atom at the surface was written down. The expectation value of the energy was minimized and the resulting Euler–Lagrange equation could be written in the form of a single-particle Schrödinger equation of the H atom in the effective potential V_{eff} of the helium. The motion of the particle in the plane (x, y) was described by free-particle momentum states, whereas the distribution in the z direction was found from

$$-\frac{\hbar^2}{2m}\frac{\mathrm{d}^2\phi(z)}{\mathrm{d}z^2} + V_{\text{eff}}(z)\phi(z) = \varepsilon_z\phi(z)\,. \tag{4.1}$$

Solutions of this equation give the bound states of hydrogen on ^{4}He, and eigenvalues

$$\varepsilon = \varepsilon_z + \hbar^2\kappa^2/2m\,, \tag{4.2}$$

where the translational energy in the plane is included, $\boldsymbol{\kappa}$ being a two-dimensional wave vector. H was found to have a single bound state, $\varepsilon_z = -\varepsilon_a$ with $\varepsilon_a/k \geq 0.63$ K. Due to the larger masses, and thus smaller zero-point energy, D and T had larger values of ε_a, as well as a very weakly bound second state. The probability density, $\phi^2(z)$, and $V_{\text{eff}}(z)$ are shown

in fig. 4.1. The peak of $\phi^2(z)$ is several Å from the surface and the distribution is quite broad, extending to ~20 Å for H. Surface deformation due to electric polarization effects which increase ε_a have been estimated by Papoular et al. (1984). The effective potential for ^{3}He on ^{4}He is also shown in fig. 4.1. By contrast to H, the ^{3}He resides right at the surface ($z = 0$). This potential has the interesting property that the energy is lower in the interior than in the vacuum so that atoms "desorb" into the bulk.

Stwalley (1982) has used a potential of the form $-c/z^3$, cut-off at a distance z_0 from the surface by an infinite repulsive wall and solved for the bound states using a semi-classical solution. His model apparently has nice predictive values for the isotopes (see table 5.1, with a comparison to experiment).

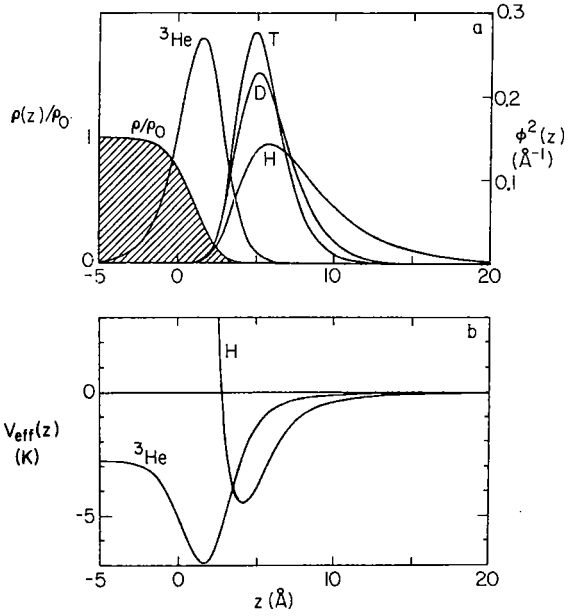

Fig. 4.1. V_{eff} for H on ^{4}He and ^{3}He on ^{4}He. The upper graph shows the probability density for H, D, T and ^{3}He as well as the surface profile of ^{4}He (after Mantz and Edwards 1979).

4.2. Inelastic surface collision

In thermodynamic equilibrium of hydrogen in a chamber with liquid-helium walls there is a rapid and continual exchange of atoms between bulk (gas) states and surface states. In this section we examine some of the

processes for establishing equilibrium. Let us first provide some numerical estimates. In the low-density, high-temperature limit, $\sigma = \lambda_{th} n \times \exp(\varepsilon_a/kT)$. The thermal de Broglie wavelength $\lambda_{th} = 39.0$ Å, and $\sigma = 5.7 \times 10^{11}$ atoms/cm^2 for $n = 10^{16}$ atoms/cm^3, $\varepsilon_a/k = 1.0$ K and $T = 0.2$ K. This is a seemingly small, but very important surface coverage. Under these conditions, the atomic collision rate per unit surface area, $\phi = \frac{1}{4} n\bar{v}$, is 1.63×10^{19} atoms cm^{-2} s^{-1} [$\bar{v} = (8kT/\pi m)^{1/2} = 6482$ cm/s is the average atomic velocity]. Alternatively, the surface coverage is given by

$$\sigma = \phi t_a \alpha_s = \tfrac{1}{4} n\bar{v} t_a \alpha_s \,, \tag{4.3}$$

where t_a is the average adsorption time and α_s is the sticking probability per collision. Using both expressions for σ yields

$$t_a = [4\lambda_{th} \exp(\varepsilon_a/kT)]/v\alpha_s \,. \tag{4.4}$$

Evaluating for our standard conditions, we find $t_a = 1 \times 10^{-6}$ s, where we have used the experimental value $\alpha_s = 0.035(4)$ measured by Jochemsen et al. (1981) using resonance techniques. They determined this from the ratio of the time between wall collisions to the time between stickings. The former was computed, the latter extracted from either relaxation time T_2 or the linewidth. For H on ^{3}He surfaces, they found $\alpha_s = 0.016(5)$.

In all experiments carried out to date, the gas and the He surface are close to being in thermodynamic equilibrium. Evidently, equilibrium is rapidly established and requires only a few surface collisions. For a sample cell with a typical wall-to-wall dimension of 1 cm, the equilibrium time is of order or less than 1 ms. This assumes that there is a reasonable transfer of energy per collision. Salonen et al. (1982) measured a fractional energy loss per collision of $\alpha = 0.2(1)$, using ballistic pulses of H↓. This experiment used the planar heater and bolometer detector shown in fig. 4.2. During a heat pulse of a few μs, gas atoms striking the heater pick up energy. This group of atoms propagates towards the bolomoter, depositing energy which is detected by monitoring the heating of the bolometer. From the time-of-flight spectra, the energy transfer coefficient α could be determined. In view of the small value of the sticking coefficient, this large value of 0.2 is surprisingly large. Recently, Salonen et al. (1984) have confirmed this result by a static measurement and find the temperature dependence shown in fig. 4.3. In this experiment a thin-film carbon bolometer is suspended in the gas and ohmically heated to temperatures above the cell temperature. Introduction of H↓ gas cools the bolometer by energy transport to the cooler walls. By monitoring the power required to

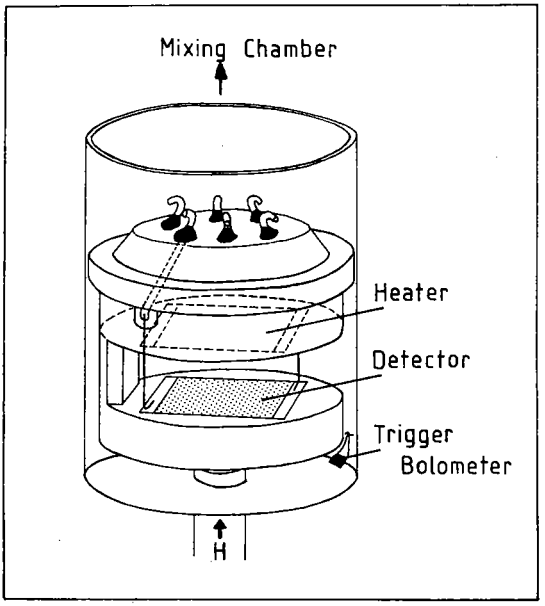

Fig. 4.2. The cell used for studying ballistic heat transfer of H to He walls. All surfaces are covered with He and the cell is filled with H↓. H↓ atoms traverse from the heater to the bolometer (after Salonen et al. 1982).

maintain a constant temperature as a function of gas density, α was determined. The important point to note in fig. 4.3 is that in this temperature range α decreases with increasing temperature, rather than increases. On theoretical grounds one expects α to go to zero as $T \rightarrow 0$ K.

There are three types of surface collisions: elastic, inelastic nonsticking and sticking collisions which are, of course, inelastic. In the following we shall discuss some of the mechanisms for energy transfer. Until now we have considered the surface to be flat and static with a uniform mass-density profile normal to the surface (z). In order to accommodate energy, the surface must have dynamical modes, and the height of the surface, $h(r)$, must be able to vary with position. Phonon excitations of the bulk liquid helium are important for higher temperatures ($T \geqslant 1$ K). The intrinsic elementary excitations of the ^{4}He surface are ripplons (Atkins 1957) which are related to film height fluctuations by

$$h(r) = \frac{1}{A^{1/2}} \sum_q h_q \, e^{iq \cdot r} , \tag{4.5}$$

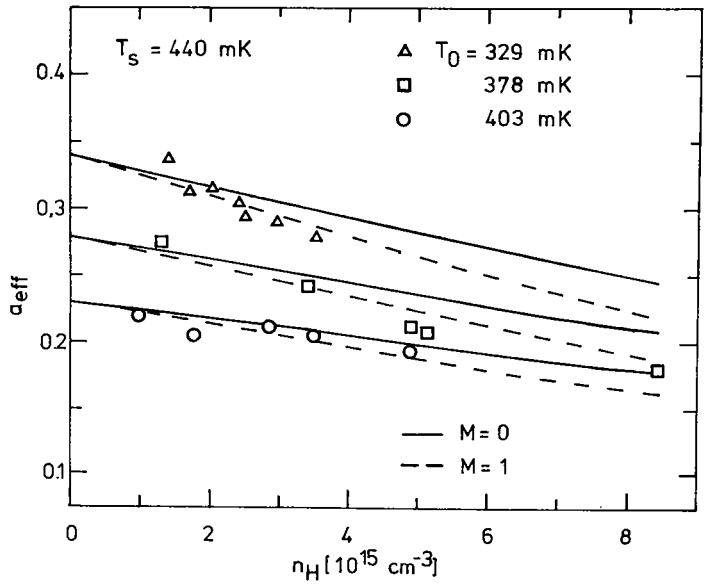

Fig. 4.3. The energy transfer coefficient as a function of H↓ density. T_s is the bolometer temperature and T_0 is the gas temperature (after Salonen et al. 1984).

where

$$h_q = (\hbar q/2\rho\omega_q)^{1/2}(r_q^\dagger + r_{-q}) . \tag{4.6}$$

Here $r_q^\dagger$ is a ripplon creation operator for wavevector q and $\omega_q^2 = gq + (\gamma/\rho_0)q^3$, where γ and ρ are the surface tension and the density of the liquid, and in this case g represents the Van der Waals force per unit mass exerted by the substrate on the helium. When an H atom strikes the surface, the surface is distorted by dynamic or static creation of ripplons. In the former case, an energy $h\omega_q$ is transferred. In the latter, the surface is statically deformed (dimpled) in the vicinity of the H atom; the distortion moves with the atom, and the atom, along with its distortion, is called a polaron. Kumar (1981) and Guyer et al. (1981, 1982) introduced the idea of a polaronic distortion, and it appeared to be an important effect with a large effective mass for H and H–H coupling via ripplons. This now is recognized as invalid, mainly due to an unphysical choice of the H–ripplon coupling (Zimmerman 1982, Wilson and Kumar 1983). The calculated effective mass of H is only a few percent larger than the bare mass and the static surface distortion is minor. This implies that two-dimensional free-particle states are a good representation for translational motion.

4.3. Sticking probability

The sticking probability of H on ^{4}He has been calculated by Zimmerman and Berlinsky (1983) and Kagan and Shlyapnikov (1983). Both articles used essentially the same model; we shall describe Zimmerman and Berlinsky's results. They expanded the film thickness dependent H–He interaction in ripplon coordinates and used time-dependent perturbation theory to calculate the transition rate of free-atoms into bound surface states. The dominant contribution arose from single-ripplon creation. Normalizing to the incident flux of atoms gave the sticking probability as a function of energy and angle of incidence. This was then averaged over the angular coordinates and averaged with a Boltzmann distribution to yield $\alpha_s(T)$, which for low T varied as $T^{1/2}$. In order to obtain numerical results with tractable integrals they modeled the Mantz–Edwards adsorption potential with a Morse potential. The calculated result, shown in fig. 4.4, is about 50% higher than the experimental value of 3.5×10^{-2}.

A serious criticism of this calculation can be presented. The approxim-

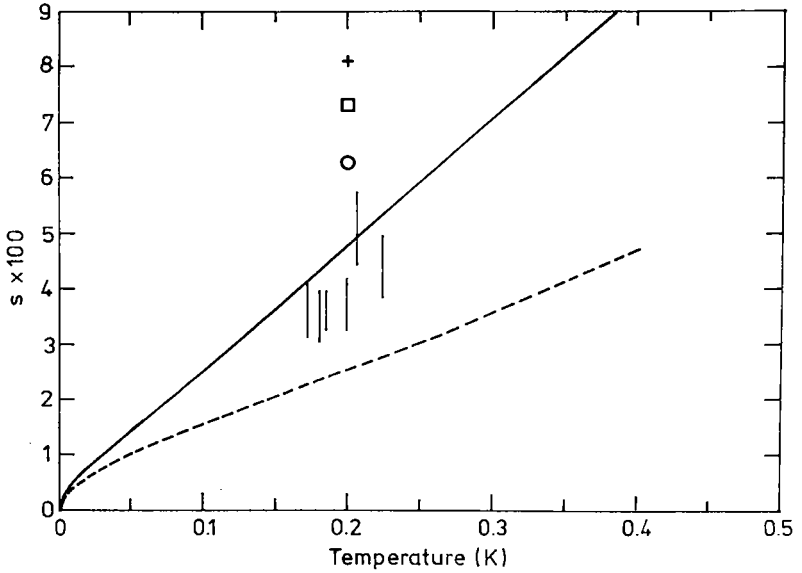

Fig. 4.4. Thermally averaged values of the sticking probability of H on ^{4}He as a function of temperature (solid line). The dashed line is an approximation using a q-independent coupling. The vertical lines represent experimental values. The circle, square and plus are values found by varying ε_a with the circle representing the lowest value (0.89 K) (after Zimmerman and Berlinsky 1983).

ation of replacing the long-range (z^{-3}) surface potential with a short-range Morse potential was not investigated and does not appear to be good. Brenig (1980) has shown that the matrix elements for the two potentials have different q dependencies which implies different temperature dependencies.

4.4. Kapitza thermal resistance at the gas–liquid interface

Due to the release of recombination energy, $D_0 = 4.6$ eV, there is a large source of internal heating in a gas of H↓. The rate of heating ($\dot{Q}$) increases with density, since $\dot{Q} = \frac{1}{2}VD_0(K^{(2)}n^2 + K^{(3)}n^3)$ where V is the volume and the K^i's represent recombination-rate constants. For the gas to remain cold, this heat must be transferred to the He film and from the film to the cell (copper) which is connected to a thermal bath (refrigerator). If the paths of thermal conduction are not well-designed, large thermal gadients can develop in the system. In the following discussion the finite thermal conductivity of the gas, the helium and the copper will be ignored, as we shall concentrate on the Kapitza resistance, R_K. R_K exists at heat path interfaces connecting materials in different phases or different materials. This results in a temperature step, ΔT, at the interface. It is defined in terms of the heat flow per unit time

$$\dot{Q} = \Delta T/R_K \,. \tag{4.7}$$

R_K is inversely proportional to the contact area, A, and in general is temperature dependent, with $R_K^{-1} \to 0$ as $T \to 0$ K. Due to the thermal step there can be three temperatures: the gas temperature, T, the helium temperature, T_{He} and the cell wall temperature, T_w. The thermal steps can be substantial, with $(T - T_w)/T \simeq 0.25$ or greater, as the cell temperature is lowered. In fact, this can be the most significant barrier for achieving BEC in H↓ as either high densities or low temperatures are required, a situation which creates a profound conflict. Unfortunately at this time the gas–liquid Kapitza resistance is not well understood.

The helium–cell wall (or helium–solid) thermal resistance is much better understood, or at least a great deal of experimental data exists. In this case R_K can be greatly reduced by increasing the interface area, using silver or copper sinter. On the other hand, very little is known about the gas–liquid R_K at present and in order to design an experiment to achieve BEC, its magnitude and temperature dependence must be known. It appears as if increasing the surface area will be of little help since the surface recombination process is expected to be dominant, so that $\dot{Q} \propto A$. The remaining alternatives are to select a critical temperature for BEC at which R_K is

not a serious problem, or find a strategy for reducing the heating. We shall concentrate further discussion on the gas–liquid Kapitza resistance.

The theoretical problem was first discussed by Castaing and Papoular (1983) who used a semi-classical model and confined their attention to nonsticking processes. Recently, Kagan et al. (1985) have made a fully quantum-mechanical calculation, including the adsorption process which turns out to be the dominant energy-transfer process at low temperature. They calculate the energy flux J from the gas to the liquid:

$$J = \int \frac{\mathrm{d}^3k}{(2\pi)^3} \frac{\mathrm{d}^2q}{(2\pi)^2} \frac{\hbar k_z}{m} \varepsilon_k W(\boldsymbol{k}, \boldsymbol{q}) \times \{n_k(T)(1 + n_q(T_{\mathrm{He}}))(1 + N_\kappa(T_{\mathrm{He}})) - (1 + n_k(T))n_q(T_{\mathrm{He}})N_\kappa(T_{\mathrm{He}})\}\,, \tag{4.8}$$

where

$$W(\boldsymbol{k}, \boldsymbol{q}) = \frac{2\pi}{\hbar} \left| \langle 0 | \frac{\partial U}{\partial z} | k_z \rangle \right|^2 \left(\frac{\hbar q}{2\rho\omega_q A} \right) \delta(\varepsilon_{\mathrm{k}} + \varepsilon_{\mathrm{a}} - \varepsilon_\kappa - \hbar\omega_q)\,. \tag{4.9}$$

Here n_q, n_k and N_κ are occupation numbers for ripplons, atoms in the bulk and adsorbed phase, respectively. ε_{k} is the bulk kinetic energy and ε_κ that on the surface; $U(Z)$ is the static adsorption potential and $\langle 0|$ represents a bound state of H. Kagan et al. use a Morse potential with a long-range z^{-3} fall-off to model the Mantz–Edwards potential and from eqs. (4.7) and (4.8) (with $J = \dot{Q}/A$) find

$$R_{\mathrm{K}}^{-1} = R_{\mathrm{Ka}}^{-1} + R_{\mathrm{Ks}}^{-1}\,, \tag{4.10}$$

where R_{Ka} is the contribution for sticking (adsorption) which is scaled to its value at $T_{\mathrm{He}} = 1\,\mathrm{K}$

$$R_{\mathrm{Ka}}(T_{\mathrm{He}}) = R_{\mathrm{Ka}}(1)/T_{\mathrm{He}}\,, \tag{4.11a}$$

and R_{Ks} is the term for inelastic scattering

$$R_{\mathrm{Ks}}(T_{\mathrm{He}}) = R_{\mathrm{Ks}}(1)/T_{\mathrm{He}}^{5/2}\,. \tag{4.11b}$$

Amongst other quantities $R_{\mathrm{K}}^{-1} \propto n$.

As a result we see that at low temperature the Kapitza conductance R_{K}^{-1}

must be dominated by the sticking term, with the weaker temperature dependence, even though the sticking probability is only of order 3×10^{-2} at 100 mK (see fig. 4.4). We also note that this picture must be incomplete as it predicts a monotonically increasing value of $R_K(T_{He})$ with decreasing temperature, whereas experiment indicates an increasing dependence in the 300 mK region (see fig. 4.3). Böheim et al. (1982) have examined sticking coefficients to second order in perturbation theory and find that they can exhibit increasing (nonmonotonic) behavior with decreasing incident energy for $T > 0$ K.

In the same approximation Kagan et al. (1985) have also considered the effect of higher surface coverages on R_K, in which ε_a is reduced in value, going to zero at the critical density n_c for BEC (see section 9). They find that the Kapitza resistance is still dominated by a term of the form R_{Ka}. Below T_c only the normal (noncondensate particles) of density n_n can adsorb (since the condensate particles are in the $k = 0$ state and behave like a gas at $T = 0$ K) and an additional temperature dependence enters since $R_K \propto 1/n_n$ and $n_n \propto (T/T_c)^{3/2}$.

It is useful to make some numerical estimates of the Kapitza resistance and compare to experiment. For the adsorption process Kagan et al. find

$$\dot{Q}/(A\Delta T) = 5nk_B^2 T/4\hbar k^* . \tag{4.12}$$

Here k_B is Boltzmann's constant, $k^* \simeq 4 \times 10^8$ cm^{-1} represents the squared matrix element (see eq. 4.9), among other constants, and T is the gas temperature. Evaluating for $T = 0.3$ K and $n = 10^{18}$/cm^3, we find $\dot{Q}/(A\Delta T) = 1.68$ mW cm^{-2} K^{-1}. To compare this to experiment, we note from section 4.2 that Salonen et al. (1982) measured the energy loss per collision with the surface, $\alpha = 0.2$ at $T \simeq 0.3$ K. We relate this to the heat transport by

$$\dot{Q} = \tfrac{1}{4} n\bar{v} A\alpha(T)\Delta E = \tfrac{1}{4} n(8k_B T/\pi m)^{1/2} A\alpha(T)(2k_B \Delta T) , \tag{4.13a}$$

where the first factor is the particle flux and ΔE is the energy transfer, from kinetic theory. This can be rewritten as

$$\dot{Q}/(A\Delta T) = \tfrac{1}{2} n(8k_B^3/\pi m)^{1/2} \alpha(T) T^{1/2} . \tag{4.13b}$$

Evaluating for the same conditions used for eq. (4.12), we find $Q/(A\Delta T) = 11$ mW cm^{-2} K^{-1}. This means that at $T = 0.3$ K, for a fixed $\dot{Q}/A$, the experimental temperature drop is 6.5 × smaller than the theoretical prediction. More important, as already pointed out, the predicted temperature dependence has a slope opposite to what is experimentally found so that the discrepancy will become larger at lower temperatures.

Kagan and Shlyapnikov (1983) point out that to achieve BEC, one may take advantage of the fact that the sticking probability goes to zero for low T. The idea is to reduce the heating by allowing the surface to get out of thermal equilibrium so that $\sigma < \sigma_{sat}$ for $T < T_c$ (see section 9 for a discussion of σ_{sat}). In equilibrium, as the atoms on the surface recombine they are replenished by atoms from the bulk, to maintain the adsorption isotherm. At a sufficiently low temperature, due to the low sticking probability and reduced flux ($\sim \frac{1}{4} n \bar{v} A$) the surface coverage becomes smaller than its equilibrium value and heating is reduced. This effect is enhanced below T_c, since condensate atoms will not stick.

Unfortunately the estimate of the temperature at which the system comes out of equilibrium is $T^* = 5$ mK. The heating rates for a saturated surface are far too high to cool a sample with $\sigma \simeq \sigma_{sat}$ to 5 mK. One experimental strategy might be to start at a temperature $T \ll T^*$ and slowly fill the cell with hydrogen so that the cell is never submitted to a severe thermal load. Even so, the experimental cooling powers available at these low temperatures appear to be incompatible with the recombination power that is dissipated and consequently this would be an extremely difficult experiment.

4.5. The hyperfine frequency shift of H

In section 3 we have introduced the single-atom hyperfine constant a (eq. 3.4) which, for a many-particle system of hydrogen atoms, can be considered to be a constant since the average H–H separation is quite large. On the other hand, when hydrogen is adsorbed on a He surface or in a high-density buffer gas, the average H–He separation is small or the collision frequency is high, giving rise to a change in a. This is usually observed by measuring the zero-field shift in the frequency of the a to c hyperfine transition of fig. 2.1. In appropriate units, this has the frequency $\nu = \langle a \rangle / h$, where $\langle\ \rangle$ represents an average over the paths or motion of the atoms. This frequency can be measured with great precision and one usually measures the fractional hyperfine shift (HFS), $\Delta\langle a \rangle / a(\infty) = [\langle a(R) \rangle - a(\infty)] / a(\infty)$. The hyperfine interaction strength is proportional to the density of electronic spin at the nucleus. Calculation of the HFS is a formidable task which involves computing the electronic spin density at the hydrogen nucleus, which will depend on the separation R between H and He

$$\rho(R) = \langle \psi(R) | \sum_i s_{iz} \delta(\boldsymbol{r}_i - \boldsymbol{r}_H) | \psi(R) \rangle , \tag{4.14}$$

where r_i is the position of electron i with spin s_i and $\psi(R)$ is the complete

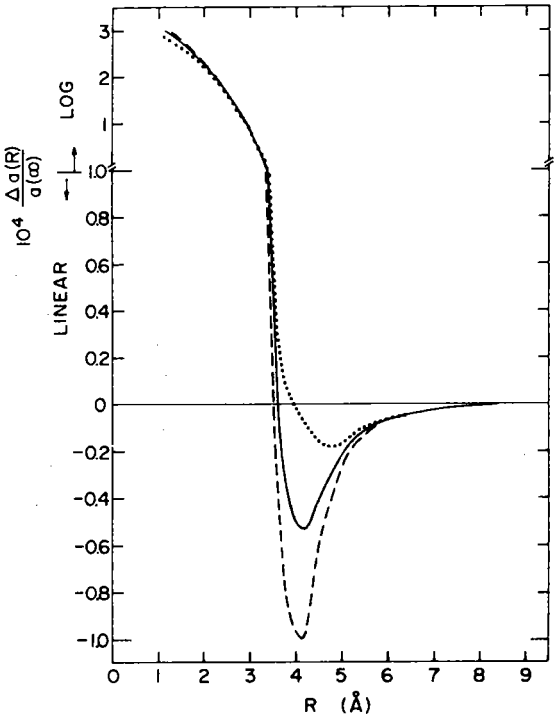

Fig. 4.5. The fractional hyperfine frequency shift calculated by Davison and Liew (1972) and Ray (1975). The solid line is the average of the two (after Jochemsen and Berlinsky 1982).

wavefunction for the He–H system. At long-range, the mutual polarization of the atoms causes a spreading of the electronic wavefunction and thus a lower spin density at the nucleus, resulting in a negative frequency shift. At short-range, the shift is positive resulting from two effects: deformation of the orbitals due to the additional interaction of the He and distortion of the wavefunction due to the Pauli exclusion principle. A detailed calculation requires a determination of the wavefunction, $\psi(R)$, using extensive multiconfigurational self-consistent field techniques. Results of calculations by Davison and Liew (1972) and Ray (1975) are shown in fig. 4.5, from the article by Jochemsen and Berlinsky (1982), who have performed quantum statistical averages of the HFS for a He buffer gas. From fig. 4.5 we see the general trend of the HFS is to be negative for large R and positive for small R, very similar to a pair potential.

For H in a He buffer gas at room temperature, a positive HFS is found since collisions favor the short range part of Δa. However, at liquid-helium temperatures the interatomic potential is such that the atoms mainly

sample the negative part of the HFS curve of fig. 4.5, and the shift is negative. When adsorbed on He, the larger average separation also results in a negative shift. Zero-field measurements of the HFS of H on ^{4}He and ^{3}He as a function of temperature have been exploited to determine ε_a (see the review by Hardy et al. 1982). The motionally averaged frequency shift depends on the percentage of time that an atom spends on the surface, which is proportional to $\sigma/n = \lambda_{th} \exp(\varepsilon_a/kT)$, so that $\langle \Delta a(R) \rangle \propto \lambda_{th} \exp(\varepsilon_a/kT)$. A measurement of $\langle \Delta a(R) \rangle$ enables extraction of ε_a. In fig. 4.6 we show the HFS as measured by Morrow et al. (1981) as a function of temperature. At high temperature the ^{4}He vapor pressure is high and the pressure-shift dominates the HFS, whereas at low temperature as the pressure drops the H atoms populate the surface, and the wall-shift becomes dominant. The experiment is described in greater detail in the following section.

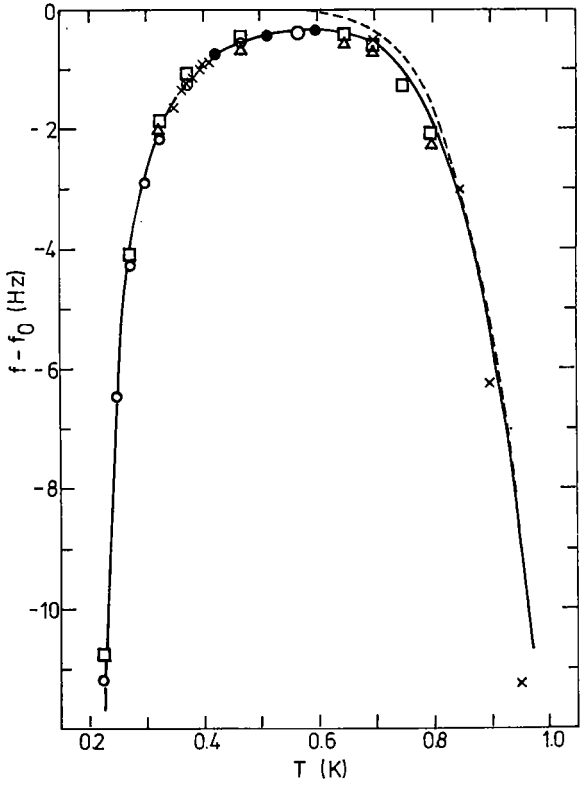

Fig. 4.6. The hyperfine shift versus temperature. The solid line is a fit to the data, the dashed line shows the gas-phase pressure shift contribution (after Morrow et al. 1981).

5. Experimental developments

In a long review such as this it is difficult to treat theory and experiment separately. We have attempted throughout to support and amplify theoretical discussions with experimental results. In this section we shall concentrate on experiment, referring to theory in previous and subsequent sections where necessary. We shall cover the principal developments of this field rather than give a complete coverage of all experiments performed. The handling of material will be in an essentially historical order, focusing on efforts to understand decay mechanisms and achieve high densities.

The earliest published suggestion that $H\downarrow$ might be an interesting system to produce and study was by Hecht (1959), with subsequent theoretical articles on the subject by Etters (1973) and Stwalley and Nosanow (1976), who were unaware of Hecht's work. Experimental work was started in the early 70's at the University of Amsterdam. Walraven et al. (1978) attempted to stabilize spin-polarized hydrogen ($H\uparrow$) on a cold surface, using atomic-beam techniques. This was unsuccessful due to rapid spin-relaxation and recombination on the surface. At MIT, Crampton et al. (1979) observed zero-field hyperfine transitions of H in contact with H_2-walls at liquid-helium temperatures; Hardy et al. (1979) at UBC studied H in the presence of H_2-covered walls and He vapor using low-field NMR; Silvera and Walraven (1979) used an atomic beam to show that H could easily be transported through teflon tubes to a region of H_2-covered liquid-helium cooled walls, and that the H thermalized with the walls. The conclusion drawn from the three latter experiments was that a reasonable flux (or density $\sim 10^{13}$ to 10^{14} cm^{-3}) of H atoms could be cooled to low temperatures in a steady-state flow experiment. However, when the H discharges were turned off the H density rapidly disappeared, indicating a short lifetime in the presence of H_2-walls at low temperature.

Spin-polarized hydrogen was first stabilized in a long-lived state in 1979 (Silvera and Walraven 1980a) and $D\downarrow$ was stabilized shortly thereafter (Silvera and Walraven 1980b). Low-density gases of $H\downarrow$ were found to have unmeasureably long lifetimes (on a scale of hours), whereas $D\downarrow$ was limited to minutes. Limitations of the lifetime and density of $D\downarrow$ were found to be due to surface recombination, and the first measurement of the adsorption energy on ^{4}He was made in the latter paper. The adsorption energy of $H\downarrow$ on ^{4}He was subsequently measured (Morrow et al. 1981, Matthey et al. 1981). Matthey et al. also showed that the surface recombination rate constant depended inversely on the square of the magnetic field. The next big step was the demonstration by Cline et al. (1981) of nuclear spin polarization in $H\downarrow$, resulting in significantly lower recombination rates and opening the way to higher densities. A series of

interesting measurements on the nuclear spin relaxation rate ensued. Until this point, densities of order $3 \times 10^{17}/\text{cm}^3$ had been achieved. Using compression techniques Sprik et al. (1983, 1985) and Hess et al. (1983, 1984) were able to increase the density by an order of magnitude; a new density limitation was encountered: three-body recombination. Recently, in a research unrelated to decay of the density, Johnson et al. (1984) have observed nuclear spin-waves in a low-density gas of $H\downarrow\ddagger$.

5.1. Stabilization of $H\downarrow$

In order to stabilize and measure atomic hydrogen several essential requirements have to be met:

(1) atoms must be made (by dissociating H_2),
(2) the electron spins must be polarized so that atoms interact via the $^3\Sigma_u^+$ potential,
(3) the spin polarization must be maintained,
(4) the atomic hydrogen must be confined to a cell, and the atomic density of the cell walls must be kept low to suppress wall-recombination, and
(5) a detector of H must be available to establish its existence.

In the following, we discuss these various requirements and show in detail how they were implemented in the apparatus of Silvera and Walraven (1980a) shown in figs. 5.1 and 5.2.

5.1.1. Dissociation of H_2

A room temperature microwave discharge was used to dissociate H_2. This is described in detail by Walraven and Silvera (1982). (rf fields can also be used.) The high-frequency electromagnetic field accelerates free electrons in a gas of H_2 and inelastic collisions create neutral hydrogen atoms through a multi-step process. This discharge can take place at room or lower temperatures. Cline et al. (1980a, b) used a liquid-nitrogen temperature rf discharge. The higher temperature source requires in the order of 5–20 W of electromagnetic power to sustain a discharge. In a good discharge, 90–95% of the gas is atomic. Hardy et al. (1980) used a helium temperature low average power pulsed discharge to produce H.

5.1.2. Polarization

At this point we discuss polarization of the samples with the aid of figs. 5.1 and 5.2. Atoms from the discharge flow up a teflon lined tube to a low-temperature sample cell in the center of a solenoidal magnetic field.

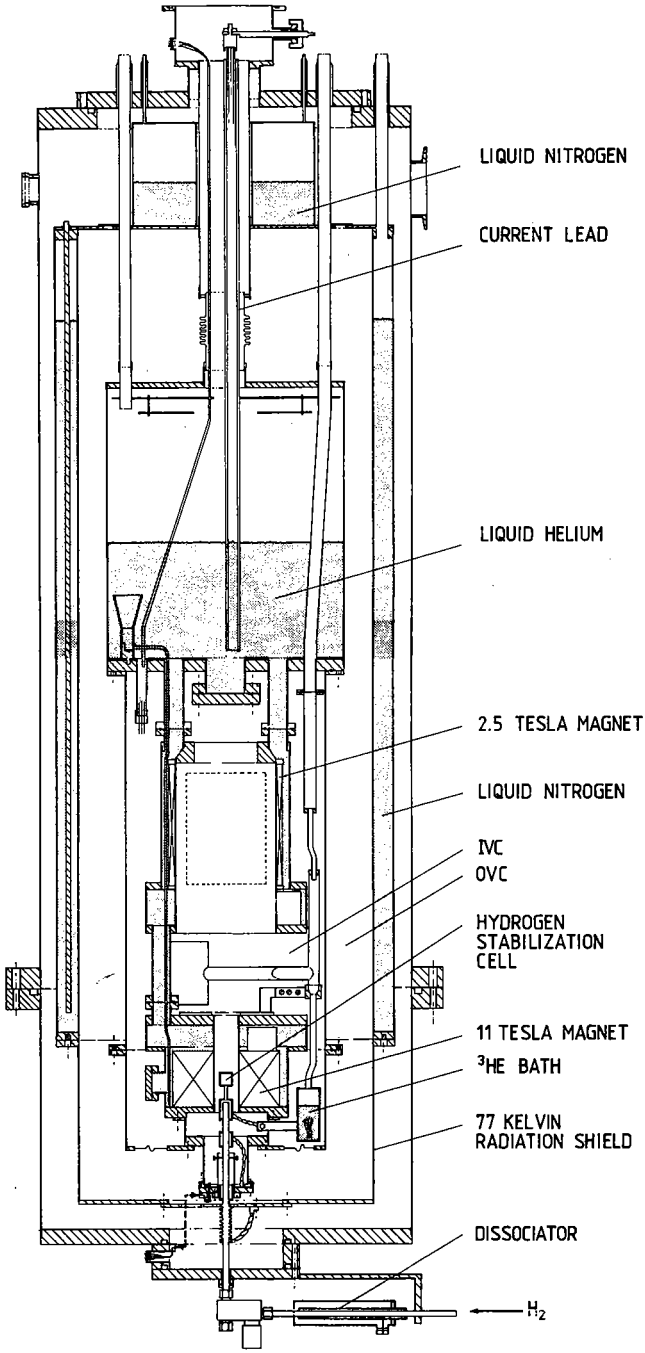

Fig. 5.1. The apparatus used to stabilize H↓ and D↓. (IVC and OVC: inner and outer vacuum chambers, respectively.) The 2.5 T magnet was not used. The ^{3}He baths used to cool the cell and the copper braid connection are not shown.

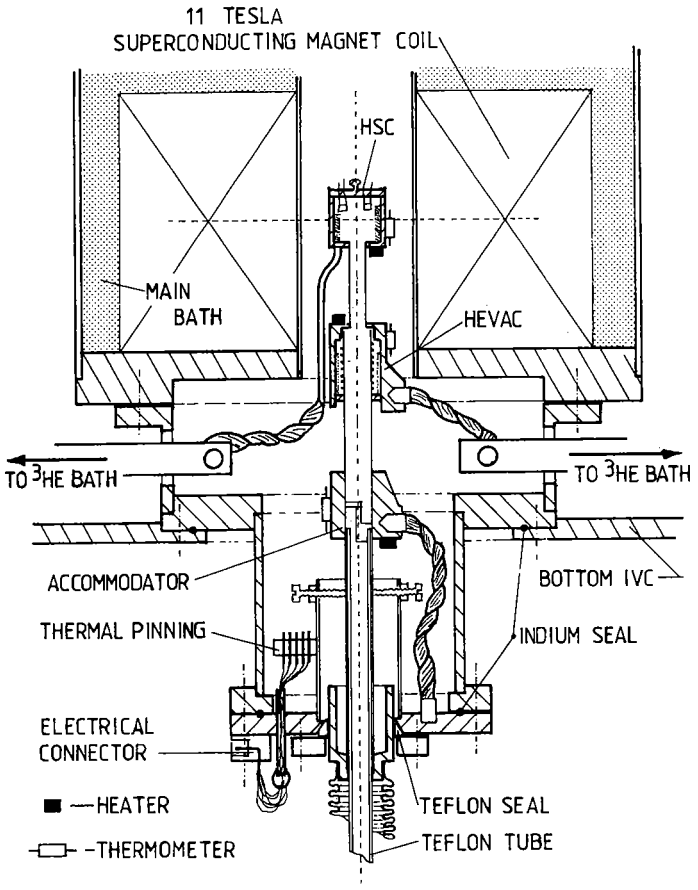

Fig. 5.2. A more detailed view of the cryostat of Silvera and Walraven. The cell (HSC) and HEVAC were cooled with ^{3}He evaporation refrigeration which could achieve no load temperatures of about 250 mK. The cell was also provided with sintered copper for cooling. This was later removed as it apparently was not necessary, and a well-defined surface area was desired.

To enter the field the atoms must pass through a field gradient and they undergo a force, $-\nabla(\boldsymbol{\mu}_{\mathrm{H}} \cdot \boldsymbol{B})$. The electron spin-up atoms are repelled by the gradient and do not enter the cell, whereas the spin-down atoms are attracted into the cell. Spin-up atoms on the wall can either recombine or relax to the spin-down state and then enter the cell.

5.1.3. Sustenance of polarization

In order to maintain the electron spins polarized, the sample must be at

low temperature and in a high magnetic field so that the spin-down state is thermally favored. As an example, in equilibrium, the ratio of down-spins to up-spins is $n\downarrow/n\uparrow = \exp(g_e\mu_B B/kT) = 2.7 \times 10^{19}$ when we evaluate for $B = 10\,\mathrm{T}$, $T = 0.3\,\mathrm{K}$.

5.1.4. *Confinement*

5.1.4.1. *Magnetic compression*

The cell in fig. 5.1 is open at the bottom, and the atoms are confined to the cell by the magnetic gradient. It is useful to analyze this in some detail. For a simple solenoidal magnet, the field can be approximated by

$$B_z(r) = B_0\left(1 - \frac{z^2}{z_0^2} + \frac{\rho^2}{2z_0^2}\right), \qquad B_\perp(r) = z\rho B_0/z_0^2,$$

$$B_\phi = 0. \tag{5.1}$$

Here, z is the axial direction, $z_0 = 51$ mm for the magnet of fig. 5.1, ρ is the transverse coordinate and $B_0 \simeq 10\,\mathrm{T}$ is the field at $\boldsymbol{r} = 0$. In what follows we neglect $B_\perp$ for simplicity. Walraven and Silvera (1980) analyzed the spatial density dependence of the gas. In the low-density high-temperature limit, neglecting interactions, we can use eq. (1.9) with $\bar{N}_0 = 0$ and $g = 1$ and approximate $g_{3/2}(z)$ by the first term in the summation,

$$n = \lambda_{\mathrm{th}}^{-3} g_{3/2}(z), \quad g_{3/2}(z) \simeq z = \exp[(\mu + \mu_B B)/kT], \tag{5.2a}$$

or

$$n = \exp[(\mu + \mu_B B)/kT]\lambda_{\mathrm{th}}^{-3}, \tag{5.2b}$$

with $g = 1$. Since the chemical potential μ must be uniform, we evaluate it at $B = 0$ to find $n(B = 0) \equiv n_0$ or

$$n(B) = n_0 \exp(\mu_B B/kT). \tag{5.2c}$$

We note from eq. (2.8) that since the gas is electron spin-polarized the density and magnetization $M = |\boldsymbol{M}|$ are related by a constant

$$M = g_e\mu_B \tfrac{1}{2}(n_a + n_b) + g_n\mu_n \tfrac{1}{2}(n_a - n_b) \simeq \mu_B n(B). \tag{5.3}$$

Here n_h is the local atomic density in hyperfine state h and we take

$n_a \simeq n_b = \frac{1}{2}n$. The nuclear contribution can be ignored, as the splitting $(E_b - E_a)/k \simeq 55\,\text{mK}$ at $B = 10\,\text{T}$. The axial and radial density distribution, $n(z)$ and $n(\rho)$, can be evaluated for the field of eq. (5.1)

$$n(z) = n(B_0)\exp[-\mu_B B_0(z/z_0)^2/kT]\,, \tag{5.4a}$$

$$n(\rho) = n(B_0)\exp[+\mu_B B_0(\rho/z_0)^2/2kT]\,, \tag{5.4b}$$

where

$$n(B_0) = n_0 \exp(\mu_B B_0/kT)\,. \tag{5.4c}$$

Thus, field gradients give rise to enormous density gradients or magnetization gradients with a Gaussian axial shape of half-width $\Delta z = z_0(kT/\mu_B B_0)^{1/2}$. At low temperatures, H$\downarrow$ will be highly localized to the center of the field and pressed against the walls of a tubular confinement cell. As a numerical example, let us assume that we have a density of $10^{10}/\text{cm}^3$ in zero field: then in a field of 10 T at 300 mK, $n(B_0) = 5 \times 10^{19}/\text{cm}^3$. A gas of H$\downarrow$ in a low-field region will be compressed into a high-field region. It is useful to introduce the compression ratio

$$c_M(B_0 - B) \equiv n(B_0)/n(B) = \exp[\mu_B(B_0 - B)/kT]\,. \tag{5.5}$$

The density $n(B_0)$, eq. (5.4c), is the maximum or saturation density to which a cell will fill, given a zero-field density, n_0.

Another consequence of eq. (5.4c) is the following: if a cell is filled with a central density $n(B_0)$ and the zero-field density is reduced to zero, n must also go to zero. The important question here is "What is the time scale for this thermal escape of out of the cell?". To analyze this, let us first consider $B = 0$ and assume that a cell with volume V is connected to a (filling) tube of cross section A with a Clausing flow conductance factor K. From kinetic theory, assuming free molecular flow, the flow of atoms out of the end of the tube is found to be $\mathrm{d}N/\mathrm{d}t = \frac{1}{4}Kn\bar{v}A$, where $n = N/V$ is the density in the volume V and $\bar{v}$ is the average atomic velocity. This gives an exponential decay of N with time constant

$$\tau_{es} = 4V/K\bar{v}A\,. \tag{5.6}$$

If we now turn the field on, the density at the tube-end will be reduced by the compression $n(B) = n(B_0)/c_M$ and the atoms will be compressed into an effective volume $V_{\text{eff}} \equiv N/n(B_0)$. The time constant becomes

$$\tau_{es} = c_M(B_0 - B)4V_{\text{eff}}/K\bar{v}A\,. \tag{5.7}$$

Because of the enormous accessible values of c_M, the gas in the cell can essentially be permanently trapped by the field, similar to the trapping of the atmosphere by the earth's gravitational field. As an example assume that we have a system for which $\tau_{es} = 0.01$ s for $B - B_0 = 0$. For a field difference $B_0 - B = 10$ T, $c_M(10) = \exp(6.7/T)$. For $T = 1$ K we find $\tau_{es} = 18.2$ s whereas for $T = 0.1$ K $\tau_{es} = 1.25 \times 10^{27}$ s.

5.1.4.2. Wall confinement, wall coverage, vapor compression and thermalization

From eq. (1.7) we see that in equilibrium the atoms are occupying both surface and volume states. Clearly if $\varepsilon_a/kT \gg 1$, the atoms reside predominantly on the surface. Since the cell must be at low temperature to maintain the polarization, ε_a/k must be of order 1 K or smaller to have gas-phase densities sufficiently high to detect and study. Furthermore if $\varepsilon_a/k \gg T$ at low temperature, the surface density becomes very large, and the atoms rapidly recombine due to a term of the form of eq. (1.4). Silvera and Walraven (1980a) found that a liquid-helium film could be used to cover the cell walls to inhibit the build-up of a surface density and suppress recombination. Later, ε_a was measured and found to have a value of ~1 K for ^{4}He.

A second method of suppressing wall recombination is to use magnetic confinement. From eq. (5.4a) we see that by using a magnetic-field gradient, the density n, and thus σ, can be reduced exponentially to zero in one direction, so that there need be no physical walls which catalyze recombination in that direction. Unfortunately, Maxwell's equations do not allow a static-field maximum in free space; magnetic fields always have saddle points wherever one component has a maximum. Thus we see, for example, from eq. (5.4b) that the density increases in the radial direction. In this case the best we can do is to construct an open ended cylindrical sample cell and use magnetic confinement to keep the atoms away from surfaces normal to the z direction, and with a radius $\rho_0 \leqslant z_0$ so that the wall density is of the same order as the central density.

Using this background let us now consider the experimental geometry shown in fig. 5.1 in greater detail. Atoms flow up the warm ($T \geqslant 20$ K) teflon lined tube towards the cell. Teflon has a relatively low adsorption energy for hydrogen and the transmission of a 50 cm long tube of 5 mm diameter at room temperature is of order 0.5 for densities ~10^{15} cm^3. Before the hydrogen enters the cell it must be cooled to liquid-helium temperatures to prevent thermal loading of the refrigerator. This happens in the accommodator (AC) (see fig. 5.2) by collisions with walls at $T = 4$–8 K. At these temperatures teflon is no longer a useful wall material so that both this and the metallic copper walls of the AC would yield very rapid recombination. Initially, the H that flows into the AC recombines;

the resultant H_2 then coats the cold teflon and copper walls. In the hierarchy of low adsorption energy walls, H_2 is second only to helium with an adsorption energy of 39.79(32) K (Crampton et al. 1982). The atoms thermalize on the H_2 walls of the AC within several wall collisions, passing up towards the cell.

The cell walls are covered with superfluid ^{4}He which flows to cover all surfaces. Due to the "fountain pressure" the superfluid film flows toward warmer regions. This has both positive and negative consequences. Flow stabilizes the film thickness against local "burn off" or thinning out due to recombination heating. However, a serious cryogenic problem exists as the film is driven towards the warmer accommodator. At a temperature of about 0.9 K the film evaporates and the vapor fluxes back to the cell where it condenses out, liberating its heat of condensation. This large heat load (several mW) due to "heat piping" drives the temperature of the cell towards that of the AC. Silvera and Walraven resolved this problem by introducing a second refrigeration point, called HEVAC (shown in more detail in fig. 5.2), between the cell and the AC. The HEVAC has a liquid-helium reservoir and is independently cooled to a temperature of 500–650 mK. At these temperatures the equilibrium He vapor pressure is very low. The film now runs between the HEVAC and the AC and the former acts as a condenser so that the vapor does not enter and condense in the cell. The cell temperature can then be varied more or less independently.

The HEVAC serves a very interesting second function. It is actually a miniature vapor pump for H↓ from which it derives its name HEVAC (HElium VApor Compresser). When the ^{4}He vaporizes, a dense cloud of ^{4}He atoms flows in the direction of the cell. Collisions between ^{4}He and H effectively transfer momentum upward to the four times lighter H and compress it into the cell. Thus, both HEVAC and magnetic field confine the atoms to the cell and the time constant for thermal leakage, eq. (5.7), becomes

$$\tau_{es} = 4c_H c_M V_{eff}/K\bar{v}A\,, \tag{5.8}$$

where c_H is the HEVAC compression (measured to be of order 50). The He–H mean free path is estimated to be about 0.2 mm based on a ^{4}He vapor density of $\simeq 2\times 10^{16}/\mathrm{cm}^3$. From the known recombination rate constant, K^{He}, it is easily seen that recombination of H in the HEVAC is negligible. Although the compression function of the HEVAC is not necessary for stabilization, it improves the confinement and was particularly useful in showing that H was long-lived, even in zero field, in the first stabilization experiment.

Returning to the cell-loading procedure, the atoms pass from the AC

into the HEVAC region. It is in this region that they begin to be sorted out into up- and down-spin. This is a critical region for loading. The atoms must pass through a temperature gradient from 4 K to 0.9 K in which the walls are H_2, but not He covered. H condenses on H_2 walls at 1 K and rapidly recombines. If this "danger" zone is too long, the transmission to the cell will approach zero. A number of experimental groups have had sustained difficulties with loading of cells and we suspect that the problem resided in this region. The length of this region can be analyzed (Tommila et al. 1984b, Silvera and Godfried 1984) and depends critically on the temperature of the HEVAC since the film burns off at about 0.9 K, i.e., for $T_{HEVAC} = 0.9$ K the film length is zero. The HEVAC should be cooled with a large cooling power refrigerator so that its temperature remains of order 0.5 to 0.6 K.

In the experimental system of Silvera and Walraven (fig. 5.1) bottom-loading of H was used, which limits the length of the filling tube. The recombination loss in the tube is not nearly as important as the losses encountered in the 4–1 K region. Accordingly, top-loading has been used successfully by a number of groups. In later experiments at Amsterdam, Sprik et al. (1983) found that when bulk quantities of ^{4}He were introduced into the cell, excessive heating due to He film–vapor coupling between the cell and the HEVAC limited the temperature to which the cell could be cooled. It was suspected that these problems could have been avoided with a top-loading geometry which apparently is better suited for experiments which use large quantities of helium. Later in this section various other experimental cells will be encountered (figs. 5.7, 5.10a, 5.18 and 5.23).

5.1.5. Detection of H↓

5.1.5.1. Bolometric detection

Once the hydrogen is in the cell it has a very long lifetime. In the first experiment, densities conservatively estimated at $1.8 \times 10^{14}/\text{cm}^3$ were stabilized for up to 9 min with no detectable decay of density.

In order to detect the H↓, Silvera and Walraven used one of two special bolometers situated in the cell (fig. 5.2). The bolometer was a small carbon chip (area about 2×1 mm^2) cut from a Speer resistor. It was suspended in the cell by fine copper wires which serve both as electrical leads and as a path which allows the ^{4}He film to cover the surface. If a sufficiently large electric current passed through the element, the ^{4}He would evaporate faster than it could be replenished by flow along the wires. When the surface was bare of ^{4}He, the resistance dropped slightly, as seen in fig. 5.3. If H↓ was in the cell when the ^{4}He was desorbed the H↓ condensed on the

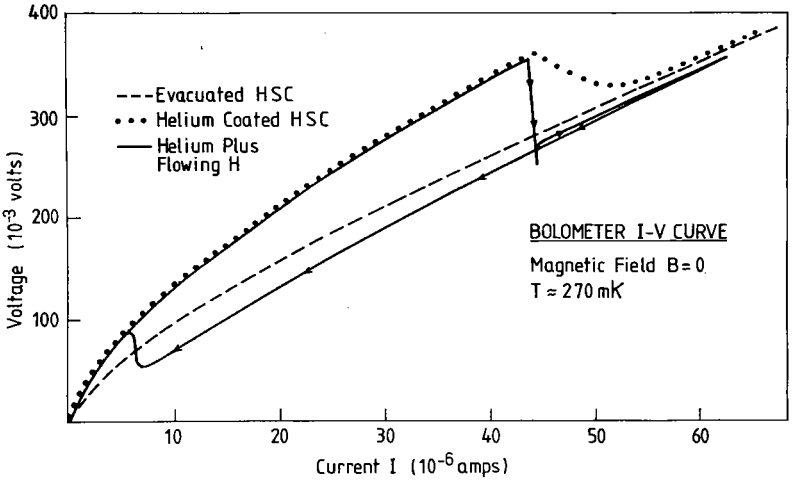

Fig. 5.3. The current–voltage characteristic of a bolometer in an empty cell, ^{4}He-coated cell and a cell with ^{4}He and H. For this zero-field trace, H was continually running into the cell giving rise to hysteresis in the I–V curve. On reducing the current, the surface remains bare of He due to continued recombination heating (after Silvera and Walraven 1980a).

surface and recombined with a time constant $\tau \simeq 4V/\bar{v}A$, where V is the cell volume, A the bolometer surface-area, and $\bar{v}$ the average atomic velocity. The recombination energy heated the bolometer and its resistance dropped sharply. The temperature rise was a measure for the number of atoms in the cell. The bolometer was extremely sensitive and could detect about 10^8–10^9 atoms. After the atoms recombined on its surface the molecules desorb in highly excited vibrational–rotational states (see section 6). Within a few wall-collisions in the cell they relax to the ground state and penetrate through the ^{4}He film to the underlying wall of the cell. Using an ohmic heater, it was found that the temperature rise of the cell as measured with a carbon resistance thermometer (Speer) provided a signal linear with the number of recombining atoms (for low density), whereas the more sensitive bolometer was highly nonlinear. The system was easily calibrated with an electrical heat pulse of known energy to determine the number of atoms in the cell absolutely.

The original apparatus, fig. 5.2, used ^{3}He one-shot evaporation refrigeration. This puts a severe limit on the running time and the temperature; dilution refrigerators are much better suited for this type of experimentation, and are now exclusively used by all workers in the field. In subsequent experiments, densities of H↓ greater than $10^{16}/\text{cm}^3$ were soon achieved (Silvera and Walraven 1980c, Walraven et al. 1980, Cline et al.

1980a,b). Hardy et al. (1980a,b) studied very low density H on ^{4}He surfaces in zero magnetic field using resonance techniques. In all of these studies H↓ was found to behave as a gas in thermodynamic equilibrium, slowly decaying away to the molecular state. Convincing evidence that H↓ was a low-temperature gas was presented by Walraven et al. (1980). They showed that at low density the saturation density was controlled by the magnetic field as expected for a gas, eq. (5.2), and that the H↓ was magnetically confined by studying the decay time for thermal escape, eq. (5.7) (see fig. 5.4). In this and similar experiments by Cline et al. (1980b) at higher densities, disturbing and, at that time, unexplained deviations which we now know to be due to recombination, were observed.

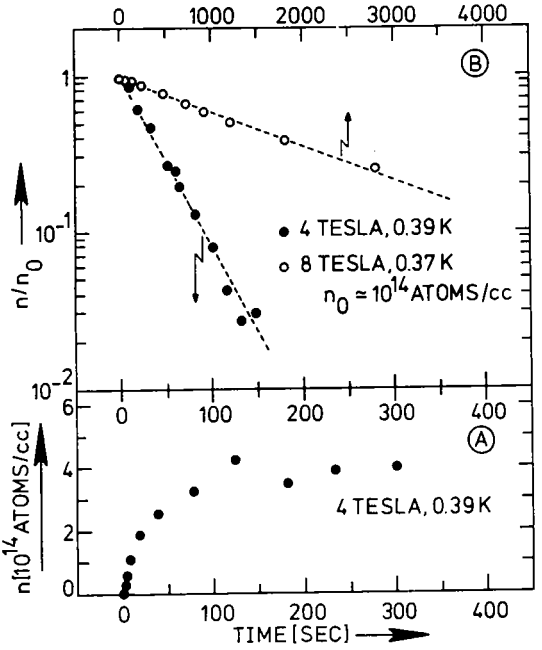

Fig. 5.4. (a) Data showing the loading of an HSC to a saturation density under conditions of constant loading flux, field and temperature. (b) The temporal decay of the density of H↓ for two field–temperature conditions, demonstrating axial magnetic confinement (after Walraven et al. 1980).

5.1.5.2. Nondestructive detection

Although the bolometer is a very sensitive detector that can be used for measuring equilibrium properties of the gas, a measurement results in the

destruction of the sample. A nondestructive detector, the capacitive pressure gauge shown in fig. 5.5 was introduced by Matthey et al. (1981). A thin gold-coated Kapton membrane (10 μm) is edge-epoxied to the inner roof of the cell with a gap of order 25 μm, forming a capacitor. The H↓ pressure deforms the membrane, changing the capacitance. The minimum detectable pressure is about 10^{-6} Torr. Since for low density the ideal gas law $p = nkT$ is obeyed, the density is easily determined. In fig. 5.5b a filling and decay sequence as measured with such a pressure gauge is shown. Other nondestructive detection methods such as NMR and ESR will be discussed later in this section.

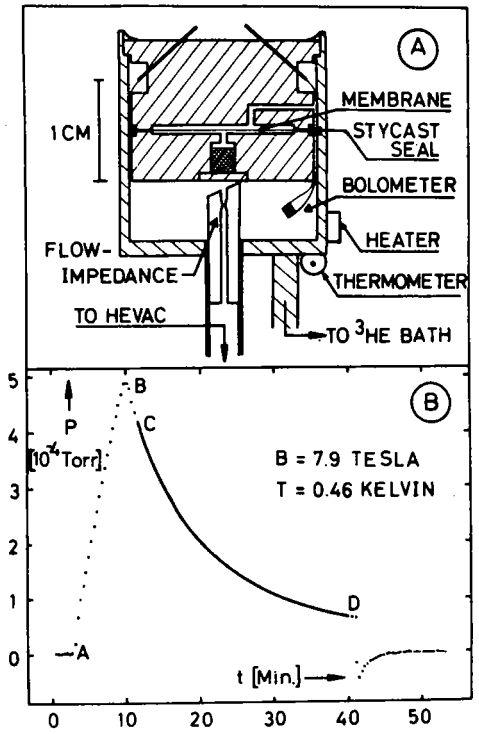

Fig. 5.5. (a) A pressure gauge built into a hydrogen stabilization cell. The pressure distorts a thin Kapton membrane which serves as one plate of a capacitor. The reference side of the gauge is pumped by a sorption pump (crosshatched area). (b) The signal from the pressure gauge during a filling (A–B) and decay (B–D) sequence. C–D represents a fit to the data points (hidden by the fit curve). At D the sample is destroyed with a trigger bolometer (after Matthey et al. 1981).

5.2. THE RATE EQUATIONS

5.2.1. Effective rate constants

One of the most useful and powerful techniques for studying H↓ and D↓ has been to monitor the rate at which the sample destroys itself, either by recombination, relaxation between the hyperfine states, or by thermal escape out of an open structured cell. All of this can be described by rate equations for the decay or growth of the densities of atoms in the various hyperfine states.

Simple forms of the decay equations were given in the introduction, eqs. (1.3)–(1.5). Before writing down the rate equations for the hyperfine states it is useful to discuss first effective rate constants and some approximations. We shall use a hypothetical model in which N^s and N^v atoms populate the surface and bulk states, respectively, and decay by a third-order recombination process with rate constants K^s and K^v. Then the time rate of change of the total number of atoms N is

$$\dot{N} = \dot{N}^v + \dot{N}^s = V\dot{n} + A\dot{\sigma} + \dot{V}n + \dot{A}\sigma \,. \tag{5.9}$$

We shall first write down an extended set of rate equations which involves population changes due to both recombination and redistribution between surface and volume states

$$\begin{aligned} \dot{N}^v &= -K^v V n^3 - R_{vs} V n + R_{sv} \sigma A \,, \\ \dot{N}^s &= -K^s A \sigma^3 + R_{vs} V n - R_{sv} \sigma A \,. \end{aligned} \tag{5.10}$$

Here R_{vs} and R_{sv} are the rates at which atoms go from bulk to surface states and vice versa. Since the time in which the surface and bulk come into thermodynamic equilibrium is much shorter than the recombination time, the last two terms in (5.10) sum to zero, and n and σ are the equilibrium values (to which we assign the same symbols). We also note that in almost all circumstances $N^v \gg N^s$ (for $A/V \simeq 10\ \mathrm{cm}^{-1}$, $n \simeq 10^{16}/\mathrm{cm}^3$, $\sigma \simeq 10^{13}/\mathrm{cm}^2$, we find $N^s/N^v \simeq 10^{-2}$) so that $\dot{N} \simeq V\dot{n} + \dot{V}n$. For the present discussion of the rate equations, we use $\dot{V} = \dot{A} = 0$ (a fixed sample volume and surface area). The explicit time dependence of A and V is important for the compression experiments to be discussed in section 5.12. From this, and eqs. (5.9) and (5.10), we find

$$\dot{n} = -K^v n^3 - \frac{A}{V} K^s \sigma^3 \,. \tag{5.11}$$

Finally, since by assumption thermodynamic equilibrium exists, we can use the adsorption isotherm, eq. (1.7), to write

$$\dot{n} = -K^{\text{eff}} n^3 , \tag{5.12}$$

with

$$K^{\text{eff}} = K^{\text{v}} + \frac{A}{V}\left(\frac{\sigma}{n}\right)^3 K^{\text{s}} ,$$

$$= K^{\text{v}} + \frac{A}{V}\lambda_{\text{th}}^3 \exp(3\varepsilon_{\text{a}}/kT) K^{\text{s}} , \tag{5.13}$$

the latter expression being valid in the low-density, high-temperature limit.

5.2.2. *Notation for rate constants*

A number of notations have been used in the literature to describe various rate constants. Here we would like to introduce a consistent set of symbols which have the virtue of presenting explicit information about the process. The two principle decay mechanisms are recombination and relaxation, denoted by symbols K and G, respectively; volume or surface processes are denoted by superscripts v and s, i.e. K^{v} or K^{s}. The order of the process is the number of subscripts, which also give the initial hyperfine states of the atoms participating in the process. Thus $K^{\text{s}}_{\text{abb}}$ is a third-order surface process involving atoms in hyperfine states a, b and b. Clearly this notation is more useful and avoids the ambiguity associated with some existing notations. For example, third-order surface recombination has been designated by the letter L, $K_{\text{v}}^{3\text{b}}$, K^3, etc., none of which distinguish between processes such as $K^{\text{s}}_{\text{bbb}}$, $K^{\text{s}}_{\text{abb}}$ and $K^{\text{s}}_{\text{aab}}$, etc. For electronic relaxation in equilibrium we have $G_{\text{bc}} = G_{\text{cb}} \exp(-E_{\text{cb}}/kT)$ with a similar relation for G_{cd}. The effective number of atoms lost from a given hyperfine state by a given process is explicitly included in the equations; the rate constants are all defined to be positive quantities.

5.2.3. *General equations*

The general rate equations for a gas of hydrogen are quite complex with a large number of variables. The most important processes which can occur are relaxation between hyperfine states, recombination to H_2 via processes of various orders, fluxing of atoms out of the system by thermal escape, and into the system from an H source. These processes can occur in the volume or on the surface and in principle both the surface area and the volume can be time dependent. For clarity we shall consider a simplified case. First of all we take $\dot{A} = \dot{V} = 0$. A second useful and experimentally

achievable approximation is the high magnetic field, low-temperature limit so that mainly the a and b states are populated. In the following, rate equations are given in a few approximations followed by a discussion of the rate constants. In the remainder of this section a number of important cases that have been experimentally realized are treated.

We shall now write down the rate equations for the hyperfine states a, b, c, and d of fig. 2.1 for the H atom. We use a shorthand in which $n_a \equiv a$, $n_b \equiv b$, $n = \Sigma n_i$, etc., and assume that in general $n_a + n_b \gg n_c + n_d$. We treat two important cases:

(i) $c = d = 0$, low-density, high-field limit:

$$\dot{a} = -2K_{aa}^{eff}a^2 - K_{ab}^{eff}ab - G_{ab}^{eff}(a+b)(a-b) - a/\tau_{es} + \phi_a/V\ , \quad (5.14a)$$

$$\dot{b} = -K_{ab}^{eff}ab + G_{ab}^{eff}(a+b)(a-b) - b/\tau_{es} + \phi_b/V\ . \quad (5.14b)$$

(ii) Lower B/T ratio with $b \gg a \gg c \gg d$, ignoring filling and thermal escape (ϕ_h/V, n_h/τ_{es}):

$$\dot{a} = -K_{ab}^{eff}ab - K_{abb}^{eff}ab^2 - G_{ab}^{eff}(a+b)(a-b) + G_E^{eff}(bd-ac)\ , \quad (5.15a)$$

$$\dot{b} = -K_{ab}^{eff}ab - K_{bc}^{eff}bc - K_{bd}^{eff}bd - (2+\xi)K_{bbb}^{eff}b^3 - K_{abb}^{eff}ab^2 - K_{bbc}^{eff}b^2c + G_{ab}^{eff}(a+b)(a-b) - G_{bc}^{eff}(b+c)b + G_{cb}^{eff}(b+c)c - G_E^{eff}(bd-ac)\ , \quad (5.15b)$$

$$\dot{c} = -K_{bc}^{eff}bc + \xi K_{bbb}^{eff}b^3 - K_{bbc}^{eff}b^2c - G_{cb}^{eff}(b+c)c + G_{bc}^{eff}(b+c)b + G_E^{eff}(bd-ac)\ ,$$

$$\dot{d} = -K_{bd}^{eff}bd - G_E^{eff}(bd-ac)\ . \quad (5.15c)$$

Summing (5.15a)–(5.15c) yields

$$\dot{n} = -2K_{ab}^{eff}ab - 2K_{bc}^{eff}bc - 2K_{bd}^{eff}bd - 2K_{bbb}^{eff}b^3 - 2K_{bbc}^{eff}b^2c - 2K_{abb}^{eff}ab^2 \quad (5.15d)$$

In (i) and (ii), K_{ab}^{eff}, K_{bc}^{eff}, etc., are two-body recombination rate constants occurring principally on the surface. The bulk contribution is important only at high temperature, where He atoms in the vapor phase can play the role of the third body. G_{ab}^{eff} is the two-body (intrinsic) magnetic dipole–dipole nuclear relaxation rate constant, the relaxation occurring

both on the surface and in the bulk; G_{bc}^{eff} and G_{cb}^{eff} are electronic relaxation terms with $G_{bc}^{eff}/G_{cb}^{eff} = \exp(-2\mu_B B/kT)$.

In our example, we assume $G_{ab}^{eff} = G_{ba}^{eff}$ which is correct for $T \gg 50$ mK. G_E represents the spin-exchange rate for a, c→ b, d, all other rates being suppressed by high fields (see section 6). This tends to maintain $a/b = d/c$. K_{bbb}^{eff}, K_{abb}^{eff} and K_{bbc}^{eff} are three-body recombination rate constants containing contributions from both the bulk and the surface. For each bbb three-body event, a fraction $\xi = 0.91$ (Verhaar 1985) yields a molecule and an atom in the c-state, and a fraction $1 - \xi$ yields a molecule and an atom in the b-state. Here ξ is assumed to be the same for the surface and volume processes. For K_{abb}^{eff} and K_{bbc}^{eff}, a prefactor of the form $(2 + \xi)$ does not appear since in high fields the reaction leads predominantly to a molecule and a b-atom in the final state (see section 6). ϕ_h are the filling fluxes and n_h/τ_{es} is the rate of thermal escape which can be ignored for sufficiently high B/T.

We shall illustrate the use of these equations with some examples, first for case (i).

5.2.3.1. Thermal escape

If the density is sufficiently low and the flux is set to zero then the thermal-escape term dominates so that $\dot{n}_h = n_h/\tau_{es}$, and the sample decays exponentially with time constant τ_{es} as demonstrated in fig. 5.4b.

5.2.3.2. Decay of H↓

Assume that in addition to the intrinsic relaxation in eq. (5.14) there is impurity induced relaxation so that we must add terms $-G_{iab}^{eff}(a - b)$ and $+G_{iab}^{eff}(a - b)$ to eqs. (5.14a) and (5.14b), respectively (Sprik et al. 1982, Statt et al. 1985). If this term is very large, then the hyperfine states a and b remain in thermal equilibrium for all densities. Adding eqs. (5.14a) and (5.14b) yields

$$\dot{n} = -K^{eff} n^2 + (\phi_a + \phi_b)/V\,, \tag{5.16}$$

with

$$K^{eff} = \tfrac{1}{2}(K_{aa}^{eff} + K_{ab}^{eff})\,,$$

where we ignore thermal escape and have also assumed $kT \gg (E_b - E_a)$ so that $a = b = \frac{1}{2}n$. This corresponds to the decay shown in fig. 5.5b.

5.2.3.3. Decay of double-polarized hydrogen H↓↓

We now ignore the flux and thermal escape in eq. (5.14a). Then, if the relaxation rate G_{ab}^{eff} is very small, the occupations of the a–b states can

come out of equilibrium. Since a–b or a–a collisions will deplete the a-state population preferentially over the b-state population, due to the action of the terms involving K_{aa}^{eff} and K_{ab}^{eff} ($K_{bb}^{eff} = 0$), in time the sample becomes polarized with $b \gg a$ (see section 5.6 for more details, including experimental verification). By studying the decay equations, it can be shown that the a/b ratio approaches a limit value. Asymptotically, $(d/dt)(a/b) \to 0$ for $t \to \infty$, then

$$\frac{a}{b} = \frac{G_{ab}^{eff}}{K_{ab}^{eff} - G_{ab}^{eff}} \simeq \frac{G_{ab}^{eff}}{K_{ab}^{eff}}, \tag{5.17a}$$

with

$$\dot{b} = \frac{-2K_{ab}^{eff}G_{ab}^{eff}}{K_{ab}^{eff} - G_{ab}^{eff}} b^2 \simeq -2G_{ab}^{eff}b^2, \tag{5.17b}$$

where the last approximation is allowed because $K_{ab}^{eff} \gg G_{ab}^{eff}$. The ratio a/b does not go to a limit value but is density dependent if a first- or third-order term is present in eq. (5.14).

Finally, in case (ii), if we exclude three-body processes, with the c-level partially populated, but the a- and d-levels weakly populated due to preferential recombination and spin-exchange, we find a limit value for the a/b and c/b ratios:

$$\frac{a}{b} = \frac{G_{ab}^{eff}}{K_{ab}^{eff} - G_{ab}^{eff} - G_{bc}^{eff}} \simeq \frac{G_{ab}^{eff}}{K_{ab}^{eff}}, \tag{5.18a}$$

$$\frac{c}{b} = \frac{G_{bc}^{eff}}{K_{bc}^{eff} + G_{cb}^{eff}}, \tag{5.18b}$$

$$\dot{b} = -2\left(\frac{K_{ab}^{eff}G_{ab}^{eff}}{K_{ab}^{eff} - G_{ab}^{eff} - G_{bc}^{eff}} + \frac{K_{bc}^{eff}G_{bc}^{eff}}{K_{bc}^{eff} + G_{cb}^{eff}}\right)b^2. \tag{5.18c}$$

5.3. Stabilization of D↓

To date the only successful attempt to accumulate a measurable density of D↓ in a cell is that of Silvera and Walraven (1980b); Mayer and Seidel (1985) have studied D in low fields but were unable to build up a measurable density.

The study of D↓ by Silvera and Walraven took place shortly after H↓

was stabilized. The most surprising aspect was that only densities of order $10^{14}/\mathrm{cm}^3$ could be built up and that the sample decayed very rapidly, in order of minutes rather than hours. Before this, no serious limitations had been observed for H↓ densities. The decay of the density, measured using bolometric techniques, was found to fit a second-order rate equation of the form of eq. (5.16). From the determination of K^{eff}, values of $\varepsilon_a/k = 2.6(4)$ K and $K^s/\sqrt{T} = 5.7 \times 10^{-7}\ \mathrm{cm}^2\ \mathrm{K}^{-1/2}\ \mathrm{s}^{-1}$ were determined for $B = 8$ T, as will be described in the next two sections. The interpretation of the second-order decay process of the bulk density was as follows: atoms recombine on the surface by a second-order process and in order to maintain equilibrium, atoms from the bulk replace atoms on the surface. Thus, an equation of the form eq. (5.16) was applicable.

Clearly the main reason for the rapid decay of D↓ was the large value of ε_a. At $T = 370$ mK the exponential factor in K^{eff}, $\exp(2\varepsilon_a/kT) = 1.3 \times 10^6$, compared to a value of 222 for H with $\varepsilon_a \simeq 1$ K. This substantially larger surface coverage results in faster decay. Other differences between D↓ and H↓ might arise due to different hyperfine state spin mixtures. Using current techniques it is not too hopeful that densities required to observe effects of quantum degeneracy in D↓ will be achieved.

5.4. Measurement of the surface adsorption energy

There are a few experimental techniques that have been used for determining ε_a. Silvera and Walraven (1980b) first introduced the decay-of-density technique in a study of D↓. They found that after filling a cell, the gas density n decayed as a second-order process, $\dot{n} = -K^{\mathrm{eff}} n^2$ (see eq. 5.16), where $K^{\mathrm{eff}} = \lambda_{\mathrm{th}}^2 (A/V) \exp(2\varepsilon_a/kT) K^s$. Here A and V are the cell area and volume, and K^s is the intrinsic surface recombination rate. By measuring K^{eff} at a series of temperatures, ε_a was determined from a least squares fit of $\ln(K_{\mathrm{eff}}\sqrt{T})$ versus $1/T$, in which ε_a is half the slope of the straight line fitted to the data. In this case, K^s is assumed to have a temperature dependence of $\sqrt{T}$, which follows from simple kinetic arguments concerning the cross section. This yields a value of $\varepsilon_a/k = 2.6(4)$ K. The originally published value of $\varepsilon_a/k = 2.5$ K by Silvera and Walraven was based on a temperature-independent value of K^s and was revised to 2.6 K by Matthey et al. (1981).

There have been several determinations of ε_a for H on ^{4}He surfaces. In a technique different from that used for D↓, Morrow et al. (1981) measured the temperature dependence of the shift of the hyperfine frequency $\Delta\omega = \Delta_s \lambda_{\mathrm{th}} (A/V) \exp(\varepsilon_a/kT)$ where Δ_s is the frequency shift for an atom on the surface relative to that of an isolated atom. A fit of $\ln(\sqrt{T}\Delta\omega)$ versus $1/T$ yields ε_a as shown in fig. 5.6. Morrow et al. also used the

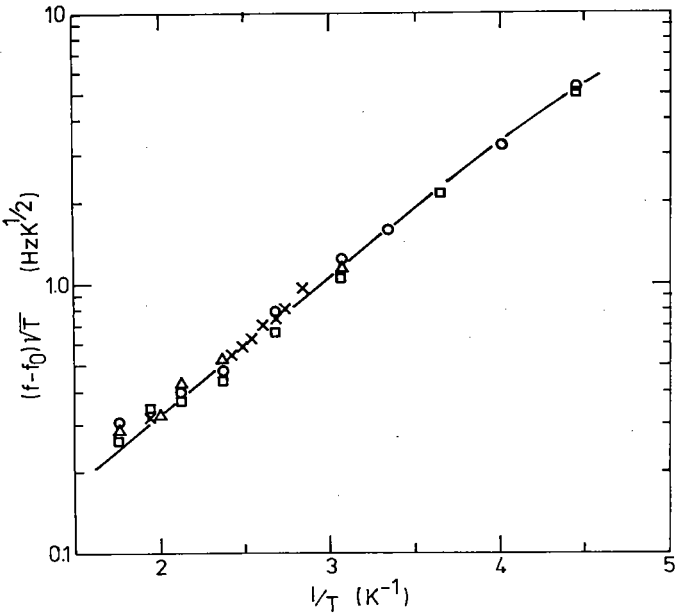

Fig. 5.6. The hyperfine frequency shift of H in contact with ^{4}He walls in zero field, plotted such that the slope is ε_a (after Morrow et al. 1981).

decay-of-density technique to determine ε_a for H on ^{4}He, in zero field, whereas Matthey et al. (1981) used this technique in high field. (Measured values of ε_a are given in table 5.1.) ε_a has also been determined from the decay of double-polarized hydrogen. For this system an effective nuclear relaxation process controls the decay rate and the data are fit to eq. (5.17). This was done by Cline et al. (1981), Sprik et al. (1982), Yurke et al. (1983), Hess et al. (1983) and Statt (1984). These results are unreliable in view of an interpretation in terms of third-order recombination as pointed out by Hess et al. (1984) (see section 5.8). Reynolds et al. (1985) have determined ε_a by directly measuring σ and n using ESR signals from surface and bulk atoms. There is large scatter in values of ε_a determined at different laboratories. Recently, Godfried et al. (1985) have performed a careful study to make a more definitive determination of ε_a, seeking to minimize systematic errors. Efforts were made to maintain a well-characterized polarization of the a- and b-states and the temperature of the gas was measured. A warming of the gas with respect to the cell-wall temperature at lower temperatures due to recombination was found to give a systematic decrease of the determined value of ε_a. Their corrected value for H$\downarrow$ on ^{4}He is $\varepsilon_a = 0.96(2)$ K. Thus the three most recent measure-

Table 5.1

Adsorption energies and two-body recombination rate constants. The theoretical values of ε_a are from Stwalley (1982). When calculating a value of K^{eff} one should use the value of ε_a and K_s determined in the same measurement to minimize problems with systematic errors.

System	Theory	Experiment		Ref.
	ε_a (K)	ε_a (K)	$K^s T^{-1/2} B^2$ ($cm^2\,K^{-1/2}\,T^2\,s^{-1}$)	
H↓ on ^{4}He	0.85	0.89(7)	$2.6(8) \times 10^{-7}$	[1]
		1.15(5)		[2]
		1.01(6)	$5.4(4) \times 10^{-8}$	[3]
		0.99(2)		[4]
		1.06(4)	4.1×10^{-8}	[5]
		1.00(5)		[6]
		0.96(2)	$5.9(5) \times 10^{-8}$	[7]
		1.10(2)	$5.7(8) \times 10^{-8}$	[8]
		0.89(6)		[9]
D on ^{4}He	2.2	2.6(4)	3.7×10^{-5}	[10]
T on ^{4}He	3.2	–	–	
H on ^{3}He–^{4}He	0.36	0.34(3)	9.0×10^{-8}	[11]
H on ^{3}He	0.36	0.42(5)	–	[12]
D on ^{3}He	1.2	–	–	
T on ^{3}He	1.9	–	–	

References:

[1] Matthey et al. (1981).
[2] Morrow et al. (1981).
[3] Cline et al. (1981).
[4] Hess et al. (1984).
[5] Yurke et al. (1983).
[6] Reynolds et al. (1985).
[7] Godfried et al. (1985).
[8] Statt (1984).
[9] Sprik et al. (1982).
[10] Silvera and Walraven (1980b).
[11] van Yperen et al. (1981).
[12] Jochemsen et al. (1981).

ments, using somewhat different techniques (Hess et al. 1984, Reynolds et al. 1985, Godfried et al. 1985) all yield results which are in close agreement: 0.99(2) K, 1.00(5) K and 0.96(2) K. Possibly the early measurements of Matthey et al. (1981) suffered slightly from heating of the gas. There is yet no explanation for the large discrepancy of the zero-field measurement of Morrow et al. (1981) from all other values.

Godfried et al. (1985) also studied the dependence of ε_a on the He film thickness. Since the underlying H_2 layer has $\varepsilon_a \simeq 40$ K, the adsorption

energy must approach 40 K as the film thickness goes to zero. On theoretical grounds ε_a is not expected to change much due to the potential of the H_2 until the film is 4–5 layers thin. A second factor which could effect ε_a is a change of the He surface density profile for very thin films. An increase in ε_a of more than 20% was seen in the thinnest films of 3–4 layers of helium. This is larger than predicted by a model which does not allow for variations in the surface density profile. Apparently, from this work, a liquid ^{4}He film only a few monolayers thick is adequate for stabilization of H↓.

In table 5.1, one notes the increased experimental value of ε_a for D on ^{4}He, as compared to H on ^{4}He. This seems to be a mass effect, i.e., since the He–D and He–H potentials are isoelectronic, D with a larger mass and smaller zero-point energy sits deeper in the adsorption potential well, so that ε_a is larger. Papoular (1983) has suggested the possibility of a dimer state of D↓ on surfaces. If this is indeed the case and the data are analyzed (ignoring this) in terms of a single-atom adsorption energy, then the experimentally determined value would be too high. There is no experimental evidence of the dimer state and the experimental value does not differ enough from the scaled value of Stwalley (table 5.1) to support Papoular's suggestion, even though the Stwalley theory is quite rough.

In comparison to ^{4}He surfaces there is a substantial reduction of ε_a for ^{3}He surfaces. This is due to the lower density of ^{3}He and its more extended surface profile. Jochemsen et al. (1981) measured this in zero-field by resonance techniques. van Yperen et al. (1981) studied ^{3}He–^{4}He mixtures. They found a value of ε_a representative of ^{3}He as the ^{3}He–^{4}He mixture phase separates and the ^{3}He resides on top of the ^{4}He in contact with the gas of H↓. Oddly enough, with this substantial advantage of a lower value of ε_a, most experimental work still seems to be concentrated on ^{4}He surfaces. This may be due to certain experimental complications and behavior when using ^{3}He. An alternate explanation is that ^{3}He is generally introduced into a cell in the latter part of an experiment to avoid impurity contamination of pure ^{4}He which results from outgassing of ^{3}He from teflon, etc., in the loading section of a cell. Small amounts of ^{3}He can have a significant effect on ε_a. Since these experiments are usually long and exhausting, fatigue of the experimenters may influence a decision to terminate with satisfactory results for ^{4}He.

5.5. Two-body surface recombination rate constants

In this section we discuss the experimental values of the two-body surface recombination rate constants such as K_{aa}^{eff}, K_{ab}^{eff} which arise in eqs. (5.14),

(see section 6). In experiments in which the occupation of the hyperfine states correspond to thermal equilibrium, $K^{\rm eff} = (A/V)\lambda_{\rm th}^2 \times \exp(2\varepsilon_a/kT)K^s$. The most common technique for determining K^s is to measure $K^{\rm eff}$ as a function of temperature (at fixed magnetic field). By plotting $\ln(K^{\rm eff}\sqrt{T})$ versus $1/T$, one finds a straight line with intercept related to K^s. It is sometimes convenient to use the crosslength, δ_s, which is the two-dimensional analogue of the cross section, defined by $K^s \equiv \delta_s \bar{v}_s$, where $\bar{v}_s = (\pi kT/2m)^{1/2}$ is the average velocity in a two-dimensional gas (see also eq. 6.79d). Jochemsen et al. (1981) used a different expression, $\bar{v}_s = (32kT/3\pi m)^{1/2}$.

5.5.1. *Deuterium*

The first measurements were made by Silvera and Walraven (1980b) on D↓, as discussed in the previous section. The difficulty they encountered in determining the intrinsic recombination rate constant was in the uncertainty of the surface area. If we assume that, as was most likely, the sinter in this cell was capillary filled with ^{4}He, then $A = 5.5\,\text{cm}^2$, $V = 0.68\,\text{cm}^3$ and $K^s B^2 T^{-1/2} = 3.7 \times 10^{-5}\,\text{cm}^2\,\text{K}^{-1/2}\,\text{T}^2\,\text{s}^{-1}$. If the sinter was not capillary filled, the area is estimated to be $400\,\text{cm}^2$ with $V = 1.14\,\text{cm}^3$, and K^s would be decreased by ~17.

5.5.2. *Hydrogen*

5.5.2.1. *Magnetic-field dependence*

K^s was first measured for H on ^{4}He in zero-field by Morrow et al. (1981) and in high fields by Matthey et al. (1981). We first discuss the UBC experimental apparatus of Morrow et al. for which the low-temperature section is shown in fig. 5.7. The cell consists of a pyrex ampule containing 0.1 bar of H_2 and 0.5 bar ^{4}He sealed in at room temperature. At low temperature the He covers the H_2 substrate with a saturated film. The H is produced in a low-temperature discharge generated by a 100 W rf pulse lasting up to 1 ms, short enough to prevent excessive heating of the cell. The detection was done with magnetic resonance at the zero-field hyperfine transition (see fig. 2.1) using a 1420 MHz spectrometer (Hardy and Whitehead 1981) which is discussed in more detail in section 5.10. The density n was proportional to the resonance line strength, and could be accurately measured as a function of time enabling a determination of the decay constant.

Matthey et al. (1981) used the cell shown in fig. 5.5a and measured the pressure and temperature, determining the density from the ideal gas law,

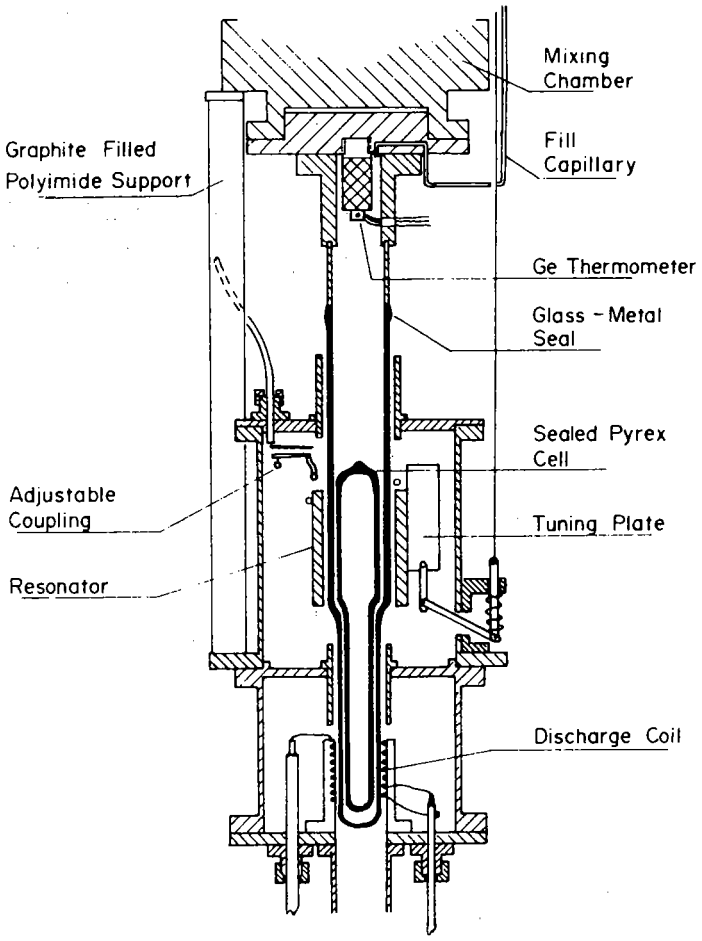

Fig. 5.7. The low-temperature part of the zero-field resonance apparatus used by Morrow et al. (1981). Hydrogen is produced by a pulsed discharge in the lower part of the glass cell and detected by resonance at 1420 MHz in the upper part.

$n = p/kT$. A typical decay curve in a magnetic field is shown in fig. 5.5b. A suitable plot and fit enables a determination of K^s. This was measured as a function of magnetic field, the results being shown in fig. 5.8b. Here the rate constant was first shown to be proportional to B^{-2} (for high fields) which lent strong experimental support to the idea that the principle open channel for recombination was due to the admixture (proportional to B^{-1}) of the up-spin into the hyperfine state $|a\rangle$ (see section 6). Subsequently there have been a number of measurements of decay at various fields and temperatures. Much of this data is collected and compared in fig. 5.9a.

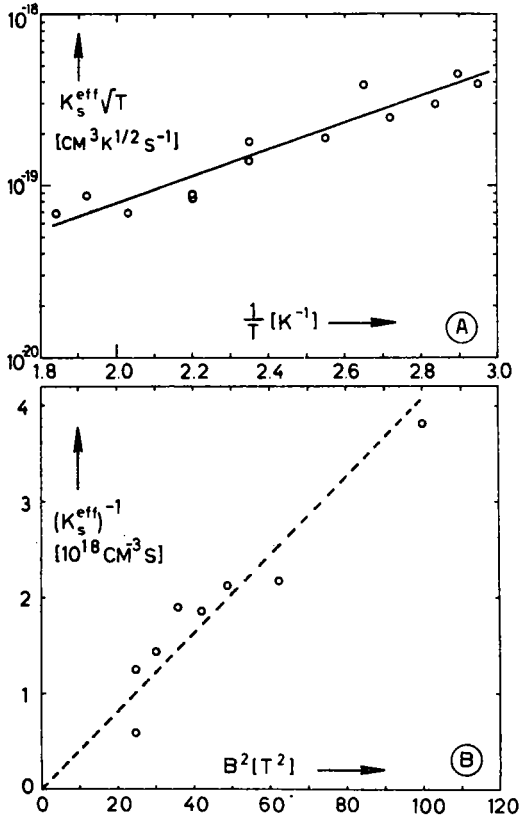

Fig. 5.8. (a) A plot of $\ln(K^{eff}\sqrt{T})$ versus $1/T$ for H↓ on ^{4}He. (b) A plot of the data demonstrating the magnetic-field dependence of K^{eff} (after Matthey et al. 1981).

The solid lines represent theoretical second-order recombination on a ^{4}He surface for magnetic fields ranging from 0–10 Tesla. The curves are obtained by scaling with f_I (eq. 6.17), assuming an equilibrium distribution over the four hyperfine levels. To fix the absolute value of the left-hand scale, the zero-field curve is fit to the UBC data of Hardy et al. (1980b) (open circles). Concentrating on the $B = 10$ T curve of fig. 5.9a one notes that with increasing temperature the rate decreases exponentially until at approximately 1 K the temperature is sufficiently high to populate the c- and d-levels. Then the rate increases sharply until the curve joins the $B = 0$ T curve indicating that all hyperfine levels are equally populated. All curvature in the $B = 0$ T curve is a result of the temperature dependence of λ_{th}. Note that for $B = 2$ T the rate is essentially constant between 300 mK and 1 K.

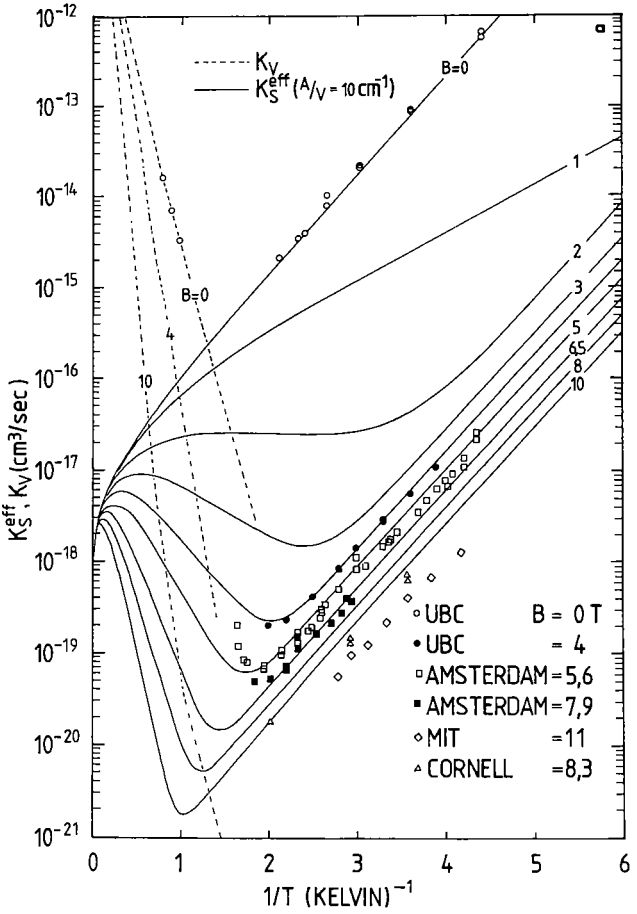

Fig. 5.9. (a) K^{eff} and K^{v} as a function of $1/T$ for H on ^{4}He surfaces. Solid line: K^{eff}; dashed line: K^{v}. [UBC: $B = 0$ T, Hardy et al. (1980b), Morrow et al. (1981); $B = 4$ T, Statt et al. (1985); Amsterdam: $B = 7.9$ T, Matthey et al. (1981); $B = 5.6$ T, Matthey et al. (1984); MIT: Cline et al. (1981); Cornell: Yurke et al. (1983).]

The dashed lines in fig. 5.9a represent second-order volume recombination, enabled by the presence of ^{4}He vapor. Morrow et al. (1981) found the zero-field rate constant of $0.28(4) \times 10^{-32}$ cm^6 s^{-1} at 1 K in ^{4}He and Jochemsen et al. (1982) found 0.12×10^{-32} cm^6 s^{-1} at 0.5 K for ^{3}He (UBC results). The various lines in fig. 5.9a are obtained by scaling the UBC results (open circles) using eq. (6.16) and ^{4}He vapor pressure data. One observes good agreement between the zero-field UBC data and the

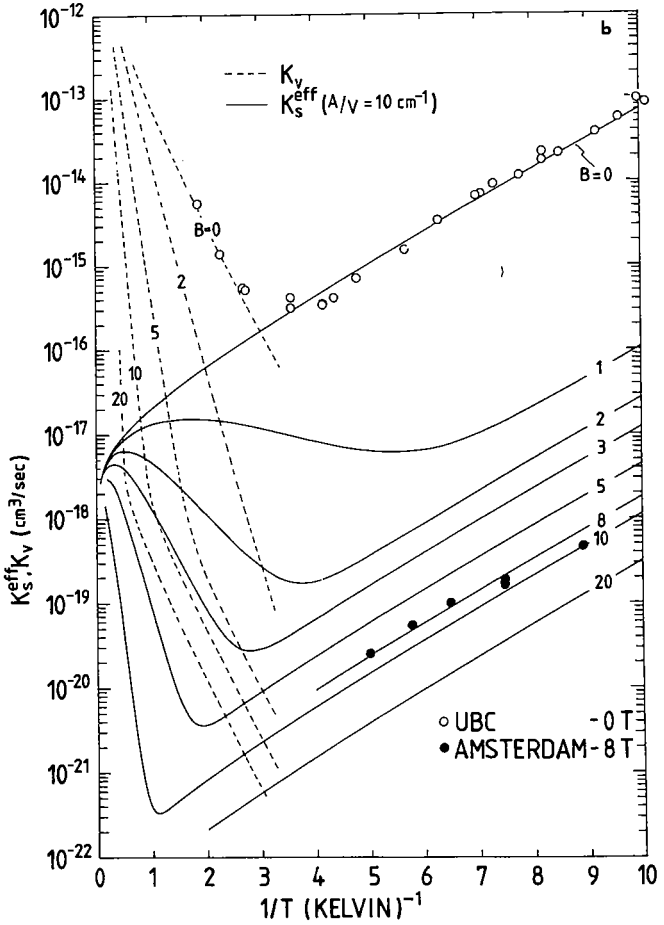

Fig. 5.9. (b) Same as (a) but now for ^{3}He or ^{3}He–^{4}He surfaces (Amsterdam: van Yperen et al. 1981; UBC: Jochemsen et al. 1982).

high-field results obtained in Amsterdam (Matthey et al. 1981). The Cornell data (obtained at $B = 8.3$ T by Yurke et al. 1983) and the MIT data at $B = 11$ T (Cline et al. 1981) lie 20–30% below the scaled curve. A similar plot for ^{3}He surfaces is given in fig. 5.9b.

The agreement between theory and experiment is quite impressive, considering that it spans eight orders of magnitude.

5.5.2.2. The value of K^s

K^s has been measured in several laboratories and there exists some scatter

with the value of Matthey et al. (see table 5.1) appearing to be much larger than the average. An accurate determination requires precision measurements as it is determined from a logarithmic plot of $\ln(K^{\text{eff}}\sqrt{T})$ versus $1/T$ in which K^{s} is proportional to the intercept on the ordinate. One might expect a smaller value of K^{s} for H↓ on ^{3}He than on ^{4}He as the helium density enters into K^{s} (analogous to eq. 6.26) and ^{3}He has a lower surface density than ^{4}He. However, to obtain a proper comparison, a measurement for both ^{4}He and ^{3}He should be made in the same cell to remove systematic errors.

5.6. Double polarization: H↓↓

With the determination of $K^{\text{eff}}(B)$, it was immediately clear that high densities of H↓ would not be easily achieved. The maximum density to which a cell can be filled is calculated by setting the recombination rate equal to the filling flux. Setting $\dot{n} = 0$ in eq. (5.16) yields

$$n^{\max} = B[\phi_n/K^{\text{s}'}V]^{1/2}\,, \tag{5.19}$$

where we have written $K^{\text{s}} = K^{\text{s}'}/B^2$. With an optimized cell the highest densities that could be achieved, with $B \simeq 10$ T and $T \simeq 300$ mK, was a few times $10^{17}/\text{cm}^3$. The highest static fields presently available could only raise this by a factor of three.

A suggestion of Hardy led Statt and Berlinsky (1980) to calculating the possibility of b-state enhancement due to preferential recombination and nuclear relaxation* bottlenecking. The idea is that if only the a and b states are populated and the (nuclear) relaxation rate G_{ab} from a to b is small, then the occupations of the states can come out of equilibrium. They calculated a favorable nuclear relaxation time $T_1 \simeq 10^4$ s for $n \simeq 10^{16}/\text{cm}^3$. Since a–a collisions and a–b collisions can lead to recombination to H_2, but collisions between fully polarized b-state atoms cannot (see section 6), and since K^{s}_{aa} or $K^{\text{s}}_{\text{ab}} \gg G_{\text{ab}}$, the b-state population will be enhanced as the sample decays away. If the population $n_{\text{b}} \gg n_{\text{a}}$, then the main channel of atomic decay will be relaxation from b to a, followed by recombination. The sample will then decay at a rate of $2G^{\text{eff}}_{\text{ab}}$ rather than K^{eff} as shown in eq. (5.17). Note that the atoms in the b-state are both electron and nuclear spin polarized.

van Yperen et al. (1981) attempted to observe this nuclear-spin enhanced state by lowering the cell's temperature to rapidly deplete the b-state, however, the entire sample decayed away [they later realized that

* We use nuclear relaxation as shorthand for nuclear spin relaxation.

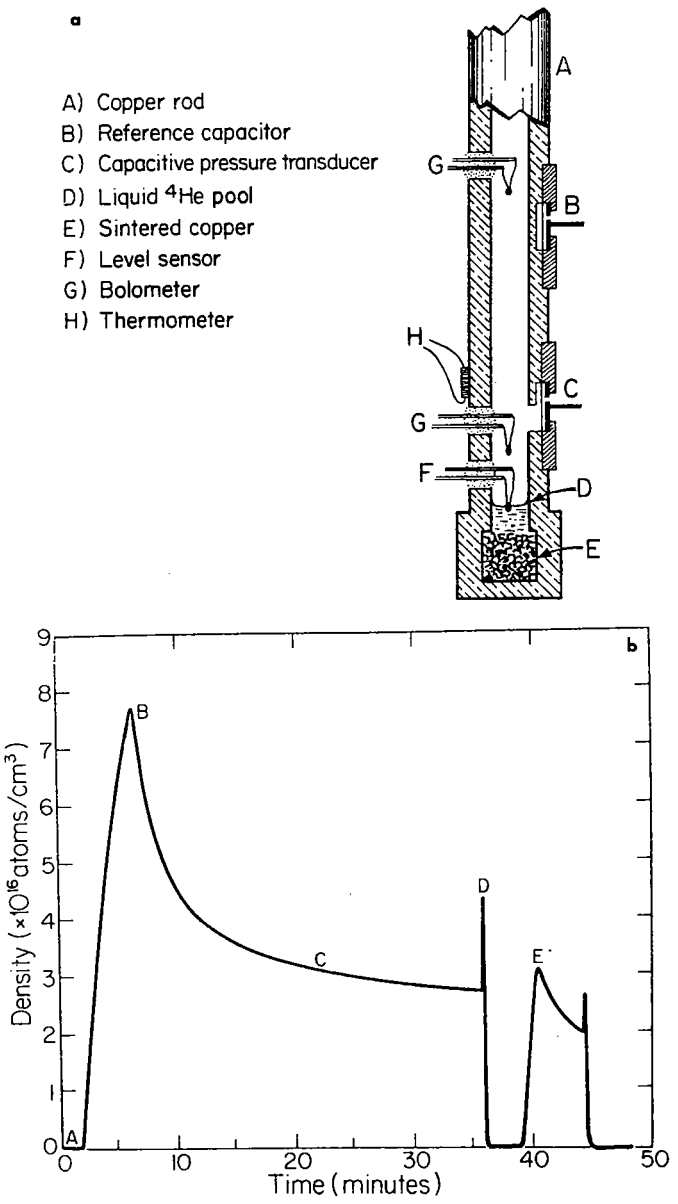

Fig. 5.10. (a) A cleanly etched copper cell with a saturated film of ^{4}He above the puddle in the bottom, used to produce H↓↓ (after Cline et al. 1981). (b) Decay of the density of H at $T = 300$ mK, $B = 11$ T. The two decays showing very different slopes for the same density was the first demonstration that the a- and b-states are coming out of equilibrium to produce a gas of enriched b-state hydrogen (after Cline et al. 1981).

macroscopic magnetic impurities in the walls of their cell enhanced the relaxation rate, keeping the occupations of the hyperfine states in equilibrium (Sprik et al. 1982)]. Cline et al. (1981) first succeeded in obtaining double-polarized hydrogen. They used a standard top-loaded cell which had cleanly etched surfaces, covered with a saturated film of ^{4}He, shown in fig. 5.10a. The production of H↓↓ is dramatically demonstrated in fig. 5.10b showing the decay of the density measured with a pressure gauge. If the occupations of the hyperfine states remain in equilibrium, then the decay rate will depend only on the density n and not on the history of filling and decay. Their cell was first loaded to a high density (point B) and allowed to decay to point D where the gas was destroyed. After reloading to the density corresponding to C, the sample was seen to decay at a much different rate which could only be explained by b-state enhancement. Subsequently, Sprik et al. (1982) constructed a cell free of macroscopic magnetic impurities and were able to fill to densities of $3 \times 10^{17}/\text{cm}^3$, decaying to polarizations estimated to be as great as 99.8%. Although higher densities cannot easily be achieved by direct filling, the production of H↓↓ made it possible to increase the density by more than an order of magnitude in subsequent compression (see section 5.12).

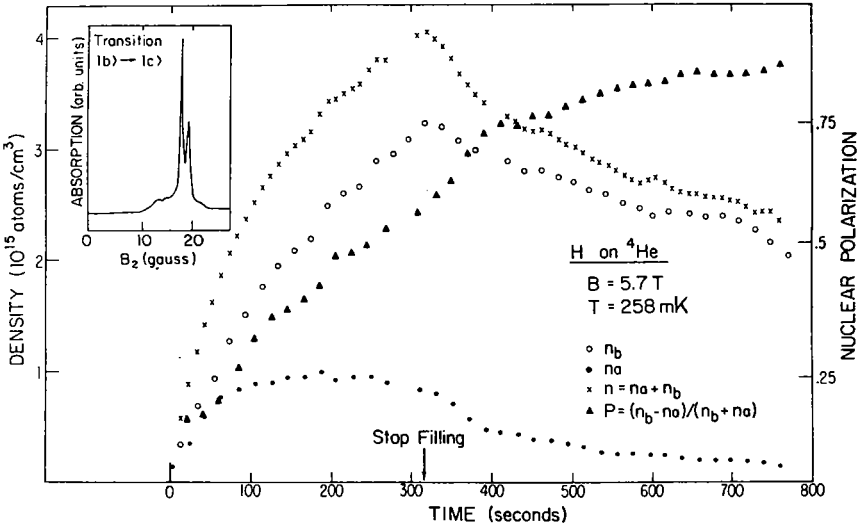

Fig. 5.11. Development of the densities of the hyperfine states and polarization as a function of time as measured by ESR. The inset shows the ESR line shape for one of the transitions (after van Yperen et al. 1983).

A direct demonstration of double-polarization was provided by the ESR measurements of van Yperen et al. (1983). The ESR signal is proportional to the differences in density between initial and final states, $(n_{h_1} - n_{h_2})$. From fig. 2.1 we see that the allowed ESR transitions are a→d and b→c. Since for H↓, the c and d states are depleted, the ESR signal is proportional to n_a and n_b for the two allowed transitions. In fig. 5.11 we show their plot of n_a, n_b and the nuclear polarization $P = (n_a - n_b)/(n_a + n_b)$ as a function of time. Both n_a and n_b start with the same slope as $\phi_a = \phi_b$, but already in the filling stage the sample becomes highly polarized. In this case conditions were such that the sample polarized for more than 80%.

5.7. Measurement of K^s_{aa} and K^s_{ab}

With the successful production of H↓↓ it becomes important to know the ratio

$$\gamma = K^s_{aa}/K^s_{ab}\,, \tag{5.20}$$

(see section 6.1 for theoretical considerations) as γ ultimately determines the density of H↓↓ to which the sample decays from its initial unpolarized mixture of a and b states (Sprik et al. 1982). Defining the final to initial density as n_∞/n_0 and assuming $n_{a_0}/n_{b_0} = 1$, the following limits are found:

(1) if $K^s_{ab} = 0$ then $n_\infty/n_0 = 0.5$ as only the a atoms will recombine,
(2) if $\gamma = 1$ then $n_\infty/n_0 = 0.25$, and
(3) if $\gamma = 0$ $(K^s_{aa} = 0)$, then $n_\infty/n_0 = 0$.

For the initial conditions given above, one finds in general

$$n_\infty/n_0 = \tfrac{1}{2}(2\gamma)^{(1-2\gamma)^{-1}}\,. \tag{5.21}$$

Sprik et al. measured γ by working at a low density (so that T_1 is long), rapidly filling a cell so that $n_{a_0}/n_{b_0} = 1$ (from fig. 5.11 we see that polarization can become substantial even during the filling phase) and then allowing the gas to decay to its asymptotic value to determine n_∞/n_0. Density was measured with a pressure gauge. Using eq. (5.21) they found $\gamma = 2.23(25)$ independent of temperature in the range of measurements (225–300 mK) this is shown in fig. 5.12, which summarizes results of different experiments.

Yurke et al. (1983) employed the same technique, however, they had an NMR coil in their cell and after filling they were able to saturate the a→b transition to equalize the densities, i.e. $n_{a_0}/n_{b_0} = 1$. They were able to detect a temperature dependence, with γ increasing from 2.8 to 3.9

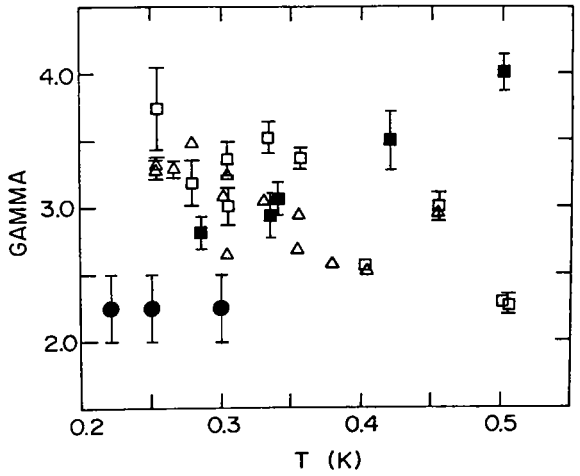

Fig. 5.12. A summary of results of measurements of $\gamma = K^s_{aa}/K^s_{ab}$ versus T. ●, Sprik et al. (1982); ■, Yurke et al. (1983); □, △, Statt et al. (1985).

between 280 and 500 mK. Their data just overlaps Sprik et al.'s and there is no serious discrepancy.

Statt et al. (1985) have used ESR to monitor the decay of density of the a and b states. By fitting rate equations they were able to determine K^s_{aa} and K^s_{ab} separately. Their values for γ which decreases with increasing temperature are also shown in fig. 5.12. We are unable to explain the differences in the measured temperature dependences.

5.8. Nuclear relaxation

5.8.1. Intrinsic relaxation

Clearly the nuclear relaxation rate between the b and a hyperfine levels plays a major role, often rate controlling, in the decay of hydrogen. The fact that it bottlenecks the recombination means that nuclear T_1's can be determined by measuring the decay of the density [see eq. (5.17), where $G^v_{ab} = (2T_1 n)^{-1}$]. In their experiment on nuclear polarization, Cline et al. (1981) first observed the T_1 bottleneck and determined G^{eff}_{ab} with $G^v_{ab}T^{-1/2} = 3.5(3) \times 10^{-21}\ \mathrm{cm^3\,s^{-1}\,K^{-1/2}}$ and $G^s_{ab}T^{-1} = 1.7(4) \times 10^{-12}\ \mathrm{cm^2\,s^{-1}\,K^{-1}}$ on a cylindrical-shaped cell with the magnetic field parallel to the cell axis. As will be discussed in section 6, G^s_{ab} is predicted to have a weak temperature dependence, and the T^{-1} behavior was used by Cline et al. in the absence of any theory at that time.

Sprik et al. (1982) designed a cell that emphasized the surface effects because of its large surface to volume ratio. It had a pancake shape, so that the field was normal to most of the surface. This design was inspired by calculations (Lagendijk 1982) which predicted an anisotropy in G^s_{ab} such that it would be zero if $\boldsymbol{B}$ was parallel to the surface normal. They found a value of G^v_{ab} in agreement with Cline et al. (1981) and a nonzero value of G^s_{ab}, contrary to expectations for this geometry. The nonzero value was explained in terms of a microscopic surface roughness such that an average over $\boldsymbol{B}\cdot\boldsymbol{n}$, where $\boldsymbol{n}$ is the surface normal, washed out the anisotropy effects. Yurke et al. (1983) found similar results.

Sprik et al. (1982) also measured the magnetic field dependence of G^s_{ab} and found reasonable agreement with the predicted dependence (see section 6.2), $(1+16.68/B)^{-2}$. For reasons to emerge later, we show their unpublished data in fig. 5.13. They quoted a value $\alpha\langle G^s_{ab}\rangle\,(1+16.68/B)^{-2} = 3.4(1.0)\times 10^{-13}\ \mathrm{cm^2/s}$, where $\langle G^s_{ab}\rangle$ is the orientational average of G^s_{ab} and α represents the microscopic to macroscopic (projected) area ratio, estimated to be 1.17. They also tried to measure G^s_{ab} on a ^{3}He surface at low temperatures down to about 80 mK but did not observe any surface relaxation. They attributed this to the ^{3}He filling in the surface roughness, so that $\langle G^s_{ab}\rangle \simeq 0$.

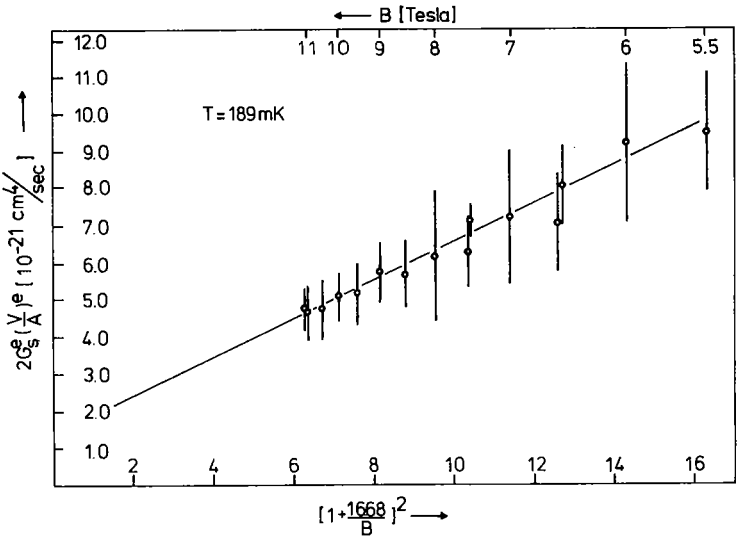

Fig. 5.13. The magnetic field dependence of G^s_{ab} [G^e_s is an effective rate constant related to G^s_{ab} as introduced in section 5.1.2] for H↓ on ^{4}He, from Sprik et al. (unpublished). This is probably more representative of the field dependence of K^s_{bbb}, as discussed in section 5.11.

The most challenging problem to emerge from these studies was that, even though G^{v}_{ab} was found to be in good agreement with theory, the experimental value of G^{s}_{ab} was about 50 times greater than predicted by theory. For a few years, a number of efforts were made to understand this. Van den Eijnde et al. (1983) made some exhaustive studies but could only bring the discrepancy down to a factor of 35.

This problem has been resolved by the experimental observations of Hess et al. (1984). In studying three-body recombination, they found a large contribution from a decay rate term of the form $L\sigma^3$ ($L \propto K^{s}_{bbb}$) which was attributed to a dipolar surface recombination process first suggested by Kagan et al. (1981). They suggested that in the interpretation of earlier measurements this term was not in the rate equations, and the decay due to this process was attributed to the second-order relaxation process. This has been supported by recent measurements of Reynolds et al. (1985) who studied decay at low temperature with ESR, and were able, as were Hess et al. (1984) (see also Bell et al. 1984b), to separate K^{s}_{bbb} and G^{s}_{ab}. In their preprint they do not quote experimental values for these two rate constants, but give results in graphical form, shown in fig. 5.14. The smaller value of G^{s}_{ab} is now in agreement with theory. However, the experimental value of the three-body surface recombination rate is substantially larger than predicted by calculations of de Goey et al. (1984).

5.8.2. Impurity relaxation

As was already mentioned, the negative result in the attempt of van Yperen et al. (1981) to observe H↓↓ was attributed to impurity relaxation on the surface of the cell. (The means of accounting for this in the rate equations is given in section 5.2.3.2.) Sprik et al. (1982) performed a chemical analysis of the surface of a machined copper piece. They found large concentrations of iron in the first few tenths of a micron and then the concentration reduced to the bulk value of about 10 ppm of Fe. Evidently, small pieces of ferromagnetic material from the machining tool were left in the surface. These grains create magnetic field inhomogeneities which fall off as the inverse third power of the distance. Since the grains are of order 10^3 Å and helium films are 200–300 Å thick, the He does not shield the H↓ from impurities. In the coordinate system of the moving hydrogen atoms, the impurity field is time varying and if this has a Fourier component at frequency $(E_a - E_b)/\hbar$, transitions can occur. A measurement of the static magnetization of the 2850 FT epoxy, used in parts of the interior of the cell, showed it to have weak ferromagnetic properties. The message from this is that cells must be prepared with painstaking precautions if H↓↓ is desired.

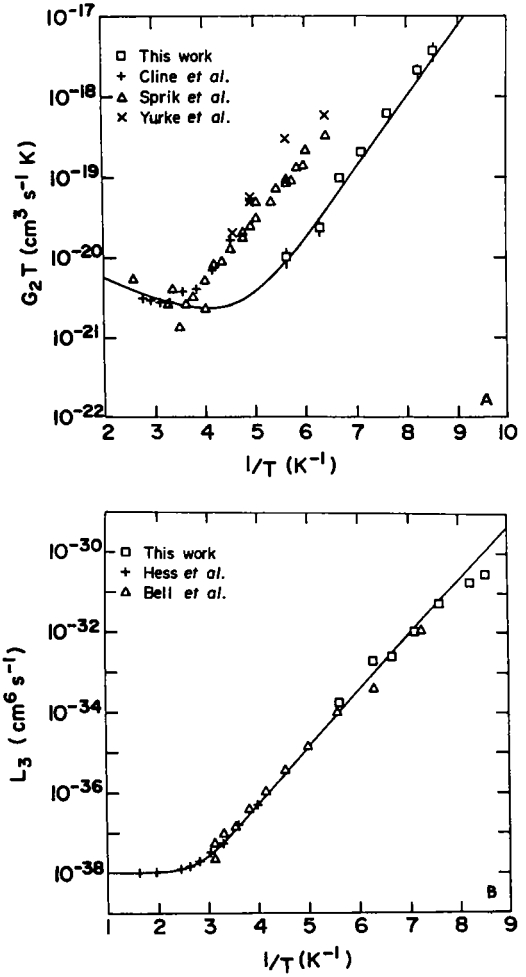

Fig. 5.14. (a) The surface relaxation rate as a function of T^{-1}. The data points of Reynolds et al. (squares) have been separated from the three-body recombination process (after Reynolds et al. 1985). (b) The third-order surface recombination rate constant $L_3 \equiv 2\theta_b K_{bbb}^{eff}$ (after Reynolds et al. 1985).

Even well etched cells usually contain submicroscopic (clusters) or atomic magnetic impurities which lead to first-order impurity relaxation. Sprik et al. (1982) studied the first-order process as a function of He film thickness. For very thin films a large first-order process was observed. This could be completely suppressed with a thick (200–300 Å) saturated film of He. The MIT group and the UBC group (Statt et al. 1985) have built up thick layers of H_2 (recombined H) in their cells to suppress first-order

relaxation. Statt et al. presented a model for impurity relaxation in which they assume the presence of 75 Å iron clusters on the surface of OFHC copper. They give the result of an unpublished calculation (Berlinsky 1984) yielding relaxation rates which depend exponentially on the thickness of the He film. Godfried et al. (1985) have taken advantage of the impurity relaxation. In their study of ε_a, an equilibrium gas was desired. A surface covered with large iron grains (~50 μ diameter) was placed in the cell to promote rapid relaxation.

5.8.3. *Relaxation and the boson nature of* H↓

In the calculation of nuclear relaxation rates of H↓, i.e., b→a relaxation, great care must be taken to properly symmetrize the wavefunctions used in calculating the matrix elements. Lagendijk et al. (1984) realized that relaxation measurements might be used to experimentally verify the boson nature of H↓. They calculated the volume relaxation rate for bosons, fermions and classical particles. Their results, shown in fig. 5.15, give strong support of the composite boson nature of H↓.

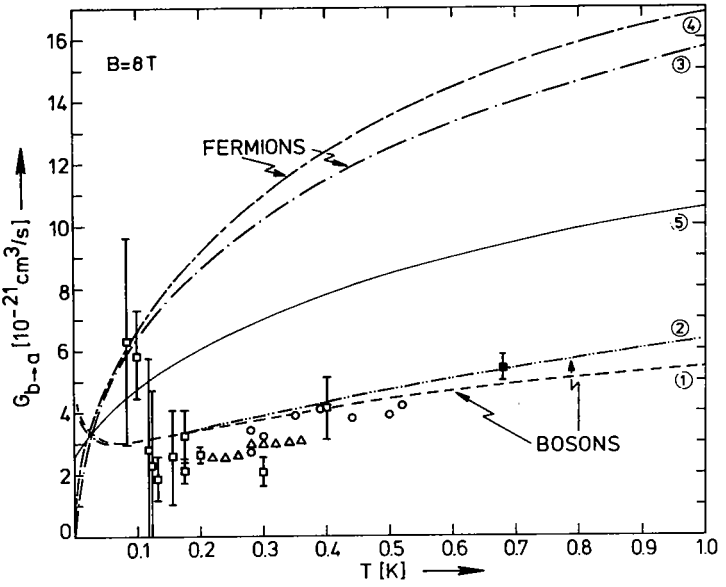

Fig. 5.15. The volume nuclear relaxation rate as a function of temperature for $B = 8$ T, calculated under various approximations. The curve labelled 5 is for classical particles. The points are experimental results (after Lagendijk et al. 1984). [△, Cline et al. (1981); □, Sprik et al. (1982); ○, Yurke et al. (1983); ■, Sprik et al. (1984).]

5.9. Electronic relaxation

Electronic relaxation corresponding to b→c or a→d transitions is more difficult to study because population of the c or d levels in H↓ leads to a highly unstable sample, i.e., the prime requirement in stabilizing hydrogen is to polarize the electronic spins to suppress recombination. In compressing samples of hydrogen to high density Sprik et al. (1983) and Tommila et al. (1984a) noted that under certain conditions samples would become unstable and explode. (See section 5.12 for a description of the experiment.) Since the atoms were all in the b-state before compression they concluded that rapid three-body recombination heated their samples and the heating populated the c-state by electronic relaxation. This process is thermally activated, i.e., $G^{v}_{bc} \propto \exp(-g_e \mu_B B/kT)$. By carefully studying the decay of a sample of b-state hydrogen at elevated temperatures near the onset of this process ($B/T \leq 10.5\,\mathrm{T/K}$), G^{v}_{bc} could be determined. b-state atoms decay either to the a-state or the c-state followed by recombination. G^{v}_{ba} is weakly field- and temperature-dependent and well studied and understood; G^{v}_{bc} could be separated out by means of its strong exponential dependence on B/T. In fig. 5.16, $G^{v} = G^{v}_{ba} + G^{v}_{bc}$ is plotted versus $(1 + 16.68/B)^2$ which is the expected field dependence for G^{v}_{ba}, so that the contribution from b→a relaxation should give a straight line. Deviations from the straight line are attributed to G^{v}_{bc}. Sprik et al. found $G^{v}_{bc}\exp(1.34B/T) = 8(4) \times 10^{-16}\,\mathrm{cm^3\,s^{-1}}$ (units: B in T, T in K) in excellent agreement with the theoretical result of $9.7 \times 10^{-16}\,\mathrm{cm^3\,s^{-1}}$ (Lagendijk et al. 1984). (See also Kagan et al. 1981.) Bell et al. (1984) have also

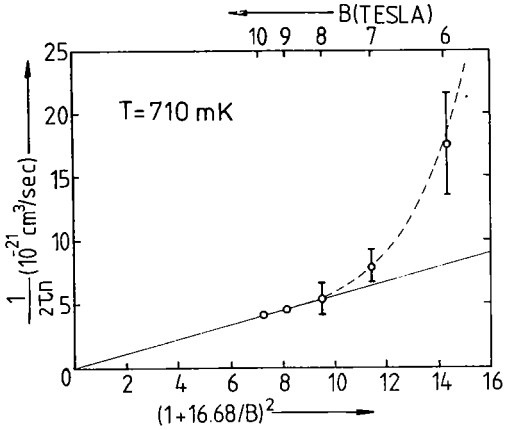

Fig. 5.16. Magnetic field dependence of the bulk relaxation rate constant $G^{v} = G^{v}_{ba} + G^{v}_{bc}$. The dashed line is the theoretically predicted value for G^{v}_{bc} (after Sprik et al. 1983).

measured $G_{bc}\exp(1.34B/T)$ and find a value $10(1)\times10^{-16}\,\mathrm{cm^3\,s^{-1}}$, in good agreement with Sprik et al. Recently, Sprik et al. (1985) have presented a new analysis of bubble decay experiments and find an improved value, $G^{v}_{bc}\exp(1.34B/T) = 12(4)\times10^{-16}\,\mathrm{cm^3\,s^{-1}}$.

5.10. Nuclear magnetic resonance

Atomic hydrogen is an unusual system for NMR: due to the hyperfine interaction, the resonance frequency is generally in the GHz frequency range, as can be seen from figs. 2.1 and 2.3. Due to the high frequency, special NMR coils with very few windings—as few as one—are used for the resonator. A split-ring resonator used by the UBC group (Hardy and Whitehead 1981) is shown in fig. 5.17 along with the 1420 MHz spectrome-

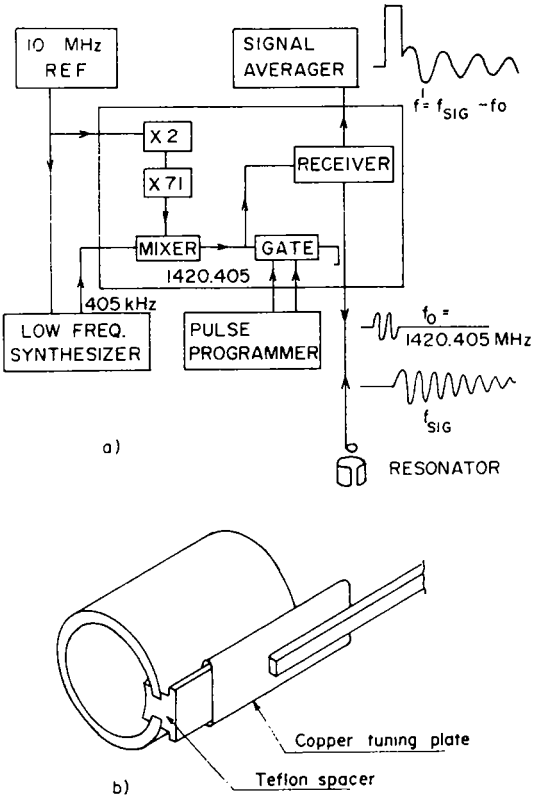

Fig. 5.17. A split ring resonator and a block diagram of a 1420 MHz pulsed spectrometer (after Hardy et al. 1982).

ter. This zero-field resonance system was used with the cell shown in fig. 5.7. Zero-field resonance has been used with great skill to study properties of atomic hydrogen, and it is useful to consider this case in some detail. The transition which is studied is the a→c transition, labeled F_{ac} in fig. 2.1. This is observed by parallel resonance in which the oscillating rf field is along, rather than perpendicular, to the (small) static field B_0. Other than this, the system behaves as a two-level spin system and can be analyzed in terms of a fictitious spin of $\frac{1}{2}$, so that the vast knowledge of this system in the existing literature can be used.

In the preceding sections (5.4 and 5.5) we have already discussed many of the experiments and results that were obtained from zero-field parallel resonance on atomic hydrogen, and a more detailed description can be found in the review by Hardy et al. (1982). The zero-field work of Hardy et al. had some distinct advantages. Shielding easily reduces the field to a few mG and as a consequence extremely narrow lines (~0.1 Hz) can be observed. Since the resonance frequency for the a→c transition is

$$h\nu = a + [\hbar(\gamma_e + \gamma_n)B]^2/2a\,, \tag{5.22}$$

and only depends on B in second order, small inhomogeneities can be tolerated for low fields. Therefore, linewidths are determined only by the interactions of the H atoms amongst themselves or with the walls. Because hydrogen is not very stable in zero-field, the densities are very low, $n \leqslant 10^{12}/\mathrm{cm}^3$. However, the very narrow linewidths give very high sensitivities, of order 10^9 atoms. Thus, as we have seen the zero-field technique is very valuable for measuring single-atom properties or the interaction of hydrogen with He surfaces. In particular the very narrow resonance lines indicate that a low-temperature hydrogen maser could be developed, with substantial advantages over the room-temperature maser (Berlinsky and Hardy 1981). Recombination rates of H at very low densities have also been measured on surfaces or in a dense buffer gas of He (which provides the third body necessary to satisfy the kinematics of recombination). The obvious limitation of this technique is that the densities of H are so low that many of the interesting properties due to H–H interactions are inaccessible.

The first high-field NMR studies of H were performed by the Cornell group (Yurke et al. 1983) using a high homogeneity superconducting solenoid operating at $B \sim 8$ T with a 1 GHz helical resonator shown in fig. 5.18, which also shows their sample cell. Samples with densities of order $10^{16}/\mathrm{cm}^3$ could be loaded into the cell. A superfluid fountain pump was then used to fill the sample chamber to a level which closed off the H↓ fill tube to isolate the sample. The cell was also equipped with a pressure

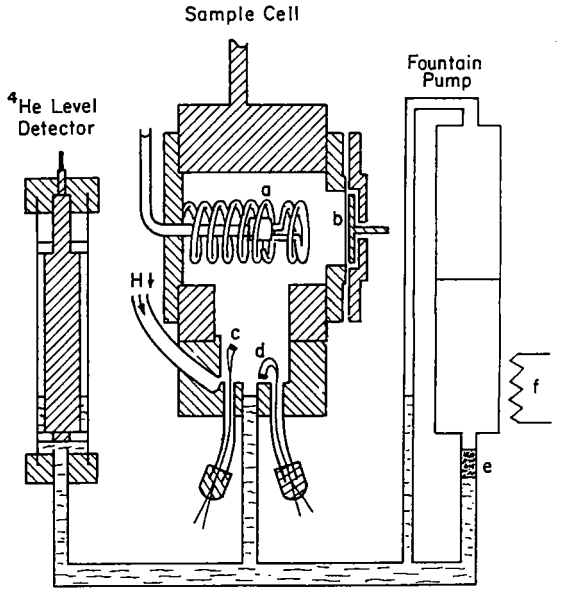

Fig. 5.18. A schematic diagram of the NMR cell used by the Cornell group (Yurke et al. 1983).

gauge to measure the H↓ pressure. Although Yurke et al. reported the observation of free induction decay signals, quantitative measurements using the NMR signal were not presented, presumably due to the inhomogeneity of the pulsed field. Instead they used the rf power to saturate the a→b transition to prepare the sample in a well-defined state of polarization. The pressure gauge was then used to study the decay of the sample and $\gamma = K^s_{aa}/K^s_{ab}$ was measured (fig. 5.12).

The Cornell group (Johnson et al. 1984) then changed their resonator to a split-ring type, similar to that shown in fig. 5.17. The resonator was embedded in solid material so only the inside volume was available for the hydrogen gas. In this way the atoms experienced a rather uniform rf field. A small static gradient field was superimposed on the uniform static field and pulse measurements with tipping angles of order 10° were made; the gradient field is used for the coupling to the rf field. In this way, they were able to observe a fascinating new phenomenon, nuclear spin waves in a gas. This effect had been predicted independently by Lhuillier and Laloë (1982a,b) and Bashkin (1981). A series of spectra for different field gradients is shown in fig. 5.19. The spectra are the Fourier transforms of the free induction decay. The various peaks are due to different spin-wave

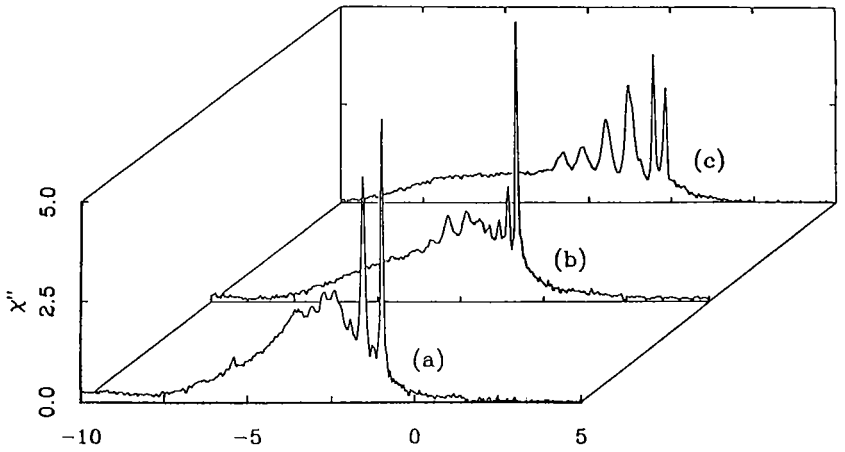

Fig. 5.19. The NMR spectra of H↓ for different field gradients showing the spin-wave modes. From trace (a) to (c) the change in the gradient field is about 1 G/cm. The density was $n = 3.2 \times 10^{16}/\text{cm}^3$ and $T = 245$ mK (after Johnson et al. 1984).

modes and have been analyzed by Lévy and Ruckenstein (1984). These spin-wave modes are a direct result of the identical-particle nature of H↓ and are discussed in section 8.

5.11. Electron spin resonance

The first quantitative ESR measurements of H↓ in high fields were made by van Yperen et al. (1983, 1984) [preliminary work at low fields was reported by Mayer et al. (1981) and at high fields by Statt and Hardy (1981)]. They used the broadband single-pass cell shown in fig. 5.20. A 160 GHz source was obtained by taking the fourth harmonic from a harmonic generator fed by a 40 GHz Gunn oscillator. The microwave radiation passed through the sample and was detected with a low-temperature bolometer. Both the a→d and b→c transitions were observed. The line shape for the b→c transition is shown in the inset of fig. 5.11. The rather strange multi-peaked line shape is due to the inhomogeneities in the magnetic field. The field is uniform up to one part in 10^3 in a sphere of radius 0.5 cm around the center, but has bumps of the order of a few Gauss outside of this region, which also contains atoms contributing to the signal. Due to the very narrow intrinsic linewidth, the line shape is a reflection of the number of atoms which satisfy the resonance condition, and large numbers of atoms satisfy this condition wherever the field has a zero gradient. An absorption line shape of the

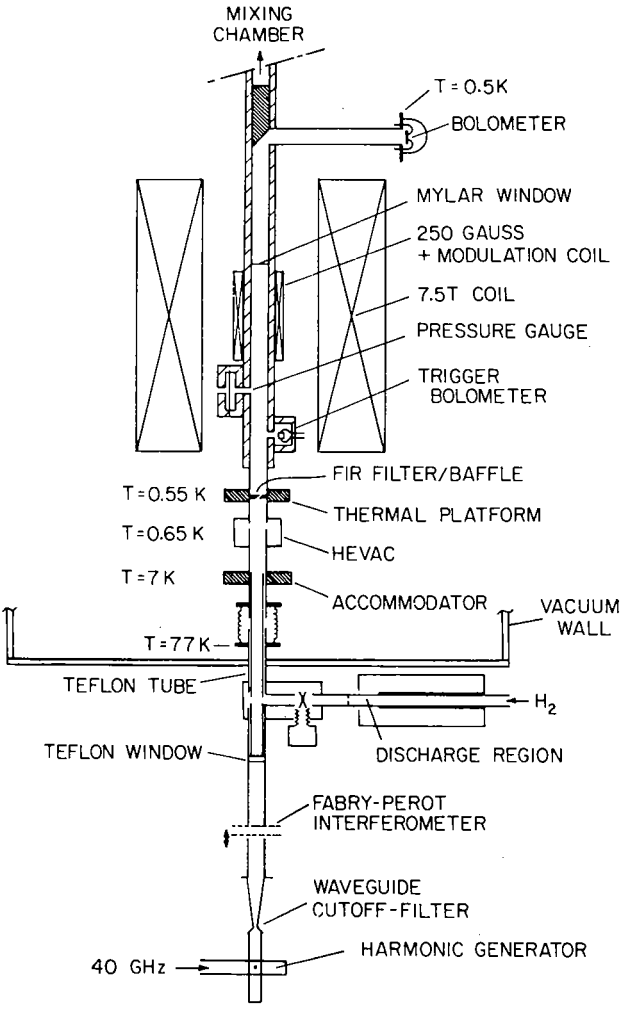

Fig. 5.20. An experimental system used for studying H↓ by ESR (after van Yperen et al. 1983).

form

$$\alpha(\nu) = \frac{\pi\mu_0}{4c}(\gamma_e + \varepsilon\gamma_n)^2 \frac{h\nu}{\gamma_e}\left(\frac{\partial B}{\partial z}\right)^{-1} n_{hi}(z) \tag{5.23}$$

was derived which gives multiple peaks if the field gradient goes to zero in several regions. Radial gradients, not accounted for in eq. (5.23) prevent $\alpha(\nu)$ from diverging. In eq. (5.23), n_{hi} is the density of the initial hyperfine

state. As explained earlier, van Yperen et al. were able to use the line strength to monitor the a and b populations and directly demonstrate that H becomes nuclear polarized as shown in fig. 5.11. The interesting multiple peaked line shape, explained by eq. (5.23), is also shown in the inset of fig. 5.11. No evidence of electronic spin-waves, analogous to nuclear spin-waves, could be observed since the cell was not optimized for such an experiment.

Statt et al. (1985) have studied hydrogen by ESR in high fields using a 3 mm diameter cavity, resonant at 114 GHz. Resonance detection was accomplished with a sensitive heterodyne spectrometer so that a very low power level could be used. This was necessary as in an earlier design the power perturbed the sample density significantly (an atom with reversed spin, due to resonance, can be lost from the system due to recombination, ejection by magnetic-field gradients or relaxation). They were able to trace the decay of the a and b densities and determine the rate constants by fitting to the rate equations. Their results for γ are shown in fig. 5.12, which has been discussed earlier. More recently with the same system, Reynolds et al. (1985) were able to separate the three-body surface recombination rate constant from the nuclear relaxation rate, shown in figs. 5.14a,b. In this same work at very low temperatures, $T \simeq 100$ mK, in addition to the signal coming from the bulk atoms they were able to observe weak signals, which they assigned to surface adsorbed atoms. This represents the first direct observation of surface adsorbed atoms and led to the value of $\varepsilon_a = 1.00$ K given in table 5.1.

5.12. Compression experiments

One of the major goals of spin-polarized hydrogen research is to obtain Bose–Einstein condensation. Evaluating eq. (1.10) for the critical temperatures shows that for $T_c = 100$ mK, a critical density of $1.6 \times 10^{19}/\text{cm}^3$ is required. By direct filling techniques, the maximum density that has been achieved is about $3 \times 10^{17}/\text{cm}^3$, which can then decay down in density to the much longer lived double-polarized state. To achieve the densities required for BEC at a reasonable temperature, a sample of H$\downarrow\downarrow$ must be compressed. Ideally, the compression apparatus should enable detection of BEC by, for example, measurement of the equation of state (p versus V at constant T) which has a characteristic shape for a Bose gas. Two compression experiments were performed at about the same time, using different techniques: Sprik et al. (1983) in an Amsterdam–Harvard collaboration and Hess et al. (1983) at MIT.

We first discuss the experiment of Sprik et al. (1983); we go into some detail as they introduced a quasi-constant pressure method of studying H$\downarrow$ which has also been used by Tommila et al. (1984a). Previous to these ex-

periments, decays were studied in a constant-volume system and the decay of the pressure or density was measured as a function of time. This has a distinct disadvantage if one is interested in studying a high-density state. Since the decay depends strongly on a higher power of the density, the highest densities are available for the shortest times. By studying a sample isobarically, the density remains constant during the decay. In this case the volume, V, of the sample decreases as the atoms recombine and decay kinetics can be studied by observing the rate of decay of V. Sprik et al.'s cell is shown in fig. 5.21. The central cell (CC) inside the bore of the magnet is divided into an upper and lower chamber. The CC is connected by a tube to a reservoir of helium; the He level can be varied by raising or lowering a weight. With the He level low, H flows into the upper chamber and diffuses through a connecting tube into the lower chamber. By raising the He level, this tube is sealed off and the He is compressed against the

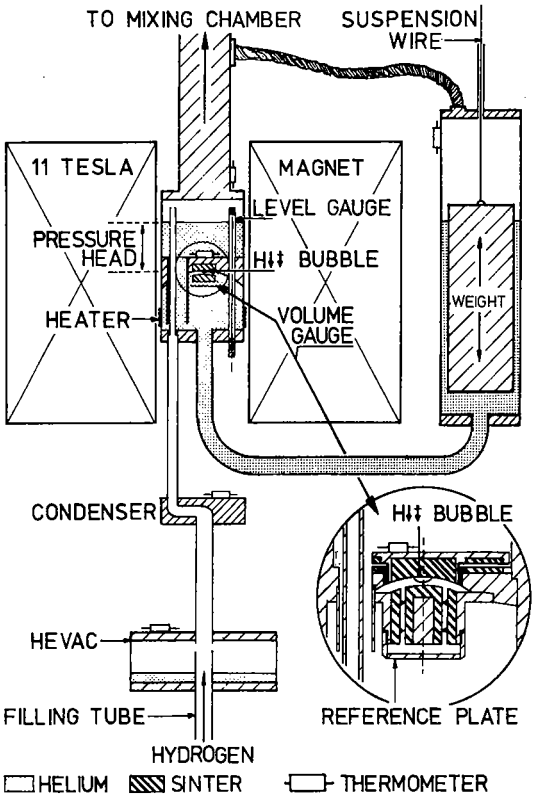

Fig. 5.21. A compression cell for quasi-isobaric measurements (after Sprik et al. 1983).

curved roof of this chamber, between two capacitor plates. The He level is now held constant so that the gas bubble in between the capacitor plates is hydrostatically compressed by a constant head of He. The capacitor serves as a volume meter. When it is completely filled with liquid He (dielectric constant $\varepsilon = 1.057$) there is a considerable change in capacitance compared to when it is empty. The H↓ bubble (dielectric constant $\simeq 1.0$) displaces a volume of He and the capacitance change is easily calibrated to yield the volume of the bubble. Very small volume changes of order 10^{-3} mm^3 could be detected. A measurement of the He head gives the hydrostatic pressure.

The actual pressure acting on the gas is increased by the surface tension (α) of the He so that

$$p = p_{\text{hydrostatic}} + p_{\text{st}} , \tag{5.24}$$

where $p_{\text{st}} = 2\alpha/r$ for a spherical bubble of radius r. Thus, as the bubble shrinks its pressure and density increases. It is easily shown for an ideal gas at constant temperature with decay rate $\dot{N}/V = -D(n)$, where $D(n)$ is a polynomial in the density, that

$$\frac{\dot{V}}{V} = -\frac{D(n)}{n}\left(1 + \frac{V}{p}\frac{\mathrm{d}p}{\mathrm{d}V}\right)^{-1} . \tag{5.25}$$

In the event that p is constant (this is approximately so for bubbles with $V \gtrsim 1$ mm^3) then V decays exponentially with a decay constant $\tau^{-1} = -D(n)/n$. Decay curves for a few different pressures, magnetic fields and temperatures are shown in fig. 5.22.

By measuring τ^{-1} as a function of density, the polynomial $D(n)$ could be determined. Using this technique Sprik et al. found that for densities above $\sim 10^{18}$/cm^3 a new decay process, three-body volume recombination of b-state atoms, becomes important and limits the growth of density. Their value of the third-order decay constant (coefficient of n^3 in the decay equation) to be associated with $K^{\text{v}}_{\text{bbb}}$ was $L^{\text{v}} = 4(1) \times 10^{-39}$ cm^6 s^{-1}, at $T = 750$ mK and $B = 9.8$ T, in reasonable agreement with the theory of Kagan et al. (1981) for three-body decay due to magnetic dipole–dipole interactions. What Kagan et al. actually calculated was the number of three-body recombination events, not the number of atoms lost to the system (Greytak 1984). Sprik et al. (1985) analyzed the problem and found for the coefficient of n^3 in the decay equations

$$L^{\text{v}} = 2\theta^{\text{v}}_{\text{b}} K^{\text{v}}_{\text{bbb}} . \tag{5.26}$$

The factor 2 corresponds to the two atoms lost in the direct recombination;

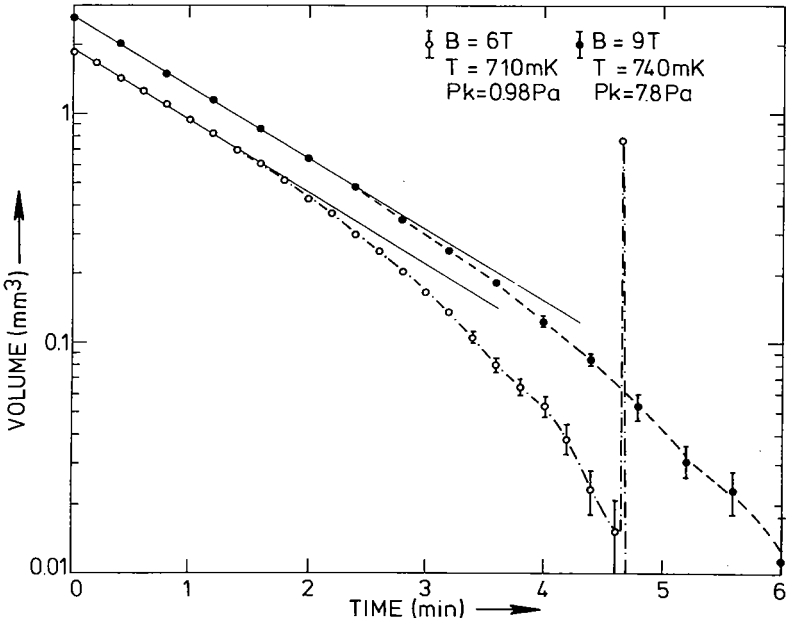

Fig. 5.22. Volume decay curves of H↓↕ bubbles. The peak in the lower curve represents the explosion of an unstable sample (after Sprik et al. 1983).

the spectator atom goes to state c with a probability $\xi^v = 0.91$ (Verhaar 1985) (see eqs. 5.15). If it recombines, $\theta_b^v = 1 + \xi^v = 1.91$, and on the average 3.82 atom are lost per event. However, there is also a probability that the c-state atom relaxes back to the b-state without recombining. For their conditions Sprik et al. found $2\theta_b^v = 3.27$.

Sprik et al. (1983) also observed instabilities in which bubbles exploded. One such event is shown in fig. 5.22 by a sudden increase in volume. This led to a measurement of G_{bc}^v which was discussed in section 5.9. A theoretical study of thermal instability of bubbles has been made by Kagan et al. (1984); Tommila et al. (1984a) have made a systematic experimental study of explosions.

More recently Sprik et al. (1985) have presented an exhaustive analysis of their bubble compression experiments with an exended set of rate equations of the form of eqs. (5.15) including all hyperfine states. They also found an important correction to the hydrostatic pressure on the bubble which was not taken into account in their 1983 article. Diamagnetic forces exerted by the gradient in the field of the main magnet on the bulk liquid-helium column (fig. 5.21) measurably reduce the actual hydrostatic

pressure on the bubble. They now find a bbb third-order value decay rate $2\theta_b^v K_{bbb}^v = 7(2) \times 10^{-39}\ \mathrm{cm^6\,s^{-1}}$ or $K_{bbb}^v = 2.0(5) \times 10^{-39}\ \mathrm{cm^6\,s^{-1}}$ with $2\theta_b^v = 3.27$, for a field of 9 T, in agreement with Hess et al. (1984).

Hess et al. (1983) developed a different compression technique in which they compressed their sample into the small volume of a pressure gauge shown in fig. 5.23. The cell was first filled with H↓↕, then compressed with a piston; the piston was sealed with superfluid ^{4}He by capillarity. High densities of order $10^{18}/\mathrm{cm^3}$ could be achieved. At these densities the cell and gas came way out of thermal equilibrium due to recombination heating. The pressure and temperature are shown in fig. 5.24. They used a thin-film thermometer deposited on the flexible pressure gauge diaphragm to measure the gas temperature. By modeling the nonequilibrium gas they were able to extract the decay constants. They studied three-body recombination in the temperature range 0.3 to 0.45 K, with evidence for both bulk and surface processes. They found good agreement with the theory of Kagan et al. (1984), but did not quote an experimental value of the recombination rate constants. In a later paper (Hess et al. 1984) they give $L^v(=2\theta_b^v K_{bbb}^v) = 7.5(3) \times 10^{-39}\ \mathrm{cm^6\,s^{-1}}$ for $B = 7.6$ T.

Hess et al. (1984) (see also Bell et al. 1984a) then studied the temperature dependence in more detail, as well as the magnetic field

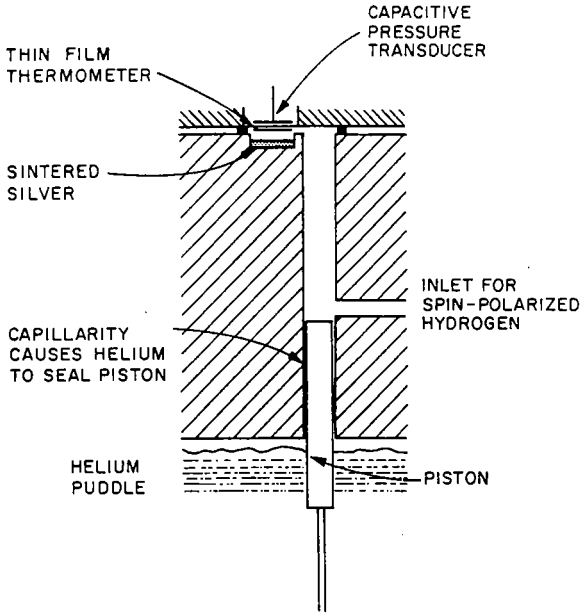

Fig. 5.23. The piston compression cell of Hess et al. (1983).

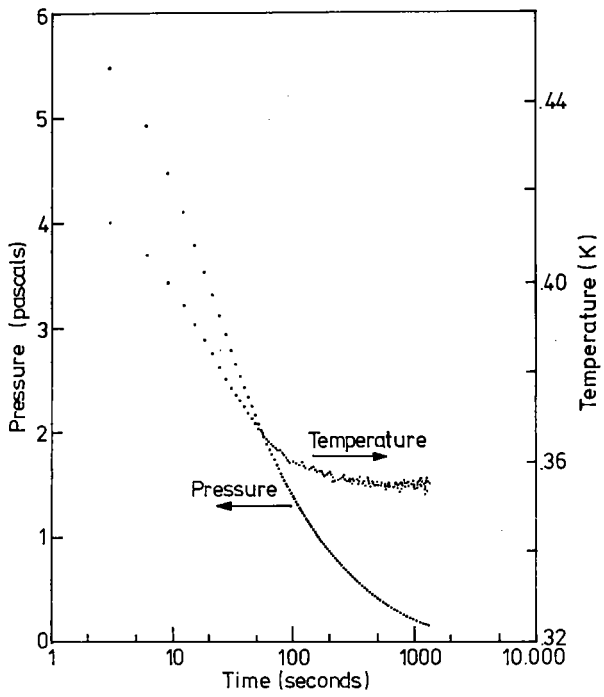

Fig. 5.24. The pressure and temperature of H↓↑ after a compression in the cell of Hess et al. (1983).

dependence of the three-body rates. From the temperature dependence they separated the three-body rate into bulk and surface contributions, with a measured surface value of $L^s(=2\theta_b^s K_{bbb}^s) = 2.0(6) \times 10^{-24}$ cm^4 s^{-1} at $B = 7.6$ T. For the surface $\xi^s = 0.87$, so that $2\theta_b^s = 3.74$ and $K_{bbb}^s = 5.3 \times 10^{-25}$ cm^4 s^{-1}, to be compared with the theoretical value (de Goey et al. 1984) of $K_{bbb}^s = 6.5 \times 10^{-26}$ cm^4 s^{-1}. For saturated surfaces (which are obtained for $T \leqslant T_c$), this surface process would be the dominant loss and heating mechanism! From these measurements they suggested that the discrepancy between theory and experiment for nuclear relaxation could be resolved by including three-body recombination terms in the decay equations for H↓↑ (see section 5.8). Kagan et al. (1981) and de Goey et al. (1984) have predicted that in the 5–15 T magnetic-field range, K_{bbb} increases for both surface and volume process. Hess et al., measuring up to about 9 T, found a weak decrease in K_{bbb}^s. We feel that it is important to carry out these measurements to much higher fields. In particular, theory predicts that K_{bbb}^s and K_{bbb}^v increase to $B \sim 15$–20 T and then decrease sharply at about 26 T, with a slow increase for still

higher fields. Reinterpreting the results of Sprik et al. (1982) in terms of surface recombination, the magnetic-field dependence of nuclear relaxation shown in fig. 5.13 probably is representative of the field dependence of K^s_{bbb}, rather than G^s_{ab}.

For $B/T \leq 10\,\mathrm{T/K}$, Bell et al. (1984a) and Sprik et al. (1985) observed an exponential increase in the third-order term which was attributed to the onset of bbc-recombination. Bell et al. found $K^3 = 7(3) \times 10^{-33}\,\mathrm{cm^6\,s^{-1}}$ which corresponds to a value $K^v_{bbc} = 3(1) \times 10^{-33}\,\mathrm{cm^6\,s^{-1}}$ of Sprik et al.

In their compression experiment Hess et al. (1984) achieved a maximum density of $4.5 \times 10^{18}/\mathrm{cm^3}$ at $T = 0.57\,\mathrm{K}$. Certainly, to date, the compression experiments are still far away from the region of quantum degeneracy in H↓↕.

6. Theoretical aspects of stability: recombination and relaxation

In the following sections we review the various processes which are known to limit the stability of the atomic hydrogens. Limited stability means that the sample decays in time to the molecular state due to recombination. This does not imply that the subject is restricted to the topic of recombination alone; relaxation processes also have to be considered as they may play an important role in the overall sequence of processes which ultimately lead to the formation of a molecule.

We shall attempt to treat all relaxation and recombination processes within the framework of a single unifying formalism making use of a Golden Rule like expression for the transition rates. This formalism can lead (and in some cases has led) to factor-of-two (or factor-of-six in the three-body case) difficulties in counting indistinguishable particles, and some emphasis will be put on this aspect. One of our objectives is to make clear the relation between calculated and experimentally determined rates.

We first discuss both volume and surface recombination (section 6.1) and pay particular attention to the magnetic-field dependence of recombination processes to explain the strongly enhanced stability of H↓ in high magnetic fields. In section 6.2 the various volume and surface relaxation processes will be discussed.

With decreasing temperatures the occupation of surface states will increase due to adsorption. As a consequence, at low temperatures, the surface relaxation and recombination processes are important, even dominant. The adsorption kinetics may also become rate limiting; however, this subject is discussed in the context of adsorption–desorption phenomena (sections 4.2 and 9.1).

6.1. Recombination

An early theoretical study of the stability of H in high magnetic fields and at low temperatures was made by Jones et al. (1958). These authors established that under laboratory conditions three bodies are required to form a hydrogen molecule. A two-body radiative process was found to be entirely negligible due to the absence of a permanent dipole moment in a homonuclear diatomic molecule. In recent years, much has been learned about three-body processes. Often the role of the third body is rather passive, just enabling the conservation of energy and momentum. In these cases the third body may be a third hydrogen atom, a helium atom from the vapor or a surface. However, sometimes the third body acts more subtly by inducing the transition via particular properties of the H–H interaction. Then the presence of a third hydrogen atom is imperative for recombination, even on a surface.

Experimentally, one aims at distinguishing the various processes by studying the decay rate of the H-density under carefully chosen conditions as a function of the H-density (n). Then the decay may be described phenomenologically by a differential equation of the type (see section 1.1)

$$dn/dt = -Kn^r . \tag{6.1}$$

The rate constant K depends in general on temperature and magnetic field, as well as the chemical and physical composition of the gas and the geometry of the experimental cell. The density dependence of order r of the decay depends on the number of hydrogen atoms that participate in the reaction. The highest order that will be considered here corresponds to $r = 3$ (see section 5.3 for phenomenological rate equations).

Under certain conditions the overall reaction rate is limited by a relaxation step. Then recombination can even appear as a first-order process (when magnetic impurities may relax the spins) in spite of the fact that the dominant recombination channel may involve two or three H atoms. This interplay between recombination and relaxation processes is left outside of the considerations of the present section and will be analyzed in detail in section 6.2.

Given the order of a recombination process the selection rules determine which molecular (ortho or para) states may be formed. The present section is intended to introduce the spin selection rules to which we return in detail in the coming sections. We first discuss selection rules accounting for the hyperfine interaction (intra-atomic Fermi contact term), the direct and exchange interactions between the hydrogen atoms and the Van der Waals-type interactions, between the H and He (vapor and surface). These

interactions all conserve the total (electron and proton) spin projection ($M_F \equiv M_I + M_S$). Moreover, the interatomic interactions considered here are diagonal with respect to the total spin basis $\{|SM_S IM_I\rangle\}$ of the interacting pair. Only the (intra-atomic) hyperfine interaction may induce transitions of (total) electron and (total) proton spin of the pair (see table 6.1) through terms of the type $s_{+k} i_{-k}$ (here k is the particle index and s_+ and i_- are raising and lowering operators of the single-atom spins). Thus we obtain the selection rule

$$\Delta M_S = -\Delta M_I = 0, \pm 1 . \tag{6.2}$$

In addition, the interactions under consideration also conserve the symmetry of the total spin state under permutation of the pair. Combining these selection rules, one derives table 6.2 in which we summarize all allowed transitions for second-order (H–H–He) recombination. The same selection rules remain valid for third-order (H–H–H) recombination (table 6.3) if one neglects the hyperfine interaction on the third body. This amounts to evaluating the transition amplitude to first order in the hyperfine mixing parameter (ε) and is correct in the limit of high magnetic fields. In section 6.1.4 the dipolar interaction which leads to new selection rules will be included.

Table 6.1

Matrix elements of the hyperfine interaction $a[s_i \cdot i_1 + s_2 \cdot i_2]$ in the total spin representation. Here P is the parity of the state and a minus sign represents a (-1).

M_I	0	1	0	−	0	1	0	−	0	1	0	−	0	1	0	−					
I	0	1	1	1	0	1	1	1	0	1	1	1	0	1	1	1					
M_S	0	0	0	0	1	1	1	1	0	0	0	0	−	−	−	−					
S	0	0	0	0	1	1	1	1	1	1	1	1	1	1	1	1	S	M_S	I	M_I	P
								$-a$			$\frac{1}{2}a$			$-a$			0	0	0	0	+
					a												0	0	1	1	−
									$\frac{1}{2}a$								0	0	1	0	−
													a				0	0	1	−	−
	a																1	1	0	0	−
					$\frac{1}{2}a$												1	1	1	1	+
										a							1	1	1	0	+
$-a$							$-\frac{1}{2}a$				a						1	1	1	−	+
		$\frac{1}{2}a$															1	0	0	0	−
						a											1	0	1	1	+
$\frac{1}{2}a$							a							a			1	0	1	0	+
															a		1	0	1	−	+
			a														1	−	0	0	−
$-a$										a			$-\frac{1}{2}a$				1	−	1	1	+
											a						1	−	1	0	+
																$\frac{1}{2}a$	1	−	1	−	+

Table 6.2

A summary of all channels allowed for second-order recombination by the selection rules $\Delta M_F \equiv \Delta M_I + \Delta M_S = 0$ and $\Delta M_S \leqslant 1$ for hydrogen. The transitions indicated by the symbol 0 are allowed by these selection rules but are in fact forbidden since they imply transitions from symmetric to antisymmetric total spin states (electron and nuclear).

h_1h_2	M_F	p-H_2 symmetric	o-H_2 antisymmetric			Remark
		$M_I = 0$	$M_I = -1$	$M_I = 0$	$M_I = 1$	
aa	0	1		0		symmetric
ab	−1		1			
ac	0	1		1		
ad	1				1	
bb	−2					symmetric
bc	−1		1			
bd	0	1		1		
cc	0	1		0		symmetric
cd	1				1	
dd	2					symmetric

Table 6.3

A summary of all channels allowed for third-order recombination by the selection rules $\Delta M_F \equiv \Delta M_I + \Delta M_S = 0$ and $\Delta M_S \leqslant 1$ for hydrogen. The allowed transitions are indicated by the symbols a, b, c, d, representing the hyperfine states of the third body after the reaction. The table includes only those channels which contribute at least to order ε.

$h_1h_2h_3$	M_F	p-H_2	o-H_2		
		$M_I = 0$	$M_I = -1$	$M_I = 0$	$M_I = 1$
aaa	0	a		a	b
aab	−1	b	a	b	
aac	0	a,c	d	a,c	b
aad	1	d		d	a,c
abb	−2		b		
abc	−1	b	a,c	b	
abd	0	a,c	d	a,c	b
acc	0	a,c	d	a,c	b
acd	1	d		d	a,c
add	2				d
bbb	−3				
bbc	−2		b		
bbd	−1	b	a,c	b	
bcc	−1	b	a,c	b	
bcd	0	a,c	d	a,c	b
bdd	1	d		d	a,c
ccc	0	c	d	c	
ccd	1	d		d	c
cdd	2				d
ddd	3				

6.1.1. *Resonance recombination*

The dominant mechanism for volume recombination at ambient temperatures is resonance recombination. This process has been widely discussed in the chemical literature since the pioneering work of Amdur and Robinson (1933) and Amdur (1935, 1938). It proceeds in two stages: First a pair of H-atoms collide and are trapped into a long-lived quasi-bound state (resonance state); subsequently this quasi-molecule is stabilized in a collision with a third body in which it has a transition into a bound state.

The triplet potential does not support any bound or quasi-bound states (see section 3, fig. 3.2). In contrast, the singlet potential supports many quasi-bound states. Hence, all resonance recombination proceeds via the latter channel. It was shown by Roberts et al. (1969) that, at room temperature and above, the occupation of the most important resonances of the singlet potential (see section 3) reaches thermodynamic equilibrium. The resonance-recombination theory then reduces to calculating the cross section for stabilization of a quasi-molecule by a third body.

For low temperatures ($T < 1$ K) resonance recombination is thought to be of minor importance. Near the dissociation limit the energy separation between quasi-bound states is typically tens of Kelvins. Thus the thermal occupation of these states is in general negligibly small. However, if a low angular-momentum resonance happens to lie within the narrow band of thermally accessible states, resonance recombination cannot be ruled out on these general grounds.

As pointed out by Greben, Thomas and Berlinsky (GTB 1981), only the $H_2(v, L) = H_2(14,4)$ level is of importance in the context of resonance recombination of H at low temperatures. As may be seen from fig. 6.1 all other levels with low J values lie relatively far from the dissociation limit. Experiment (Dabrowsky 1984) indicates that this level is marginally bound by 0.26(46) K and this conclusion appears to be consistent with theory (Kolos and Wolniewicz 1975, Wolniewicz 1983). In zero magnetic field this excludes resonance recombination and leaves only direct (i.e., one stage) three-body processes as important decay channels for low-temperature H. For deuterium (Bredohl and Herzberg 1973) the $D_2(21,0)$ and $D_2(21,1)$ levels (see fig. 6.1) appear to be most relevant.

Stwalley (1976) pointed out that with increasing magnetic field resonance transitions are tuned above threshold once the $M_S = -1$ asymptote of the triplet potential (see fig. 3.1) is shifted below the $H_2(14,4)$ or $D_2(21,0)$ levels. We first focus on the para-state, $H_2(14,4)$. With the aid of table 6.2 one finds that only aa, ac, bd and cc pairs satisfy the selection rules to form p-H_2. Of these pair states, only the aa-initial state may be shifted below the $H_2(14,4)$ level. Thus, above a magnetic field $B \simeq 1$ T, recombination channels involving two a-state atoms may be enhanced due

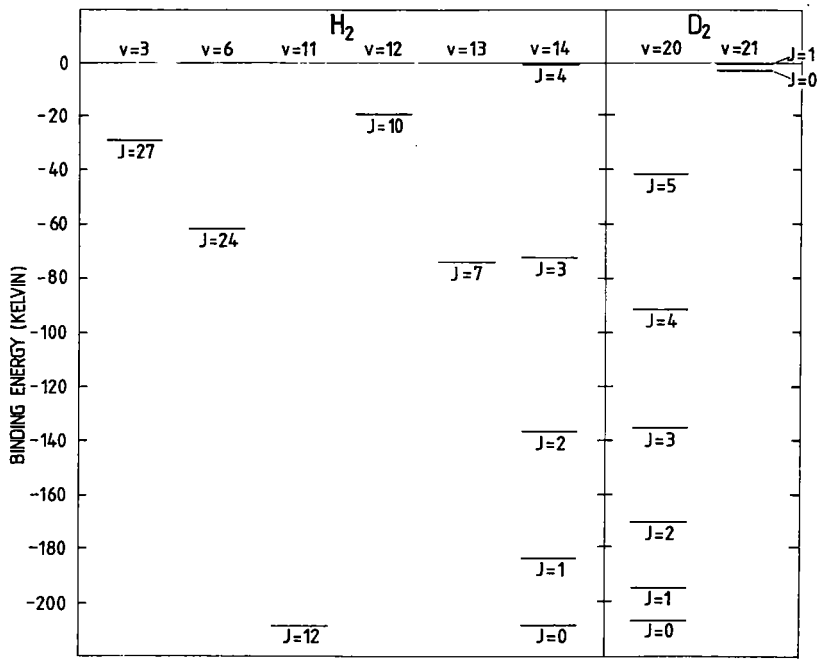

Fig. 6.1. The observed vibration–rotation levels of H_2 and D_2 for the electronic ground state $X^1\Sigma_g^+$ near the dissociation limit. The data are obtained from an analysis of the Lyman and Werner bands by Dabrowski (for H_2, 1984) and Bredohl and Herzberg (for D_2, 1973). The rotational quantum number J is used here in place of L in the text.

to the presence of the resonance. However, the $L = 4$ rotational barrier appears to be too high and broad to enable any appreciable occupation of the $H_2(14,4)$ state (Stwalley 1976).

Another p-H_2 level, $H_2(12,10)$, was considered in detail by Kagan, Vartanyantz and Shlyapnikov (KVS 1981). These authors also arrived at the result that due to the rotational barrier the resonance process is inefficient. We note that KVS based their value for the binding energy of this level $E_{12,10} \simeq -10$ K on the results of Herzberg and Howe (1959) and Kolos and Wolniewicz (1968). However, recent measurements by Dabrowsky (1984), with an estimated accuracy of 0.1 cm^{-1}, indicate a value $E_{12,10} = -19.71$ K. This implies a threshold field $B \simeq 14.6$ T which is higher than the range of fields currently used in experiments with H↓.

For the $D_2(21,0)$ level the situation is different due to the absence of a rotational barrier ($L = 0$). This implies a resonance-recombination channel to open up at $B \simeq 5.9$ T. For higher fields the channel requires thermal activation and may be rendered negligible in the limit of very high fields.

6.1.2. *Second-order recombination*

The first detailed theoretical studies of direct recombination processes were made by GTB (1981) and KVS (1981). We first present a detailed discussion of the process studied by GTB: recombination of H in the presence of He vapor at temperatures $T \leqslant 1$ K. This study was stimulated by the experimental determination of the recombination rate constant in zero field by Hardy et al. (1980a, b). We shall then discuss the more exhaustive work of KVS who studied three-body recombination in pure H.

6.1.2.1. *Van der Waals recombination*

In the process studied by GTB, two hydrogen atoms recombine in the presence of a helium atom as the third body; hence the process is of second order in the density. Assuming singlet character in the interaction between the H-atoms, the crucial momentum transfer required for recombination is provided by the Van der Waals interaction of the recombining pair with the helium atom. We refer to recombination processes with this signature as Van der Waals recombination. By summing over both initial and final states we write the total rate of recombination events (in every event two atoms are lost) as

$$\Gamma = \frac{2\pi}{\hbar} \sum_{\mathrm{i,f}} P_{\mathrm{i}} |\langle \mathrm{f}|T|\mathrm{i}\rangle|^2 \delta(E_{\mathrm{i}} - E_{\mathrm{f}}) , \tag{6.3}$$

where $|\mathrm{i}\rangle$ and $|\mathrm{f}\rangle$ represent symmetrized three-body initial and final states, respectively, P_{i} is the probability that an initial state is occupied and $\langle \mathrm{f}|T|\mathrm{i}\rangle$ is the full three-body T-matrix. This expression goes beyond the Golden Rule to the extent that the transition amplitude is evaluated beyond the Born approximation. The δ-function assures the conservation of energy in the process. Momentum conservation is satisfied implicitly by expressing $|\mathrm{i}\rangle$ and $|\mathrm{f}\rangle$ in the three-body center of mass (3BCM) system (see fig. 6.2). For the Van der Waals recombination:

$$\begin{aligned} |\mathrm{i}\rangle &= |\mathrm{h}_1\mathrm{h}_2; \boldsymbol{p}, \boldsymbol{q}\rangle , \\ |\mathrm{f}\rangle &= |SM_S IM_I; v, L, M_L, \boldsymbol{q}'\rangle = |00IM_I; v, L, M_L, \boldsymbol{q}'\rangle . \end{aligned} \tag{6.4}$$

The initial state $|\mathrm{i}\rangle$ represents a pair of H-atoms in hyperfine states h_1 and h_2, moving with relative momentum $\boldsymbol{p}$. The third-body (He-atom) moves with momentum $\boldsymbol{q}$ relative to the center of mass (2BCM) of the H–H pair. The final state $|\mathrm{f}\rangle$ is a molecule in vibration–rotation state $\mathrm{H}_2(v, L)$ and spin-state $|SM_S IM_I\rangle$, which moves with momentum $\boldsymbol{q}'$ with respect to the third body.

The probability P_{i} is normalized by

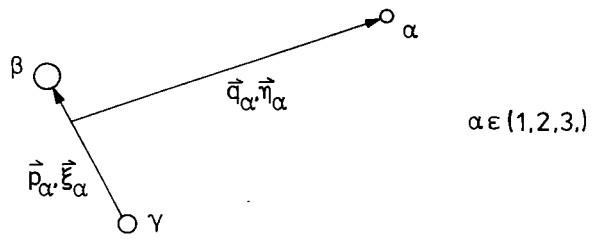

Fig. 6.2. (a) Relative momentum wave vector ($\boldsymbol{p}_\alpha$ and $\boldsymbol{q}_\alpha$) and position vectors ($\boldsymbol{\xi}_\alpha$ and $\boldsymbol{\eta}_\alpha$) for a three-body system.

$$\sum_i P_i \equiv \sum_{|h_1 h_2; \boldsymbol{p},\boldsymbol{q}\rangle} P_{|h_1 h_2; \boldsymbol{p},\boldsymbol{q}\rangle} \tag{6.5a}$$

$$= \sum_{|h_1 h_2; \boldsymbol{p},\boldsymbol{q})} P_{|h_1 h_2; \boldsymbol{p},\boldsymbol{q})} \tag{6.5b}$$

$$= \frac{1}{2} \sum_{h_1 h_2 \boldsymbol{p}\boldsymbol{q}} N_{h_1} N_{h_2} N_{He} P_\mu(\boldsymbol{p}) P_\nu(\boldsymbol{q})$$

$$= \tfrac{1}{2} N_H^2 N_{He} \sum_{h_1 h_2} \hat{h}_1 \hat{h}_2 \sum_{\boldsymbol{p}} P_\mu(\boldsymbol{p}) \sum_{\boldsymbol{q}} P_\nu(\boldsymbol{q})$$

$$= \tfrac{1}{2} N_H^2 N_{He} ,$$

with $\Sigma_h \hat{h} = 1$; $\Sigma_{h_1 h_2} \hat{h}_1 \hat{h}_2 = 1$; $\Sigma_{\boldsymbol{k}} P_m(\boldsymbol{k}) = 1$, and using the ket notation $|\ \rangle$ for symmetrized states and $|\ )$ for unsymmetrized states. We first define the symbols used and then return to the equation for a short discussion of noteworthy aspects of the derivation. The total number of H–H–He triples in a sample of volume V is $\Sigma_i P_i = \binom{N_H}{2} N_{He} = \frac{1}{2} N_H^2 N_{He}$; $\hat{h} = N_h / N_H$ is the fraction of H-atoms in hyperfine state $|h\rangle$, and $P_m(\boldsymbol{k})$ represents a Boltzmann momentum distribution for a particle of mass m

$$P_m(k) \equiv (\lambda_{th}^3 / V) \exp(-\hbar^2 k^2 / 2mkT) ,$$
$$\lambda_{th} \equiv (2\pi\hbar^2 / mkT)^{1/2} , \tag{6.6}$$

where λ_{th} is the thermal wavelength. In eq. (6.5b), two of these distributions appear, one for the relative motion of the H–H pair, where $m = \mu$ ($\mu = \frac{1}{2} m_H$ is the reduced mass of the pair) and one, with $m = \nu$, for the motion of the 2BCM of the H-pair with respect to the H-atom (with corresponding reduced mass $\nu = \frac{4}{3} m_H$).

Notice from eq. (6.5) that $\Sigma_i P_i = \frac{1}{2} N_H^2 N_{He}$ holds whether one treats the H-atoms as distinguishable or as indistinguishable, i.e, the total number of

Fig. 6.2. (b) Summary of three-body Jacobi coordinate convention.

Entity	Specification	Entity	Specification
Individual atoms			
Labels	$(i, j, k) = (1, 2, 3)$ or cyclic permutation		
Mass	m_i		
Wave vector	$\boldsymbol{k}_i$		
Position vectors	$\boldsymbol{r}_i$		
Pairs		**Spectator relative to pair**	
Label (spectator index)	$(\alpha, \beta, \gamma) = (1, 2, 3)$ or cyclic permutation	Reduced mass	$\nu_\alpha^{-1} \equiv m_\alpha^{-1} + M_\alpha^{-1}$
Mass	$M_\alpha \equiv m_\beta + m_\gamma$	Relative wavevector	$\boldsymbol{q}_\alpha \equiv (M_\alpha \boldsymbol{k}_\alpha - m_\alpha \boldsymbol{Q}_\alpha)/M$
Wave vector of 2BCM	$\boldsymbol{Q}_\alpha \equiv \boldsymbol{k}_\beta + \boldsymbol{k}_\gamma$	Relative positionvector	$\boldsymbol{\eta}_\alpha \equiv \boldsymbol{r}_\alpha - \boldsymbol{R}_\alpha$
Position vector of 2BCM	$\boldsymbol{R}_\alpha \equiv (m_\beta \boldsymbol{r}_\beta + m_\gamma \boldsymbol{r}_\gamma)/M_\alpha$		
Reduced mass	$\mu_\alpha^{-1} \equiv m_\beta^{-1} + m_\gamma^{-1}$		
Relative wavevector	$\boldsymbol{p}_\alpha \equiv (m_\gamma \boldsymbol{k}_\beta - m_\beta \boldsymbol{k}_\gamma)/M_\alpha$		
Relative positionvector	$\boldsymbol{\xi}_\alpha \equiv \boldsymbol{r}_\beta - \boldsymbol{r}_\gamma$		
Triple		**Spectator relative to pair in 3BCM system** $(\boldsymbol{Q} \equiv 0; \boldsymbol{R} = 0)$	
Mass	$M \equiv m_1 + m_2 + m_3 = m_\alpha + M_\alpha$		
Mass vector of 3BCM	$\boldsymbol{Q} \equiv \boldsymbol{k}_1 + \boldsymbol{k}_2 + \boldsymbol{k}_3 = \boldsymbol{k}_\alpha + \boldsymbol{Q}_\alpha$		
Position vector of 3BCM	$\boldsymbol{R} \equiv (m_1 \boldsymbol{r}_1 + m_2 \boldsymbol{r}_2 + m_3 \boldsymbol{r}_3)/M$ $= (m_\alpha \boldsymbol{r}_\alpha + M_\alpha \boldsymbol{R}_\alpha)/M$	Relative wavevector	$\boldsymbol{q}_\alpha = \boldsymbol{k}_\alpha = -\boldsymbol{Q}_\alpha$
		Relative positionvector	$\boldsymbol{\eta}_\alpha \equiv (M/M_\alpha)\boldsymbol{r}_\alpha = -(M/m_\alpha)\boldsymbol{R}_\alpha$

Transformation between spectator indices in 3BCM system

$$\boldsymbol{q}_\alpha = -[(m_\alpha/M_\beta)\boldsymbol{q}_\beta + \boldsymbol{p}_\beta]$$
$$\boldsymbol{p}_\alpha = [m_\gamma(M/M_\beta)\boldsymbol{q}_\beta - m_\beta \boldsymbol{p}_\beta]/M_\alpha$$

$$\boldsymbol{q}_\alpha = -[(m_\alpha/M_\gamma)\boldsymbol{q}_\gamma - \boldsymbol{p}_\gamma]$$
$$\boldsymbol{p}_\alpha = -[m_\beta(M/M_\gamma)\boldsymbol{q}_\gamma + m_\gamma \boldsymbol{p}_\gamma]/M_\alpha$$

pairs does not depend on the statistical nature of the particles. This allows us to sum over all states as if the particles are distinguishable, i.e. sum over nonsymmetrized states $|\mathrm{i}\rangle$. This transition is realized in going from eq. (6.5a) to eq. (6.5b) observing that there are twice as many unsymmetrized states as symmetrized states, but that the probability to find a pair in a given symmetrized state (one particle in state "1" and the other in state "2") is twice as large as the probability to find a pair in one of the corresponding nonsymmetrized states (particle "a" in state "1" and particle "b" in state "2" or vice versa). Once the transition to counting "as distinguishable" has been made the rest of the derivation is straightforward.

Returning to eq. (6.3), we stress the point that although we reduced the summation to a form, eq. (6.5b), in which the summation index runs over all classically distinguishable states, the matrix element still remains unchanged, i.e., composed of properly symmetrized and normalized states. To evaluate the summation one has to relate these symmetrized states to the corresponding (preferably normalized) unsymmetrized states:

$$|\mathrm{i}\rangle = \sqrt{\tfrac{1}{2}}[1 + P]|\mathrm{i}) = \sqrt{\tfrac{1}{2}}[|\mathrm{i}) + |-\mathrm{i})]\,, \tag{6.7}$$

where $|-\mathrm{i})$ is obtained by a permutation (P) of the H atoms in $|\mathrm{i})$. If desired, a similar procedure may be followed for $|\mathrm{f}\rangle$.

With the usual continuum transition $\Sigma_k \rightarrow V/(2\pi)^3 \int \mathrm{d}\boldsymbol{k}$, and integrating over all final $q(\equiv|\boldsymbol{q}|)$ states, the energy δ-function disappears and eq. (6.3) becomes

$$\Gamma/V = \tfrac{1}{2} n^2 n_{\mathrm{He}} \sum_{\mathrm{h_1 h_2}} \hat{h}_1 \hat{h}_2 \Gamma_{\mathrm{h_1 h_2 He}}\,, \tag{6.8a}$$

with

$$\Gamma_{\mathrm{h_1 h_2 He}} \equiv \sum_{I, M_I, \upsilon, L, M_L} \int \mathrm{d}\boldsymbol{p} \int \mathrm{d}\boldsymbol{q}\; P_\mu(\boldsymbol{p}) P_\nu(\boldsymbol{q}) \times \left(\frac{\nu}{2\pi\hbar^2}\right)^2 \int \mathrm{d}\hat{\boldsymbol{q}}'\, \frac{\hbar}{\nu}\, q' |\langle \mathrm{f}|T|\mathrm{i}\rangle|^2\,. \tag{6.8b}$$

Here n and n_{He} are the bulk H and He gas densities, $\hat{\boldsymbol{q}}'$ denotes the unit vector corresponding to $\boldsymbol{q}'$ and $\nu\hbar q'/(2\pi)^3$ is the density of final states evaluated at $q = q'$, where (see fig. 6.3)

$$\hbar^2 q'^2/2\nu = E_{\mathrm{i}} - E_{IM_I \upsilon L} \equiv E'\,. \tag{6.9}$$

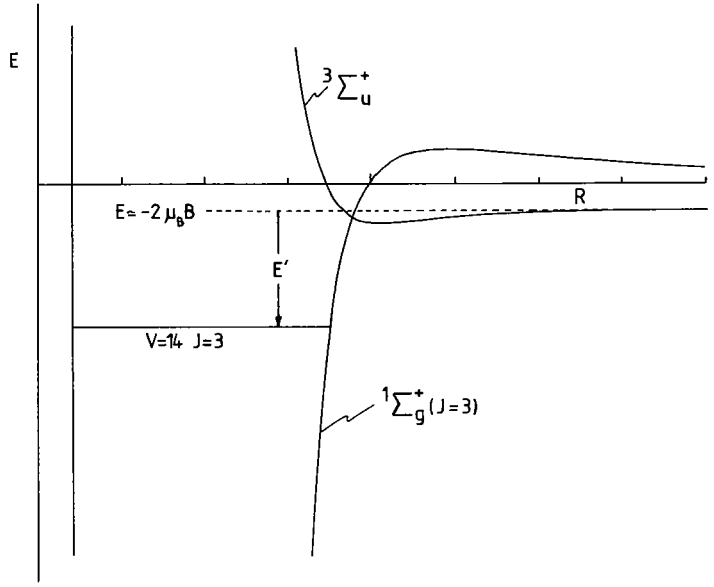

Fig. 6.3. Schematic diagram showing for $T=0$ the energy E' released in the recombination process. This energy is transferred to the relative motion between the recombined pair and third body. The larger E', the larger the number of final states available for recombination.

The phenomenology of recombination at low temperature may be illustrated on the basis of eq. (6.8). At low temperature the initial state $|i\rangle$ will contain a slowly oscillating wavefunction with little angular momentum, describing the motion of the body relative to the recombining pair. Also the distorted incoming wave (the distortion is due to the action of the T-operator) will have this character since the interaction between the He-atom and the H-pair is very weak. In contrast $|f\rangle$ is a rapidly oscillating function, since q' corresponds in general to hundreds of Kelvin (except for the $H_2(14,4)$ final state, see fig. 6.1). This implies the overlap of initial and final state wavefunctions to be averaged closer to zero the larger the binding of the molecule in the final state. Thus low-lying vibration–rotation states are of minor importance to our problem since the perturbation of the H–H system due to the He-atom is not sufficiently strong to enable the large momentum transfer required for recombination to these states.

Weakly bound, high-L ($L>4$) molecular states such as $H_2(3,27)$ may also be neglected. Conservation of angular momentum implies for these cases a high-L end-over-end rotation (in the opposite direction) of the

third body with respect to the molecule. The correspondingly large centrifugal barrier prevents a close approach of the two final-state bodies, the atom and the molecule, and thus reduces the transition amplitude due to lack of overlap within the range of the interaction.

Another interesting and important feature occurs for incoming energies at or just above a bound-state level. According to eq. (6.9) E' and thus q' must be small. Hence the transition rate vanishes due to the absence of sufficient density of final states (see eq. 6.8b). This aspect holds in general for direct three-body recombination processes.

Combining these various aspects, the GTB result that mainly the $H_2(14,3)$ and $H_2(14,2)$ final states contribute, in spite of the proximity of the $H_2(14,4)$, is put into perspective.

To gain further insight into the Van der Waals recombination we analyze the matrix element in some detail. The T-operator is written as

$$T \equiv \lim_{\eta \downarrow 0} i\eta V^3 G_+(E + i\eta) , \quad G_+(E + i\eta) \equiv [E - H + i\eta]^{-1} , \qquad (6.10a)$$

where $H = H_3 + V^3$ and $H_3 = K + H_Z + H_{hf} + V_D + V_{exch}$ (analogous to eq. 3.1). The subindex is used for the spectator label. The $\{|f\rangle\}$ are eigenstates of H_3. The perturbation V^3 enables the transition and describes the weak interaction between the two H-atoms and the helium third body. Neglecting pure three-body forces:

$$V^3 = V_1 + V_2 \equiv V^{(2-3)}_{H-He} + V^{(1-3)}_{H-He} . \qquad (6.10b)$$

Using the G_+ operator we rewrite the transition amplitude as

$$\langle f|T|i\rangle = \lim_{\eta \downarrow 0} i\eta \langle f|(V_1 + V_2) G_+|i\rangle . \qquad (6.11)$$

The G_+ operator induces the proper distortion of the initial state to account for the interaction between the atoms. GTB use the sudden appoximation for the spin part of the incoming wavefunction. This is equivalent to neglecting the time dependence of $|SM_S IM_I\rangle$, arising from the off-diagonal elements of H_{hf} (see table 6.1). This approximation is plausible since the three-body scattering time, $\tau_c \simeq 10^{-11}$ s, is short in comparison to the characteristic time $\tau_{hf} = 2\pi\hbar/a \simeq 10^{-9}$ s, associated with the hyperfine interaction. The approximation is referred to as the Wigner rule (see the discussion of this effect by Pinard and Laloë 1980) and may break down at low temperatures. It amounts to the same as replacing the hyperfine adiabatic potentials (see section 3) by diabatic analogues in the form of the singlet and triplet potentials. To go beyond this approximation requires a close coupling treatment of the H–H scattering.

We illustrate this point with an example. Just before the collision the atoms may be in a hyperfine pair state such as $|\mathrm{aa}\rangle$ (see table 6.4a),

$$|\mathrm{aa}\rangle = \varepsilon\eta|0000\rangle + \varepsilon^2|111\,{-1}\rangle - \varepsilon\eta|1010\rangle + \eta^2|1\,{-111}\rangle\,.$$

Hence, at any given time a fraction $(\varepsilon\eta)^2$ of the pairs will be in the spin state $|0000\rangle$. Since this is not an eigenstate of H_{hf} (see table 6.1), this pair will be found in a relative triplet state after the characteristic time τ_{hf}. Of course this is of little consequence in the absence of a spin-dependent potential since the various components of the spin wavefunction propagate coherently so that the spin state $|\mathrm{aa}\rangle$ is conserved. However, the H–H potential depends strongly on S so that for a collision time $\tau_c \ll \tau_{\mathrm{hf}}$ the difference in singlet and triplet phase shifts will break the coherence and mix up the hyperfine pair states. In the limit of short collision times, the hyperfine interaction apparently only acts to yield a small (quasi-stationary) population of the high-lying (see fig. 3.1) spin states $|0000\rangle$, $|111\,{-1}\rangle$ and $|1010\rangle$.

For an arbitrary initial state, we write the decomposition as

$$|\mathrm{i}\rangle = |\mathrm{h}_1\mathrm{h}_2;\, \boldsymbol{p},\, \boldsymbol{q}\rangle = \sqrt{\tfrac{1}{2}}[|\mathrm{h}_1\mathrm{h}_2;\, \boldsymbol{p},\, \boldsymbol{q}) + |\mathrm{h}_2\mathrm{h}_1;\, -\boldsymbol{p},\, \boldsymbol{q})]$$

$$= \sum_{SM_SIM_I} |SM_SIM_I;\, \boldsymbol{p},\, \boldsymbol{q}\rangle\, \langle SM_SIM_I|\mathrm{h}_1\mathrm{h}_2)\,. \tag{6.12}$$

The state $|SM_SIM_I;\, \boldsymbol{p},\, \boldsymbol{q}\rangle$ represents an even $(S + I = 0)$ or odd $(S + I = 1)$ orbital wavefunction for the H–H motion. This results from the property $\langle SM_SIM_I|\mathrm{h}_1\mathrm{h}_2) = (-1)^{S+I}\langle SM_SIM_I|\mathrm{h}_2\mathrm{h}_1)$, which is easily verified in table 6.4a.

We insert eq. (6.12) into eq. (6.11) for the transition amplitude. As V^3 is spin independent the explicit spin parts project out of the matrix element, leaving only the spin dependence of the orbital wavefunction $|SI;\, \boldsymbol{p},\, \boldsymbol{q}\rangle$:

$$\langle \mathrm{f}|V^3G_+|\mathrm{i}\rangle = \sum_{IM_I} \langle 0I;\, v,\, L,\, M_L,\, \boldsymbol{q}'|V^3G_+|0I;\, \boldsymbol{p},\, \boldsymbol{q}\rangle\langle SM_SIM_I|\mathrm{h}_1\mathrm{h}_2)\,, \tag{6.13a}$$

$$|SI;\, \boldsymbol{p},\, \boldsymbol{q}\rangle \equiv \sqrt{\tfrac{1}{2}}\,[|\boldsymbol{p},\, \boldsymbol{q}) + (-1)^{S+I}|-\boldsymbol{p},\, \boldsymbol{q})]\,. \tag{6.13b}$$

Equations (6.13) clearly display the property that distinguishes Van der Waals recombination from all other known three-body recombination processes: Since the perturbation V^3 cannot induce spin transitions (and the collision times are very short) the transition amplitude vanishes unless $|\mathrm{i}\rangle$ already contains the singlet character required to form a bound state.

Table 6.4a

Decomposition of hyperfine pair states of hydrogen with respect to the total spin representation $|SM_SIM_I\rangle$. The states that contribute for $T \to 0$ K are indicated with an asterisk. Note: $\alpha = (\frac{1}{2})^{1/2}$, $\varepsilon \equiv \sin\theta$, and $\eta \equiv \cos\theta$; θ is defined in section 2.1. P is the parity of the state.

h_2h_1 / h_1h_2	ba / ab	ca / ac	da / ad	bb	cb / bc	db / bd	cc	dc / cd	dd	S	M_S	I	M_I	P
aa		$\frac{1}{2}(\eta^2-\varepsilon^2)$				$\frac{1}{2}$	$-\varepsilon\eta$			*0	0	0	0	+
			$\mp\alpha\eta$					$\pm\alpha\varepsilon$		0	0	1	1	−
		$\mp\frac{1}{2}$				$\pm\frac{1}{2}$				0	0	1	0	−
	$\mp\alpha\varepsilon$				$\mp\alpha\eta$					0	0	1	−	−
			$\pm\alpha\varepsilon$					$\pm\alpha\eta$		1	1	0	0	−
									1	*1	1	1	1	+
			$\alpha\varepsilon$					$\alpha\eta$		*1	1	1	0	+
ε^2		$\varepsilon\eta$					η^2			*1	1	1	−	+
		$\pm\frac{1}{2}$				$\pm\frac{1}{2}$				1	0	0	0	−
			$-\alpha\eta$					$\alpha\varepsilon$		*1	0	1	1	+
$-\varepsilon\eta$		$-\frac{1}{2}(\eta^2-\varepsilon^2)$				$\frac{1}{2}$	$\varepsilon\eta$			*1	0	1	0	+
	$\alpha\varepsilon$				$\alpha\eta$					*1	0	1	−	+
	$\pm\alpha\eta$				$\mp\alpha\varepsilon$					1	−	0	0	−
η^2		$-\varepsilon\eta$					ε^2			*1	−	1	1	+
	$-\alpha\eta$				$\alpha\varepsilon$					*1	−	1	0	+
				1						*1	−	1	−	+

Table 6.4b

Decomposition of hyperfine states of deuterium with respect to the total spin representation $|SM_SIM_I\rangle$. The states that contribute for $T = 0$ K are indicated with an asterisk. η_+, η_-, ε_+ and ε_- are defined in section 2.1; $a = \sqrt{\frac{1}{2}}$, $b = \sqrt{\frac{1}{3}}$ and $c = \sqrt{\frac{1}{6}}$.

S	M_S	I	M_I	$\alpha\alpha$	$\beta\alpha$ $\alpha\beta$	$\gamma\alpha$ $\alpha\gamma$	$\delta\alpha$ $\alpha\delta$	$\varepsilon\alpha$ $\alpha\varepsilon$	$\zeta\alpha$ $\alpha\zeta$	$\beta\beta$
0	0	0	0*		$\mp c[\eta_+\varepsilon_- + \varepsilon_+\eta_-]$		$\mp c[\eta_+\eta_- - \varepsilon_+\varepsilon_-]$			
0	0	1	1	$\eta_+\varepsilon_+$				$\frac{1}{2}[\eta_+^2 - \varepsilon_+^2]$		
0	0	1	0		$\frac{1}{2}\eta_+\varepsilon_-$		$\frac{1}{2}\eta_+\eta_-$			
0	0	1	−1			$\frac{1}{2}\varepsilon_+$				$\eta_-\varepsilon_-$
0	0	2	2*						$\mp a\eta_+$	
0	0	2	1*					$\mp\frac{1}{2}$		
0	0	2	0*		$\mp b[\frac{1}{2}\eta_+\varepsilon_- - \varepsilon_+\eta_-]$		$\mp b[\frac{1}{2}\eta_+\eta_- + \varepsilon_+\varepsilon_-]$			
0	0	2	−1*			$\mp\frac{1}{2}\varepsilon_+$				
0	0	2	−2*							
1	1	0	0	$-b\varepsilon_+^2$				$-b\varepsilon_+\eta_+$		
1	1	1	1*						$\pm a\varepsilon_+$	
1	1	1	0*							
1	1	1	−1*		$\mp a\varepsilon_+\varepsilon_-$		$\mp a\varepsilon_+\eta_-$			
1	1	2	2							
1	1	2	1						$a\varepsilon_+$	
1	1	2	0	$(b/a)\varepsilon_+^2$				$(b/a)\varepsilon_+\eta_+$		
1	1	2	−1		$a\varepsilon_+\varepsilon_-$		$a\varepsilon_+\eta_-$			
1	1	2	−2							ε_-^2
1	0	0	0		$-c[\eta_+\varepsilon_- - \varepsilon_+\eta_-]$		$-c[\eta_+\eta_- + \varepsilon_+\varepsilon_-]$			
1	0	1	1*					$\pm\frac{1}{2}$		
1	0	1	0*		$\pm\frac{1}{2}\eta_+\varepsilon_-$		$\pm\frac{1}{2}\eta_+\eta_-$			
1	0	1	−1*			$\mp\frac{1}{2}\varepsilon_+$				
1	0	2	2						$-a\eta_+$	
1	0	2	1	$-\eta_+\varepsilon_+$				$-\frac{1}{2}[\eta_+^2 - \varepsilon_+^2]$		
1	0	2	0		$-b[\frac{1}{2}\eta_+\varepsilon_- + \varepsilon_+\eta_-]$		$-b[\frac{1}{2}\eta_+\eta_- - \varepsilon_+\varepsilon_-]$			
1	0	2	−1			$\frac{1}{2}\varepsilon_+$				$-\eta_-\varepsilon_-$
1	0	2	−2							
1	−1	0	0			$-b\eta_+$				$-b\eta_-^2$
1	−1	1	1*		$\mp a\eta_+\eta_-$		$\pm a\eta_+\varepsilon_-$			
1	−1	1	0*			$\pm a\eta_+$				
1	−1	1	−1*							
1	−1	2	2	η_+^2				$-\eta_+\varepsilon_+$		
1	−1	2	1		$a\eta_+\eta_-$		$-a\eta_+\varepsilon_-$			
1	−1	2	0			$-c\eta_+$				$(b/a)\eta_-^2$
1	−1	2	−1							
1	−1	2	−2							

Table 6.4b (cont'd)

S	M_S	I	M_I	$\zeta\gamma$ $\gamma\zeta$	$\delta\delta$	$\varepsilon\delta$ $\delta\varepsilon$	$\zeta\delta$ $\delta\zeta$	$\varepsilon\varepsilon$	$\zeta\varepsilon$ $\varepsilon\zeta$	$\zeta\zeta$
0	0	0	0	$\pm c$		$\mp c[\varepsilon_+\eta_- + \eta_+\varepsilon_-]$				
0	0	1	1				$\frac{1}{2}\varepsilon_-$	$-\eta_+\varepsilon_+$		
0	0	1	0	$\frac{1}{2}$		$-\frac{1}{2}\varepsilon_+\eta_-$				
0	0	1	−1		$-\eta_-\varepsilon_-$					
0	0	2	2*						$\pm a\varepsilon_+$	
0	0	2	1*				$\pm\frac{1}{2}\varepsilon_-$			
0	0	2	0*	$\pm\frac{1}{2}b$		$\mp b[\frac{1}{2}\varepsilon_+\eta_- - \eta_+\varepsilon_-]$				
0	0	2	−1*							
0	0	2	−2*							
1	1	0	0				$b\eta_-$	$-b\eta_+^2$		
1	1	1	1*						$\pm a\eta_+$	
1	1	1	0*				$\pm a\eta_-$			
1	1	1	−1*			$\pm a\eta_+\eta_-$				
1	1	2	2							1
1	1	2	1						$a\eta_+$	
1	1	2	0				$c\eta_-$	$(b/a)\eta_+^2$		
1	1	2	−1			$a\eta_+\eta_-$				
1	1	2	−2		η_-^2					
1	0	0	0	c		$c[\varepsilon_+\eta_- - \eta_+\varepsilon_-]$				
1	0	1	1*				$\pm\frac{1}{2}\varepsilon_-$			
1	0	1	0*	$\pm\frac{1}{2}$		$\pm\frac{1}{2}\varepsilon_+\eta_-$				
1	0	1	−1*							
1	0	2	2						$a\varepsilon_+$	
1	0	2	1				$\frac{1}{2}\varepsilon_-$	$\eta_+\varepsilon_+$		
1	0	2	0	$\frac{1}{2}b$		$b[\frac{1}{2}\varepsilon_+\eta_- + \eta_+\varepsilon_-]$				
1	0	2	−1		$\eta_-\varepsilon_-$					
1	0	2	−2							
1	−1	0	0		$-b\varepsilon_-^2$					
1	−1	1	1*			$\pm a\varepsilon_+\varepsilon_-$				
1	−1	1	0*							
1	−1	1	−1*							
1	−1	2	2					ε_+^2		
1	−1	2	1			$a\varepsilon_+\varepsilon_-$				
1	−1	2	0		$(b/a)\varepsilon_-^2$					
1	−1	2	−1							
1	−1	2	−2							

Table 6.4b (cont'd)

S	M_S	I	M_I	$\gamma\beta$ / $\beta\gamma$	$\delta\beta$ / $\beta\delta$	$\varepsilon\beta$ / $\beta\varepsilon$	$\zeta\beta$ / $\beta\zeta$	$\gamma\gamma$	$\delta\gamma$ / $\gamma\delta$	$\varepsilon\gamma$ / $\gamma\varepsilon$
0	0	0	0			$\pm c[\eta_+\eta_- - \varepsilon_+\varepsilon_-]$				
0	0	1	1				$-\frac{1}{2}\eta_-$			
0	0	1	0			$-\frac{1}{2}\varepsilon_+\varepsilon_-$				
0	0	1	−1		$\frac{1}{2}[\eta_-^2 - \varepsilon_-^2]$					$\frac{1}{2}\eta_+$
0	0	2	2*							
0	0	2	1*				$\mp\frac{1}{2}\eta_-$			
0	0	2	0*			$\mp b[\eta_+\eta_- + \frac{1}{2}\varepsilon_+\varepsilon_-]$				
0	0	2	−1*		$\mp\frac{1}{2}$					$\pm\frac{1}{2}\eta_+$
0	0	2	−2*	$\mp a\varepsilon_-$					$\pm a\eta_-$	
1	1	0	0				$b\varepsilon_-$			
1	1	1	1*							
1	1	1	0*				$\pm a\varepsilon_-$			
1	1	1	−1*			$\pm a\eta_+\varepsilon_-$				
1	1	2	2							
1	1	2	1							
1	1	2	0				$c\varepsilon_-$			
1	1	2	−1			$a\eta_+\varepsilon_-$				
1	1	2	−2		$\eta_-\varepsilon_-$					
1	0	0	0			$c[\eta_+\eta_- + \varepsilon_+\varepsilon_-]$				
1	0	1	1*				$\mp\frac{1}{2}\eta_-$			
1	0	1	0*			$\pm\frac{1}{2}\varepsilon_+\varepsilon_-$				
1	0	1	−1*		$\pm\frac{1}{2}$					$\pm\frac{1}{2}\eta_+$
1	0	2	2							
1	0	2	1				$-\frac{1}{2}\eta_-$			
1	0	2	0			$-b[\eta_+\eta_- - \frac{1}{2}\varepsilon_+\varepsilon_-]$				
1	0	2	−1		$-\frac{1}{2}[\eta_-^2 - \varepsilon_-^2]$					$\frac{1}{2}\eta_+$
1	0	2	−2	$a\varepsilon_-$					$a\eta_-$	
1	−1	0	0		$b\eta_-\varepsilon_-$					$b\varepsilon_+$
1	−1	1	1*			$\mp a\varepsilon_+\eta_-$				
1	−1	1	0*							$\pm a\varepsilon_+$
1	−1	1	−1*	$\pm a\eta_-$					$\pm a\varepsilon_-$	
1	−1	2	2							
1	−1	2	1			$-a\varepsilon_+\eta_-$				
1	−1	2	0		$-(b/a)\eta_-\varepsilon_-$					$c\varepsilon_+$
1	−1	2	−1	$-a\eta_-$					$a\varepsilon_-$	
1	−1	2	−2					1		

This enables us to factor the spin part out from the matrix element, and eq. (6.8) becomes

$$\Gamma/V = \tfrac{1}{2} n^2 n_{\mathrm{He}} \sum_{\mathrm{h_1 h_2}} \hat{h}_1 \hat{h}_2 \Gamma_{\mathrm{h_1 h_2 He}} , \tag{6.14a}$$

with

$$\Gamma_{\mathrm{h_1 h_2 He}} \equiv \sum_{I,v,L,M_L} |\langle 00 I M_I | \mathrm{h_1 h_2}\rangle|^2 \int \mathrm{d}\boldsymbol{p} \int \mathrm{d}\boldsymbol{q}\, P_\mu(\boldsymbol{p}) P_\nu(\boldsymbol{q}) \left(\frac{\nu}{2\pi\hbar^2}\right)^2$$
$$\times \int \mathrm{d}\hat{\boldsymbol{q}}' \frac{\hbar}{\nu} q' |\langle 0 I, v, L, M_L, q' | V^3 G_+ | 0 I \boldsymbol{p}, \boldsymbol{q}\rangle|^2 , \tag{6.14b}$$

where we assume the $\lim_{\eta \downarrow 0}$ to be implicit and $M_I = M_{F_{\mathrm{h}_1}} + M_{F_{\mathrm{h}_2}}$. The probability amplitudes $\langle S M_S I M_I | \mathrm{h_1 h_2}\rangle$ are summarized in table 6.4a (for H and T). The corresponding amplitudes for D are given in table 6.4b. For a tabulation of the restricted class of probabilities, $|\langle 00 I M_I | \mathrm{h_1 h_2}\rangle|^2$, the reader is referred to the GTB paper.

Apart from the point that the matrix element may be factorized into a spin part and an orbital part, eq. (6.13) displays another interesting feature. With the spin symmetry shown in eq. (6.13b), a condition exists on the relative angular momentum of the H–H pair. As a consequence, for recombination to ortho-H_2 ($I = 1$), angular momentum has to be present in the orbital motion of the incoming hydrogen atoms. Since for $T \to 0$ scattering primarily occurs via s-waves, the recombination rate to o-H_2 should fall off dramatically with decreasing temperature. This feature clearly projects out of the GTB results. The incoming spin-states that contribute at $T = 0$ K are labeled with an asterisk in table 6.4a.

Summing over the hyperfine levels, GTB (in a slightly different notation) arrive at

$$\Gamma/V \equiv \tfrac{1}{2} n^2 n_{\mathrm{He}} \sum_{I,v,L,M_L} f_I \int \mathrm{d}\boldsymbol{p} \int \mathrm{d}\boldsymbol{q}\, P_\mu(\boldsymbol{p}) P_\nu(\boldsymbol{q}) \left(\frac{\nu}{2\pi\hbar^2}\right)^2$$
$$\times \int \mathrm{d}\hat{\boldsymbol{q}} \frac{\hbar}{\nu} q' |\langle 0 I, v, L, M_L, q' | V^3 G_+ | 0 I \boldsymbol{p}, \boldsymbol{q}\rangle|^2 , \tag{6.15}$$

where f_I represents a wonderfully compact expression for the spin dependence of the probability to recombine to an ortho ($I = 1$) or para ($I = 0$) molecular state:

$$f_I \equiv \sum_{\mathrm{h_1 h_2}} \hat{h}_1 \hat{h}_2 |\langle 00 I M_I | \mathrm{h_1 h_2}\rangle|^2 . \tag{6.16}$$

To the extent that the orbital part of eq. (6.15) (second line) does not vary with magnetic field, eq. (6.16) provides us with the field dependence of Van der Waals recombination. This assumption is likely to be quite good for recombination to o-H_2. For recombination to p-H_2 the contribution to the $H_2(14,4)$ level should be strongly field dependent. However, the GTB results show that this final state does not have an important contribution to the recombination rate.

To calculate the distortion due to G_+ requires, in principle, the solution of the Faddeev equations for the three-body problem [for an introduction to this theory see the books by Glöckle (1983), Schmid and Ziegelmann (1974) and Thomas (1977)]. The three-body G_+ operator may be expanded in a multiple scattering series using a method developed by Alt, Grassberger and Sandhas (AGS 1967) and based on the Faddeev formalism. The first two terms in this expansion describe single scattering of the He-atom off of the two H-atoms and is known as the impulse approximation. The GTB results are obtained within this approximation. The validity of the impulse approximation is questionable in view of the low incoming energies which favor multiple scattering effects. Moreover the expansion does not necessarily converge. Alternatively one may say that the distortion of the initial wavefunction due to the H–H interaction is neglected. A rigorous solution requires the numerical integration of the Faddeev equations, which is much more involved than the already sizeable task of solving the impulse approximation.

A rather dramatic consequence of eqs. (6.15) and (6.16) was first realized by Hardy (see ref. 1 of Statt, 1982). In high fields, where only the $|a\rangle$ and $|b\rangle$ states are populated, eq. (6.16) implies preferential recombination of the $|a\rangle$ state. In the absence of sufficiently fast magnetic relaxation this leads to a depletion of this state, leaving the system in the pure b-state, the doubly polarized state H↓‡. Thus the Van der Waals recombination channel is bottlenecked by (nuclear) magnetic relaxation from the b- to the a-level. A discussion of this relaxation bottleneck is postponed until sections 6.1.4 and 6.2.3.

If the gas is doubly polarized, then after $b \rightarrow a$ relaxation, recombination takes place via the a–b channel to yield (nuclear) spin-polarized o-H_2 (with $M_I = -1$, see table 6.2). For applications in particle physics and possible fusion, Kleppner and Greytak (1983) have suggested that the analogous process in deuterium might be useful in producing (nuclear) spin-polarized D_2, since spin conversion is very slow.

The ideas just discussed that recombination rates would be controlled by the spin projection of the hyperfine pair states on the molecular state so that magnetic fields would suppress recombination and stabilize the gas, was first presented by Silvera (1979). The concept was published by Silvera

and Walraven (1981b), along with the consequence that H↓ should recombine to specific ratios of ortho- and para-H_2 depending on the magnetic field. This can be easily read off from table 6.4a. The spin-projection concept was one of the significant motivating theoretical principles which provided early hope that atomic hydrogen could be stabilized. In essence it says that if a second-order process is the dominant channel for recombination, then complete polarization renders recombination a spin-forbidden process. Complete polarization corresponds to the case of b–b or d–d collisions in which the initial state has zero projection on the (electron spin singlet) molecular states (see table 6.4a). However, due to the hyperfine interaction the a-state of H↓ is not completely polarized (see eq. 2.4a), so that even though the magnetic field stabilizes H↓, there is a small but significant recombination rate. From table 6.2 we observe that a–a recombination can only result in the formation of p-H_2, whereas a–b recombination leads to o-H_2. This table shows for which channels recombination is spin allowed for H and T, while table 6.4a gives the actual (spin) probability amplitudes. For D the spin probability amplitudes are given in table 6.4b.

For convenience we provide explicit expressions for f_I for H (and T) and D. With the aid of table 6.4a, eq. (6.16) may be expressed in terms of the fractional densities $\hat{h}$ of the hyperfine states:

$$\begin{aligned} f_0 &= \tfrac{1}{4}[(\hat{a}^2 + \hat{c}^2)\sin^2 2\theta + 2\hat{a}\hat{c}\cos^2 2\theta + 2\hat{b}\hat{d}]\,, \\ f_1 &= (\hat{a}\hat{b} + \hat{c}\hat{d})\sin^2\theta + (\hat{a}\hat{d} + \hat{b}\hat{c})\cos^2\theta + \tfrac{1}{2}(\hat{a}\hat{c} + \hat{b}\hat{d})\,. \end{aligned} \tag{6.17}$$

Similarly, we obtain for D, using Table 6.4b,

$$\begin{aligned} f_{\text{even}} = \tfrac{1}{2}[&\eta_+^2\varepsilon_-^2(\hat{\alpha}\hat{\beta} + 2\hat{\delta}\hat{\varepsilon}) + \varepsilon_+^2\eta_-^2(2\hat{\alpha}\hat{\beta} + \hat{\delta}\hat{\varepsilon}) + \eta_+^2\eta_-^2(\hat{\alpha}\hat{\delta} + 2\hat{\beta}\hat{\varepsilon}) \\ &+ \varepsilon_+^2\varepsilon_-^2(2\hat{\alpha}\hat{\delta} + \hat{\beta}\hat{\varepsilon}) + \varepsilon_+^2(\hat{\alpha}\hat{\gamma} + 2\hat{\varepsilon}\hat{\zeta}) + \eta_+^2(2\hat{\alpha}\hat{\zeta} + \hat{\gamma}\hat{\varepsilon}) \\ &+ \eta_-^2(\hat{\beta}\hat{\zeta} + 2\hat{\gamma}\hat{\delta}) + \varepsilon_-^2(2\hat{\beta}\hat{\gamma} + \hat{\delta}\hat{\zeta}) + (\hat{\alpha}\hat{\varepsilon} + \hat{\beta}\hat{\delta} + \hat{\gamma}\hat{\zeta})]\,, \\ f_{\text{odd}} = \tfrac{1}{2}[&2\eta_+^2\varepsilon_+^2(\hat{\alpha}^2 + \hat{\varepsilon}^2) + 2\eta_-^2\varepsilon_-^2(\hat{\beta}^2 + \hat{\delta}^2) + \eta_+^2\varepsilon_-^2\hat{\alpha}\hat{\beta} + \eta_+^2\eta_-^2\hat{\alpha}\hat{\delta} \\ &+ \varepsilon_+^2\varepsilon_-^2\hat{\beta}\hat{\varepsilon} + \varepsilon_+^2\eta_-^2\hat{\delta}\hat{\beta} + \varepsilon_+^2\hat{\alpha}\hat{\gamma} + \eta_-^2\hat{\beta}\hat{\zeta} + \eta_+^2\hat{\gamma}\hat{\varepsilon} + \varepsilon_-^2\hat{\delta}\hat{\zeta} \\ &+ \hat{\gamma}\hat{\zeta} + (\eta_+^2 - \varepsilon_+^2)(\hat{\alpha}\hat{\varepsilon} + \hat{\beta}\hat{\delta})]\,. \end{aligned} \tag{6.18}$$

We consider, in particular, two cases:

(i) all hyperfine states equally populated (zero field; rapid relaxation). For hydrogen: $\hat{a} = \hat{b} = \hat{c} = \hat{d} = \frac{1}{4}$,

$$f_0 = \tfrac{1}{16}\,, \qquad f_1 = \tfrac{3}{16}\,,$$

For deuterium: $\hat{\alpha} = \hat{\beta} = \hat{\gamma} = \hat{\delta} = \hat{\varepsilon} = \hat{\zeta} = \frac{1}{6}$,

$$f_{\text{even}} = \tfrac{1}{6}\,, \qquad f_{\text{odd}} = \tfrac{1}{12}\,.$$

For both hydrogen and deuterium we find that only one out of four collisions may lead to the formation of a molecule. This is as expected, since only one out of four collisions proceeds via the singlet potential.

(ii) The a- and b- state equally populated (very high field; rapid relaxation).

For hydrogen: $\hat{a} = \hat{b} = \frac{1}{2}$,

$$f_0 \simeq \tfrac{1}{4}\varepsilon^2\,, \qquad f_1 \simeq \tfrac{1}{4}\varepsilon^2\,.$$

For deuterium: $\hat{\alpha} = \hat{\beta} = \hat{\gamma} = \frac{1}{3}$,

$$f_{\text{even}} \simeq \tfrac{1}{6}[\varepsilon_+^2 + \varepsilon_-^2] \simeq \tfrac{1}{3}\varepsilon_{\text{D}}^2\,, \qquad f_{\text{odd}} \simeq \tfrac{1}{6}[\varepsilon_+^2 + \varepsilon_-^2] \simeq \tfrac{1}{3}\varepsilon_{\text{D}}^2\,.$$

With the assumption that the orbital part of the transition amplitudes is field independent, the ratio of high field and zero-field recombination rates is given by $2\varepsilon^2$ ($=1.3 + 10^{-5}$ for $B = 10\,\text{T}$) and $(8/3)\varepsilon_{\text{D}}^2$ ($=1.8 \times 10^{-6}$ for $B = 10\,\text{T}$) for H and D, respectively. As may be seen from eq. (2.4) the rates are suppressed as B^{-2} with growing magnetic field. This was established experimentally by Matthey et al. (1981), who compared their high-field results with the zero-field measurements of Morrow et al. (1981), as discussed in detail in section 5.

6.1.2.2. Van der Waals recombination on the surface

Before we compare the GTB theory with experiment we discuss the case where the surface acts as the third body. Although no detailed theory has been developed for this case, it is not difficult to generalize the remarks of the previous section. Instead of the bulk gas density (n) and volume (V) we consider the surface density (σ) and area (A), so that

$$\Gamma/A = \tfrac{1}{2}\sigma^2 \sum_{\text{h}_1\text{h}_2} \hat{h}_1 \hat{h}_2 \Gamma_{\text{sh}_1\text{h}_2}\,. \tag{6.19}$$

Neglecting, for simplicity, any surface excitations (static surface) the analog of eq. (6.8) is

$$\Gamma_{\text{sh}_1\text{h}_2} \equiv \sum_{I,M_I,v,L,M_L} \int \mathrm{d}\boldsymbol{p}\, P_\mu(\boldsymbol{p}) |\langle \text{f}|T|\text{i}\rangle|^2\,. \tag{6.20}$$

The initial state

$$|\mathrm{i}\rangle = |\mathrm{h}_1\mathrm{h}_2;\ \boldsymbol{p}\rangle \tag{6.21}$$

consists of two H-atoms moving along the surface with relative momentum $\boldsymbol{p}$. Since energy exchange with the surface is neglected, the CM-momentum of the pair along the surface is conserved during the reaction and recombination can only take place through desorption of the molecule. As the atoms are in bound states, the momenta perpendicular to the surface vary rapidly in time, resulting in a continuous exchange of angular momentum between pair and surface with only the normal component of the angular-momentum vector being conserved.

The final state

$$|\mathrm{f}\rangle = |00IM_I;\ v,\ L,\ M_L,\ q_z'\rangle \tag{6.22}$$

appears to be similar to eq. (6.4), but q_z' replaces $\boldsymbol{q}'$ since all recombination energy (minus the adsorption energy of two H-atoms) is transferred to the normal component of the molecular motion. Equation (6.9) now holds for q_z' provided the adsorption energy is included in E_i.

For the surface case the perturbation that enables the transition is the H_2-surface potential, as in the bulk case a nonmagnetic interaction, thus conserving the significance of the f_I factor of eq. (6.16). This property also remains conserved if inelastic surface interactions are included.

The density of the surface helium σ_{He} does not appear explicitly in eq. (6.19) as it did in the volume reaction, eq. (6.15), yet Γ should depend in detail on the character and the excitation spectrum of the surface. For liquid helium the low-lying excitations are the hydrodynamic modes, whereas for high energy the excitations are free-particle like. Since in recombination a substantial amount of energy is liberated (of order 70 K for recombination to o-H_2), one may speculate (Silvera and Walraven 1980b) that the He surface atoms should behave free-particle like and can be treated as a surface gas of density $\sigma_{\mathrm{He}} \simeq n_{\mathrm{He}}^{2/3} = 7.4 \times 10^{14}\ \mathrm{cm}^{-2}$, where n_{He} is the liquid density (the surface density is expected to be a bit lower due to its extended density profile). Thus $\Gamma_{\mathrm{sh_1h_2}}$ should be proportional to σ_{He}. If we compare the intrinsic rates of recombination of ^{3}He and ^{4}He, then (ignoring the density profiles) we might expect $\Gamma^{^3\mathrm{He}}/\Gamma^{^4\mathrm{He}} = 0.83$ (=the two thirds power of the ratios of the density of ^{3}He to ^{4}He). Uncertainties in experimental values are too large at present to comment further on this point (see table 5.1).

6.1.2.3. Relationship to phenomenological experimental rates

In section 5.2, phenomenological rate constants were given for the recombination-rate constants of H; here we relate the second-order rate constants of the form $K_{h_1h_2}$, for recombination of two atoms with initial hyperfine states h_1 and h_2, to the theoretical transition rates. Noting from eq. (5.13) that effective rates are composed of intrinsic surface and volume rates,

$$K^{\text{eff}}_{h_1h_2} = K^{\text{v}}_{h_1h_2} n_{\text{He}} + (A/V)(\sigma_{h_1}/n_{h_1})(\sigma_{h_2}/n_{h_2}) K^{\text{s}}_{h_1h_2} , \tag{6.23}$$

we now find relationships for both contributions in terms of the formalism of the previous two sections.

We shall treat the volume part in detail for a system of constant volume. For second-order recombination of H↓

$$\dot{a} = -2K^{\text{v}}_{aa} a^2 n_{\text{He}} - K^{\text{v}}_{ab} abn_{\text{He}} , \qquad \dot{b} = -K^{\text{v}}_{ab} abn_{\text{He}} , \tag{6.24}$$

adding this we obtain the total rate of decay of atomic density,

$$\dot{n} = -2K^{\text{v}}_{aa} a^2 n_{\text{He}} - 2K^{\text{v}}_{ab} abn_{\text{He}} . \tag{6.25}$$

We relate this to eq. (6.8) for the total rate of recombination events per unit volume, which is (minus) half the rate given by eq. (6.25), since each recombination destroys two atoms. In summing eq. (6.8) over h_i, we get a factor two for $h_1 \neq h_2$ and one for $h_1 = h_2$, so that

$$-2K^{\text{v}}_{aa} a^2 - 2K^{\text{v}}_{ab} ab = -(\Gamma_{\text{aaHe}}) a^2 - 2(\Gamma_{\text{abHe}}) ab . \tag{6.26}$$

Comparing, and using analogous reasoning for surface events, using eq. (6.19), we can relate the recombination part of eqs. (5.14) to eqs. (6.15) and (6.19) to yield

$$K^{\text{v}}_{aa} = \tfrac{1}{2}\Gamma_{\text{aaHe}} , \qquad K^{\text{s}}_{aa} = \tfrac{1}{2}\Gamma_{\text{saa}}$$

$$K^{\text{v}}_{ab} = \Gamma_{\text{abHe}} , \qquad K^{\text{s}}_{ab} = \Gamma_{\text{sab}} . \tag{6.27}$$

One easily derives for the general case

$$K_{hh} = \tfrac{1}{2}\Gamma_{hh} , \qquad K_{h_1h_2} = \Gamma_{h_1h_2} \quad (\text{for } h_1 \neq h_2) . \tag{6.28}$$

The ratio $\gamma \equiv (K^s_{aa}/K^s_{ab})$, which has drawn considerable interest in the literature (Sprik et al. 1982, Yurke et al. 1983; Statt et al. 1985), is found to be

$$\gamma = \frac{K^s_{aa}}{K^s_{ab}} = \frac{1}{2}\frac{\Gamma_{saa}}{\Gamma_{sab}} = \frac{1}{2}\frac{|\langle 0000|aa\rangle|^2}{|\langle 001-1|ab\rangle|^2} R^{aa}_{ab} = \eta^2 R^{aa}_{ab} \simeq R^{aa}_{ab}, \qquad (6.29)$$

where R^{aa}_{ab} is the ratio of the orbital matrix elements which appear in $\Gamma_{sh_1h_2}$ and $\eta \equiv (1-\varepsilon^2)^{1/2}$. As discussed in section 5, $\gamma \simeq 2$.

An overall view of the predictive power of the second-order recombination model for the limit of rapid spin relaxation is shown in fig. 5.9a of the experimental section. The solid lines represent second-order recombination on a ^{4}He surface, for magnetic fields ranging from 0 to 10 T. To fix the absolute value of the left-hand scale, the zero-field curve is fit to the UBC data (open circles; adsorption energy $\varepsilon_a = 1.15$ K), taking quite arbitrarily a classical $T^{1/2}$ temperature dependence for the orbital parts of eqs. (6.15) and (6.20). We return to the latter approximation shortly. The other curves are obtained scaling with f_I, eq. (6.16), assuming an equilibrium distribution over the four hyperfine levels. For the $B = 10$ T curve one notes an exponential decrease in recombination rate with increasing temperature. For temperatures above approximately 0.9 K the temperature is sufficiently high to populate the c- and d-levels and the rate increases sharply to join the $B = 0$ curve, indicating that all hyperfine levels are equally populated. All curvature in the $B = 0$ curve is a result of the temperature dependence of λ_{th}. Note that for $B = 2$ T the rate is essentially constant between 300 mK and 1 K.

The agreement with experiment is remarkable and turns out to be rather insensitive to the precise value of ε_a. This is the origin of the 25% spread in experimental values for ε_a (see section 5). Implicit to the present use of the second-order recombination model to extract ε_a is the use of the $T^{1/2}$ temperature dependence of the orbital parts of eqs. (6.15) and (6.20). Since no detailed theory is available for Van der Waals recombination on the surface it is hard to assess the error introduced by this approximation. An indication for non-$T^{1/2}$ behavior is the observed temperature dependence of γ (see section 5).

The dashed lines in fig. 5.9a represent second-order volume recombination enabled by the presence of ^{4}He vapor. The various lines are obtained by scaling the UBC results (open circles) using eq. (6.16) and ^{4}He vapor pressure data. The zero-field measurements represent the only data for which a quantitative comparison with theory is available. The calculated rate constant $K^{th}_{total}(B=0) = 1.8 \times 10^{-33}$ cm^6 s^{-1} (GTB 1981) is in remark-

ably good agreement with the experimental value $K_{\text{total}}^{\text{exp}}(B=0) = 2.8 \times 10^{-33}\,\text{cm}^6\,\text{s}^{-1}$ (Hardy et al. 1981). More than 80% of the total rate was calculated to be contributed by the $H_2(14,3)$ (ortho) final state. The theory predicts the rate to drop to $K_{\text{total}}^{\text{th}}(B=0) = 3.0 \times 10^{-34}\,\text{cm}^6\,\text{s}^{-1}$ at $T = 0.1\,\text{K}$ due to the sharp temperature dependence of the dominant channel. No experimental temperature dependence is available for comparison.

6.1.3. Third-order recombination

6.1.3.1. General

In the previous sections we analyzed a three-body recombination mechanism where the transition is enabled by the Van der Waals interaction between the recombining pair and a helium atom or surface atoms. Now we replace the helium third-body by a hydrogen atom to obtain a third-order recombination process. We first generalize the formalism of section 6.1.2 to handle three identical particles. Then, in section 6.1.3.1, we discuss how direct and exchange forces between the atoms lead to recombination. The dipolar interaction between particles is still neglected so that the selection rules of table 6.3 still hold. We shall emphasize the similarities and differences between Van der Waals recombination and the exchange recombination process as distinguished by KVS (1981) in an unusually complete exploratory study of the decay kinetics of H↓. Later, in section 6.1.4, we also include the dipolar interaction and derive new selection rules. The inverse problem, dissociation in $H-H_2$ collisions, also requires an understanding of the dynamics of three hydrogen atoms. An early study of this problem within the Faddeev formalism was made by Micha (1972).

We start again with eq. (6.3) for the total rate of recombination events. The initial states now represent three hydrogen atoms, two of which are in hyperfine states h_1 and h_2 and move with relative momentum $\boldsymbol{p}$, while the third atom is in hyperfine state h_3 and moves with momentum $\boldsymbol{q}$ with respect to the 2BCM of the pair; the final states describe H-atoms in hyperfine state h_3', moving with momentum $\boldsymbol{q}'$ relative to an H_2 molecule:

$$|\mathrm{i}\rangle = |h_1 h_2 h_3;\, \boldsymbol{p},\, \boldsymbol{q}\rangle\,, \tag{6.30a}$$

$$|\mathrm{f}\rangle = |SM_S IM_I, h_3';\, v,\, L,\, M_L,\, \boldsymbol{q}'\rangle = |00 IM_I, h_3;\, v,\, L,\, M_L,\, \boldsymbol{q}'\rangle\,. \tag{6.30b}$$

The probability P_i is again normalized to yield the total number of triples (this time H-triples) $\binom{N_H}{3} \simeq \frac{1}{6} N_H^3$ in the sample:

$$\sum_i P_i = \sum_{|h_1h_2h_3;\, p,\, q\rangle} P_{|h_1h_2h_3;p,q\rangle} \tag{6.31a}$$

$$= \sum_{|h_1h_2h_3;p,q)} P_{|h_1h_2h_3;p,q)} \tag{6.31b}$$

$$= \tfrac{1}{6} N_H^3 \sum_{h_1h_2h_3} \hat{h}_1\hat{h}_2\hat{h}_3 \sum_p P_\mu(p) \sum_q P_\nu(q)$$

$$= \tfrac{1}{6} N_H^3 ,$$

with

$$\sum_{h_1h_2h_3} \hat{h}_1\hat{h}_2\hat{h}_3 = 1 .$$

The P_m's are defined as in eq. (6.6), be it that for our present problem the reduced mass ν is half as large due to the lighter mass of the H-third body, $\nu = \frac{2}{3} m_H$.

Since the H-atoms are bosons, the wavefunction should remain invariant under any permutation of the atoms (electrons and protons simultaneously). The even permutations of the group P_3 are denoted by E, A and B and the odd by K, L and M. Permuting the particle labels we obtain:

$$E|h_1h_2h_3;\, p_3,\, q_3) = |h_1h_2h_3;\, p_3,\, q_3) ,$$

$$A|h_1h_2h_3;\, p_3,\, q_3) = |h_3h_1h_2;\, p_2,\, q_2) ,$$

$$B|h_1h_2h_3;\, p_3,\, q_3) = |h_2h_3h_1;\, p_1,\, q_1) ,$$

$$K|h_1h_2h_3;\, p_3,\, q_3) = |h_1h_3h_2;\, -p_2,\, q_2) ,$$

$$L|h_1h_2h_3;\, p_3,\, q_3) = |h_3h_2h_1;\, -p_1,\, q_1) ,$$

$$M|h_1h_2h_3;\, p_3,\, q_3) = |h_2h_1h_3;\, -p_3,\, q_3) . \tag{6.32}$$

Here $|h_a h_b h_c;\, p_c,\, q_c)$ designates that particles 1, 2, 3 are in hyperfine states h_a, h_b, h_c, respectively, and that the relative momentum of the 1–2 pair equals the relative momentum of the atoms in the h_a and h_b states, while particle 3 carries the momentum of the atom in state h_c. Transformations between the various p_α and q_α are given in the summary of the Jacobi notation (fig. 6.2b).

To evaluate the sum (6.31) we generate symmetrized states, $|\ \rangle$, by operating the norm-conserving symmetrization operator on unsymme-

trized states |):

$$|\mathrm{i}\rangle = \sqrt{\tfrac{1}{6}}[E + A + B + K + L + M]|\mathrm{i}) \tag{6.33a}$$

$$= \sqrt{\tfrac{1}{2}}[E + M] \times \sqrt{\tfrac{1}{3}}[E + A + B]|\mathrm{i}) \,. \tag{6.33b}$$

The second line is obtained from the first by factoring out the subgroup of even permutations, using the multiplication table of the group P_3 (table 6.5). Note that $[E + A + B]$ and $[E + M]$ commute. Equation (6.33b) shows that one needs only even permutations in combination with explicit symmetrization of the 1–2 pair of the unsymmetrized three-body state. The net result is that we may label one of the atoms with the index j and treat it as the helium atom in Van der Waals recombination, even if the interatomic potential depends via the exchange interaction on the spin states of the atoms. The effect of indistinguishability is accounted for by cyclically permuting the particle labels (with the operator $[E + A + B]$) and adding the amplitudes coherently.

The symmetrization procedure of eq. (6.33b) is also well suited for the final state, where one has to symmetrize the molecular state, but also should account for the fact that we do not know which two atoms constitute the molecule

$$|\mathrm{f}\rangle = \sqrt{\tfrac{1}{3}}[E + A + B]|\mathrm{f}\rangle_{psj} \,. \tag{6.34}$$

The subscript ps implies that the three-body state is only partially symmetrized, the subscript j refers to the label of the third body (the spectator index; we shall use the convention $j = 3$) which is treated as distinguishable. Equation (6.34) points the way to evaluating the sum over all final states in eq. (6.3) without running in double-counting errors: to generate all (symmetrized) final states just once we should sum over all

Table 6.5
Multiplication table for the group 32.

	E	A	B	K	L	M	(applied first)
E	E	A	B	K	L	M	
A	A	B	E	M	K	L	
B	B	E	A	L	M	K	
K	K	L	M	E	A	B	
L	L	M	K	B	E	A	
M	M	K	L	A	B	E	
(applied second)							

molecular states (which are symmetrized pair states) and over all relative momenta between the molecule and the third atom. Note that this is in fact one third of all classically distinguishable final states (there are three ways to break up three bodies into a pair and a third body).

Using the group properties and the symmetry of T it is straightforward to show that the transition matrix may be written as

$$\langle \mathrm{f}|T|\mathrm{i}\rangle = \sqrt{3}_{\mathrm{ps3}}\langle \mathrm{f}|T|\mathrm{i}\rangle \,. \tag{6.35}$$

We are now in a position to evaluate eq. (6.3) by making the continuum transition and obtain the equivalent of eq. (6.8) for three-body H recombination

$$\Gamma/V = \tfrac{1}{6} n^3 \sum_{\mathrm{h}_1\mathrm{h}_2\mathrm{h}_3} \hat{h}_1\hat{h}_2\hat{h}_3 \Gamma_{\mathrm{h}_1\mathrm{h}_2\mathrm{h}_3} \,, \tag{6.36a}$$

with

$$\Gamma_{\mathrm{h}_1\mathrm{h}_2\mathrm{h}_3} \equiv \sum_{\mathrm{h}_3'} \sum_{I,M_I,v,L,M_L} \int \mathrm{d}\boldsymbol{p} \int \mathrm{d}\boldsymbol{q}\, P_\mu(\boldsymbol{p}) P_\nu(\boldsymbol{q}) \times \left(\frac{\nu}{2\pi\hbar^2}\right)^2 \int \mathrm{d}\hat{\boldsymbol{q}}_{\mathrm{h}_3'} \frac{\hbar}{\nu}\, q_{\mathrm{h}_3'3}|_{\mathrm{ps3}} \langle \mathrm{f}|T|\mathrm{i}\rangle|^2 \,. \tag{6.36b}$$

Comparing with eq. (6.8), one notes that conservation of energy here leads to more than one allowed value (one for each allowed h_3') for the relative energy $E_{\mathrm{h}_3'}$ (and momentum $q_{\mathrm{h}_3'}$) of the third atom with respect to the molecule in the final state:

$$\hbar^2 q_{\mathrm{h}_3'}^2/(2\nu) = E_{\mathrm{i}} - (E_{IM_I\nu L} + \varepsilon_{\mathrm{h}_3'}) \equiv E_{\mathrm{h}_3'} \,. \tag{6.37}$$

6.1.3.2. Exchange recombination

As mentioned at the beginning of the previous section we persist in neglecting the dipolar interaction, only accounting for direct and exchange interactions between the three atoms. The T-operator for exchange recombination is given by eq. (6.10a), where $H = H_3 + V^3$ and $H_3 = K + H_{\mathrm{Z}} + H_{\mathrm{hf}} + V_3$ [$V_i \equiv V_{\mathrm{D}}^{j-k} + V_{\mathrm{exch}}^{j-k}$; i is the spectator index; $(i, j, k) = (1, 2, 3)$ or even permutation of $(1, 2, 3)$]. The perturbation V^3 enables the transition and describes the interaction between the two H-atoms that recombine and the third atom. Neglecting pure three-body forces,

$$V^3 = V_1 + V_2 \,. \tag{6.38}$$

This is a questionable approximation for small separations of three H-atoms but only dispensable at the expense of a considerable increase of labor. The transition matrix becomes

$$T \equiv T_E + T_A + T_B = \sqrt{3} \lim_{\eta \downarrow 0} i\eta_{\,ps3} \langle f|(V_1 + V_2) G_+ |i\rangle \tag{6.39}$$

Before we discuss the effect of the G_+ operator, we write out the initial state in more detail

$$\sqrt{3}|i\rangle = \sqrt{\tfrac{1}{2}}[E + M] \times [E + A + B]|h_1 h_2 h_3;\, \boldsymbol{p}_3, \boldsymbol{q}_3) \tag{6.40a}$$

$$= \sqrt{\tfrac{1}{2}}[E + M]\{|h_1 h_2 h_3;\, \boldsymbol{p}_3, \boldsymbol{q}_3) + |h_3 h_1 h_2;\, \boldsymbol{p}_2, \boldsymbol{q}_2) + |h_2 h_3 h_1;\, \boldsymbol{p}_1, \boldsymbol{q}_1)\} . \tag{6.40b}$$

First consider the first term of eq. (6.40b). Our aim is to rewrite this term in a form that enables us to evaluate T_E in eq. (6.39). The G_+ operator distorts the initial-state wavefunction so as to account for the interaction between the atoms. As the interactions depend on the relative electronic spin states, we first decompose the spin state of the 1–2 pair in terms of the $|SM_S IM_I\rangle$ representation (using table 6.4a). Then we couple the hyperfine state of the third atom to obtain the total spin representation of the three-body system, $|SM_S S_3 IM_I I_3\rangle$. Here S_3 and I_3 represent the total electron and nuclear spin of the 1–2 pair. These quantum numbers have to be added because the total spin depends on the sequence by which the spins are coupled. The various states $|SM_S S_i IM_I I_i\rangle$, $i \in (1, 2, 3)$, are interrelated by Wigner $6-j$ symbols. With the above decomposition scheme, the first term of eq. (6.40b) is written as

$$\sum_{S_3 I_3} \sum_{SM_S IM_I} |SM_S S_3 IM_I I_3;\, \boldsymbol{p}_3, \boldsymbol{q}_3) \langle \tfrac{1}{2} M_S S_3 IM_I I_3 | h_1 h_2 h_3) . \tag{6.41a}$$

Similarly, we also rewrite the final state $|f\rangle_{ps3}$,

$$\sum_{M_S IM_I} |\tfrac{1}{2} M_S 0 IM_I I_3;\, v, L, M_L, \boldsymbol{q}_3'\rangle_{ps3} \langle SM_S 0 IM_I I_3 | 00 I_3 M_{I_3}, h_3'\rangle_{ps3} . \tag{6.41b}$$

For convenience we have summarized in table 6.6 the probability amplitudes $\langle \frac{1}{2} M_S S_3 IM_I I_3 | h_1 h_2 h_3)$ for projection of the initial spin state $|h_1 h_2 h_3)$ on the $S = \frac{1}{2}$ part of the total spin representation. Similarly the projection amplitudes for the final spin states $|00 I_3 M_{I_3}, h_3'\rangle_{ps3}$ are given in table 6.7.

Partially symmetrizing eq. (6.41a) using $\sqrt{\frac{1}{2}}[E + M]$, yields for the

Table 6.6

Decomposition of the hydrogen hyperfine three-body states $|h_1h_2h_3)$ with respect to the total spin representation $|SM_SS_3IM_II_3\rangle$. The states that contribute for $T = 0$ K are indicated with an asterisk. The symbols are defined as $\alpha = \sqrt{1/2}$, $\beta = \sqrt{1/3}$, $\gamma = \sqrt{2/3}$, $\varepsilon = \sin\theta$ and $\eta = \cos\theta$; θ is defined in section 2.1. The $\pm$ signs refer to the upper or lower three-body state in the upper row. The decomposition is described in the text following eq. (6.41).

						$h_1h_2h_3$					
						cac		cbd	dcb	bdc	
S	M_S	S_3	I	M_I	I_3	acc	cca	bcd	cdb	dbc	ccc
$M_S + M_I = 0$											
$\frac{1}{2}$	$\frac{1}{2}$	0	$\frac{1}{2}$	$\frac{1}{2}$	0*						
			$\frac{1}{2}$	$-\frac{1}{2}$	0*	$\frac{1}{2}\eta(\eta^2-\varepsilon^2)$	$-\varepsilon^2\eta$			$\frac{1}{2}\eta$	$-\varepsilon\eta^2$
			$\frac{1}{2}$	$\frac{1}{2}$	1						
			$\frac{1}{2}$	$-\frac{1}{2}$	1	$\mp\frac{1}{2}\eta\beta$		$\pm\alpha\eta\gamma$		$\mp\frac{1}{2}\eta\beta$	
			$\frac{3}{2}$	$\frac{3}{2}$							
			$\frac{3}{2}$	$\frac{1}{2}$							
			$\frac{3}{2}$	$-\frac{1}{2}$		$\mp\frac{1}{2}\eta\gamma$		$\mp\alpha\eta\beta$		$\mp\frac{1}{2}\eta\gamma$	
			$\frac{3}{2}$	$-\frac{3}{2}$							
$\frac{1}{2}$	$-\frac{1}{2}$	0	$\frac{1}{2}$	$\frac{1}{2}$	0*	$\frac{1}{2}\varepsilon(\eta^2-\varepsilon^2)$	$\varepsilon\eta^2$			$\frac{1}{2}\varepsilon$	$-\varepsilon^2\eta$
			$\frac{1}{2}$	$-\frac{1}{2}$	0*						
			$\frac{1}{2}$	$\frac{1}{2}$	1	$\pm\frac{1}{2}\varepsilon\beta$			$\pm\alpha\varepsilon\gamma$	$\pm\frac{1}{2}\varepsilon\beta$	
			$\frac{1}{2}$	$-\frac{1}{2}$	1						
			$\frac{3}{2}$	$\frac{3}{2}$							
			$\frac{3}{2}$	$\frac{1}{2}$		$\mp\frac{1}{2}\varepsilon\gamma$			$\pm\alpha\varepsilon\beta$	$\mp\frac{1}{2}\varepsilon\gamma$	
			$\frac{3}{2}$	$-\frac{1}{2}$							
			$\frac{3}{2}$	$-\frac{3}{2}$							
$\frac{1}{2}$	$\frac{1}{2}$	1	$\frac{1}{2}$	$\frac{1}{2}$	0						
			$\frac{1}{2}$	$-\frac{1}{2}$	0	$\mp\frac{1}{2}\eta\beta$			$\pm\alpha\eta\gamma$	$\pm\frac{1}{2}\eta\beta$	
			$\frac{1}{2}$	$\frac{1}{2}$	1*						
			$\frac{1}{2}$	$-\frac{1}{2}$	1*	$\eta[\frac{1}{2}\beta^2(\eta^2-\varepsilon^2)-\varepsilon^2\gamma^2]$	$\eta(\eta^2\gamma^2-\varepsilon^2\beta^2)$	$\alpha\eta\beta\gamma$	$\alpha\eta\beta\gamma$	$-\frac{1}{2}\eta\beta^2$	$-\varepsilon\eta^2$
			$\frac{3}{2}$	$\frac{3}{2}$	*						
			$\frac{3}{2}$	$\frac{1}{2}$	*						
			$\frac{3}{2}$	$-\frac{1}{2}$	*	$\frac{1}{2}\eta\beta\gamma$	$-\eta\beta\gamma$	$-\alpha\eta\beta^2$	$\alpha\eta\gamma^2$	$-\frac{1}{2}\eta\beta\gamma$	0
			$\frac{3}{2}$	$-\frac{3}{2}$	*						
$\frac{1}{2}$	$-\frac{1}{2}$	1	$\frac{1}{2}$	$\frac{1}{2}$	0	$\pm\frac{1}{2}\varepsilon\beta$		$\pm\alpha\varepsilon\gamma$		$\mp\frac{1}{2}\varepsilon\beta$	
			$\frac{1}{2}$	$-\frac{1}{2}$	0						
			$\frac{1}{2}$	$\frac{1}{2}$	1*	$\varepsilon[\frac{1}{2}\beta^2(\eta^2-\varepsilon^2)+\eta^2\gamma^2]$	$\varepsilon(\eta^2\beta^2-\varepsilon^2\gamma^2)$	$\alpha\varepsilon\beta\gamma$	$\alpha\varepsilon\beta\gamma$	$-\frac{1}{2}\varepsilon\beta^2$	$-\varepsilon^2\eta$
			$\frac{1}{2}$	$-\frac{1}{2}$	1*						
			$\frac{3}{2}$	$\frac{3}{2}$	*						
			$\frac{3}{2}$	$\frac{1}{2}$	*	$\frac{1}{2}\varepsilon\beta\gamma$	$-\varepsilon\beta\gamma$	$-\alpha\varepsilon\gamma^2$	$\alpha\varepsilon\beta^2$	$\frac{1}{2}\varepsilon\beta\gamma$	0
			$\frac{3}{2}$	$-\frac{1}{2}$	*						
			$\frac{3}{2}$	$-\frac{3}{2}$	*						

Table 6.6 (cont'd)

						$h_1h_2h_3$		
						bad	dba	adb
S	M_S	S_3	I	M_I	I_3	abd	bda	dab
$M_S + M_I = 0$								
$\frac{1}{2}$	$\frac{1}{2}$	0	$\frac{1}{2}$	$\frac{1}{2}$	0*			
			$\frac{1}{2}$	$-\frac{1}{2}$	0*		$\frac{1}{2}\varepsilon$	
			$\frac{1}{2}$	$\frac{1}{2}$	1			
			$\frac{1}{2}$	$-\frac{1}{2}$	1	$\pm\alpha\varepsilon\gamma$	$\pm\frac{1}{2}\varepsilon\beta$	
			$\frac{3}{2}$	$\frac{3}{2}$				
			$\frac{3}{2}$	$\frac{1}{2}$				
			$\frac{3}{2}$	$-\frac{1}{2}$		$\mp\alpha\varepsilon\beta$	$\pm\frac{1}{2}\varepsilon\gamma$	
			$\frac{3}{2}$	$-\frac{3}{2}$				
$\frac{1}{2}$	$-\frac{1}{2}$	0	$\frac{1}{2}$	$\frac{1}{2}$	0*		$-\frac{1}{2}\eta$	
			$\frac{1}{2}$	$-\frac{1}{2}$	0*			
			$\frac{1}{2}$	$\frac{1}{2}$	1		$\pm\frac{1}{2}\eta\beta$	$\pm\alpha\eta\gamma$
			$\frac{1}{2}$	$-\frac{1}{2}$	1			
			$\frac{3}{2}$	$\frac{3}{2}$				
			$\frac{3}{2}$	$\frac{1}{2}$			$\mp\frac{1}{2}\eta\gamma$	$\pm\alpha\eta\beta$
			$\frac{3}{2}$	$-\frac{1}{2}$				
			$\frac{3}{2}$	$-\frac{3}{2}$				
$\frac{1}{2}$	$\frac{1}{2}$	1	$\frac{1}{2}$	$\frac{1}{2}$	0			
			$\frac{1}{2}$	$-\frac{1}{2}$	0		$\mp\frac{1}{2}\varepsilon\beta$	$\mp\alpha\varepsilon\gamma$
			$\frac{1}{2}$	$\frac{1}{2}$	1*			
			$\frac{1}{2}$	$-\frac{1}{2}$	1*	$\alpha\varepsilon\beta\gamma$	$-\frac{1}{2}\varepsilon\beta^2$	$\alpha\varepsilon\beta\gamma$
			$\frac{3}{2}$	$\frac{3}{2}$	*			
			$\frac{3}{2}$	$\frac{1}{2}$	*			
			$\frac{3}{2}$	$-\frac{1}{2}$	*	$-\alpha\varepsilon\beta^2$	$-\frac{1}{2}\varepsilon\beta\gamma$	$\alpha\varepsilon\gamma^2$
			$\frac{3}{2}$	$-\frac{3}{2}$	*			
$\frac{1}{2}$	$-\frac{1}{2}$	1	$\frac{1}{2}$	$\frac{1}{2}$	0	$\mp\alpha\eta\gamma$	$\mp\frac{1}{2}\eta\beta$	
			$\frac{1}{2}$	$-\frac{1}{2}$	0			
			$\frac{1}{2}$	$\frac{1}{2}$	1*	$-\alpha\eta\beta\gamma$	$\frac{1}{2}\eta\beta^2$	$-\alpha\eta\beta\gamma$
			$\frac{1}{2}$	$-\frac{1}{2}$	1*			
			$\frac{3}{2}$	$\frac{3}{2}$	*			
			$\frac{3}{2}$	$\frac{1}{2}$	*	$\alpha\eta\gamma^2$	$-\frac{1}{2}\eta\beta\gamma$	$-\alpha\eta\beta^2$
			$\frac{3}{2}$	$-\frac{1}{2}$	*			
			$\frac{3}{2}$	$-\frac{3}{2}$	*			

Table 6.6 (cont'd)

						$h_1h_2h_3$		
							caa	
S	M_S	S_3	I	M_I	I_3	aac	aca	aaa
$M_S + M_I = 0$								
$\frac{1}{2}$	$\frac{1}{2}$	0	$\frac{1}{2}$	$\frac{1}{2}$	0*			
			$\frac{1}{2}$	$-\frac{1}{2}$	0*	$\varepsilon\eta^2$	$\frac{1}{2}\varepsilon(\eta^2-\varepsilon^2)$	$\varepsilon^2\eta$
			$\frac{1}{2}$	$\frac{1}{2}$	1			
			$\frac{1}{2}$	$-\frac{1}{2}$	1		$\mp\frac{1}{2}\varepsilon\beta$	
			$\frac{3}{2}$	$\frac{3}{2}$				
			$\frac{3}{2}$	$\frac{1}{2}$				
			$\frac{3}{2}$	$-\frac{1}{2}$			$\mp\frac{1}{2}\varepsilon\gamma$	
			$\frac{3}{2}$	$-\frac{3}{2}$				
$\frac{1}{2}$	$-\frac{1}{2}$	0	$\frac{1}{2}$	$\frac{1}{2}$	0*	$\varepsilon^2\eta$	$-\frac{1}{2}\eta(\eta^2-\varepsilon^2)$	$-\varepsilon\eta^2$
			$\frac{1}{2}$	$-\frac{1}{2}$	0*			
			$\frac{1}{2}$	$\frac{1}{2}$	1		$\mp\frac{1}{2}\eta\beta$	
			$\frac{1}{2}$	$-\frac{1}{2}$	1			
			$\frac{3}{2}$	$\frac{3}{2}$				
			$\frac{3}{2}$	$\frac{1}{2}$			$\pm\frac{1}{2}\eta\gamma$	
			$\frac{3}{2}$	$-\frac{1}{2}$				
			$\frac{3}{2}$	$-\frac{3}{2}$				
$\frac{1}{2}$	$\frac{1}{2}$	1	$\frac{1}{2}$	$\frac{1}{2}$	0			
			$\frac{1}{2}$	$-\frac{1}{2}$	0		$\mp\frac{1}{2}\varepsilon\beta$	
			$\frac{1}{2}$	$\frac{1}{2}$	1*			
			$\frac{1}{2}$	$-\frac{1}{2}$	1*	$\varepsilon(\eta^2\beta^2-\varepsilon^2\gamma^2)$	$\varepsilon[\eta^2\gamma^2+\frac{1}{2}\beta^2(\eta^2-\varepsilon^2)]$	$\varepsilon^2\eta$
			$\frac{3}{2}$	$\frac{3}{2}$	*			
			$\frac{3}{2}$	$\frac{1}{2}$	*			
			$\frac{3}{2}$	$-\frac{1}{2}$	*	$\varepsilon\beta\gamma$	$-\frac{1}{2}\varepsilon\beta\gamma$	
			$\frac{3}{2}$	$-\frac{3}{2}$	*			
$\frac{1}{2}$	$-\frac{1}{2}$	1	$\frac{1}{2}$	$\frac{1}{2}$	0		$\mp\frac{1}{2}\eta\beta$	
			$\frac{1}{2}$	$-\frac{1}{2}$	0			
			$\frac{1}{2}$	$\frac{1}{2}$	1*	$\eta[\varepsilon^2\beta^2-\eta^2\gamma^2]$	$\eta[\varepsilon^2\gamma^2-\frac{1}{2}\beta^2(\eta^2-\varepsilon^2)]$	$-\varepsilon\eta^2$
			$\frac{1}{2}$	$-\frac{1}{2}$	1*			
			$\frac{3}{2}$	$\frac{3}{2}$	*			
			$\frac{3}{2}$	$\frac{1}{2}$	*	$-\eta\beta\gamma$	$\frac{1}{2}\eta\beta\gamma$	
			$\frac{3}{2}$	$-\frac{1}{2}$	*			
			$\frac{3}{2}$	$-\frac{3}{2}$	*			

Table 6.6 (cont'd)

						$h_1h_2h_3$				
S	M_S	S_3	I	M_I	I_3	aad	daa ada	cad acd	dca cda	adc dac
$M_S + M_I = 1$										
$\frac{1}{2}$	$\frac{1}{2}$	0	$\frac{1}{2}$	$\frac{1}{2}$	0*	$\varepsilon\eta$		$\frac{1}{2}(\eta^2 - \varepsilon^2)$		
			$\frac{1}{2}$	$-\frac{1}{2}$	0*					
			$\frac{1}{2}$	$\frac{1}{2}$	1		$\mp\alpha\varepsilon\eta\gamma$	$\pm\frac{1}{2}\beta$	$\pm\alpha\varepsilon^2\gamma$	$\pm\alpha\eta^2\gamma$
			$\frac{1}{2}$	$-\frac{1}{2}$	1					
			$\frac{3}{2}$	$\frac{3}{2}$						
			$\frac{3}{2}$	$\frac{1}{2}$			$\mp\alpha\varepsilon\eta\beta$	$\mp\frac{1}{2}\gamma$	$\pm\alpha\varepsilon^2\beta$	$\pm\alpha\eta^2\beta$
			$\frac{3}{2}$	$-\frac{1}{2}$						
			$\frac{3}{2}$	$-\frac{3}{2}$						
$\frac{1}{2}$	$-\frac{1}{2}$	0	$\frac{1}{2}$	$\frac{1}{2}$	0*					
			$\frac{1}{2}$	$-\frac{1}{2}$	0*					
			$\frac{1}{2}$	$\frac{1}{2}$	1					
			$\frac{1}{2}$	$-\frac{1}{2}$	1					
			$\frac{3}{2}$	$\frac{3}{2}$			$\pm\alpha\eta^2$		$\mp\alpha\varepsilon\eta$	$\pm\alpha\varepsilon\eta$
			$\frac{3}{2}$	$\frac{1}{2}$						
			$\frac{3}{2}$	$-\frac{1}{2}$						
			$\frac{3}{2}$	$-\frac{3}{2}$						
$\frac{1}{2}$	$\frac{1}{2}$	1	$\frac{1}{2}$	$\frac{1}{2}$	0		$\mp\alpha\varepsilon\eta\gamma$	$\mp\frac{1}{2}\beta$	$\mp\alpha\eta^2\gamma$	$\mp\alpha\varepsilon^2\gamma$
			$\frac{1}{2}$	$-\frac{1}{2}$	0					
			$\frac{1}{2}$	$\frac{1}{2}$	1*	$-\varepsilon\eta\beta^2$	$\varepsilon\eta\gamma^2$	$-\frac{1}{2}\beta^2(\eta^2 - \varepsilon^2)$	$\alpha\beta\gamma(\eta^2 - \varepsilon^2)$	$\alpha\beta\gamma(\eta^2 - \varepsilon^2)$
			$\frac{1}{2}$	$-\frac{1}{2}$	1*					
			$\frac{3}{2}$	$\frac{3}{2}$	*					
			$\frac{3}{2}$	$\frac{1}{2}$	*	$\varepsilon\eta\beta\gamma$	$-\alpha\varepsilon\eta\beta^2$	$\frac{1}{2}\beta\gamma(\eta^2 - \varepsilon^2)$	$-\alpha(\eta^2\gamma^2 + \varepsilon^2\beta^2)$	$\alpha(\eta^2\beta^2 + \varepsilon^2\gamma^2)$
			$\frac{3}{2}$	$-\frac{1}{2}$	*					
			$\frac{3}{2}$	$-\frac{3}{2}$	*					
$\frac{1}{2}$	$-\frac{1}{2}$	1	$\frac{1}{2}$	$\frac{1}{2}$	0					
			$\frac{1}{2}$	$-\frac{1}{2}$	0					
			$\frac{1}{2}$	$\frac{1}{2}$	1*					
			$\frac{1}{2}$	$-\frac{1}{2}$	1*					
			$\frac{3}{2}$	$\frac{3}{2}$	*	$-\eta^2\gamma$	$+\alpha\eta^2\beta$	$\varepsilon\eta\gamma$	$-\alpha\varepsilon\eta\beta$	$-\alpha\varepsilon\eta\beta$
			$\frac{3}{2}$	$\frac{1}{2}$	*					
			$\frac{3}{2}$	$-\frac{1}{2}$	*					
			$\frac{3}{2}$	$-\frac{3}{2}$	*					

Table 6.6 (cont'd)

						$h_1h_2h_3$			
						dbd			dcc
S	M_S	S_3	I	M_I	I_3	bdd	ddb	ccd	cdc
$M_S + M_I = 1$									
$\frac{1}{2}$	$\frac{1}{2}$	0	$\frac{1}{2}$	$\frac{1}{2}$	0*	$\frac{1}{2}$		$-\varepsilon\eta$	
			$\frac{1}{2}$	$-\frac{1}{2}$	0*				
			$\frac{1}{2}$	$\frac{1}{2}$	1	$\mp\frac{1}{2}\beta$			$\pm\alpha\varepsilon\eta\gamma$
			$\frac{1}{2}$	$-\frac{1}{2}$	1				
			$\frac{3}{2}$	$\frac{3}{2}$					
			$\frac{3}{2}$	$\frac{1}{2}$		$\pm\frac{1}{2}\gamma$			$\pm\alpha\varepsilon\eta\beta$
			$\frac{3}{2}$	$-\frac{1}{2}$					
			$\frac{3}{2}$	$-\frac{3}{2}$					
$\frac{1}{2}$	$-\frac{1}{2}$	0	$\frac{1}{2}$	$\frac{1}{2}$	0*				
			$\frac{1}{2}$	$-\frac{1}{2}$	0*				
			$\frac{1}{2}$	$\frac{1}{2}$	1				
			$\frac{1}{2}$	$-\frac{1}{2}$	1				
			$\frac{3}{2}$	$\frac{3}{2}$					$\pm\alpha\varepsilon^2$
			$\frac{3}{2}$	$\frac{1}{2}$					
			$\frac{3}{2}$	$-\frac{1}{2}$					
			$\frac{3}{2}$	$-\frac{3}{2}$					
$\frac{1}{2}$	$\frac{1}{2}$	1	$\frac{1}{2}$	$\frac{1}{2}$	0	$\mp\frac{1}{2}\beta$			$\pm\alpha\varepsilon\eta\gamma$
			$\frac{1}{2}$	$-\frac{1}{2}$	0				
			$\frac{1}{2}$	$\frac{1}{2}$	1*	$\frac{1}{2}\beta^2$	γ^2	$\varepsilon\eta\beta^2$	$-\varepsilon\eta\gamma^2$
			$\frac{1}{2}$	$-\frac{1}{2}$	1*				
			$\frac{3}{2}$	$\frac{3}{2}$	*				
			$\frac{3}{2}$	$\frac{1}{2}$	*	$-\frac{1}{2}\beta\gamma$	$\beta\gamma$	$-\varepsilon\eta\beta\gamma$	$\alpha\varepsilon\eta\beta^2$
			$\frac{3}{2}$	$-\frac{1}{2}$	*				
			$\frac{3}{2}$	$-\frac{3}{2}$	*				
$\frac{1}{2}$	$-\frac{1}{2}$	1	$\frac{1}{2}$	$\frac{1}{2}$	0				
			$\frac{1}{2}$	$-\frac{1}{2}$	0				
			$\frac{1}{2}$	$\frac{1}{2}$	1*				
			$\frac{1}{2}$	$-\frac{1}{2}$	1*				
			$\frac{3}{2}$	$\frac{3}{2}$	*			$-\varepsilon^2\gamma$	$\alpha\varepsilon^2\beta$
			$\frac{3}{2}$	$\frac{1}{2}$	*				
			$\frac{3}{2}$	$-\frac{1}{2}$	*				
			$\frac{3}{2}$	$-\frac{3}{2}$	*				

Table 6.6 (cont'd)

						$h_1h_2h_3$				
							baa	bac	cba	acb
S	M_S	S_3	I	M_I	I_3	aab	aba	abc	bca	cab
$M_S + M_I = -1$										
$\frac{1}{2}$	$\frac{1}{2}$	0	$\frac{1}{2}$	$\frac{1}{2}$	0*					
			$\frac{1}{2}$	$-\frac{1}{2}$	0*					
			$\frac{1}{2}$	$\frac{1}{2}$	1					
			$\frac{1}{2}$	$-\frac{1}{2}$	1					
			$\frac{3}{2}$	$\frac{3}{2}$						
			$\frac{3}{2}$	$\frac{1}{2}$						
			$\frac{3}{2}$	$-\frac{1}{2}$						
			$\frac{3}{2}$	$-\frac{3}{2}$			$\mp\alpha\varepsilon^2$	$\mp\alpha\varepsilon\eta$	$\mp\alpha\varepsilon\eta$	
$\frac{1}{2}$	$-\frac{1}{2}$	0	$\frac{1}{2}$	$\frac{1}{2}$	0*					
			$\frac{1}{2}$	$-\frac{1}{2}$	0*	$\varepsilon\eta$				$\frac{1}{2}(\eta^2 - \varepsilon^2)$
			$\frac{1}{2}$	$\frac{1}{2}$	1					
			$\frac{1}{2}$	$-\frac{1}{2}$	1		$\mp\alpha\varepsilon\eta\gamma$	$\pm\alpha\varepsilon^2\gamma$	$\mp\alpha\eta^2\gamma$	$\pm\frac{1}{2}\beta$
			$\frac{3}{2}$	$\frac{3}{2}$						
			$\frac{3}{2}$	$\frac{1}{2}$						
			$\frac{3}{2}$	$-\frac{1}{2}$			$\pm\alpha\varepsilon\eta\beta$	$\mp\alpha\varepsilon^2\beta$	$\pm\alpha\eta^2\beta$	$\pm\frac{1}{2}\gamma$
			$\frac{3}{2}$	$-\frac{3}{2}$						
$\frac{1}{2}$	$\frac{1}{2}$	1	$\frac{1}{2}$	$\frac{1}{2}$	0					
			$\frac{1}{2}$	$-\frac{1}{2}$	0*					
			$\frac{1}{2}$	$\frac{1}{2}$	1*					
			$\frac{1}{2}$	$-\frac{1}{2}$	1*					
			$\frac{3}{2}$	$\frac{3}{2}$	*					
			$\frac{3}{2}$	$\frac{1}{2}$	*					
			$\frac{3}{2}$	$-\frac{1}{2}$	*					
			$\frac{3}{2}$	$-\frac{3}{2}$	*	$\varepsilon^2\gamma$	$-\alpha\varepsilon^2\beta$	$-\alpha\varepsilon\eta\beta$	$-\alpha\varepsilon\eta\beta$	$\varepsilon\eta\gamma$
$\frac{1}{2}$	$-\frac{1}{2}$	1	$\frac{1}{2}$	$\frac{1}{2}$	0					
			$\frac{1}{2}$	$-\frac{1}{2}$	0		$\mp\alpha\varepsilon\eta\gamma$	$\mp\alpha\eta^2\gamma$	$\pm\alpha\varepsilon^2\gamma$	$\mp\frac{1}{2}\beta$
			$\frac{1}{2}$	$\frac{1}{2}$	1*					
			$\frac{1}{2}$	$-\frac{1}{2}$	1*	$-\varepsilon\eta\beta^2$	$\varepsilon\eta\gamma^2$	$\alpha\beta\gamma(\eta^2 - \varepsilon^2)$	$\alpha\beta\gamma(\eta^2 - \varepsilon^2)$	$-\frac{1}{2}\beta^2(\eta^2 - \varepsilon^2)$
			$\frac{3}{2}$	$\frac{3}{2}$	*					
			$\frac{3}{2}$	$\frac{1}{2}$	*					
			$\frac{3}{2}$	$-\frac{1}{2}$	*	$-\varepsilon\eta\beta\gamma$	$\alpha\varepsilon\eta\beta^2$	$\alpha(\eta^2\gamma^2 + \varepsilon^2\beta^2)$	$-\alpha(\eta^2\beta^2 + \varepsilon^2\gamma^2)$	$-\frac{1}{2}\beta\gamma(\eta^2 - \varepsilon^2)$
			$\frac{3}{2}$	$-\frac{3}{2}$	*					

Table 6.6 (cont'd)

						$h_1h_2h_3$			
S	M_S	S_3	I	M_I	I_3	bbd	dbb bdb	cbc bcc	ccb
$M_S + M_I = -1$									
$\frac{1}{2}$	$\frac{1}{2}$	0	$\frac{1}{2}$	$\frac{1}{2}$	0*				
			$\frac{1}{2}$	$-\frac{1}{2}$	0*				
			$\frac{1}{2}$	$\frac{1}{2}$	1				
			$\frac{1}{2}$	$-\frac{1}{2}$	1				
			$\frac{3}{2}$	$\frac{3}{2}$					
			$\frac{3}{2}$	$\frac{1}{2}$					
			$\frac{3}{2}$	$-\frac{1}{2}$					
			$\frac{3}{2}$	$-\frac{3}{2}$				$\mp\alpha\eta^2$	
$\frac{1}{2}$	$-\frac{1}{2}$	0	$\frac{1}{2}$	$\frac{1}{2}$	0*				
			$\frac{1}{2}$	$-\frac{1}{2}$	0*		$\frac{1}{2}$		$-\varepsilon\eta$
			$\frac{1}{2}$	$\frac{1}{2}$	1				
			$\frac{1}{2}$	$-\frac{1}{2}$	1		$\pm\frac{1}{2}\beta$	$\pm\alpha\varepsilon\eta\gamma$	
			$\frac{3}{2}$	$\frac{3}{2}$					
			$\frac{3}{2}$	$\frac{1}{2}$					
			$\frac{3}{2}$	$-\frac{1}{2}$			$\pm\frac{1}{2}\gamma$	$\mp\alpha\varepsilon\eta\beta$	
			$\frac{3}{2}$	$-\frac{3}{2}$					
$\frac{1}{2}$	$\frac{1}{2}$	1	$\frac{1}{2}$	$\frac{1}{2}$	0				
			$\frac{1}{2}$	$-\frac{1}{2}$	0				
			$\frac{1}{2}$	$\frac{1}{2}$	1*				
			$\frac{1}{2}$	$-\frac{1}{2}$	1*				
			$\frac{3}{2}$	$\frac{3}{2}$	*				
			$\frac{3}{2}$	$\frac{1}{2}$	*				
			$\frac{3}{2}$	$-\frac{1}{2}$	*				
			$\frac{3}{2}$	$-\frac{3}{2}$	*			$-\alpha\eta^2\beta$	$\eta^2\gamma$
$\frac{1}{2}$	$-\frac{1}{2}$	1	$\frac{1}{2}$	$\frac{1}{2}$	0				
			$\frac{1}{2}$	$-\frac{1}{2}$	0		$\pm\frac{1}{2}\beta$	$\pm\alpha\varepsilon\eta\gamma$	
			$\frac{1}{2}$	$\frac{1}{2}$	1*				
			$\frac{1}{2}$	$-\frac{1}{2}$	1*	γ^2	$\frac{1}{2}\beta^2$	$-\varepsilon\eta\gamma^2$	$\varepsilon\eta\beta^2$
			$\frac{3}{2}$	$\frac{3}{2}$	*				
			$\frac{3}{2}$	$\frac{1}{2}$	*				
			$\frac{3}{2}$	$-\frac{1}{2}$	*	$-\beta\gamma$	$\frac{1}{2}\beta\gamma$	$-\alpha\varepsilon\eta\beta^2$	$\varepsilon\eta\beta\gamma$
			$\frac{3}{2}$	$-\frac{3}{2}$	*				

Table 6.6 (cont'd)

						$h_1h_2h_3$			
						dad		dcd	
S	M_S	S_3	I	M_I	I_3	add	dda	cdd	ddc
$M_S + M_I = 2$									
$\frac{1}{2}$	$\frac{1}{2}$	0	$\frac{1}{2}$	$\frac{1}{2}$	0*				
			$\frac{1}{2}$	$-\frac{1}{2}$	0*				
			$\frac{1}{2}$	$\frac{1}{2}$	1				
			$\frac{1}{2}$	$-\frac{1}{2}$	1				
			$\frac{3}{2}$	$\frac{3}{2}$		$\mp\alpha\eta$		$\pm\alpha\varepsilon$	
			$\frac{3}{2}$	$\frac{1}{2}$					
			$\frac{3}{2}$	$-\frac{1}{2}$					
			$\frac{3}{2}$	$-\frac{3}{2}$					
$\frac{1}{2}$	$-\frac{1}{2}$	0	$\frac{1}{2}$	$\frac{1}{2}$	0*				
			$\frac{1}{2}$	$-\frac{1}{2}$	0*				
			$\frac{1}{2}$	$\frac{1}{2}$	1				
			$\frac{1}{2}$	$-\frac{1}{2}$	1				
			$\frac{3}{2}$	$\frac{3}{2}$					
			$\frac{3}{2}$	$\frac{1}{2}$					
			$\frac{3}{2}$	$-\frac{1}{2}$					
			$\frac{3}{2}$	$-\frac{3}{2}$					
$\frac{1}{2}$	$\frac{1}{2}$	1	$\frac{1}{2}$	$\frac{1}{2}$	0				
			$\frac{1}{2}$	$-\frac{1}{2}$	0				
			$\frac{1}{2}$	$\frac{1}{2}$	1*				
			$\frac{1}{2}$	$-\frac{1}{2}$	1*				
			$\frac{3}{2}$	$\frac{3}{2}$	*	$\alpha\eta\beta$	$-\eta\gamma$	$-\alpha\varepsilon\beta$	$\varepsilon\gamma$
			$\frac{3}{2}$	$\frac{1}{2}$	*				
			$\frac{3}{2}$	$-\frac{1}{2}$	*				
			$\frac{3}{2}$	$-\frac{3}{2}$	*				
$\frac{1}{2}$	$-\frac{1}{2}$	1	$\frac{1}{2}$	$\frac{1}{2}$	0				
			$\frac{1}{2}$	$-\frac{1}{2}$	0				
			$\frac{1}{2}$	$\frac{1}{2}$	1*				
			$\frac{1}{2}$	$-\frac{1}{2}$	1*				
			$\frac{3}{2}$	$\frac{3}{2}$	*				
			$\frac{3}{2}$	$\frac{1}{2}$	*				
			$\frac{3}{2}$	$-\frac{1}{2}$	*				
			$\frac{3}{2}$	$-\frac{3}{2}$	*				

Table 6.6 (cont'd)

						$h_1h_2h_3$			
						bab			cbb
S	M_S	S_3	I	M_I	I_3	abb	bba	bbc	bcb
$M_S + M_I = -2$									
$\frac{1}{2}$	$\frac{1}{2}$	0	$\frac{1}{2}$	$\frac{1}{2}$	0*				
			$\frac{1}{2}$	$-\frac{1}{2}$	0*				
			$\frac{1}{2}$	$\frac{1}{2}$	1				
			$\frac{1}{2}$	$-\frac{1}{2}$	1				
			$\frac{3}{2}$	$\frac{3}{2}$					
			$\frac{3}{2}$	$\frac{1}{2}$					
			$\frac{3}{2}$	$-\frac{1}{2}$					
			$\frac{3}{2}$	$-\frac{3}{2}$					
$\frac{1}{2}$	$-\frac{1}{2}$	0	$\frac{1}{2}$	$\frac{1}{2}$	0*				
			$\frac{1}{2}$	$-\frac{1}{2}$	0*				
			$\frac{1}{2}$	$\frac{1}{2}$	1				
			$\frac{1}{2}$	$-\frac{1}{2}$	1				
			$\frac{3}{2}$	$\frac{3}{2}$					
			$\frac{3}{2}$	$\frac{1}{2}$					
			$\frac{3}{2}$	$-\frac{1}{2}$					
			$\frac{3}{2}$	$-\frac{3}{2}$		$\mp\alpha\varepsilon$			$\mp\alpha\eta$
$\frac{1}{2}$	$\frac{1}{2}$	1	$\frac{1}{2}$	$\frac{1}{2}$	0				
			$\frac{1}{2}$	$-\frac{1}{2}$	0				
			$\frac{1}{2}$	$\frac{1}{2}$	1*				
			$\frac{1}{2}$	$-\frac{1}{2}$	1*				
			$\frac{3}{2}$	$\frac{3}{2}$	*				
			$\frac{3}{2}$	$\frac{1}{2}$	*				
			$\frac{3}{2}$	$-\frac{1}{2}$	*				
			$\frac{3}{2}$	$-\frac{3}{2}$	*				
$\frac{1}{2}$	$-\frac{1}{2}$	1	$\frac{1}{2}$	$\frac{1}{2}$	0				
			$\frac{1}{2}$	$-\frac{1}{2}$	0				
			$\frac{1}{2}$	$\frac{1}{2}$	1*				
			$\frac{1}{2}$	$-\frac{1}{2}$	1*				
			$\frac{3}{2}$	$\frac{3}{2}$	*				
			$\frac{3}{2}$	$\frac{1}{2}$	*				
			$\frac{3}{2}$	$-\frac{1}{2}$	*				
			$\frac{3}{2}$	$-\frac{3}{2}$	*	$\alpha\varepsilon\beta$	$-\varepsilon\gamma$	$-\eta\gamma$	$\alpha\eta\beta$

Table 6.7

Spin decomposition of the final state $|S_3 M_{S_3} I_3 M_{I_3}; h_3\rangle_{ps_3}$ with respect to the total spin representation $|SM_S S_3 I M_I I_3\rangle$. The symbols are defined as $\alpha = \sqrt{\frac{1}{2}}$, $\beta = \sqrt{\frac{1}{3}}$, $\gamma = \sqrt{\frac{2}{3}}$, $\varepsilon = \sin\theta$, $\eta = \cos\theta$; θ is defined in section 2.1.

						$S_3 M_{S_3} I_3 M_{S_3}$															
S	M_S	S_3	I	M_I	I_3	0000 $h_3=a$	0011 $h_3=a$	0010 $h_3=a$	001 −1 $h_3=a$	0000 $h_3=b$	0011 $h_3=b$	0010 $h_3=b$	001 −1 $h_3=b$	0000 $h_3=c$	0011 $h_3=c$	0010 $h_3=c$	001 −1 $h_3=c$	0000 $h_3=d$	0011 $h_3=d$	0010 $h_3=d$	001 −1 $h_3=d$
$\frac{1}{2}$	$\frac{1}{2}$	0	$\frac{1}{2}$	$\frac{1}{2}$	0													1			
			$\frac{1}{2}$	$-\frac{1}{2}$	0	ε								η							
			$\frac{1}{2}$	$\frac{1}{2}$	1		$\varepsilon\gamma$								$\eta\gamma$					$-\beta$	
			$\frac{1}{2}$	$-\frac{1}{2}$	1			$\varepsilon\beta$								$\eta\beta$					$-\gamma$
			$\frac{3}{2}$	$\frac{3}{2}$	1														1		
			$\frac{3}{2}$	$\frac{1}{2}$	1		$\varepsilon\beta$								$\eta\beta$					γ	
			$\frac{3}{2}$	$-\frac{1}{2}$	1			$\varepsilon\gamma$								$\eta\gamma$					β
			$\frac{3}{2}$	$-\frac{3}{2}$	1				ε								η				
$\frac{1}{2}$	$-\frac{1}{2}$	0	$\frac{1}{2}$	$\frac{1}{2}$	0	$-\eta$								ε							
			$\frac{1}{2}$	$-\frac{1}{2}$	0					1											
			$\frac{1}{2}$	$\frac{1}{2}$	1			$\eta\beta$			γ					$-\varepsilon\beta$					
			$\frac{1}{2}$	$-\frac{1}{2}$	1				$\eta\gamma$			β					$-\varepsilon\gamma$				
			$\frac{3}{2}$	$\frac{3}{2}$	1		$-\eta$								ε						
			$\frac{3}{2}$	$\frac{1}{2}$	1			$-\eta\gamma$			β					$\varepsilon\gamma$					
			$\frac{3}{2}$	$-\frac{1}{2}$	1				$-\eta\beta$			γ					$\varepsilon\beta$				
			$\frac{3}{2}$	$\frac{3}{2}$	1								1								

orbital part

$$|(S_3 I_3);\, \boldsymbol{p}_3,\, \boldsymbol{q}_3\rangle_{\mathrm{ps3}} = \sqrt{\tfrac{1}{2}}[|\boldsymbol{p}_3,\, \boldsymbol{q}_3) + (-1)^{S_3+I_3}|-\boldsymbol{p}_3,\, \boldsymbol{q}_3)]\,. \tag{6.42}$$

Hence, for $S_3 + I_3 =$ even (odd), only even (odd) partial waves occur for the relative orbital motion of the 1–2 pair.

KVS consider the $T \to 0$ limit, where s-wave scattering is dominant. This implies that only the even $S_3 + I_3$ terms of eq. (6.41a) contribute. The corresponding coefficients are labelled with an asterisk in table 6.6. As in the case of Van der Waals recombination the time evolution of the spins due to the hyperfine interaction is neglected during the collision (sudden approximation, Wigner spin rule).

If the interaction of the 1–2 pair with particle three were purely of the Van der Waals type only the singlet terms ($S_3 = 0$) of eq. (6.41a) would lead to recombination. KVS first pointed out that the triplet terms ($S_3 = 1$) also contribute, as both the exchange and direct terms of the interaction admix the singlet character in the 1–2 relative spin state required for recombination. Following KVS, we use the term exchange recombination for the process where direct and exchange forces between three H-atoms enable recombination.

The selection rules are obtained by observing that the direct and exchange interactions cannot induce a change in the total spin or its projection, nor do they affect the nuclear spin:

$$\Delta S = \Delta I = \Delta I_3 = 0\,, \qquad \Delta M_S = \Delta M_I = \Delta M_{I_3} = 0\,. \tag{6.43}$$

With these selection rules the contribution of the first term of eq. (6.40b) to the transition matrix becomes

$$T_E \equiv \sum_i \sum_{S_3} \sum_{M_S I M_I} {}_{\mathrm{ps3}}\langle \tfrac{1}{2} M_S 0 I_3;\, v,\, L,\, M_L,\, \boldsymbol{q}_3' | V_i G_+ | \tfrac{1}{2} M_S S_3 I_3;\, \boldsymbol{p}_3,\, \boldsymbol{q}_3\rangle_{\mathrm{ps3}}$$

$$\times\, {}_{\mathrm{ps3}}\langle 00 I_3 M_{I_3},\, \mathrm{h}_3' | \tfrac{1}{2} M_S 0 I M_I I_3\rangle \langle \tfrac{1}{2} M_S S_3 I M_I I_3 | \mathrm{h}_1 \mathrm{h}_2 \mathrm{h}_3)\,, \tag{6.44}$$

where we have suppressed the I and M_I quantum numbers in the matrix element. The operators V_i, $i \in (1, 2)$, yield the singlet (V_i^{s}) or the triplet (V_i^{t}) potential depending on the total electron spin S_i of the pair i, where i is again the spectator index. The singlet and triplet fractions are determined by transforming the electron-spin part of the initial state to the i-subsystem using Wigner $6-j$ symbols. We use the convention of Messiah (1970) to find

$$V_i G_+ |\tfrac{1}{2} M_S S_3 I_3;\ \boldsymbol{p}_3,\ \boldsymbol{q}_3\rangle_{ps3} \tag{6.45a}$$

$$= V_i G_+ \sum_{S_i} |\tfrac{1}{2} M_S S_i (S_3 I_3);\ \boldsymbol{p}_3,\ \boldsymbol{q}_3\rangle_{ps3} \begin{bmatrix} \frac{1}{2} & \frac{1}{2} & S_3 \\ \frac{1}{2} & \frac{1}{2} & S_i \end{bmatrix} \times (2S_3+1)^{1/2}(2S_i+1)^{1/2}$$

$$= V_i^s G_+ |\tfrac{1}{2} M_S 0 (S_3 I_3);\ \boldsymbol{p}_3,\ \boldsymbol{q}_3\rangle_{ps3} \begin{bmatrix} \frac{1}{2} & \frac{1}{2} & S_3 \\ \frac{1}{2} & \frac{1}{2} & 0 \end{bmatrix} (2S_3+1)^{1/2}$$

$$+ V_i^t G_+ |\tfrac{1}{2} M_S 1 (S_3 I_3);\ \boldsymbol{p}_3,\ \boldsymbol{q}_3\rangle_{ps3} \begin{bmatrix} \frac{1}{2} & \frac{1}{2} & S_3 \\ \frac{1}{2} & \frac{1}{2} & 1 \end{bmatrix} (2S_3+1)^{1/2} 3^{1/2}.$$

Analogously, we decompose the final state side of eq. (6.44)

$$|\tfrac{1}{2} M_S 0 I_3;\ v,\ L,\ M_L,\ \boldsymbol{q}_3'\rangle_{ps3} = |\tfrac{1}{2} M_S 0 (0 I_3);\ v,\ L,\ M_L,\ \boldsymbol{q}_3'\rangle_{ps3} \begin{bmatrix} \frac{1}{2} & \frac{1}{2} & 0 \\ \frac{1}{2} & \frac{1}{2} & 0 \end{bmatrix}$$

$$+ |\tfrac{1}{2} M_S 1 (0 I_3);\ v,\ L,\ M_L,\ \boldsymbol{q}_3'\rangle_{ps3} \begin{bmatrix} \frac{1}{2} & \frac{1}{2} & 0 \\ \frac{1}{2} & \frac{1}{2} & 1 \end{bmatrix} 3^{1/2}. \tag{6.45b}$$

The relevant $6-j$ symbols are

$$\begin{bmatrix} s_1 & s_2 & S_3 \\ s_3 & S & S_i \end{bmatrix} = \begin{bmatrix} \frac{1}{2} & \frac{1}{2} & 0 \\ \frac{1}{2} & \frac{1}{2} & 0 \end{bmatrix} = -\frac{1}{2}, \quad \begin{bmatrix} \frac{1}{2} & \frac{1}{2} & 0 \\ \frac{1}{2} & \frac{1}{2} & 1 \end{bmatrix} = \frac{1}{2},$$

$$\begin{bmatrix} \frac{1}{2} & \frac{1}{2} & 1 \\ \frac{1}{2} & \frac{1}{2} & 0 \end{bmatrix} = \frac{1}{2}, \quad \begin{bmatrix} \frac{1}{2} & \frac{1}{2} & 1 \\ \frac{1}{2} & \frac{1}{2} & 1 \end{bmatrix} = \frac{1}{6}, \tag{6.46}$$

where the s_i refer to the electronic spins of the individual atoms. Combining eqs. (6.45a) and (6.45b) we obtain the following expression for the matrix element in eq. (6.44)

$$M \equiv {}_{ps3}\langle \tfrac{1}{2} M_S 0 I_3;\ v,\ L,\ M_L,\ \boldsymbol{q}_3' | V_i G_+ | \tfrac{1}{2} M_S S_3 I_3;\ \boldsymbol{p}_3,\ \boldsymbol{q}_3\rangle_{ps3}$$

$$= {}_{ps3}\langle (0 I_3);\ v,\ L,\ M_L,\ \boldsymbol{q}_3' | V_i^t G_+ | (S_3 I_3);\ \boldsymbol{p}_3,\ \boldsymbol{q}_3\rangle_{ps3} \times \tfrac{3}{2}(2S_3+1)^{1/2} \begin{bmatrix} \frac{1}{2} & \frac{1}{2} & S_3 \\ \frac{1}{2} & \frac{1}{2} & 1 \end{bmatrix}$$

$$- {}_{ps3}\langle (0 I_3);\ v,\ L,\ M_L,\ \boldsymbol{q}_3' | V_i^s G_+ | (S_3 I_3);\ \boldsymbol{p}_3,\ \boldsymbol{q}_3\rangle_{ps3} \times \tfrac{1}{2}(2S_3+1)^{1/2} \begin{bmatrix} \frac{1}{2} & \frac{1}{2} & S_3 \\ \frac{1}{2} & \frac{1}{2} & 0 \end{bmatrix}, \tag{6.47a}$$

where we have suppressed the S and M_S quantum numbers. For $S_3 = 0$ this becomes, in a straightforward symbolic notation,

$$M = \tfrac{3}{4}\langle V_i^{\mathrm{t}}\rangle + \tfrac{1}{4}\langle V_i^{\mathrm{s}}\rangle \equiv \langle V_i^{\mathrm{D}}\rangle \,. \tag{6.47b}$$

Similarly, for $S_3 = 1$ one obtains

$$M = \tfrac{1}{4}\sqrt{3}\langle V_i^{\mathrm{t}}\rangle - \tfrac{1}{4}\sqrt{3}\langle V_i^{\mathrm{s}}\rangle \equiv \tfrac{1}{4}\sqrt{3}\langle J_i\rangle \,. \tag{6.47c}$$

One observes that the perturbation carries the signature of the direct interaction if the recombining pair is in a relative singlet state while it has an exchange origin for $S_3 = 1$.

With the aid of eq. (6.47), eq. (6.44) may be drastically simplified to

$$\begin{aligned} T_E = &\sum_i \sum_{M_S I M_I} \langle V_i^{\mathrm{D}}\rangle \langle 00 I_3 M_{I_3}, \mathrm{h}_3' | \tfrac{1}{2} M_S 0 I M_I I_3\rangle \langle \tfrac{1}{2} M_S 0 I M_I I_3 | \mathrm{h}_1 \mathrm{h}_2 \mathrm{h}_3) \\ &+ \sum_i \sum_{M_S I M_I} \tfrac{1}{4}\sqrt{3}\langle J_i\rangle \langle 00 I_3 M_{I_3}, \mathrm{h}_3' | \tfrac{1}{2} M_S 0 I M_I I_3\rangle \\ &\qquad \times \langle \tfrac{1}{2} M_S 1 I M_I I_3 | \mathrm{h}_1 \mathrm{h}_2 \mathrm{h}_3) \end{aligned} \tag{6.48a}$$

$$\begin{aligned} = &\sum_i \langle V_i^{\mathrm{D}}\rangle \langle 00 I_3 M_{I_3} | \mathrm{h}_1 \mathrm{h}_2\rangle \delta_{\mathrm{h}_3, \mathrm{h}_3'} \\ &+ \sum_i \sum_{M_S I M_I} \tfrac{1}{4}\sqrt{3}\langle J_i\rangle \langle 00 I_3 M_{I_3}, \mathrm{h}_3' | \tfrac{1}{2} M_S 0 I M_I I_3\rangle \\ &\qquad \times \langle \tfrac{1}{2} M_S 1 I M_I I_3 | \mathrm{h}_1 \mathrm{h}_2 \mathrm{h}_3) \,. \end{aligned} \tag{6.48b}$$

The first line of eq. (6.48b) has the same signature as Van der Waals recombination: singlet character has to be present in the 1–2 relative wavefunction for recombination to proceed via the direct interaction with the third body. The second line contains the feature contributed by KVS. Atoms initially interacting via the triplet potential may pick up relative singlet character by spin-exchange with an appropriate third H atom which simultaneously can carry away the energy liberated in the recombination process. If the three terms T_E, T_A and T_B, corresponding to the three terms of eq. (6.40b) add constructively and one assumes V_i^{D} to be equally efficient for recombination as $V_i^{\mathrm{H-He}}$, H–H–H recombination via the direct channel alone will be 9× more efficient as H–H–He recombination. We shall return to this point in section 6.1.5. Moreover, $\langle V^{\mathrm{D}}\rangle \equiv \frac{3}{4}\langle V^{\mathrm{t}}\rangle + \frac{1}{4}\langle V^{\mathrm{s}}\rangle$ contains an average over the strongly attractive singlet potential which is better suited to enable the large momentum transfer

required for recombination (see the discussion concerning this point below eq. 6.9). On the other hand, in view of the smaller reduced mass ν in the H–H–H case, the density of final states will be $\sqrt{2}$ smaller. Later in this section we shall discuss examples of constructive and destructive interference (aaa- and bbc-recombination, respectively, at $T = 0$ K).

We may further simplify eq. (6.48) by limiting ourselves to $T = 0$ K where only those amplitudes contribute that are marked with an asterisk in table 6.6. We consider recombination to o-H_2 and p-H_2 separately. For recombination to para-H_2, at $T = 0$ K,

$$T_E^{\text{para}} = \sum_i \langle V_i^{\text{D}} \rangle \langle 0000 | \mathrm{h}_1 \mathrm{h}_2 \rangle \delta_{\mathrm{h}_3, \mathrm{h}_3'} , \tag{6.49a}$$

for recombination to ortho-H_2 ($T = 0$ K)

$$T_E^{\text{ortho}} = \sum_i \sum_{M_S I M_I} \tfrac{1}{4}\sqrt{3} \langle J_i \rangle \langle 001 M_{I_3}, \mathrm{h}_3' | \tfrac{1}{2} M_S 0 I M_I 1 \rangle \langle \tfrac{1}{2} M_S 1 I M_I \mathrm{h}_1 \mathrm{h}_2 \mathrm{h}_3 \rangle . \tag{6.49b}$$

Although the limitation to $T = 0$ K is convenient in view of the discussion of the KVS theory, we stress the point that the GTB results indicate that for temperatures in the experimental regime, in fact recombination to the ortho state is dominant for the Van der Waals process while it should be absent in the $T = 0$ K limit. Experimentally, recombination to ortho-H_2 reflects itself in high magnetic field as the K_{ab} contribution to second-order recombination (see section 5). This could well imply that also in the H–H–H case, recombination to ortho-H_2 via the V^{D} channel is important for the interpretation of experiments.

KVS restrict their theory to $T = 0$ K, where $|\boldsymbol{p}_1, \boldsymbol{q}_1)$, $|\boldsymbol{p}_2, \boldsymbol{q}_2)$ and $|\boldsymbol{p}_3, \boldsymbol{q}_3)$ become identical and T_E, T_A and T_B are easily summed. Furthermore, summing over all final spin states, eq. (6.36) may be brought into a form which is the analogue of the $T = 0$ K limit of eq. (6.15).
For recombination to para-H_2:

$$\Gamma/V = \tfrac{1}{6} n^3 g_0 (2L+1) \sum_{v,L} \left(\frac{\nu}{2\pi\hbar^2} \right)^2 \int \mathrm{d}\hat{\boldsymbol{q}}' \, \frac{\hbar}{\nu} \, q' | \langle V_1^{\text{D}} \rangle + \langle V_2^{\text{D}} \rangle |^2 . \tag{6.50a}$$

For recombination to ortho-H_2:

$$\Gamma/V = \tfrac{1}{6} n^3 g_1 (2L+1) \sum_{v,L} 3 \left(\frac{\nu}{2\pi\hbar^2} \right)^2 \int \mathrm{d}\hat{\boldsymbol{q}}' \, \frac{\hbar}{\nu} \, q' | \tfrac{1}{4} [\langle J_1 \rangle + \langle J_2 \rangle] |^2 , \tag{6.50b}$$

where g_0 and g_1 are defined by

$$g_0 \equiv \sum_{h_1h_2h_3} \hat{h}_1\hat{h}_2\hat{h}_3 |\langle 0000|h_1h_2\rangle + \langle 0000|h_2h_3\rangle + \langle 0000|h_3h_1\rangle|^2 , \tag{6.51a}$$

$$g_1 \equiv \sum_{h_1h_2h_3} \hat{h}_1\hat{h}_2\hat{h}_3 \sum_{M_SIM_I} |\langle \tfrac{1}{2}M_S 1 I M_I 1|E + A + B|h_1h_2h_3\rangle|^2 . \tag{6.51b}$$

Just as for the f_I in the case of Van der Waals recombination, we provide explicit expressions for g_0 and g_1. These expressions were obtained using tables 6.4 and 6.6.

$$\begin{aligned} g_0 = \tfrac{3}{4}[&(3\hat{a}^3 + 3\hat{c}^3 + \hat{a}^2\hat{b} + \hat{a}^2\hat{d} + \hat{c}^2\hat{b} + \hat{c}^2\hat{d}) \sin^2 2\theta \\ &+ 2(\hat{a}\hat{c}\hat{b} + \hat{a}\hat{c}\hat{d}) \cos^2 2\theta + \hat{a}^2\hat{c}(2\cos 2\theta + \sin^2\theta)^2 \\ &+ \hat{a}\hat{c}^2(2\cos 2\theta - \sin^2\theta)^2 + 2(\hat{a}\hat{b}\hat{d} + \hat{c}\hat{b}\hat{d} + 2\hat{b}^2\hat{d} + 2\hat{d}^2\hat{b})] , \end{aligned} \tag{6.52a}$$

$$\begin{aligned} g_1 = \tfrac{3}{4}[&(3\hat{a}^3 + 3\hat{c}^3 + \hat{a}^2\hat{b} + \hat{a}^2\hat{d} + \hat{c}^2\hat{b} + \hat{c}^2\hat{d}) \sin^2 2\theta \\ &+ 2(\hat{a}\hat{c}\hat{b} + \hat{a}\hat{c}\hat{d}) \cos^2 2\theta + 4(\hat{a}^2\hat{c} + \hat{a}\hat{c}^2)(\cos^6\theta + \sin^6\theta) \\ &+ 2(\hat{a}\hat{b}\hat{d} + \hat{c}\hat{b}\hat{d} + 2\hat{b}^2\hat{d} + 2\hat{d}^2\hat{b})] . \end{aligned} \tag{6.52b}$$

Unfortunately, the usefulness of eq. (6.52) is more restricted than that of eq. (6.15). The latter enabled the rough extraction of the temperature and field dependence of Van der Waals recombination. The former, at most can give us roughly the field and temperature dependence of the terms that do not vanish at $T = 0$ K.

So far we have not discussed the distortion of the orbital part of the initial state due to the action of G_+. As GTB, KVS choose for an approximate solution. GTB used the impulse approximation, which has the advantage that the relative motion between the recombining pair and third-body is treated fairly exact (to the level that three-body forces may be neglected) but, unfortunately, completely ignores the strong distortion of the 1–2 motion due to the singlet potential. GTB also extracted the temperature dependence from their theory. KVS properly distort the wavefunction of the recombining pair but assume the distortion of the wavefunction to be triplet-like with regard to the third-body, independent of the perturbation. It is hard to assess the reliability of this approximation, but it clearly has the advantage of reducing the numerical work. For this review we shall not enter into a more detailed description of the orbital wavefunctions.

As an example we discuss two special cases, aaa and bbc-recombination in the $T = 0$ K limit.

(i) aaa-recombination. Here T_E, T_A and T_B are identical and hence add constructively. First, we consider recombination to para-H_2. From the selection rules of table 6.3, we see that the third body remains in the a-state yielding p-H_2 + $|a\rangle$, with

$$T = 3[\langle V_1^D\rangle + \langle V_2^D\rangle]\langle 0000|aa) = 3\varepsilon\eta[\langle V_1^D\rangle + \langle V_2^D\rangle]$$

For recombination to the ortho state two channels exist, according to the selection rules:

(1) o-$H_2(M_I = 0)$ + $|a\rangle$:

$$\begin{aligned} T &= \tfrac{3}{4}\sqrt{3}[\langle J_1\rangle + \langle J_2\rangle][\langle 0010, a|\tfrac{1}{2}\ \tfrac{1}{2}\ 0\ \tfrac{1}{2}\ -\tfrac{1}{2}\ 1\rangle\langle\tfrac{1}{2}\ \tfrac{1}{2}\ 0\ \tfrac{1}{2}\ -\tfrac{1}{2}\ 1|aaa) \\ &\quad + \langle 0010, a|\tfrac{1}{2}\ -\tfrac{1}{2}\ 0\ \tfrac{1}{2}\ \tfrac{1}{2}\ 1\rangle\langle\tfrac{1}{2}\ -\tfrac{1}{2}\ 0\ \tfrac{1}{2}\ \tfrac{1}{2}\ 1|aaa)] \\ &= \tfrac{3}{4}\sqrt{3}(\varepsilon^3\eta\beta - \varepsilon\eta^3\beta)[\langle J_1\rangle + \langle J_2\rangle] \simeq -\tfrac{3}{4}\sqrt{3}\varepsilon\eta\beta[\langle J_1\rangle + \langle J_2\rangle]\,. \end{aligned}$$

(2) o-$H_2(M_I = 1)$ + $|b\rangle$:

$$\begin{aligned} T &= \tfrac{3}{4}\sqrt{3}[\langle J_1\rangle + \langle J_2\rangle]\langle 0011, b|\tfrac{1}{2}\ -\tfrac{1}{2}\ 0\ \tfrac{1}{2}\ \tfrac{1}{2}\ 1\rangle\langle\tfrac{1}{2}\ -\tfrac{1}{2}\ 1\ \tfrac{1}{2}\ \tfrac{1}{2}\ 1|aaa) \\ &= -\tfrac{3}{4}\sqrt{3}\varepsilon\eta^2\gamma[\langle J_1\rangle + \langle J_2\rangle]\,. \end{aligned}$$

Processes where the third body in the final state is a $|c\rangle$ or $|d\rangle$ state atom only contribute to higher order in ε and are hence negligible in high magnetic field:

(3) o-$H_2(M_I = 0)$ + $|c\rangle$.

$$\begin{aligned} T &= \tfrac{3}{4}\sqrt{3}[\langle J_1\rangle + \langle J_2\rangle][\langle 0010, c|\tfrac{1}{2}\ \tfrac{1}{2}\ 0\ \tfrac{1}{2}\ -\tfrac{1}{2}\ 1\rangle\langle\tfrac{1}{2}\ \tfrac{1}{2}\ 0\ \tfrac{1}{2}\ -\tfrac{1}{2}\ 1|aaa) \\ &\quad + \langle 0010, c|\tfrac{1}{2}\ -\tfrac{1}{2}\ 0\ \tfrac{1}{2}\ \tfrac{1}{2}\ 1\rangle\langle\tfrac{1}{2}\ -\tfrac{1}{2}\ 0\ \tfrac{1}{2}\ \tfrac{1}{2}\ 1|aaa)] \\ &= \tfrac{3}{4}\sqrt{3}(\varepsilon^2\eta^2\beta + \varepsilon^2\eta^2\beta)[\langle J_1\rangle + \langle J_2\rangle] = \tfrac{3}{2}\sqrt{3}\varepsilon^2\eta^2\beta[\langle J_1\rangle + \langle J_2\rangle]\,. \end{aligned}$$

(4) o-$H_2(M_I = -1)$ + $|d\rangle$.

$$\begin{aligned} T &= \tfrac{3}{4}\sqrt{3}[\langle J_1\rangle + \langle J_2\rangle]\langle 001\,-1, d|\tfrac{1}{2}\ \tfrac{1}{2}\ 0\ \tfrac{1}{2}\ -\tfrac{1}{2}\ 1\rangle\langle\tfrac{1}{2}\ \tfrac{1}{2}\ 1\ \tfrac{1}{2}\ -\tfrac{1}{2}\ 1|aaa) \\ &= -\tfrac{3}{4}\sqrt{3}\varepsilon^2\eta\gamma[\langle J_1\rangle + \langle J_2\rangle]\,. \end{aligned}$$

(ii) bbc-recombination. According to the selection rules (table 6.3) we expect, to first order in ε, only the o-$H_2(M_I = -1)$ + $|b\rangle$ final state to contribute. Tables 6.6 and 6.7 show that this is in fact the only final state

that contributes at $T = 0$ K. However, this contribution also vanishes due to destructive interference of T_E^{ortho}, T_A^{ortho} and T_B^{ortho}. We find the final state o-$H_2(M_I = -1) + |\text{b}\rangle$ with probability

$$\begin{aligned} T &= \tfrac{1}{4}\sqrt{3}[\langle J_1\rangle + \langle J_2\rangle]\langle 001\ -1, \text{b}|\tfrac{1}{2}\ -\tfrac{1}{2}\ 1\ \tfrac{3}{2}\ -\tfrac{3}{2}\ 1\rangle \\ &\quad \times [\langle \tfrac{1}{2}\ -\tfrac{1}{2}\ 0\ \tfrac{3}{2}\ -\tfrac{3}{2}\ 1|\text{bbc}) + \langle \tfrac{1}{2}\ -\tfrac{1}{2}\ 0\ \tfrac{3}{2}\ -\tfrac{3}{2}\ 1|\text{bcb}) \\ &\quad\quad + \langle \tfrac{1}{2}\ -\tfrac{1}{2}\ 0\ \tfrac{3}{2}\ -\tfrac{3}{2}\ 1|\text{cbb})] \\ &= \tfrac{1}{4}\sqrt{3}[-\eta\gamma + \alpha\eta\beta + \alpha\eta\beta] = 0\,. \end{aligned}$$

We note that analogous reasoning leads to a zero bba-recombination rate at $T = 0$ K. The relation to the rate equations is discussed in section 6.1.5.

6.1.4. Dipolar recombination

Thus far in discussing recombination we neglected the magnetic dipolar interactions between the atoms. Although this approximation is often well justified, it breaks down when the initial state lacks the singlet character. Experimentally, applying a high magnetic field, the electronic polarization may become essentially complete through preferential recombination of a-state atoms (see section 6.1.2.1) which leaves a sample of atoms in the b-state from which the singlet character is absent. Recombination can then proceed in one of two ways: relaxation from the b-state to the a-state followed by a–b recombination via the Van der Waals channel, or via a direct bbb-recombination process. The weak dipolar interactions provide the leading relaxation mechanism (see section 6.2). Kagan et al. (KVS 1981) pointed out that at high densities, a combined relaxation/recombination mechanism involving three hydrogen atoms (bbb-recombination), should be the leading decay channel for H↓↕.

6.1.4.1. bb–He recombination

Before we embark on a discussion of the KVS process we first introduce the dipolar interaction in the H–H–He problem to show that it may be entirely neglected in this case. The dipolar interaction between the electronic spins of two hydrogen atoms is given by

$$(\mu_0\hbar^2/4\pi)r^{-3}\gamma_e^2 f(\boldsymbol{S}_1, \boldsymbol{S}_2)\,, \tag{6.53}$$

where the notation is defined in section 3 and $r \equiv r_{12}$. The matrix elements of eq. (6.53) are given in table 6.8 for the total spin representation of the pair $\{|SM_S IM_I\rangle\}$. One observes that eq. (6.53) does not induce the triplet→singlet transitions required for recombination.

Table 6.8

Matrix elements $f(S_1, S_2)$ for the dipolar interaction between electron spins $V_{dd} = (\mu_0\hbar^2/4\pi)\gamma_e^2 r^{-3} f(S_1, S_2)$. See section 3 for the definition of $f(S_1, S_2)$. $a \equiv \sqrt{\pi/5}\,Y_2^0{}^*(\hat{r})$; $c \equiv \sqrt{3\pi/5}\,Y_2^1{}^*(\hat{r})$; $d \equiv \sqrt{6\pi/5}\,Y_2^2{}^*(\hat{r})$.

$S\ M_S$	0 0	1 1	1 0	1 −1
0 0				
1 1		a	$-c^*$	d^*
1 0		$-c$	$-2a$	c^*
1 −1		d	c	a

The case is different for the dipolar interaction between the proton spin on one atom and the electron spin on another H-atom,

$$-(\mu_0\hbar^2/4\pi)r^{-3}\gamma_e\gamma_p[f(s_1, i_2) + f(i_1, s_2)]\,. \tag{6.54}$$

For the notation we refer again to section 3, the matrix elements are given in table 6.9. Here one term transforming as $Y_2^2(\hat{r})$, connects the fully

Table 6.9

Matrix elements of $-[f(s_1, i_2) + f(i_1, s_2)]$ for the electron–proton contribution to the dipolar interaction between two hydrogen atoms: $V_{dd} = -(\mu_0\hbar^2/4\pi)r^{-3}\gamma_e\gamma_p[f(s_1, i_2) + f(i_1, s_2)]$. The symbols a, c and d are as defined in table 6.8. For the definition of $f(s_1, i_2)$, see section 3.

0	1	0	−	0	1	0	−	0	1	0	−	0	1	0	−	M_I
0	1	1	1	0	1	1	1	0	1	1	1	0	1	1	1	I
0	0	0	0	1	1	1	1	0	0	0	0	−	−	−	−	M_S
0	0	0	0	1	1	1	1	1	1	1	1	1	1	1	1	S

				S	M_S	I	M_I
	d c a $-a$ c $-d$	c $2a$ $-c^*$ c^* $2a$ $-c$	a $-c^*$ d^* $-d^*$ $-c^*$ $-a$	0	0	0	0
				0	0	1	1
				0	0	1	0
				0	0	1	−
$-a$ c^* $-d^*$ d^* c^* a	$-2a$ c^* c c^* c $2a$	c^* $-d^*$ a $-d^*$ a $-c^*$		1	1	0	0
				1	1	1	1
				1	1	1	0
				1	1	1	−
c $2a$ $-c^*$ c^* $2a$ $-c$	c a $-d$ a $-d$ $-c$		c^* $-d^*$ a $-d^*$ a $-c^*$	1	0	0	0
				1	0	1	1
				1	0	1	0
				1	0	1	−
$-d$ $-c$ $-a$ a $-c$ d		c a $-d$ a $-d$ $-c$	$2a$ $-c^*$ $-c$ $-c^*$ $-c$ $-2a$	1	−	0	0
				1	−	1	1
				1	−	0	0
				1	−	1	−

aligned state $|1\ -11\ -1\rangle$ to the (para) singlet state $|0000\rangle$, and hence may cause recombination. It is a kind of dipole-induced Van der Waals recombination, where the dipolar interaction replaces the intra-atomic hyperfine interaction.

Historically, it seemed quite logical to calculate this contribution of the dipolar interaction to second-order recombination, as the $\gamma_e\gamma_n$ terms were found to play an important role in b$\rightarrow$a magnetic relaxation. It was thought that b–b-recombination could possibly explain a discrepancy of order 50 between the experimental value for second-order decay of H$\downarrow\downarrow$ (see section 5) and the theoretical value based on relaxation alone. However, for recombination one also has to account for the large momentum mismatch between initial and final state. As we discussed in section 6.1.2.1 of the present chapter, the H–He potential is not very efficient in accommodating the momentum transfer. This suggests that b–b-recombination would be less efficient than b$\rightarrow$a relaxation. Alternatively, instead of comparing with the relaxation channel we may also compare the $\gamma_e\gamma_p$ term with the intra-atomic hyperfine interaction which is presumed for Van der Waals recombination. Both processes then have the momentum mismatch in common and the former is found to be much weaker than the latter. At an inter-nuclear separation of 4 Å, the $\gamma_e\gamma_p$ term represents an energy of approximately 60 μK, three orders of magnitude weaker than the hyperfine interaction. Moreover, the dipolar interaction falls off rapidly with distance. Thus, one estimates b–b recombination to be more than three orders of magnitude weaker than a–b recombination. In turn, a–b relaxation is observed to be two to three orders of magnitude smaller than a–b recombination.

Two independent unpublished calculations (Haftel 1985, Verhaar 1985) dealing with recombination via this second-order channel exist. Both calculations were done for the adsorbed state (b–b recombination on the surface of ^{4}He). The results show b–b recombination to be a much slower process than b$\rightarrow$a relaxation. In both calculations uncertainties exist concerning the treatment of the helium surface, but it is considered unlikely that improvement of the theory on this point would change the overall conclusion.

6.1.4.2. The KVS mechanism

We return to the original suggestion of KVS that at high densities of H$\downarrow\downarrow$ the dipolar interactions between three H-atoms give rise to the dominant decay channel. As in the case of exchange recombination we divide the three hydrogen atoms up into a recombining pair and a third body. The dipolar interactions between the recombining atoms are neglected, using

the argumentation presented in the previous subsection. This leaves the dipolar interactions between the recombining pair and the third H-atom. In principle, the third atom need not be an H-atom, but may also be a magnetic impurity of some kind. KVS consider the high-field, $T \to 0$ limit and neglect the hyperfine interaction. Only three-body combinations of a- and b-state atoms are considered.

The relations for the rate of third-order recombination (eq. 6.36) and for the final-state relative energy (eq. 6.37) remain valid for the KVS process. The three-body T-operator for the dipolar mechanism is given by eq. (6.10a) where $H = H_3 + V^3$ and $H_3 = K + H_Z + V_1^t + V_2^t + V_3^t$ [V_i^t is the triplet interaction between the particles observed by the spectator i]. The perturbation is given by

$$V^3 = V_1^{dd} + V_2^{dd} , \tag{6.55}$$

and represents the dipolar interaction between the recombining pair 1–2 and the third atom. We split the initial state into three terms, using the cyclic permutation operators E, A and B as in eq. (6.40) and project the initial and final states on the total spin representation as in eq. (6.41). We retain only terms of order 1, i.e., the hyperfine admixtures are neglected. The results only hold for the high-field, low-temperature regime where only the lowest two hyperfine states are populated ($h_1, h_2, h_3 \in a, b$). Using the same notation as in eq. (6.41), we decompose the initial states (distorted by the interaction)

$$\begin{aligned} |i) &= |h_1 h_2 h_3; \boldsymbol{p}_3, \boldsymbol{q}_3) \\ &= \sum_{I_3} \sum_{IM_I} |\tfrac{3}{2} - \tfrac{3}{2}\, 1 I M_I I_3; \boldsymbol{p}_3, \boldsymbol{q}_3)\langle \tfrac{3}{2} - \tfrac{3}{2}\, 1 I M_I I_3 | h_1 h_2 h_3) , \end{aligned} \tag{6.56a}$$

and final states

$$\begin{aligned} |f\rangle_{ps3} &= |00 I_3 M_{I_3}, v, L, M_L; h_3', \boldsymbol{q}_3'\rangle_{ps3} \\ &= \sum_{IM_I} |\tfrac{1}{2} M_S 0 I M_I I_3; v, L, M_L, \boldsymbol{q}_3'\rangle_{ps3} \\ &\quad \times \langle \tfrac{1}{2} M_S 0 I M_I I_3 | 00 I_3 M_{I_3}, h_3'\rangle_{ps3} . \end{aligned} \tag{6.56b}$$

The relevant spin projection amplitudes $\langle \frac{3}{2} - \frac{3}{2}\, 1 I M_I I_3 | h_1 h_2 h_3)$ and $\langle \frac{1}{2} M_S 0 I M_I I_3 | 00 I_3 M_{I_3}, h_3'\rangle_{ps3}$ are given in tables 6.10 and 6.7, respectively. The amplitudes corresponding to nonvanishing terms at $T = 0$ K (even values of $S_3 + I_3$) are indicated with an asterisk in table 6.10. Note that for

Table 6.10

Decomposition of the hydrogen hyperfine three-body states with respect to the total spin representation $|SM_S S_3 I M_I I_3\rangle$. The states that contribute for $T = 0$ K are indicated with an asterisk. The table covers a restricted set of $h_1h_2h_3$. The symbols are $\alpha \equiv \sqrt{\frac{1}{2}}$, $\beta \equiv \sqrt{\frac{1}{3}}$ and $\gamma \equiv \sqrt{\frac{2}{3}}$.

						$h_1h_2h_3$					
S	M_S	S_3	I	M_I	I_3	aaa	aab	baa aba	bba	bab abb	bbb
$\frac{3}{2}$	$\frac{3}{2}$	1	$\frac{1}{2}$	$\frac{1}{2}$	0						
			$\frac{1}{2}$	$-\frac{1}{2}$	0						
			$\frac{1}{2}$	$\frac{1}{2}$	1*						
			$\frac{1}{2}$	$-\frac{1}{2}$	1*						
			$\frac{3}{2}$	$\frac{3}{2}$	1*						
			$\frac{3}{2}$	$\frac{1}{2}$	1*						
			$\frac{3}{2}$	$-\frac{1}{2}$	1*						
			$\frac{3}{2}$	$-\frac{3}{2}$	1*	ε^3					
$\frac{3}{2}$	$\frac{1}{2}$	1	$\frac{1}{2}$	$\frac{1}{2}$	0						
			$\frac{1}{2}$	$-\frac{1}{2}$	0						
			$\frac{1}{2}$	$\frac{1}{2}$	1*						
			$\frac{1}{2}$	$-\frac{1}{2}$	1*						
			$\frac{3}{2}$	$\frac{3}{2}$	1*						
			$\frac{3}{2}$	$\frac{1}{2}$	1*						
			$\frac{3}{2}$	$-\frac{1}{2}$	1*						
			$\frac{3}{2}$	$-\frac{3}{2}$	1*	$-\varepsilon^2\eta$	$\varepsilon^2\beta$	$\alpha\varepsilon^2\gamma$			
$\frac{3}{2}$	$-\frac{1}{2}$	1	$\frac{1}{2}$	$\frac{1}{2}$	0						
			$\frac{1}{2}$	$-\frac{1}{2}$	0			$\pm\alpha\varepsilon\eta\beta$			
			$\frac{1}{2}$	$\frac{1}{2}$	1*						
			$\frac{1}{2}$	$-\frac{1}{2}$	1*		$-\varepsilon\eta\gamma\beta$	$\alpha\varepsilon\eta\beta^2$			
			$\frac{3}{2}$	$\frac{3}{2}$	1*						
			$\frac{3}{2}$	$\frac{1}{2}$	1*	$\varepsilon^2\eta$	$-\varepsilon\eta\gamma^2$				
			$\frac{3}{2}$	$-\frac{1}{2}$	1*			$-\varepsilon\eta\gamma^2$			
			$\frac{3}{2}$	$-\frac{3}{2}$	1*				$\varepsilon\beta$	$\alpha\varepsilon\eta$	
$\frac{3}{2}$	$-\frac{3}{2}$	1	$\frac{1}{2}$	$\frac{1}{2}$	0			$\mp\alpha\eta^2$		$\pm\alpha\eta$	
			$\frac{1}{2}$	$-\frac{1}{2}$	0						
			$\frac{1}{2}$	$\frac{1}{2}$	1*		$\eta^2\gamma$	$-\alpha\eta^2\beta$			
			$\frac{1}{2}$	$-\frac{1}{2}$	1*				$\eta\gamma$	$-\alpha\eta\beta$	
			$\frac{3}{2}$	$\frac{3}{2}$	1*	$-\eta^3$					
			$\frac{3}{2}$	$\frac{1}{2}$	1*		$\eta^2\beta$	$\alpha\eta^2\gamma$			
			$\frac{3}{2}$	$-\frac{1}{2}$	1*				$-\eta\beta$	$-\alpha\eta\gamma$	
			$\frac{3}{2}$	$-\frac{3}{2}$	1*						1

$T \to 0$ only terms with $I_3 = 1$ remain, i.e., at low temperature the KVS process only leads to ortho-H_2 molecular states. For the final state, one may distinguish two important cases corresponding to recombination processes in which one or two electron spins are flipped:

$$M_S = -\tfrac{1}{2}\text{: Single spin-flip process } (h_3' \in a, b)\,,$$
$$M_S = \tfrac{1}{2}\text{: Double spin-flip process } (h_3' \in c, d)\,. \tag{6.56c}$$

An expression for the transition matrix must satisfy the selection rules

$$\Delta I = \Delta I_3 = 0\,, \qquad \Delta M_I = \Delta M_{I_3} = 0\,, \tag{6.57}$$

reflecting the fact that the dipolar interaction between the electronic spins does not affect the nuclear spins in the recombination process. Although the selection rules are less restrictive than in the case of exchange recombination (eq. 6.43), the expressions for T_E, T_A and T_B may be kept relatively simple as we restrict ourselves to the high-field, $T = 0$ K regime and only consider $|a\rangle$ and $|b\rangle$ initial states

$$T_E = \sum_i \sum_{IM_I} {}_{ps3}\langle \tfrac{1}{2} M_S 01; v, L, M_L, \boldsymbol{q}_3' | V_i^{dd} G_+ | \tfrac{3}{2} -\tfrac{3}{2}\, 11; \boldsymbol{p}_3, \boldsymbol{q}_3 \rangle_{ps3}$$
$$\times {}_{ps3}\langle 001 M_{I_3}, h_3' | \tfrac{1}{2} M_S 0 I M_I 1 \rangle \langle \tfrac{3}{2} -\tfrac{3}{2}\, 1 I M_I 1 | h_1 h_2 h_3 \rangle\,. \tag{6.58}$$

Here the quantum numbers within the matrix element are defined by

$${}_{ps3}\langle S' M_{S'} S_3' I_3; v, L, M_L, \boldsymbol{q}_3' | V_i^{dd} G_+ | S M_S S_3 I_3; \boldsymbol{p}_3, \boldsymbol{q}_3 \rangle_{ps3}\,.$$

To evaluate the matrix element, we transform the initial state from spectator 3 to spectator i:

$$V_i^{dd} G_+ | \tfrac{3}{2} -\tfrac{3}{2}\, 11; \boldsymbol{p}_3, \boldsymbol{q}_3 \rangle_{ps3}$$
$$= V_i^{dd} G_+ \sum_{S_i} -|\tfrac{3}{2} -\tfrac{3}{2} S_i (11); \boldsymbol{p}_3, \boldsymbol{q}_3 \rangle_{ps3} \begin{bmatrix} \frac{1}{2} & \frac{1}{2} & 1 \\ \frac{1}{2} & \frac{1}{2} & S_i \end{bmatrix} \sqrt{3} (2S_i + 1)^{1/2}$$
$$= V_i^{dd} G_+ | \tfrac{3}{2} -\tfrac{3}{2}\, 1 (11); \boldsymbol{p}_3, \boldsymbol{q}_3 \rangle_{ps3}\,. \tag{6.59a}$$

This reflects the trivial result that three aligned spins may only be split up in spin-aligned pairs. The relevant $6-j$ symbols are:

$$\begin{bmatrix} \frac{1}{2} & \frac{1}{2} & 1 \\ \frac{1}{2} & \frac{3}{2} & 1 \end{bmatrix} = -\frac{1}{3}\,, \qquad \begin{bmatrix} \frac{1}{2} & \frac{1}{2} & 1 \\ \frac{1}{2} & \frac{3}{2} & 0 \end{bmatrix} = 0\,. \tag{6.59b}$$

Similarly, one has to transform the spin part of the final state to the perspective of the spectator i. For this, eq. (6.45b) remains valid. We substitute eq. (6.59) and eq. (6.45b) into eq. (6.58) and use the property that the dipolar interaction (eq. 6.53) cannot induce singlet–triplet transitions as discussed in the previous section and as may be read from table 6.8. This yields

$$T_E = \sum_i \sum_{IM_I} {}_{\mathrm{ps3}}\langle \tfrac{1}{2} M_S 1(01); v, L, M_L, \boldsymbol{q}_3' | V_i^{\mathrm{dd}} G_+ | \tfrac{3}{2} - \tfrac{3}{2} 1(11); \boldsymbol{p}_3, \boldsymbol{q}_3 \rangle_{\mathrm{ps3}} \times \sqrt{\tfrac{3}{4}}\, {}_{\mathrm{ps3}}\langle 001 M_{I_3}, \mathrm{h}_3' | \tfrac{1}{2} M_S 0 I M_I 1 \rangle \langle \tfrac{3}{2} - \tfrac{3}{2} 1 I M_I 1 | \mathrm{h}_1 \mathrm{h}_2 \mathrm{h}_3 \rangle . \tag{6.60}$$

The quantum numbers in the matrix element are defined by

$${}_{\mathrm{ps3}}\langle S' M_{S'} S_i (S_3' I_3); v, L, M_L, \boldsymbol{q}_3' | V_i^{\mathrm{dd}} G_+ | S M_S S_i (S_3 I_3); \boldsymbol{p}_3, \boldsymbol{q}_3 \rangle_{\mathrm{ps3}} ,$$

for which we shall use the abbreviated notation $\langle M_S | V_i^{\mathrm{dd}} | -\tfrac{3}{2} \rangle$. To evaluate the matrix element we decompose the spin part in the $\{|S_i M_{S_i} s_i m_{s_i}\rangle\}$ representation, where s_i is the electron spin of the spectator i:

$$|S M_S S_i\rangle = \sum_{S_i M_{S_i}} \sum_{m_{s_i}} |S_i M_{S_i} \tfrac{1}{2} m_{s_i}\rangle \langle S_i M_{S_i} \tfrac{1}{2} m_{s_i} | S M_S S_i \rangle . \tag{6.61}$$

The projection amplitudes $\langle S_i M_{S_i} \frac{1}{2} m_{s_i} | S M_S S_i \rangle$ are summarized in table 6.11. In this new representation the matrix elements of V_i^{dd} are readily

Table 6.11

Decomposition of the total election spin representation $|S M_S S_i\rangle$ with respect to the partially symmetrized spin states $|S_i M_{S_i} m_{s_i}\rangle_{\mathrm{psi}}$. Here $\beta = \sqrt{\frac{1}{3}}$ and $\gamma = \sqrt{\frac{2}{3}}$.

			$S_3 M_{S_3}$									
			$m_{s_3} = \frac{1}{2}$					$m_{s_3} = -\frac{1}{2}$				
S	M_S	S_3	0 0	1 1	1 0	1 −1		0 0	1 1	1 0	1 −1	
$\frac{1}{2}$	$\frac{1}{2}$	0	1									
$\frac{1}{2}$	$-\frac{1}{2}$	0						1				
$\frac{1}{2}$	$\frac{1}{2}$	1			$-\beta$				γ			
$\frac{1}{2}$	$-\frac{1}{2}$	1				$-\gamma$				β		
$\frac{3}{2}$	$\frac{3}{2}$	1		1								
$\frac{3}{2}$	$\frac{1}{2}$	1			γ				β			
$\frac{3}{2}$	$-\frac{1}{2}$	1				β				γ		
$\frac{3}{2}$	$-\frac{3}{2}$	1										1

evaluated using table 6.8. We obtain for the single spin-flip process

$$\langle -\tfrac{1}{2}|V_i^{\mathrm{dd}}|-\tfrac{3}{2}\rangle = -\sqrt{\tfrac{1}{3}}(\mu_0\hbar^2/4\pi)\gamma_e^2(3\pi/5)^{1/2}\langle Y_2^{1*}(\hat{r}_i)/r_i^3\rangle\,. \quad (6.62a)$$

Here $\hat{r}_i \equiv \hat{\xi}_i$ in the notation of fig. 6.2 and the quantization axis is the direction of the applied magnetic field. In the transition, angular momentum is transferred from the spin system to the orbital system. Similarly for the double spin-flip process

$$\langle \tfrac{1}{2}|V_i^{\mathrm{dd}}|-\tfrac{3}{2}\rangle = \sqrt{\tfrac{2}{3}}(\mu_0\hbar^2/4\pi)\gamma_e^2(6\pi/5)^{1/2}\langle Y_2^{2*}(\hat{r}_i)/r_i^3\rangle\,. \quad (6.62b)$$

Thus, as far as the spin part is concerned, the transition amplitude for the double spin-flip process is twice as large as that for the single spin-flip process. This leads to a factor 4 difference in the transition rate.

As in the case of exchange recombination, KVS evaluated their theory in the $T = 0$ K limit, where the unperturbed orbital wavefunction is invariant under permutation of the atoms $[|\boldsymbol{p}_1, \boldsymbol{q}_1) = |\boldsymbol{p}_2, \boldsymbol{q}_2) = |\boldsymbol{p}_3, \boldsymbol{p}_3)$, and the states are meant to be undistorted] and the sum $T_E + T_A + T_B$ is obtained by simply adding the spin parts. Squaring the matrix element and summing over all final spin states, the transition rate may be compactly expressed (note the absence of the thermal average which arises from the well-behaved $T = 0$ K limit of the initial-state orbital wavefunction, see section (6.2)

$$\Gamma/V = -\tfrac{1}{6}n^3 e_1 \sum_{v,L,M_L} \tfrac{3}{4}(v/2\pi\hbar^2)^2(\mu_0\hbar^2/4\pi)^2(\pi/5) \times \int \mathrm{d}\hat{\boldsymbol{q}}'\left(\frac{\hbar}{v}\right) q'\left[\left|\sum_i \langle Y_2^{1*}(\hat{r}_i)/r_i^3\rangle\right|^2 + 4\left|\sum_i \langle Y_2^{2*}(\hat{r}_i)/r_i^3\rangle\right|^2\right], \quad (6.63)$$

where

$$e_1 \equiv \sum_{\mathrm{h}_1\mathrm{h}_2\mathrm{h}_3} \hat{h}_1\hat{h}_2\hat{h}_3 \sum_{IM_I} |\langle \tfrac{3}{2} - \tfrac{3}{2}1IM_I1|E + A + B|\mathrm{h}_1\mathrm{h}_2\mathrm{h}_3\rangle|^2\,. \quad (6.64a)$$

An explicit expression for e_1 in terms of $\hat{a}$ and $\hat{b}$ is obtained using table 6.10,

$$e_1 = 9[\hat{a}^3 + \hat{a}^2\hat{b} + \hat{a}\hat{b}^2 + \hat{b}^3]\,. \quad (6.64b)$$

In writing eq. (6.63) and eq. (6.64), we have lost the information on the final hyperfine state of the third body. To retrieve this information one has to compare the probabilities $|\langle 001M_{I_3}, \mathrm{h}_3'|\tfrac{1}{2}M_S 0IM_I1\rangle|^2$ for the various

processes, as may be seen from eq. (6.60). Using table 6.7, we have calculated these probabilities for both single ($M_S = -\frac{1}{2}$) and double ($M_S = +\frac{1}{2}$) spin-flip process in the high-field, $T = 0$ K limit. The results are listed in table 6.12. The I and M_I quantum numbers to be used are obtained for any set $h_1h_2h_3$ from the projection on the total spin representation (table 6.10).

A point of great practical importance in view of the stability of H↓‡ at high density is the magnetic field dependence of dipolar recombination. Comparing with eq. (6.15) or eq. (6.50) we note that in eq. (6.63) an explicit field dependence is absent, yet the calculated rate for dipolar recombination between three H-atoms in the b-state shows a pronounced field dependence as illustrated in fig. 6.4. The curves shown were obtained by de Goey and Verhaar (1984) and represent the single and double spin-flip contributions for recombination to the $v = 14$, $L = 3$ molecular final state. In contrast to Van der Waals or exchange recombination, this field dependence does not arise from the spin part of the matrix elements but originates in the momentum mismatch and density of final states considerations discussed in section 6.1.2.1. We illustrate this point using eq. (6.37) and fig. (6.5). The final-state relative wave vector is given by

$$q_{h_3'} = [(2\nu)^{1/2}/\hbar][\varepsilon_{h_1} + \varepsilon_{h_2} + \varepsilon_{h_3} - \varepsilon_{h_3'} - E_{vL}]^{1/2}, \tag{6.65}$$

where ε_{h_i} is the Zeeman energy of hyperfine state $|h_i\rangle$. For the single spin-flip process (E' in fig. 6.5)

$$q_{h_3'} = [(2\nu)^{1/2}/\hbar][|E_{vL}| - 2\mu_B B]^{1/2}. \tag{6.66a}$$

This implies a cut-off field $B = |E_{vL}|/(2\mu_B)$ beyond which thermal acti-

Table 6.12

Relative probabilities of various dipolar recombination channels. Both the single and double spin-flip cases are presented. The table is valid for the high-field, $T = 0$ K limit. The hyperfine states of the incoming atoms are given on the left. The molecular final states are indicated by the nuclear spin projection M_I (only ortho final states are allowed at $T = 0$ K). The final hyperfine state of the third body is given in parentheses.

	Double spin-flip			Single spin-flip		
$h_1h_2h_3$	$M_I = 1$	$M_I = 0$	$M_I = -1$	$M_I = 1$	$M_I = 0$	$M_I = -1$
aaa	1(d)			1(a)		
aab	$\frac{1}{3}$(c)	$\frac{2}{3}$(d)		$\frac{1}{3}$(b)	$\frac{2}{3}$(a)	
abb		$\frac{2}{3}$(c)	$\frac{1}{3}$(d)		$\frac{2}{3}$(b)	$\frac{1}{3}$(a)
bbb			1(c)			1(b)

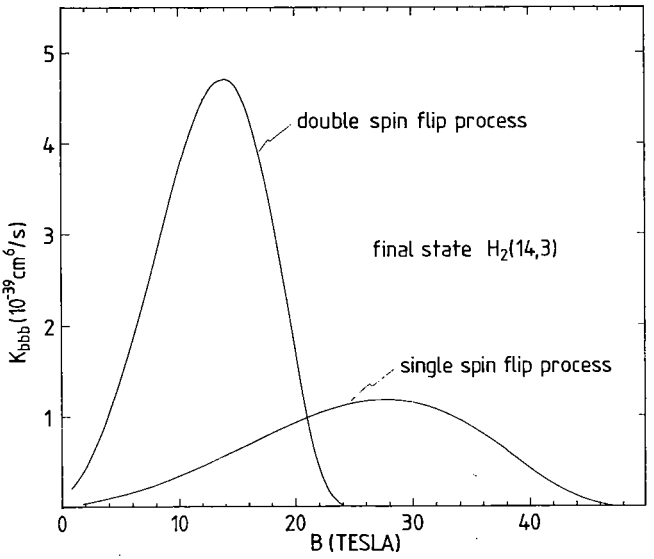

Fig. 6.4. Theoretical results for the Kagan process in the volume. The single and double spin-flip contributions to the volume rate K_{bbb} are shown separately.

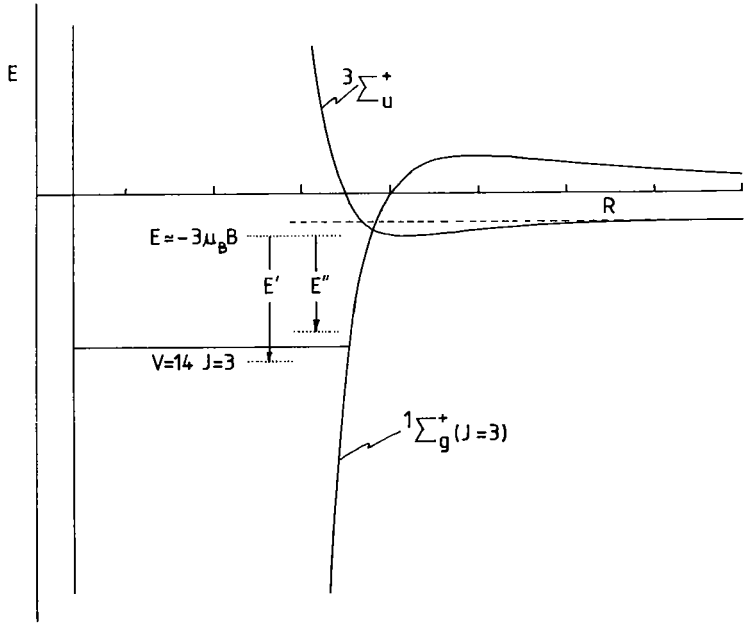

Fig. 6.5. Diagram showing the energy available for the relative motion of the third atom with respect to the molecule for both the single (E') and double (E'') spin-flip process.

vation is required for recombination to the $H_2(v, L)$ final state. For the double spin-flip process (E'' in fig. 6.5)

$$q_{h\downarrow} = [(2\nu)^{1/2}/\hbar][|E_{vL}| - 4\mu_B B]^{1/2}, \tag{6.66b}$$

corresponding to a cut-off field which is a factor 2 lower. For the $H_2(14,3)$ molecular final state, the cut-off fields are $B \simeq 48$ T (single spin-flip) and $B \simeq 24$ T (double spin-flip), as may be seen in fig. 6.4. The maxima in this figure are due to two competing effects. With growing field the initial- and final-state momenta are better matched while the density of final states (proportional to $q_{h\downarrow}$, see eq. 6.8) is decreasing, becoming zero at the cut-off field. Note that the maximum in the double spin-flip curve is four times higher than the maximum for the single spin-flip case. This difference is due to the difference in spin matrix elements for the two channels (eq. 6.62) and appears explicitly in eq. (6.63). A plot similar to fig. 6.4 could be made for the $H_2(14,1)$ molecular final state. For this channel cut-offs would be found at $B \simeq 68$ T and $B \simeq 136$ T. The maxima would be lower than for the $H_2(14,3)$ channel in view of the difference in rotational degeneracy of the final state ($2L + 1 = 3$ versus $2L + 1 = 7$). We note the latest experimental results for the vibrational–rotational levels (Dabrowsky 1984) imply a cut-off field of 26.85 T for recombination to the $H_2(14,3)$ molecular state via the double spin-flip process.

The results quoted in the previous paragraph were obtained for bbb-recombination in the $T = 0$ K limit. It requires little argument that the qualitative aspects presented remain valid for $T > 0$. It is therefore unlikely that the field dependence would depend strongly on temperature. However, if some a-state is present in the gas, recombination to para-H_2 final states becomes possible at higher temperatures. The appearance of this new channel will affect the overall field dependence in a qualitative manner.

6.1.4.3. The KVS mechanism on the surface

It was first pointed out by KVS that three H-atoms are required on a surface for direct recombination of H↓‡. These authors estimated the surface rate using a scaling argument in which the pair-correlation between the atoms on the surface is assumed to be identical to that in the bulk. Such a quasi-bulk theory in a good ansatz, in particular if the bound-state wavefunction on the surface has a wide extent as is the case for H on ^{4}He (see fig. 4.1). The quasi-bulk model is discussed in some detail by Kagan et al. (1982) and implies the conservation of essentially the complete phenomenology discussed in the previous paragraphs when changing from bulk- to surface-dipolar recombination. Thus, the dominant molecular

final state is $H_2(14,3)$ and the matrix elements for the double spin-flip process dominate by a factor four over the single spin-flip process.

A more detailed analysis of the KVS dipole mechanism for bbb-recombination on the surface of ^{4}He was made by de Goey et al. (1984) who were interested in the limitations of the quasi-bulk model. On the surface one deals with a very anisotropic situation. Only the component of the momentum parallel to the surface is conserved; similarly, only the normal components of the angular momentum vector. As a result, in a partial wave analysis of surface scattering, the surface normal is the natural choice for the quantization axis. In contrast, the spin system is quantized with respect to the direction of the applied magnetic field. As the dipolar recombination mechanism involves the transfer of angular momentum from the spin system to the orbital system the above considerations lead to an intrinsic anisotropy of surface dipolar recombination with respect to the angle between magnetic field and surface normal. Such an anisotropy is lost when using the scaling argument.

De Goey et al. (1984) applied a "$2\frac{1}{2}$-dimensional" ($2\frac{1}{2}$-dim) model, used earlier by Ahn et al. (1982) for a calculation of the surface dipolar relaxation rate (see section 6.2), to describe the relative motion of the H-atoms on the He surface. The model was found to agree on a 30% level with a full three-dimensional description of the surface relaxation. In the $2\frac{1}{2}$-dim model, the b–b relative wavefunction $\psi_k^t(\rho)$ consists of a 2-dimensional plane-wave $\exp(i\boldsymbol{k}\cdot\rho)$, distorted near the scattering center by the triplet interaction averaged over the z-motion of the atoms. The full initial state is written as

$$|\mathrm{bbb};\, \boldsymbol{p}_3,\, \boldsymbol{q}_3) = \phi_0(z_1)\phi_0(z_2)\phi_0(z_3)\psi^t_{p_3}(\boldsymbol{\xi}_3)\psi^t_{q_3}(\boldsymbol{\eta}_3)|\mathrm{bbb}\rangle\,, \qquad (6.67)$$

where the $\phi_0(z)$ represent single-atom bound-state wavefunctions of the type shown in fig. 4.1, the $\boldsymbol{p}_3$ and $\boldsymbol{\xi}_3$ are defined as in fig. 6.2, be it that the symbols now represent two-dimensional vectors in the plane of the surface. As for bulk bbb-recombination the two-dimensional vectors $\boldsymbol{q}_3$ and $\boldsymbol{\eta}_3$ represent either $\boldsymbol{p}_1$ and $\boldsymbol{\xi}_1$ or $\boldsymbol{p}_2$ and $\boldsymbol{\xi}_2$ depending on the dipolar interaction under consideration (V_1^{dd} or V_2^{dd}, respectively). This extremely useful approximation was first introduced by KVS in relation to bulk exchange and dipolar recombination, and amounts to the neglect of the distortion of the wavefunction due to the third atom when considering the interaction of the remaining pair.

For the final state the same wavefunction is used as the bulk bbb-recombination (eq. 6.56b). This choice may be unexpected at first sight. We therefore deviate a bit and compare the role of the adsorption potential in dipolar and Van der Waals recombination mechanisms on the surface. In

the latter case the potential not only serves to confine the initial state wavefunction to the surface, but also enables the momentum transfer required for recombination. Hence the molecule has to desorb. On the contrary, in the surface KVS mechanism, in principle, the potential only serves the confinement role. Since the interaction with the third H-atom may also account for the momentum transfer, the 3BCM can remain on the surface and the final state particles do not necessarily have to desorb. The approximation that the 3BCM remains on the surface is reasonable, in particular for low magnetic fields where up to 73 K (see fig. 6.1) is available for the relative $H-H_2$ motion so that one of the final-state particles can enter the bulk of the He liquid, while the other particle is desorbing. In fact, this approximation, adopted both by Kagan et al. and de Goey et al., amounts to a complete neglect of the He surface in the final state, and the bulk wavefunction may be used.

In high magnetic fields, the complete neglect of the He surface is much less realistic. This triggered de Goey et al. to investigate the case where the wave associated with the relative $H-H_2$ motion, expanding around the 3BCM, reflects elastically from the surface. However, this approach did not lead to a significantly different qualitative behavior, but only to modest quantitative differences of order 10% in the overall rates.

The effects of the anisotropy may be very pronounced. Lagendijk (1982) pointed out that in the case of surface dipolar relaxation the relaxation rate can be made to vanish by orientating the magnetic field along the surface normal. This will be discussed in some detail in section 6.2 of this chapter. For surface dipolar recombination the effects are less pronounced. This is due to the desorption of the final-state particles.

To calculate the bbb-recombination rate on the surface, an expression of the type given in eq. (6.36) may be used. For the quasi-bulk model used by Kagan et al. (1982), explicit thermal averaging may be avoided by working in the $T = 0$ K limit. This leads to an expression quite similar to eq. (6.63). In the $2\frac{1}{2}$-dimensional model such a simplification is not feasible due to the logarithmic nature of the relative wavefunction $\psi_k^t(\boldsymbol{\rho})$. We return to this 2-dimensional pathology in section 6.2. Hence, de Goey et al. were forced to do the thermal average over the initial-state wavefunction and found the rate to increase roughly by a factor of 2 over the temperature range 0.2–0.6 K. It may be useful to point out that this does not imply that the full temperature dependence was extracted. In fact, the calculation carries a strong $T = 0$ K signature since only s-wave scattering was considered and the (unperturbed) incoming orbital wavefunction was taken to be invariant under permutation of the atoms as was done in deriving eq. (6.63).

The theoretical results of de Goey et al. may be expressed as

$$K_{\mathrm{bbb}} = \frac{1}{2} \sum_{M_S} \sum_{n=0,2,4} A_{n,M_S}(B) P_n(\cos\theta) , \tag{6.68}$$

where P_n is a Legendre polynomial and θ is the angle between $\boldsymbol{B}$ and the surface normal. The coefficients A_n are shown in fig. 6.6, and display a behavior which is quite similar to that of fig. 6.4. For $\theta = 0$ the calculated rate is $K_{\mathrm{bbb}} = 6.5 \times 10^{-26}\ \mathrm{cm^4\ s^{-1}}$ for $B = 7.6$ T. The experimental value of Hess et al. (1984) is an order of magnitude larger, $K_{\mathrm{bbb}} = 5.3 \times 10^{-25}\ \mathrm{cm^4\ s^{-1}}$, moreover the rate was found to drop slightly with growing field. Hence, it is quite possible that yet something else is going on at these very high surface densities.

A possible explanation for the discrepancy (Haftel 1985, Verhaar 1985) could be a combined process of three-body dipolar relaxation and Van der Waals recombination, which we briefly compare with the KVS process to conclude this section. In the KVS process both the singlet admixture and the momentum transfer associated with the recombination is enabled by the presence of a third H-atom. In the above mentioned combined process

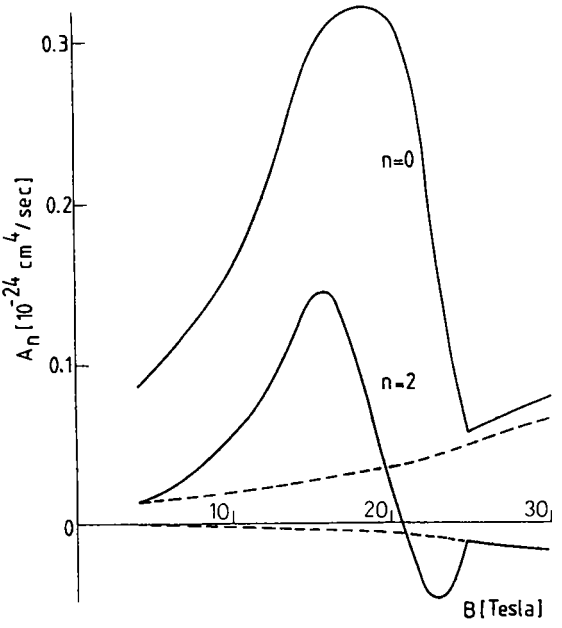

Fig. 6.6. The rate constant for surface dipolar recombination as a function of magnetic field. For the definition of the A_n see the text.

the singlet character is admixed by the passage of a third H-atom, but the momentum transfer is realized by the molecule–surface interaction as in the case of surface Van der Waals recombination. To our knowledge no other suggestions exist in the current literature that may explain this discrepancy.

6.1.5. Relationship to phenomenological experimental rates

In the coming section we wish to bridge the gap between the rather formal theoretical discussion of the sections 6.1.3 and 6.1.4 and the rate equations which are used for analyzing the experiments. The procedure is more involved than that of section 6.1.2.3, where we gave some examples for writing down rate equations for second-order processes. For third-order processes we not only have to account for the loss of two atoms per recombination event, but also keep track of what happens with the spins on the third body.

We first consider the example of aaa-recombination via the exchange process in the volume for the high field, $T = 0\,\mathrm{K}$ limit, an example considered before in some detail at the end of section 6.1.3.1. The overall recombination rate is written down in terms of Γ_{aaa} using eq. (6.36),

$$\dot{N}/V = -2\Gamma/V = -\tfrac{1}{3}a^3\Gamma_{aaa}\,. \tag{6.69a}$$

In terms of a simple rate equation we write

$$\dot{N}/V = -2K_{aaa}a^3\,. \tag{6.69b}$$

Comparing we find

$$K_{aaa} = \tfrac{1}{6}\Gamma_{aaa}\,. \tag{6.69c}$$

Along the same lines of reasoning this result may be readily generalized to

$$\begin{aligned} K_{h_1h_1h_1} &= \tfrac{1}{6}\Gamma_{h_1h_1h_1}\,, \\ K_{h_1h_2h_2} &= \tfrac{1}{2}C_{h_1h_2h_2}\,, \quad h_1 \neq h_2 \\ K_{h_1h_2h_3} &= \Gamma_{h_1h_2h_3}, \qquad h_1 \neq h_2;\, h_1 \neq h_3;\, h_2 \neq h_3 \end{aligned} \tag{6.70}$$

We next look at the recombination probabilities for the various aaa-channels:

$$\text{aaa} \rightarrow \text{p-H}_2 + \text{a}, \qquad \Gamma_1 \simeq 9\varepsilon^2 \Gamma^{\text{para}}_{\text{orbital-1}} ,$$

$$\text{aaa} \rightarrow \text{o-H}_2(M_I = 0) + \text{a}, \qquad \Gamma_2 \simeq \tfrac{9}{16}\varepsilon^2 \Gamma^{\text{ortho}}_{\text{orbital-2}} ,$$

$$\text{aaa} \rightarrow \text{o-H}_2(M_I = 1) + \text{b}, \qquad \Gamma_3 \simeq \tfrac{9}{8}\varepsilon^2 \Gamma^{\text{ortho}}_{\text{orbital-3}} .$$

here Γ_1, Γ_2 and Γ_3 are the partial contributions of the processes considered for the rate Γ_{aaa} (see eq. 6.36) and the $\Gamma^{\text{para}}_{\text{orbital-1}}$, etc., are the factors due to the overlap of the orbital parts alone. Assuming the volume, V, to be time independent, we obtain

$$\dot{a} = -(2 + \xi)\tfrac{1}{6}\Gamma_{\text{aaa}} a^3 , \qquad \dot{b} = +\tfrac{1}{6}\xi\Gamma_{\text{aaa}} a^3 , \tag{6.71}$$

where

$$\xi \simeq \frac{9}{8}\left[9(\Gamma^{\text{para}}_{\text{orbital}}/\Gamma^{\text{ortho}}_{\text{orbital}}) + \frac{9}{16} + \frac{9}{8}\right]^{-1}$$

represents the fraction of recombination events in which the third body changes hyperfine state. Thus aaa-recombination gives rise to a source term in the rate equation for the b-state, with the result

$$\dot{a} = -(2 + \xi)K_{\text{aaa}} a^3 , \qquad \dot{b} = +\xi K_{\text{aaa}} a^3 . \tag{6.72}$$

We estimate $\xi \simeq \frac{2}{3}$, using the KVS result that $\Gamma^{\text{para}}_{\text{orbital}} < \Gamma^{\text{ortho}}_{\text{orbital}}$. Any three-body process may lead to source terms of the kind that appear in eq. (6.72). The importance of these source terms depends on the details of the process considered, hence, general rules cannot be given here. Later in this section we shall return to these source terms when discussing the example of dipolar recombination. First, however, we compare the K_{aaa} for exchange recombination with the rate constant K_{aaHe} for Van der Waals recombination to obtain information about the difference in recombination efficiency when one replaces the helium atom by a third H-atom. For this purpose we somewhat crudely assume $\Gamma_{\text{orbital-1}} = \Gamma_{\text{orbital-2}} = \Gamma_{\text{orbital-3}}$, and add the rates for the three channels for aaa-recombination

$$K_{\text{aaa}} \simeq \tfrac{1}{6}[9 + \tfrac{9}{16} + \tfrac{9}{8}]\varepsilon^2 \Gamma_{\text{orbital}} . \tag{6.73}$$

This result is compared with a similar expression for K_{aaHe}, derived by using eq. (6.27) and eq. (6.14),

$$K_{\text{aaHe}} \simeq \tfrac{1}{2}\varepsilon^2 \Gamma_{\text{orbital}} . \tag{6.74}$$

Hence $K_{\text{aaa}} \simeq 3K_{\text{aaHe}}$ and we conclude that aaa-collisions are $\sim 9\times$ more

efficient than aaHe-collisions. The additional factor 3 arises because for a = He there are 3× more aaHe triples in a H–He mixture than in a pure a-state gas (note that for the aaa-process, the total gas density is a, whereas for aaHe it is $a + n_{He}$). The K_{aaa} efficiency may deviate significantly from the above result, as determined by the details of the orbital integrals.

To conclude this section we present the rate equations associated with the dipolar recombination terms included in (6.64b). The equations were derived using table 6.12

$$\dot{a} = -(2+\xi)\dot{R}_a\,, \qquad \dot{d} = +\xi\dot{R}_a\,,$$
$$\dot{b} = -(2+\xi)\dot{R}_b\,, \qquad \dot{c} = +\xi\dot{R}_b\,, \tag{6.75a}$$

where

$$\dot{R}_a = K_{aaa}a^3 + \tfrac{2}{3}K_{aab}a^2b + \tfrac{1}{3}K_{abb}ab^2\,,$$
$$\dot{R}_b = K_{bbb}b^3 + \tfrac{1}{3}K_{aab}a^2b + \tfrac{2}{3}K_{abb}ab^2\,.$$

The rate of recombination events is given by $\dot{R}_a + \dot{R}_b$; ξ is the fraction of events that proceed via the double spin-flip process. From eq. (6.63) one concludes that $K_{aaa} = K_{aab} = K_{abb} = K_{bbb}$.

In the limit that the a-state density vanishes eq. (6.75a) reduces to

$$\dot{b} = -(2+\xi)K_{bbb}b^3\,, \qquad \dot{c} = \xi K_{bbb}b^3\,. \tag{6.75b}$$

When the c-state atoms have a larger probability to recombine than to relax back to the b-state the total loss of particles is given by

$$\dot{n} = -2(1+\xi)K_{bbb}n^3 (\equiv -Ln^3)\,, \quad (n \simeq b)\,.$$

The symbol L has been used to characterize the rate of the KVS process in the literature. From the above discussion it will be clear that accurate experimental information concerning the KVS process may only be obtained if the state of polarization and the efficiency of the various relaxation channels are well-known.

6.2. Relaxation

The wealth of recombination processes discussed in section 6.1 is by itself not sufficient to estimate the stability of a gas of hydrogen atoms at low temperature. A key ingredient is missing as long as the occupation of the various hyperfine levels is unknown. To obtain this information the various

spin-relaxation mechanisms have to be included in the rate equations. Fortunately, from the abundance of relaxation channels at our disposal a rather restricted set appears to be relevant to our problem. In low field, spin-exchange is dominant, whereas in high magnetic fields dipolar processes govern the physics of relaxation. Moreover, at least for the currently accessible density regime, only two-body relaxation mechanisms come into play. This has led us to divide section 6.2 of this chapter into three subsections. First we give an introduction, comparing the particularities of three-dimensional and two-dimensional scattering as far as is relevant to the relaxation problem. The next two subsections deal with spin-exchange and dipolar relaxation, and we also make the link with the phenomenological rate equations.

6.2.1. *Introduction—Volume and surface processes*

For the relaxation problem we are interested in the transition rates between the various hyperfine levels. The total rate of relaxation events is given by eq. (6.3), where $|\mathrm{i}\rangle$ and $|\mathrm{f}\rangle$ now represent symmetrized two-body initial and final states, respectively. P_i is the probability that an initial pair-state is occupied and $\langle \mathrm{f}|T|\mathrm{i}\rangle$ is the two-body T-matrix. Momentum conservation is satisfied implicitly by expressing $|\mathrm{i}\rangle$ and $|\mathrm{f}\rangle$ in two-body center of mass (2BCM) system

$$|\mathrm{i}\rangle = |\mathrm{h}_1\mathrm{h}_2; \boldsymbol{k}\rangle\,, \qquad |\mathrm{f}\rangle = |\mathrm{h}_1'\mathrm{h}_2'; \boldsymbol{k}'\rangle\,. \tag{6.76}$$

The initial state $|\mathrm{i}\rangle$ represents a pair of H-atoms in hyperfine states h_1 and h_2, moving with relative momentum $\boldsymbol{k}$. The final state $|\mathrm{f}\rangle$ is defined analogously. The probability P_i is normalized to the total number of H–H pairs, analogous to eq. (6.5),

$$\begin{aligned}\sum_\mathrm{i} P_\mathrm{i} &\equiv \sum_{|\mathrm{h}_1\mathrm{h}_2;\boldsymbol{k}\rangle} P_{|\mathrm{h}_1\mathrm{h}_2;\boldsymbol{k}\rangle} \\ &= \sum_{|\mathrm{h}_1\mathrm{h}_2;\boldsymbol{k})} P_{|\mathrm{h}_1\mathrm{h}_2;\boldsymbol{k})} \\ &= \tfrac{1}{2}N_\mathrm{H}^2 \sum_{\mathrm{h}_1\mathrm{h}_2} \hat{h}_1\hat{h}_2 \sum_{\boldsymbol{p}} P_\mu(\boldsymbol{p}) = \tfrac{1}{2}N_\mathrm{H}^2\,,\end{aligned} \tag{6.77}$$

with

$$\sum_\mathrm{h} \hat{h} = 1, \qquad \sum_{\mathrm{h}_1\mathrm{h}_2} \hat{h}_1\hat{h}_2 = 1, \qquad \sum_{\boldsymbol{k}} P_m(\boldsymbol{k}) = 1\,,$$

$P_m(\boldsymbol{k})$ represents a Boltzmann momentum distribution (eq. 6.6) and $\mu = \frac{1}{2}m_H$ is the reduced mass of the pair. For some remarks concerning the use of symmetrized versus nonsymmetrized states, the reader is referred to the discussion of eq. (6.5).

With the usual continuum transition $\Sigma_f \rightarrow [V/(2\pi)^3] \int d\boldsymbol{k}$ and integrating over all final k ($\equiv|\boldsymbol{k}|$) states, the energy δ-function disappears and eq. (6.3) becomes

$$\Gamma/V = \tfrac{1}{2}n^2 \sum_{h_1 h_2} \hat{h}_1 \hat{h}_2 \Gamma_{h_1 h_2}\,, \tag{6.78a}$$

with

$$\Gamma_{h_1 h_2} = \frac{1}{2} \sum_{h_1' h_2'} \Gamma_{h_1 h_2 \rightarrow h_1' h_2'}\,,$$

$$\Gamma_{h_1 h_2 \rightarrow h_1' h_2'} \equiv \int d\boldsymbol{k}\, P_\mu(\boldsymbol{k}) \left(\frac{\mu}{2\pi\hbar^2}\right)^2 \int d\hat{\boldsymbol{k}}'\, \frac{\hbar}{\mu}\, k' |\langle f|T|i\rangle|^2\,. \tag{6.78b}$$

Here, n is the bulk density of the H gas, $\hat{\boldsymbol{k}}'$ denotes the unit vector corresponding to $\boldsymbol{k}'$ and we evaluated the three-dimensional density of final states $\rho_3(E) = \mu\hbar k/(2\pi)^3$ for the momentum $k = k'$. The factor $\frac{1}{2}$ in eq. (6.78b) serves to assure that the symmetrized final states contribute just once in the summation. Energy conservation is satisfied if

$$\hbar^2 k'^2/(2\mu) = E_i - E_{h_1'} - E_{h_2'} \equiv E' \geqslant 0\,.$$

For $k < k'$, the process is thresholdless; for $k > k'$ it is (thermally) activated (see also the discussion below eq. 6.9). The transition rate is related to an energy-dependent cross section $\sigma(E)$ via

$$\begin{aligned}\Gamma_{h_1 h_2 \rightarrow h_1' h_2'} &= 4\pi\, \frac{\hbar}{\mu} \int dk\, k^3 P_\mu(\boldsymbol{k}) \sigma_{h_1 h_2 \rightarrow h_1' h_2'}(k) \\ &= \bar{v} \left(\frac{1}{kT}\right)^2 \int_{\Delta E}^{\infty} dE\, E \exp(-E/kT) \sigma_{h_1 h_2 \rightarrow h_1' h_2'}(E) \\ &\equiv \bar{v}\bar{\sigma}_{h_1 h_2 \rightarrow h_1' h_2'}\,,\end{aligned} \tag{6.78c}$$

where $E = \hbar^2 k^2/(2\mu)$ and $\bar{v} = (8kT/\pi\mu)^{1/2}$. The $\bar{v}$ and $\bar{\sigma}_{h_1 h_2 \rightarrow h_1' h_2'}$ represent thermally averaged quantities. ΔE is the activation threshold ($\Delta E \geqslant 0$). The cross section is defined as

$$\sigma_{h_1 h_2 \rightarrow h_1' h_2'}(k) = \frac{1}{4\pi} \left(\frac{\mu}{2\pi\hbar^2}\right)^2 \frac{k'}{k} \int d\hat{\boldsymbol{k}} \int d\hat{\boldsymbol{k}}'\, |\langle f|T|i\rangle|^2\,. \tag{6.78d}$$

Analogously, one derives the total transition rate on the surface in a two-dimensional treatment

$$\Gamma/A = \tfrac{1}{2}\sigma^2 \sum_{h_1 h_2} \hat{h}_1 \hat{h}_2 \Gamma_{h_1 h_2} , \tag{6.79a}$$

with

$$\Gamma_{h_1 h_2} = \frac{1}{2} \sum_{h_1' h_2'} \Gamma_{h_1 h_2 \to h_1' h_2'} ,$$

$$\Gamma_{h_1 h_2 \to h_1' h_2'} = \int \mathrm{d}k\, P_\mu(k)\, \frac{\mu}{\hbar}\, (2\pi\hbar^2)^{-1} \int \mathrm{d}\hat{k}' \, |\langle \mathrm{f}|T|\mathrm{i}\rangle|^2 , \tag{6.79b}$$

where σ is the surface density of H and $\boldsymbol{k}$ and $\boldsymbol{k}'$ refer to two-dimensional vectors in the plane of the surface. The two-dimensional density of momentum states is a constant, $\rho_2(E') = \mu/2\pi\hbar^2$.

The transition rate is related to an energy-dependent cross length via

$$\begin{aligned} \Gamma_{h_1 h_2 \to h_1' h_2'} &= \frac{2\pi\hbar}{\mu} \int \mathrm{d}k\, k^2 P_\mu(\boldsymbol{k}) \lambda_{h_1 h_2 \to h_1' h_2'}(k) \\ &= \bar{v}\, \frac{2}{\pi^{1/2}}\, \frac{1}{(kT)^{3/2}} \int_{\Delta E}^{\infty} \mathrm{d}E\, E^{1/2} \lambda_{h_1 h_2 \to h_1' h_2'}(E) \\ &\equiv \bar{v} \bar{\lambda}_{h_1 h_2 \to h_1' h_2'} , \end{aligned} \tag{6.79c}$$

where $E = \hbar^2 k^2/2\mu$; $\bar{v} = (\pi kT/2\mu)^{1/2}$. The cross length is defined as

$$\lambda_{h_1 h_2 \to h_1' h_2'}(k) = \frac{1}{2\pi} \left(\frac{\mu}{2\pi\hbar^2}\right)^2 \frac{1}{k} \int \mathrm{d}\hat{k} \int \mathrm{d}\hat{k}' \, |\langle \mathrm{f}|T|\mathrm{i}\rangle|^2 . \tag{6.79d}$$

The various two-body relaxation processes may be described with eq. (6.78) or eq. (6.79) as they only differ in the choice of the T-operator. Here we do not enter in the details of the evaluation of the matrix elements, which is left for the coming sections, but rather discuss some fundamental differences between two-dimensional and three-dimensional pair wavefunctions when the distortion due to the interatomic potential is taken into account. Such wavefunctions are needed for calculations within the distorted wave Born approximation (DWBA), which is often required to obtain accurate results.

We first consider scattering between two H-atoms in free space, interacting via the central potential $V(r)$, which may be the singlet or triplet potential. Since $V(r)$ is short-ranged and well-behaved, the solution

to the three-dimensional Schrödinger equation for the relative motion of the two atoms may be expressed in terms of a partial wave expansion (Messiah 1970)

$$\xi_{\boldsymbol{k}}^{\pm}(\boldsymbol{r}) = \frac{4\pi}{kr} \sum_{l,m} \mathrm{i}^l \, \mathrm{e}^{\pm \mathrm{i}\eta_l} F_l(k, r) Y_l^m{}^*(\hat{\boldsymbol{k}}) Y_l^m(\hat{\boldsymbol{r}}) \,. \tag{6.80a}$$

Here $\boldsymbol{k}$ and $\boldsymbol{r}$ are the relative wave-vector and position, l and $m = m_l$ are the quantum numbers of the orbital angular momentum of the pair, $Y_l^m{}^*(\boldsymbol{k})$ and $Y_l^m(\boldsymbol{r})$ are spherical harmonics describing the angular dependence of the wavefunction in terms of the directions of $\boldsymbol{k}$ and $\boldsymbol{r}$ with respect to an appropriate quantization axis, and $F_l(k, r)$ is related to the distorted radial wavefunction $(1/r)y_l(k, r)$ via

$$y_l(k, r) = (2l + 1)\mathrm{i}^l \, \mathrm{e}^{\pm \mathrm{i}\eta_l} F_l(k, r)/k \,. \tag{6.80b}$$

The phase shift η_l is defined by the asymptotic behavior of $F_l(k, r)$.

$$F_l(k, r) \sim \sin(kr - \tfrac{1}{2}l\pi + \eta_l), \quad r \to \infty \,, \tag{6.80c}$$

$$k \operatorname{cotan} \eta_0(k) = \frac{1}{a} + \frac{1}{2} r_e k^2 \,. \tag{6.80d}$$

Here r_e is the effective range of the potential and a the s-wave scattering length [for H-atoms interacting via the triplet potential $a = 1.33\, a_0$ and $r_e = 323\, a_0$ (Friend and Etters 1980, Uang and Stwalley 1980a)]. For vanishing potential the phase shift vanishes ($\eta_l \to 0$) and eq. (6.80a) changes continuously into the partial wave expansion of a plane wave, while $F_l(k, r)/kr$ approaches the Bessel function $j_l(kr)$, as may be seen from the radial Schrödinger equation

$$[\mathrm{d}^2/\mathrm{d}r^2 - l(l+1)/r^2 - U(r) + k^2] y_l(k, r) = 0 \,, \tag{6.81}$$

where $U(r) \equiv (2\mu/\hbar^2)V(r)$ and $k^2 \equiv (2\mu/\hbar^2)E$. The second term in eq. (6.81) is the effective centrifugal barrier which is illustrated in fig. 3.2.

Also the $l = 0$, $k \to 0$ limit of eq. (6.80a) is well-behaved in three dimensions. If we substitute $\lim_{k\to 0} \eta_0 = ka$ into eq. (6.80c) we find $y_l(k, r) \sim (1/k)\sin k(r + a) \sim (r + a)$ for $r > r_e$ and $y_0(k, r)$ becomes k-independent:

$$\xi_{\boldsymbol{k}}^{\pm}(\boldsymbol{r}) = \frac{1}{r} y_0(r) \quad \text{(for small values of } k) \,. \tag{6.82}$$

Here $y_0(r)$ is the $l = 0$, $k = 0$ solution of eq. (6.81). This is particularly

useful in the context of this section as it enables rapid estimates of processes by taking the $T \to 0$ limit for the relative motion, thus avoiding elaborate thermal averaging. This approach has been followed quite impressively by Kagan et al. (KVS 1981) in their exploratory study of many decay processes in H.

Scattering of two H-atoms bound to a surface of liquid helium is quite different. Although for a single H-atom on a perfectly flat surface the motions parallel and normal to the surface are decoupled, such a simplifying feature is absent, at least in principle, for interacting atoms where both degrees of freedom are coupled via the interatomic potential $V(r)$. Hence, in principle, scattering on a surface is a highly anisotropic three-dimensional problem. Fortunately, in practice, a three-dimensional analysis is not required since the characteristic times for the events in which we are interested are much longer than the oscillation time of the bound-state so that it is sufficient to work with a quasi-two-dimensional approach and average quantities of interest over the bound-state wavefunction. This last approximation is called the $2\frac{1}{2}$-dimensional approach by van den Eijnde et al. (1983), who compared the three-dimensional approach with the $2\frac{1}{2}$-dimensional approach for the case of nuclear dipolar relaxation on a He-surface.

To derive the radial Schrödinger equation for the $2\frac{1}{2}$-dimensional case, the three-dimensional wavefunction for the surface problem $F_m(\boldsymbol{\rho}, z_1, z_2)$ is approximated by $\phi_0(z_1)\phi_0(z_2)y_m(\rho)\exp(im\phi)$, where $\phi_0(z)$ is the bound-state wavefunction, real and normalized to unity (see fig. 4.1), and $\boldsymbol{\rho}$ is the relative position vector in the plane of the surface. Then the three-dimensional radial equation reduces to

$$[(\partial^2/\partial\rho^2) + \tfrac{1}{4}(1-4m^2)/\rho^2 - U(\rho, z_1, z_2) - 2U_a + k^2]\,\phi_0(z_1)\phi_0(z_2)y_m(\rho) = 0\,. \tag{6.83}$$

U_a is related to the surface adsorption energy through $U_a = (2\mu/\hbar^2)\varepsilon_a$. Multiplying on the left by $\phi_0(z_1)\phi_0(z_2)$ and integrating over z_1 and z_2 one arrives at the $2\frac{1}{2}$-dimensional radial equation

$$[(\mathrm{d}^2/\mathrm{d}\rho^2) + \tfrac{1}{4}(1-4m^2)/\rho^2 - U(\rho) + k^2]y_m(\rho) = 0\,. \tag{6.84a}$$

Note that the zero of energy has been shifted for convenience; further,

$$U(\rho) \equiv \int \mathrm{d}z_1 \int \mathrm{d}z_2\, \phi_0^2(z_1)\phi_0^2(z_2)U(\rho, z_1, z_2)\,. \tag{6.84b}$$

The $2\frac{1}{2}$-dimensional model was first applied to the H–H problem on the

He surface by Edwards and Mantz (1980) in their mean-field estimate of ε_a as a function of the H coverage (see section 9). Further simplifying eq. (6.84a) by replacing $U(\rho)$ by $U_{2D}(\rho) \equiv U(\rho, 0, 0)$, one obtains the pure two-dimensional limit for the radial equation.

In contrast to the three-dimensional case, the $2\frac{1}{2}$-dimensional (or two dimensional) case has not such a nice limiting behavior for $T \to 0$ K. This is discussed in detail by Verhaar et al. (1984, 1985). First of all notice that for $m = 0$ the centrifugal "barrier" is attractive, thus increasing the binding forces between the atoms. For $U(\rho) = 0$, eq. (6.84a) is perfectly well-behaved and the solution consists of cylindrical Bessel functions. However, for $U(\rho) \neq 0$ the phase-shift is given by

$$\operatorname{cotan} \eta_0(k) = \frac{2}{\pi} (\gamma + \log \tfrac{1}{2} ka) + \frac{1}{2\pi} r_e^2 k^2 , \tag{6.85}$$

where a and r_e are the two-dimensional scattering length and effective range, respectively, and $\gamma = 0.577\,215\,665\ldots$ is Euler's constant [for H-atoms interacting via the triplet potential $a = 2.3\, a_0$ and $r_e = 14.3\, a_0$ (Verhaar et al. 1984, 1985)]. Equation (6.85) is plotted in fig. 6.7 along with approximate expressions for η_0. Although it is encouraging that the effective range theory may be carried over to two dimensions, its use is more involved in view of the logarithmic dependence on k (and a) of the phase shift for $k \to 0$. In practice, this implies that a vanishingly weak

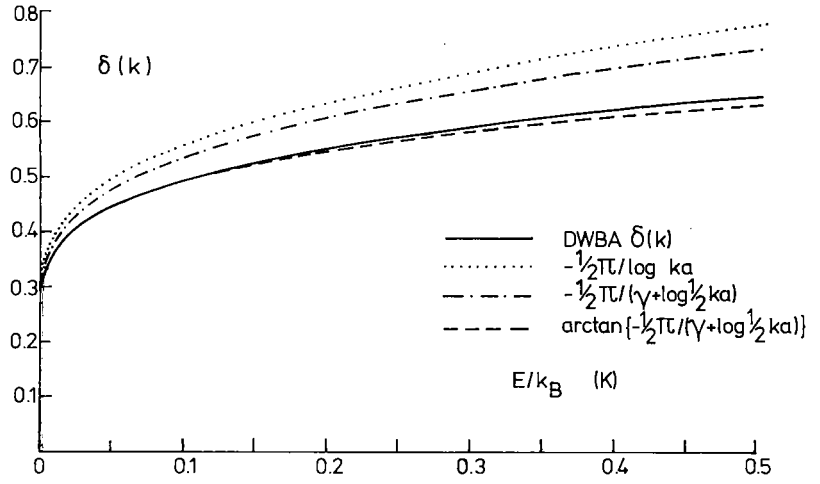

Fig. 6.7. The triplet phase shift as a function of the relative energy of two H-atoms for the two-dimensional scattering model.

potential may lead to large phase shifts and that in two dimensions thermal averaging cannot be avoided even for s-wave scattering in the $T \rightarrow 0$ K limit.

6.2.2. Spin-exchange relaxation

In zero magnetic field spin-exchange is known to be the dominant relaxation channel. It has been extensively studied in relation to experiments with the atomic hydrogen MASER. The classic reference for spin-exchange scattering is the paper by Balling et al. (1964). Indistinguishability effects have been discussed in detail by Pinard and Laloë (1980). Berlinsky and Shizgal (1980) did the first low-temperature calculation of the spin-exchange cross sections and phase shifts. KVS (1981) studied exchange depolarization as a function of magnetic field for a few initial and final state energies. Morrow and Berlinsky (1983) did an improved low-temperature calculation, using the best currently available potential energy curves and also calculated spin-exchange between atoms in the adsorbed state. Statt (1984) analyzed the magnetic field dependence. Following the line of Pinard and Laloë (1980), Bouchaud and Lhuillier (1985) recently reanalyzed spin-exchange in relation to a study of novel spin-wave modes in H↓. To our knowledge, in all, except the KVS calculation, spin-exchange was treated as an elastic process. In this section we aim to review the essentials of spin-exchange, including the field dependence. We shall discuss why the process, while dominant for $B = 0$, is completely negligible in high fields, unless the gas is brought out of thermal equilibrium with respect to the population of c- and d-hyperfine levels, for instance by absorption of microwave radiation.

We also choose to discuss spin-exchange within the golden-rule approach used throughout this section. This implies explicit incoherent summations over initial and final states, which is correct as long as the phase of the wavefunction may be treated as a random property such as in a system in thermal equilibrium. Usually (see for instance Balling et al. 1964), spin-exchange is treated within the density-matrix formalism, which implicitly keeps track of the occupation of all states. This is of course extremely convenient for calculational purposes but has the disadvantage that the contributions of the various spin-exchange channels do not appear in a transparent manner. Another feature of the density matrix is that it enables the user to keep track of the phase of the wavefunction. This is indispensable if one is interested in coherently excited systems such as spin-exchange in a hydrogen maser but is merely ballast for our present purpose where we are interested in T_1-like relaxation phenomena in a (quasi-)thermal system.

We start with the matrix element in the expression for the transition rate (eq. 6.78). For spin-exchange the two-body T-operator is given by eq. (6.10a) where $H = H_0 + V$ and $H_0 = K + H_Z + H_{hf}$ (analogous to eq. 3.1). The $\{|i\rangle\}$ and $\{|f\rangle\}$ are eigenstates of H_0. The interaction $V = V_D + V_{exch}$ enables the transition and describes the interaction between the two H-atoms. The triplet potential is obtained for V acting on a pair state with total electronic spin $S = 1$, and the singlet for $S = 0$. Using the G_+ operator, we rewrite the transition amplitude,

$$\langle f|T|i\rangle = \lim_{\eta\to 0} i_\eta \langle f|VG_+|i\rangle \,. \tag{6.86}$$

The G_+ operator induces the proper distortion of the initial state due to the interaction between the atoms. As in section 6.1, we use the sudden approximation for the spin part of the incoming wavefunction (Wigner spin rule), neglecting the time dependence of $|SM_SIM_I\rangle$, arising from the off-diagonal elements of H_{hf} (see table 6.1). References to the limitations of these approximations which may break down at very low temperatures are given by Pinard and Laloë (1980).

To evaluate the T-matrix we project the hyperfine states h_1 and h_2 onto the total spin basis $\{|SM_SIM_I\rangle\}$

$$\begin{aligned}|i\rangle = |h_1h_2; \boldsymbol{k}\rangle &= \sqrt{\tfrac{1}{2}}[|h_1h_2; \boldsymbol{k}) + |h_2h_1; -\boldsymbol{k})] \\ &= \sqrt{\tfrac{1}{2}} \sum_{SM_SIM_I} [|SM_SIM_I; \boldsymbol{k}\rangle\langle SM_SIM_I|h_1h_2) \\ &\qquad + |SM_SIM_I; -\boldsymbol{k}\rangle\langle SM_SIM_I|h_2h_2)] \,. \end{aligned} \tag{6.87}$$

A similar expression holds for the final pair state $|f\rangle$. Here, as is commonly done, we treat the H-atoms as simple composite bosons. The states $|\boldsymbol{k})$ represent plane waves. Pinard and Laloë also analyzed the internal structure of the atoms. The spin-projection amplitudes $\langle SM_SIM_I|h_2h_1\rangle$ are summarized in table 6.4a.

Substituting eq. (6.87) into (6.86) and taking advantage of the diagonality of V within the total spin representation, we find for the T-matrix

$$\begin{aligned}\langle f|T|i\rangle = \sum_{IM_I} &[(h_1'h_2'|00IM_I\rangle\langle 00IM_I|h_1h_2)(\boldsymbol{k}'|V^sG_+|\boldsymbol{k}) \\ &+ (h_1'h_2'|00IM_I\rangle\langle 00IM_I|h_2h_1)(\boldsymbol{k}'|V^sG_+|-\boldsymbol{k})] \\ + \sum_{M_SIM_I} &[(h_1'h_2'|1M_SIM_I\rangle\langle 1M_SIM_I|h_1h_2)(\boldsymbol{k}'|V^tG_+|\boldsymbol{k}) \\ &+ (h_1'h_2'|1M_SIM_I\rangle\langle 1M_SIM_I|h_2h_1)(\boldsymbol{k}'|V^tG_+|-\boldsymbol{k})] \,. \end{aligned} \tag{6.88a}$$

With the substitution

$$\sum_{M_S I M_I} |1 M_S I M_I\rangle\langle 1 M_S I M_I| \equiv 1 - \sum_{I M_I} |00 I M_I\rangle\langle 00 I M_I| ,$$

and using the relation $\langle 00 I M_I|\mathrm{h}_2\mathrm{h}_1\rangle = (-1)^I \langle 00 I M_I|\mathrm{h}_1\mathrm{h}_2\rangle$, eq. (6.88a) is drastically simplified

$$\begin{aligned}\langle \mathrm{i}|T|\mathrm{f}\rangle = \sum_{I M_I} (\mathrm{h}_1'\mathrm{h}_2'|00 I M_I\rangle\langle 00 I M_I|\mathrm{h}_1\mathrm{h}_2)[(\boldsymbol{k}'|V_{\mathrm{s}} G_+|\boldsymbol{k}\rangle_I - (\boldsymbol{k}'|V_{\mathrm{t}} G_+|\boldsymbol{k}\rangle_I] \\ + (\boldsymbol{k}'|V_{\mathrm{s}} G_+|\boldsymbol{k}) \delta_{\mathrm{h}_1,\mathrm{h}_1'} \delta_{\mathrm{h}_2,\mathrm{h}_2'} + (\boldsymbol{k}|V_{\mathrm{t}} G_+|-\boldsymbol{k}) \delta_{\mathrm{h}_1,\mathrm{h}_1'} \delta_{\mathrm{h}_2,\mathrm{h}_2'} ,\end{aligned} \tag{6.88b}$$

where we have suppressed the explicit use of $\lim_{\eta\to 0} \mathrm{i}\eta$ and

$$|\boldsymbol{k}\rangle_I \equiv |\boldsymbol{k}) + (-1)^I |-\boldsymbol{k}) . \tag{6.88c}$$

Expanding eq. (6.88b) into partial waves, one is left (for $\mathrm{h}_1, \mathrm{h}_2 \neq \mathrm{h}_1', \mathrm{h}_2'$, which we assume from now on) at most with one term. For I = even this is the $|0000\rangle$ term; for I = odd this is one of the three $|001 M_I\rangle$ terms. Since both the singlet and triplet potential are isotropic, the orbital angular momentum is conserved during the collision and the angular dependence may be factored out of the T-matrix. Squaring the T-matrix and integrating over the angles $\hat{\boldsymbol{k}}$ and $\hat{\boldsymbol{k}}'$ expressions may be derived, using eq. (6.78d), for cross sections σ^+ and σ^- corresponding to even and odd partial waves respectively:

$$\begin{aligned}\sigma^+_{\mathrm{h}_1\mathrm{h}_2\to\mathrm{h}_1'\mathrm{h}_2'}(k) &= 8|(\mathrm{h}_1'\mathrm{h}_2'|0000\rangle|^2 \, |\langle 0000|\mathrm{h}_1\mathrm{h}_2)|^2 \sigma^+(k) , \\ \sigma^-_{\mathrm{h}_1\mathrm{h}_2\to\mathrm{h}_1'\mathrm{h}_2'}(k) &= \sum_{M_I=-1}^{+1} 8|(\mathrm{h}_1'\mathrm{h}_2'|001 M_I\rangle|^2 \, |\langle 001 M_I|\mathrm{h}_1\mathrm{h}_2)|^2 \sigma^-(k) ,\end{aligned} \tag{6.89a}$$

where at most one term in the sum contributes, as may be seen from table 6.4a and

$$\sigma^{\pm}(k) = \left(\frac{\mu}{\hbar^2}\right)^2 \frac{8\pi}{k^3 k'} \sum_{\{l^{\pm}\}} (2l+1)|T_l(k, k')|^2 . \tag{6.89b}$$

The $\{l^+\}$ and $\{l^-\}$ represent even and odd integers, respectively. Further,

$$\begin{aligned}T_l(k, k') &= \int \mathrm{d}r \, j_l^0(k'r) V^{\mathrm{t}} F_l^{\mathrm{t}}(k, r) - \int \mathrm{d}r \, j_l^0(k'r) V^{\mathrm{s}} F_l^{\mathrm{s}}(k, r) , \\ j_l^0(kr) &\equiv kr j_l(kr) ,\end{aligned} \tag{6.89c}$$

where $F_l^s(kr)$ and $F_l^t(kr)$ are radial wavefunctions distorted by singlet and triplet potential, respectively (see eq. 6.80) and $j_l(kr)$ is a Bessel function. For thermally activated processes $\sigma^{\pm}(k)$ vanishes below the threshold value. Treating the scattering as elastic ($k = k'$), the cross sections are usually given in terms of the triplet and singlet phase shifts

$$\sigma^{\pm}(k) = (2\pi/k^2) \sum_{\{l^{\pm}\}} (2l+1) \sin^2(\eta_l^t - \eta_l^s) . \tag{6.89d}$$

Equation (6.89a) shows very concisely which spin-exchange transitions are allowed within the sudden approximation (Wigner spin rule), at the same time providing the field dependence. For a precise determination of the cross sections, both the singlet and the triplet phase shift should be known to high accuracy. In particular, the singlet phase shift is extremely sensitive for small variations in the potential and likely to be not accurately known. In fig. 6.8 we show the results of Berlinsky and Shizgal (1980). Note the important contribution (σ_5) of the $H_2(14,5)$ resonance to the σ^- cross section. In view of the recent experimental observation by Dabrowski (1984) that $H_2(14,5)$ is not quasi-bound, this contribution is likely to be much smaller. In fig. 6.9 we show the thermally averaged spin-exchange cross sections calculated by Berlinsky and Shizgal (1980). Only the s-wave contribution is seen to be important for typical experimental conditions, $T < 1$ K. These results were obtained with the (1965) results of Kolos and Wolniewicz for the singlet and triplet potentials. With better potentials (Kolos and Wolniewicz 1974, 1975), which are refinements to the 1965 results, the cross sections are reduced by approximately a factor 2 or 3, witnessing the strong dependence of spin-exchange on the detailed shape

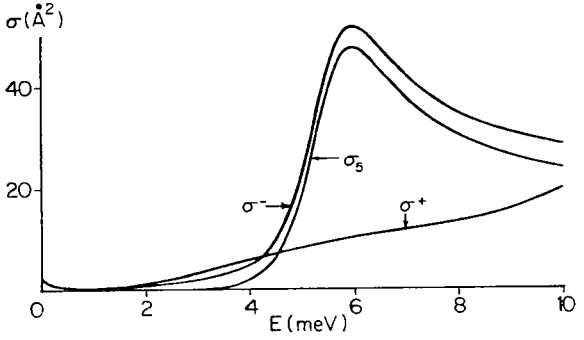

Fig. 6.8. The spin-exchange cross section σ^+ and σ^- as a function of the relative energy. Only the σ^+ does not vanish for $E \to 0$. σ_5 is the contribution of the $v = 14$, $L = 5$ level to σ^- (after Berlinsky and Shizgal 1980).

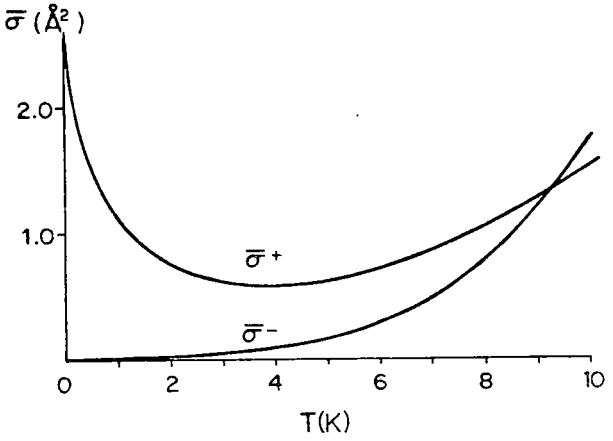

Fig. 6.9. The thermally averaged spin exchange cross sections $\bar{\sigma}^+$ and $\bar{\sigma}^-$ as calculated by Berlinsky and Shizgal (1980). Note that at low temperature s-wave scattering ($\bar{\sigma}^+$) is dominant.

of the potential (Morrow and Berlinsky 1983, Bouchaud and Lhuillier 1985). From fig. 6.9 one notes that $\bar{\sigma}^+$ is of order 1 Å^2 which is much smaller than the room temperature value $\bar{\sigma}^+ \simeq 23$ Å^2 (Allison 1972) and therefore attractive for those interested in a cryogenic hydrogen maser (Berlinsky and Hardy 1981). Nevertheless, as a relaxation cross section this value is extremely large. Comparing eq. (6.89a) with a diffusion cross section estimated from the diffusion constant of Lhuillier (1983), $\sigma_D \simeq 16$ Å^2 at $T = 0.5$ K, one finds that one out of 10–20 collisions leads to spin-exchange. In high field all but the bd $\rightleftarrows$ ac spin-exchange cross sections are suppressed by a factor $\varepsilon^2 = [a/(4\mu_B)]^2 (\simeq 10^{-5}$ for $B = 10$ T).

We consider two examples in detail; first the high-field, low-temperature limit, where only the a- and b-states are populated in thermal equilibrium. We use eq. (6.89b) and table 6.4a to analyze the field dependence of the various cross sections for aa, ab and bb collisions and the exchange depolarization rate as introduced by KVS.

(a) aa-collisions. In aa-collisions only even partial waves contribute as may be seen from table 6.4, where the total spin states corresponding to even partial waves ($I + S$, even) are labelled with an asterisk. As a consequence all σ^- cross sections vanish identically

$$\sigma^+_{aa\to ac}(k) = 8|(ac|0000\rangle|^2\,|\langle 0000|aa)|^2\sigma^+(k)$$
$$= 2\varepsilon^2\eta^2(\eta^2 - \varepsilon^2)^2\sigma^+(k) \quad (k \geqslant k_{ac})\,. \tag{6.90a}$$

Here k_{ac} is the momentum threshold value for the a→c transition.
Likewise:

$$\sigma^{+}_{aa\to bd}(k) = 2\varepsilon^2\eta^2\sigma^{+}(k) \quad (k \geq k_{ad}) , \tag{6.90b}$$

$$\sigma^{+}_{aa\to cc}(k) = 8\varepsilon^4\eta^4\sigma^{+}(k) \quad (k \geq 2k_{ac}) . \tag{6.90c}$$

(b) ab-collisions.

$$\sigma^{+}_{ab\to bc}(k) = 0 , \tag{6.90d}$$

$$\sigma^{-}_{ab\to bc}(k) = 8|(bc|001\,-1\rangle|^2\,|\langle 001\,-1|ab)|^2\sigma^{-}(k)$$

$$= 2\varepsilon^2\eta^2\sigma^{-}(k) \quad (k \geq k_{ac}) . \tag{6.90e}$$

(c) bb-collisions. Here, the exchange of the electronic spins does not affect the hyperfine states of the individual atoms which trivially excludes any spin relaxation.

This example shows that the cross section decreases as $1/B^2$ with growing magnetic field. In fact the rate decreases even faster. Only atoms from the high energy tail of the momentum distribution carry with them enough energy to enable the transition. As this fraction of atoms drops off exponentially with magnetic field, spin-exchange depolarization is entirely negligible in the high-field/low-temperature limit. Note further that spin-exchange does not lead to b→a relaxation in H↓↕. These features cause nuclear magnetic b→a relaxation to be dominant over spin-exchange in high field (see section 6.2.3).

As a second example we treat bd→ac spin-exchange. From table 6.4a it may be seen that this is the only spin-exchange channel which is not suppressed in high magnetic fields:

$$\sigma^{+}_{bd\to ac}(k) = 8|(ac|0000\rangle|^2\,|\langle 0000|bd)^2\sigma^{+}(k)$$

$$= \tfrac{1}{2}(\eta^2 - \varepsilon^2)^2\bar{\sigma}^{+}$$

$$\simeq \tfrac{1}{2}\bar{\sigma}^{+} \quad (\text{for } B \gg 5\times 10^{-2}T) , \tag{6.91a}$$

$$\sigma^{-}_{bc\to ac}(k) = 8|(ac|0010\rangle|^2\,|\langle 0010|bd)|^2\sigma^{-}(k)$$

$$= \tfrac{1}{2}\bar{\sigma}^{-} . \tag{6.91b}$$

A compilation of all spin-exchange cross sections derived using eq. (6.89a) is given in table 6.13.

Table 6.13

Compilation of all spin-exchange cross sections $\bar{\sigma}_{h_1h_2h_1'h_2'}$. The Δh_i columns contain the number of h_i-atoms lost (−) or gained (+) per event. The weight reflects the relative contribution to the sum over all initial and final states (see eq. 6.78b). Note that all but the ac→bd spin-exchange contributions vanish as $\varepsilon^2 \sim B^{-2}$ in high field. Moreover, many of the terms are strongly suppressed in high field due to the inelastic nature of the process.

$h_1h_2 \to h_1'h_2'$	Δa	Δb	Δc	Δd	Weight	$\bar{\sigma}_{h_1h_2\to h_1'h_2'}$
aa→cc	−2	0	+2	0	$\frac{1}{4}\hat{a}^2$	$\bar{\sigma}^+(aa\to cc)8\varepsilon^4\eta^4$
cc→aa	+2	0	−2	0	$\frac{1}{4}\hat{c}^2$	$\bar{\sigma}^+(cc\to ac)8\varepsilon^4\eta^4$
aa→ac	−1	0	+1	0	$\frac{1}{2}\hat{a}^2$	$\bar{\sigma}^+(aa\to ca)2\varepsilon^2\eta^2(\eta^2-\varepsilon^2)^2$
ac→aa	+1	0	−1	0	$\frac{1}{2}\hat{a}\hat{c}$	$\bar{\sigma}^+(ac\to aa)2\varepsilon^2\eta^2(\eta^2-\varepsilon^2)^2$
aa→bd	−2	+1	0	+1	$\frac{1}{2}\hat{a}^2$	$\bar{\sigma}^+(aa\to bd)2\varepsilon^2\eta^2$
bd→aa	+2	−1	0	−1	$\frac{1}{2}\hat{b}\hat{d}$	$\bar{\sigma}^+(bd\to aa)2\varepsilon^2\eta^2$
ac→bd	−1	+1	−1	+1	$\hat{a}\hat{c}$	$\bar{\sigma}^+(ac\to bd)\frac{1}{2}(\eta^2-\varepsilon^2)^2$
bd→ac	+1	−1	+1	−1	$\hat{b}\hat{d}$	$\bar{\sigma}^+(bd\to ac)\frac{1}{2}(\eta^2-\varepsilon^2)^2$
ac→bd	−1	+1	−1	+1	$\hat{a}\hat{c}$	$\bar{\sigma}^-(ac\to bd)\frac{1}{2}$
bd→ac	+1	−1	+1	−1	$\hat{b}\hat{d}$	$\bar{\sigma}^-(bd\to ac)\frac{1}{2}$
ac→cc	−1	0	+1	0	$\frac{1}{2}\hat{a}\hat{c}$	$\bar{\sigma}^+(ac\to cc)2\varepsilon^2\eta^2(\eta^2-\varepsilon^2)^2$
cc→ac	+1	0	−1	0	$\frac{1}{2}\hat{c}^2$	$\bar{\sigma}^+(cc\to ac)2\varepsilon^2\eta^2(\eta^2-\varepsilon^2)^2$
bd→cc	0	−1	+2	−1	$\frac{1}{2}\hat{b}\hat{d}$	$\bar{\sigma}^+(bd\to cc)2\varepsilon^2\eta^2$
cc→bd	0	+1	−2	+1	$\frac{1}{2}\hat{c}^2$	$\bar{\sigma}^+(cc\to bd)2\varepsilon^2\eta^2$
ab→bc	−1	0	+1	0	$\hat{a}\hat{b}$	$\bar{\sigma}^-(ab\to bc)2\varepsilon^2\eta^2$
bc→ab	+1	0	−1	0	$\hat{b}\hat{c}$	$\bar{\sigma}^-(bc\to ab)2\varepsilon^2\eta^2$
ad→cd	−1	0	+1	0	$\hat{a}\hat{d}$	$\bar{\sigma}^-(ad\to cd)2\varepsilon^2\eta^2$
cd→ad	+1	0	−1	0	$\hat{c}\hat{d}$	$\bar{\sigma}^-(cd\to ad)2\varepsilon^2\eta^2$

6.2.2.1. Relation to the rate equations

With the overall rate of spin-exchange events given by eq. (6.78) and the cross sections given in table 6.13, it is straightforward to derive the rate equations for spin-exchange. The result is given somewhat schematically in table 6.14, for zero field and $T \gg 68$ mK. To be specific we consider a ⇄ c

Table 6.14

Summary of all zero-field contributions to the spin-exchange transition rate for $T \gg 68$ mK where inelastic effects are negligible. The h_i columns contain the number of h_i-atoms lost (−) or gained (+) per event. This number appears as a prefactor to the rate constant $G_E(h_1h_2 \leftrightarrow h_1'h_2')$ in the rate equations. The weight reflects the density dependence of the various terms.

$h_1h_2 \leftrightarrow h_1'h_2'$	$\dot{a}$	$\dot{b}$	$\dot{c}$	$\dot{d}$	$G_E(h_1h_2 \leftrightarrow h_1'h_2')$	Weight
aa↔cc	−2	0	+2	0	$\frac{1}{8}\bar{v}\bar{\sigma}^+$	(a^2-c^2)
aa↔bd	−2	+1	0	+1	$\frac{1}{4}\bar{v}\bar{\sigma}^+$	(a^2-bd)
ac↔bd	−1	+1	−1	+1	$\frac{1}{2}\bar{v}\bar{\sigma}^-$	$(ac-bd)$
bd↔cc	0	−1	+2	−1	$\frac{1}{4}\bar{v}\bar{\sigma}^+$	$(bd-c^2)$
ab↔bc	−1	0	+1	0	$\frac{1}{2}\bar{v}\bar{\sigma}^-$	$(ab-bc)$
ad↔cd	−1	0	+1	0	$\frac{1}{2}\bar{v}\bar{\sigma}^-$	$(ad-cd)$

relaxation in detail. For this we sum the $\dot{a}$ and $\dot{c}$ columns with the appropriate weights, accounting explicitly for the number of a- and c-state atoms gained or lost per event. Subtracting the results we find

$$\frac{\mathrm{d}}{\mathrm{d}t}(a-c) = -n^2\bar{v}\bar{\sigma}^+(\hat{a}+\hat{c})(\hat{a}-\hat{c}) - n^2\bar{v}\bar{\sigma}^-(\hat{b}+\hat{d})(\hat{a}-\hat{c})$$

$$= -\frac{1}{T_1}(a-c)\,. \tag{6.92a}$$

For the special case that $\hat{a} = \hat{b} = \hat{c} = \hat{d} = \frac{1}{4}$, this leads to the well-known result (see for instance Berlinsky and Shizgal 1980) that

$$\frac{1}{T_1} = \tfrac{1}{2}\bar{v}n(\bar{\sigma}^+ + \bar{\sigma}^-)\,. \tag{6.92b}$$

Another interesting example is the high-field limit for $T \gg 68$ mK. From table 6.13, one finds only the ac $\rightleftarrows$ bd spin-exchange channel is left. Hence, guided by eq. (6.78) one finds

$$\begin{aligned}
\dot{a} &= -\tfrac{1}{2}\bar{v}(\bar{\sigma}^+ + \bar{\sigma}^-)(ac - bd)\,,\\
\dot{b} &= +\tfrac{1}{2}\bar{v}(\bar{\sigma}^+ + \bar{\sigma}^-)(ac - bd)\,,\\
\dot{c} &= -\tfrac{1}{2}\bar{v}(\bar{\sigma}^+ + \bar{\sigma}^-)(ac - bd),\\
\dot{d} &= +\tfrac{1}{2}\bar{v}(\bar{\sigma}^+ + \bar{\sigma}^-)(ac - bd)\,.
\end{aligned} \tag{6.93a}$$

Comparing with the notation of section 5 (eq. 5.15) one finds for the rate constant for spin-exchange

$$G_{\mathrm{E}} = \tfrac{1}{2}\bar{v}(\bar{\sigma}^+ + \bar{\sigma}^-)\,. \tag{6.93b}$$

In particular,

$$\frac{\mathrm{d}}{\mathrm{d}t}(ac - bd) = \dot{a}c + a\dot{c} - \dot{b}d - b\dot{d}$$

$$= -\tfrac{1}{2}\bar{v}(\bar{\sigma}^+ + \bar{\sigma}^-)(ac - bd)\,. \tag{6.93c}$$

Hence, in high field, spin-exchange drives the system to a state in which $(a/b) = (d/c)$. The relaxation time T_1 is also as given by eq. (6.92b). This effect plays an important role in ESR experiments in high field where it may prevent the experimental modification of the a/b ratio by selectively pumping the a$\rightarrow$d or b$\rightarrow$c ESR transitions.

6.2.3. Dipolar relaxation

In high magnetic fields only the weak interatomic dipolar forces are effective in establishing thermal equilibrium between the various hyperfine levels. We distinguish nuclear-spin relaxation between a and b levels or c and d levels, and electron-spin relaxation, between the lower and upper pair of hyperfine levels. For convenience these names are used over the full range of magnetic fields although the simple distinction is only correct in a strict sense when hyperfine admixtures are absent or negligible. Apart from these intrinsic processes, dipolar interactions with impurity spins on the substrate surface may also lead to relaxation.

The nuclear relaxation process was first studied by Statt and Berlinsky (1980), predicting the double-polarized state (H$\downarrow\downarrow$), and also by Siggia and Ruckenstein (1981) in relation to collective phenomena in the Bose condensed gas. Factor-of-two inaccuracies were resolved in a careful study by Ahn et al. (1982, 1983) who also accounted for the inelastic ($k \neq k'$) nature of the relaxation process. Lagendijk et al. (1984) showed the process to be particularly suited to look for exchange effects of complete hydrogen atoms and used this to demonstrate the Bose nature of the H-atom.

The surface process was first analyzed by Lagendijk (1982) in a two-dimensional picture, predicting an anisotropy depending on the direction of the magnetic field with respect to the surface normal. Improved calculations were done by Ruckenstein and Siggia (1982), Statt (1982) and Ahn et al. (1982), all within the $2\frac{1}{2}$-dimensional model. The last authors also discuss a reduction of the anisotropy due to surface roughness of the helium film substrate. A full three-dimensional calculation of the surface process was done by van den Eijnde et al. (1983).

The electronic relaxation process was studied by KVS (1981) to estimate the dipolar depolarization rate in high field. The process was also considered by Lagendijk et al. (1984).

In the coming sections we shall discuss why the dipolar interaction although much weaker than the direct and exchange forces, plays an important role in spin relaxation. First, we present general features of the dipolar interaction, showing how it may be decomposed into terms transforming like the spherical harmonics $Y_2^m(\hat{r})$. Subsequently, we study the transition rate from the double-polarized state H$\downarrow\downarrow$. Comparing with surface Van der Waals recombination, we discuss the result of Statt and Berlinsky (1980) that at low temperatures the nuclear dipolar relaxation process is limiting the overall decay of the sample. Then we turn to nuclear relaxation on a helium surface. The section is concluded with a discussion of the electronic relaxation process, showing that in high magnetic fields it dominates over spin-exchange.

6.2.3.1. Dipolar relaxation—general

In this section we discuss both the nuclear and electronic depolarization of pure H↓↕, i.e., a gas of only b-state atoms. To calculate these transition rates we pick up the treatment of section 6.2.1 at eq. (6.78). The T-operator is given by eq. (6.10a) where $H = H_0 + V_{dd}$ and $H_0 = K + H_Z + H_{hf} + V_D + V_{exch}$ (analogous to eq. 3.1). The $\{|i\rangle\}$ and $\{|f\rangle\}$ are eigenstates of H_0, which are written as a linear combination of waves distorted by the singlet and the triplet interactions. Here the collision is treated within the sudden approximation with regard to the hyperfine interaction (Wigner spin rule). This approximation was checked against a close-coupling treatment by Ahn et al. (1983). The dipolar interaction between the atoms is given by V_{dd},

$$V_{dd} = \frac{\mu_0 \hbar^2}{4\pi}\left(\frac{1}{r}\right)^3 \gamma_e^2 \times [f(\boldsymbol{s}_1, \boldsymbol{s}_2) - (\gamma_n/\gamma_e)\{f(\boldsymbol{s}_1, \boldsymbol{i}_2) + f(\boldsymbol{i}_1, \boldsymbol{s}_2)\} + (\gamma_n/\gamma_e)^2 f(\boldsymbol{i}_1, \boldsymbol{i}_2)], \tag{6.94a}$$

where the operator expressions $f(\boldsymbol{i}_1, \boldsymbol{i}_2)$ (eq. 3.9b) are defined in terms of second-rank tensor operators by

$$f(\boldsymbol{s}_1, \boldsymbol{i}_2) = \sum_{m=-2}^{+2} T_2^m Y_2^{m*}(\hat{\boldsymbol{r}}),$$

$$T_2^0 \equiv (6\pi/5)^{1/2}[s_z i_z - \tfrac{1}{4}(s_+ i_- + s_- i_+)],$$

$$T_2^{\pm 1} \equiv \mp(6\pi/5)^{1/2}[s_\pm i_z + s_z i_\pm], \quad T_2^{\pm 2} \equiv (6\pi/5)^{1/2} s_\pm i_\pm . \tag{6.94b}$$

Here the s_+ and s_- are raising and lowering operators for the spin angular momentum. s_z is the component of $\boldsymbol{s}$ along the quantization axis. Similar definitions hold for i_+, i_- and i_z. The matrix elements of $f(\boldsymbol{s}_1, \boldsymbol{s}_2)$ and $-\{f(\boldsymbol{s}_1, \boldsymbol{i}_2) + f(\boldsymbol{i}_1, \boldsymbol{s}_2)\}$ in the total spin representation, $\{|SM_S IM_I\rangle\}$, are given in tables 6.8 and 6.9, respectively. The matrix elements of $f(\boldsymbol{i}_1, \boldsymbol{i}_2)$ are identical to those of $f(\boldsymbol{s}_1, \boldsymbol{s}_2)$.

The dipolar interaction is very weak in comparison to the direct and exchange interactions. At the zero-crossing of the triplet potential ($r \simeq 3.66$ Å) the electron–electron contribution represents only 51 mK, which is more than two orders of magnitude weaker than the triplet interaction around its minimum. Hence, the motion of the particles is

negligibly distorted by the dipolar interaction, enabling an accurate perturbative calculation within the distorted-wave Born approximation (DWBA). The electron–proton term is even weaker by a factor $\gamma_e/\gamma_n = 658$. The proton–proton term is negligible for all practical purposes. The range of the dipolar interaction is large in comparison to the range of the triplet potential, so that even a simple plane-wave Born approximation (PWBA) yields accurate results. This feature makes dipolar relaxation, in contrast to spin-exchange, into a property which is very insensitive for the exact shape of the potential and as such ideal for studying particle-exchange effects in H↓‡, as shown by Lagendijk et al. (1984).

In H↓‡ the initial-state pair wavefunction involves a bb-pair and is distorted purely by the triplet potential. In principle, the final state may contain both triplet and singlet character. Within the DWBA the transition amplitude is given by

$$\langle \mathrm{f}|T|\mathrm{i}\rangle = \langle \mathrm{f}|V_{\mathrm{dd}}|\mathrm{i}\rangle = \tfrac{1}{2}(\mathrm{f}|[1+P]V_{\mathrm{dd}}[1+P]|\mathrm{i}) = \sqrt{2}(\mathrm{f}|V_{\mathrm{dd}}|\mathrm{i}) \,. \tag{6.95a}$$

Here we have treated the H atoms as simple composite bosons and used the invariance of V_{dd} under permutation of total atoms. Note that only one side of the T-matrix needs to be symmetrized. A complete treatment, also addressing the internal structure of the atoms, was given by Ahn et al. (1983).

To evaluate the T-matrix within the sudden approximation, we reexpress the initial state in the total spin basis $\{|SM_SIM_I\rangle\}$:

$$\begin{aligned} |\mathrm{i}\rangle = |\mathrm{h}_1\mathrm{h}_2; \boldsymbol{k}\rangle &= \sqrt{\tfrac{1}{2}}\,[|\mathrm{h}_1\mathrm{h}_2; \boldsymbol{k}) + |\mathrm{h}_2\mathrm{h}_1; -\boldsymbol{k})] \\ &= \sqrt{\tfrac{1}{2}} \sum_{SM_SIM_I} [|SM_SIM_I; \boldsymbol{k}) + (-1)^{S+I}|SM_SIM_I; -\boldsymbol{k})] \\ &\qquad \times \langle SM_SIM_I|\mathrm{h}_1\mathrm{h}_2) \\ &\equiv \sqrt{\tfrac{1}{2}} \sum_{SM_SIM_I} |SM_SIM_I; \boldsymbol{k}\rangle_{S+I} \langle SM_SIM_I|\mathrm{h}_1\mathrm{h}_2) \,. \end{aligned} \tag{6.95b}$$

Here we have used the relation $\langle SM_SIM_I|\mathrm{h}_2\mathrm{h}_1) = (-1)^{I+S}\langle SM_SIM_I|\mathrm{h}_1\mathrm{h}_2)$ and the shorthand notation of eq. (6.88c) (see table 6.4). States with $S = 1$ ($S = 0$) are implicitly assumed to be distorted by the triplet (singlet) potential. Analogously, for the final state we have

$$|\mathrm{f}) = |\mathrm{h}_1\mathrm{h}_2; \boldsymbol{k}) = \sum_{SM_SIM_I} |SM_SIM_I; \boldsymbol{k})\langle SM_SIM_I|\mathrm{h}_1\mathrm{h}_2) \,. \tag{6.95c}$$

Table 6.15

Summary of the transition matrix elements for electronic and nuclear relaxation starting from bb, ab and ac initial pair states. Only the terms contributing to highest order are included. The symbols c (single spin-flip) and d (double spin-flip) are defined in table 6.8. Scattering is assumed to proceed exclusively via s-waves in the initial state. All terms have a common factor, $(\mu_0\hbar^2/4\pi)\,(1/r)^3(6\pi/5)^{1/2}$.

	bb	ab	ac
aa		$\alpha\gamma_e\gamma_n c[1+\varepsilon\gamma_e/\gamma_n]$	
ab	$\alpha\gamma_e\gamma_n c[1+\varepsilon\gamma_e/\gamma_n]$		$\alpha\gamma_e\gamma_n c^*[1+\varepsilon\gamma_e/\gamma_n]$
ac		$\frac{1}{2}\alpha c\gamma_e^2$	
ad			$\alpha c\gamma_e^2$
bb		$\alpha\gamma_e\gamma_n c^*[1+\varepsilon\gamma_e/\gamma_n]$	
bc	$\alpha c\gamma_e^2$		
bd		$-\frac{1}{2}\alpha c\gamma_e^2$	
cc	$d\gamma_e^2$		
cd		$-\frac{1}{2}d\gamma_e^2$	
dd			$d\gamma_e^2$

Substituting eqs. (6.95b) and (6.95c) into (6.95a) we find for the T-matrix

$$\langle f|V^{dd}|i\rangle = \sum_{SM_SIM_I} \sum_{S'M_{S'}I'M_{I'}} (h_1'h_2'|S'M_{S'}I'M_{I'}\rangle\langle SM_SIM_I|h_1h_2) \times (S'M_{S'}I'M_{I'};\boldsymbol{k}'|V_{dd}|SM_SIM_I;\boldsymbol{k}\rangle_{S+I}\,. \tag{6.95d}$$

In H↓, the only available initial pair states are of the type $|bb;\boldsymbol{k}\rangle$, $|ab;\boldsymbol{k}\rangle$ and $|aa;\boldsymbol{k}\rangle$. Equation (6.95) and eq. (6.94), in combination with table 6.8 and table 6.9, enable us to calculate the contributions of all final states allowed by V_{dd}. The results are listed in table 6.15.

From table 6.15, one finds that the dominant nuclear relaxation process is the bb→ab channel. For electronic relaxation, two spin matrix elements are of the same order. These correspond to bb→bc and bb→cc channels. The latter may be excluded as it is a double (electron) spin-flip process. These are negligible in comparison to single spin-flip processes due to the lack of high momentum states in the translational bath which are required for energy conservation in the transition.

6.2.3.2. Nuclear spin relaxation in the bulk gas

For the bb→ab relaxation channel, the transition matrix (eq. 6.95d) reduces to

$$\langle \mathrm{f}|V_{\mathrm{dd}}|\mathrm{i}\rangle = (\mu_0\hbar^2/4\pi)\gamma_{\mathrm{e}}\gamma_{\mathrm{n}}(3\pi/10)^{1/2}(1+\varepsilon\gamma_{\mathrm{e}}/\gamma_{\mathrm{n}}) \times [(\boldsymbol{k}'|\, y_2^1{}^*(\hat{\boldsymbol{r}})/r^3|\boldsymbol{k}) + (\boldsymbol{k}'|\, y_2^1{}^*(\hat{\boldsymbol{r}})/r^3|-\boldsymbol{k})]\,. \tag{6.96}$$

The ab$\rightarrow$aa channel leads to identically the same result. The factor $(1+\varepsilon\gamma_{\mathrm{e}}/\gamma_{\mathrm{n}}) = (1+16.68/B)$, with B in Tesla, arises since both the $\gamma_{\mathrm{e}}\gamma_{\mathrm{n}}$ and the γ_{e}^2 terms of V_{dd} contribute to the rate. The former represents the process where the nuclear spin is flipped due to the passage of another atom carrying a Bohr magneton. The latter term corresponds to an electronic spin-flip, allowed energetically due to the presence of the spin-up admixture in the a-state, vanishing in high field as $1/B$ with the ε-admixture of spin-up. For typical magnetic fields used in the experiments $\varepsilon \simeq \gamma_{\mathrm{n}}/\gamma_{\mathrm{e}}$ and the two processes contribute by approximately the same amount.

Using eq. (6.78d) to relate the T-matrix to the scattering cross section, expanding $|\boldsymbol{k})$ and $|\boldsymbol{k}')$ into partial waves (see eq. 6.80a) and integrating over all angles $\hat{\boldsymbol{k}}$ and $\hat{\boldsymbol{k}}'$ we find, after a tedious calculation,

$$\sigma_{\mathrm{bb}\rightarrow\mathrm{ab}}(k) = Q_{\mathrm{en}}\,1/(k'k^3)[1+(16.68/B)]^2 \times \sum_{l,l'=\mathrm{even}} |T_{l,l'}(k,k')|^2(2l+1)(2l'+1)\begin{bmatrix} l & 2 & l' \\ 0 & 0 & 0 \end{bmatrix}^2, \tag{6.97a}$$

where

$$Q_{\mathrm{en}} \equiv (24\pi/5)[(\mu_0\mu/4\pi)\gamma_{\mathrm{e}}\gamma_{\mathrm{n}}]^2 = 2.34\times10^{-24}\ \mathrm{cm}^2\,, \tag{6.97b}$$

$$T_{l,l'}(k,k') = \int \mathrm{d}r\, F_{l'}^{\mathrm{t}}(k',r)(1/r^3)F_l^{\mathrm{t}}(k,r)\,. \tag{6.97c}$$

In the relaxation process, angular momentum is transferred from the spin system to the orbital system, with the component of the angular momentum along the quantization axis being conserved. At low temperature, the $l, m_l = 0, 0 \rightarrow l, m_l = 2, \pm1$ transition is dominant. In fig. 6.10 the cross sections for the bb$\rightarrow$ab and ab$\rightarrow$bb are compared. The difference between both cross sections is due to the difference in the overlap integral (eq. 6.97c). At low relative energies, the elastic-scattering approximation breaks down. Note the cut-off at $E/k \simeq 50$ mK for the ab$\rightarrow$bb cross section. Below this threshold there is not sufficient energy in the translational motion to flip the nuclear spin. One also observes that the PWBA yields a very accurate result. From fig. 6.10 one notes that the cross section

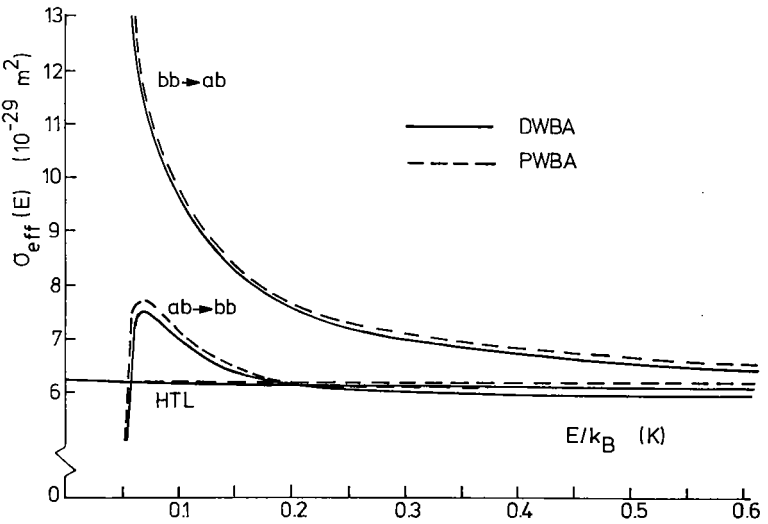

Fig. 6.10. Spin-relaxation cross sections, $\sigma_{bb\to ab}$ and $\sigma_{ab\to bb}$ as functions of energy. Also shown is the elastic scattering approximation (HTL). Each function has been calculated in DWBA (drawn curves) and in PWBA (dashed curves). The plot is for $B = 8$ T (after van den Eijnde 1984).

for b→a dipolar relaxation is of order 10^{-8} Å^2 for $T \gg 50$ mK. The reason that this very weak process is the dominant decay mechanism in high magnetic fields is that bb→ab or ab→aa spin-exchange channels do not exist (hence absent from table 6.13) and all allowed spin-exchange channels for ab initial states are strongly suppressed as they scale with $1/B^2$ and involve transitions to the c- and d-states.

The b→a transition rate $\Gamma(\mathrm{b}\to\mathrm{a})$ is found using eq. (6.78)

$$\Gamma(\mathrm{b}\to\mathrm{a})/V = \tfrac{1}{2}b^2\bar{v}\bar{\sigma}_{bb\to ab} + \tfrac{1}{2}ab\bar{v}\bar{\sigma}_{ab\to aa} = \tfrac{1}{2}bn\bar{v}\bar{\sigma}_{bb\to ab}\,. \tag{6.98a}$$

Here we have used the result (see eq. 6.96) that $\bar{\sigma}_{bb\to ab} = \bar{\sigma}_{ab\to aa}$. Rate equations of the kind used in section 5 are obtained if we identify

$$G^{v}_{ab} \equiv \tfrac{1}{2}\bar{v}\bar{\sigma}_{ab\to bb}\,, \qquad G^{v}_{ba} \equiv \tfrac{1}{2}\bar{v}\bar{\sigma}_{bb\to ab}\,. \tag{6.98b}$$

where we have used the relation $\bar{\sigma}_{ab\to bb} = \bar{\sigma}_{aa\to ab}$. Treating the system as an effective two-level system, considering only relaxation between the a and b levels and keeping track of the gain or loss of atoms per event, the rate equations become

$$\begin{aligned} \dot{b} &= -G^{v}_{ba}nb + G^{v}_{ab}na \simeq -G^{v}_{ab}(b^2 - a^2)\,, \\ \dot{a} &= +G^{v}_{ba}nb - G^{v}_{ab}na \simeq +G^{v}_{ab}(b^2 - a^2)\,. \end{aligned} \tag{6.98c}$$

The approximate expressions hold for temperatures much higher than the level splitting ($T \gg 50$ mK). The relationship between the relaxation rate constants G^{v}_{ba} and G^{v}_{ab} and the relaxation time T_1 is found by adding $\dot{a}$ and $\dot{b}$ in eq. (6.89c) and comparing with

$$\frac{d}{dt}(b-a) = -\frac{1}{T_1}(b-a)\,. \tag{6.98d}$$

One finds

$$\frac{1}{T_1} = (G^{v}_{ba} + G^{v}_{ab})n \simeq 2G^{v}_{ba}n\,. \tag{6.98e}$$

An important general relation between G^{v}_{ba} and G^{v}_{ab} is derived by assuming the system to be in thermal equilibrium ($\dot{a} = \dot{b} = 0$)

$$(G^{v}_{ab}/G^{v}_{ba}) = b/a = \exp[-(E_b - E_a)/kT]\,. \tag{6.98f}$$

To first order the b$\rightarrow$a relaxation rate will become independent of temperature for $T \rightarrow 0$ K, being dominated by s-wave scattering. Equation (6.89f) implies that G^{v}_{ab} vanishes exponentially at low temperature ($T \ll 50$ mK).

Both theoretical and experimental values for G^{v}_{ba} are given in fig. 5.15. Note the weak temperature dependence of the rate constant. This figure, taken from Lagendijk et al. (1984), also shows the dramatic importance of symmetrization. Symmetrizing H atoms as composite fermions, i.e., summing over odd l and l' in eq. (6.97a), leads to a rate constant which deviates way beyond experimental error from that with proper Bose symmetrization. As such, this result provides a clear demonstration of the Bose character of H$\downarrow\downarrow$.

An accurate expression for G^{v}_{ba} is given by van den Eijnde (1984)

$$G^{v}_{ba} = (6.329T^{1/2} + 7.572\Delta_{ab}T^{-1/2})(1 + 16.68/B)^2 \times 10^{-22}\ \mathrm{cm^3\,s^{-1}} \tag{6.99a}$$

$$\Delta_{ab} = \frac{1}{2}\frac{a}{k}[1 + 2\gamma_n \hbar B/a] \quad (\text{for } B \geq 1\,\mathrm{T})\,. \tag{6.99b}$$

6.2.3.3. Nuclear spin relaxation on the surface

For bb$\rightarrow$ab relaxation on the surface, eq. (6.96) remains valid; however, we must interpret $\boldsymbol{k}$ as a two-dimensional vector in the plane of the surface. To obtain the cross length, $|\boldsymbol{k})$ and $|\boldsymbol{k}')$ are expanded in two-dimensional

partial waves. Before we present an expression for the cross length, we give some general considerations concerning the two-dimensional relaxation process.

One of the most fascinating features of surface dipolar relaxation is the anisotropy of the rate with respect to the angle between magnetic field $\boldsymbol{B}$ and surface normal $\boldsymbol{n}$. It was first pointed out by Lagendijk (1982) that the surface rate can be made to vanish by orienting $\hat{\boldsymbol{B}}$ parallel to $\hat{\boldsymbol{n}}$. This effect may be seen from eq. (6.96). If $\hat{\boldsymbol{B}}//\hat{\boldsymbol{n}}$ the direction $\hat{\boldsymbol{r}}$ of the interatomic vector is perpendicular to $\hat{\boldsymbol{n}}$, i.e. in polar coordinates $\theta = \frac{1}{2}\pi$, which is a condition for which $Y_2^1{}^*(\hat{\boldsymbol{r}})$ vanishes.

Another interesting point is that the selection rules are affected by the presence of the surface. As discussed in section 6.1.2.2, only the component of the angular momentum along the surface normal is conserved. This implies that spin transitions can occur without a change in motional angular momentum.

Evaluating eq. (6.79d), one finds for the cross length, within the pure two-dimensional model,

$$\lambda_{h_1h_2\to h_1'h_2'} = (15/32\pi)Q_{en}[1/(k'k^2)][1+(16.68/B)]^2 \times \sum_{m=\text{even}} [\sin^2 2\theta]|T_{m,m}|^2 + \sin^2\theta\,(1+\cos^2\theta)[|T_{m,m+2}|^2 + |T_{m+2,m}|^2]\,, \tag{6.100a}$$

where θ is the angle between $\hat{\boldsymbol{B}}$ and $\hat{\boldsymbol{n}}$, and

$$T_{m,m'} = \int \mathrm{d}\rho\; y_{m'}(\rho)(1/r^3)y_m(\rho)\,. \tag{6.100b}$$

The relaxation rate may be written as

$$G_s(\theta) = G_{s,0}\sin^2 2\theta + G_{s,2}\sin^2\theta\,(1+\cos^2\theta)\,,$$

where in the elastic approximation $G_{s,0}$ and $G_{s,2}$ are given by

$$G_{s,0}(T) = (0.96 - 0.82T + 0.74T^2)[1+(16.68/B)]^2 \times 10^{-18}\ \mathrm{m^2\,s^{-1}}\,,$$

$$G_{s,2}(T) = (0.038 + 0.278T)[1+(16.68/B)]^2 \times 10^{-18}\ \mathrm{m^2\,s^{-1}}\,.$$

The expressions are from the paper by Ahn et al. (1982). These authors also give an angular average accounting for surface roughness:

$$\langle G_s(T)\rangle = (0.69 - 0.45T + 0.52T^2)[1+(16.68/B)]^2 \times 10^{-18}\ \mathrm{m^2\,s^{-1}}\,.$$

Here $\bar{\theta}$, the angle between the field and macroscopic surface normal, is zero.

6.2.3.4. Electronic spin relaxation

As far as the theory is concerned, there is little difference between nuclear and electronic dipolar relaxation in H↓↕. The main aspect to point out is that under typical experimental conditions in a high field we are dealing with the extreme inelastic limit. For the bb→bc relaxation channel, the transition matrix, eq. (6.95d) reduces to

$$\langle \mathrm{f}|V_{\mathrm{dd}}|\mathrm{i}\rangle = (\mu_0\hbar^2/4\pi)\gamma_{\mathrm{e}}^2(3\pi/10)^{1/2}\langle \boldsymbol{k}'|Y_2^{1*}(\hat{\boldsymbol{r}})/r^3|\boldsymbol{k}\rangle_{\mathrm{even}} . \tag{6.101}$$

The cross section becomes, analogous to eq. (6.97a),

$$\sigma_{\mathrm{bb}\to\mathrm{bc}}(k) = Q_{\mathrm{ee}}\frac{1}{k'k^3}\sum_{l,l'=\mathrm{even}}|T_{l,l'}(k,k')|^2(2l+1)(2l'+1) \times \begin{bmatrix} l & 2 & l' \\ 0 & 0 & 0 \end{bmatrix}^2 , \tag{6.102a}$$

where $T_{l,l'}(k,k')$ is defined as in eq. (6.97) and

$$Q_{\mathrm{ee}} \equiv (24\pi/5)[(\mu_0\mu/4\pi)\gamma_{\mathrm{e}}^2]^2 = 1.02\times10^{-19}\ \mathrm{cm}^2 . \tag{6.102b}$$

One may analyze b→c relaxation as a two-level system, analogously to eq. (6.98), while defining $G_{\mathrm{bc}}^{\mathrm{v}} \equiv \frac{1}{2}\bar{v}\bar{\sigma}_{\mathrm{bb}\to\mathrm{bc}}$ and $G_{\mathrm{cb}}^{\mathrm{v}} \equiv \frac{1}{2}\bar{v}\bar{\sigma}_{\mathrm{cb}\to\mathrm{bb}}$. The strong inelastic nature, in which only the atoms in the fast tail of the Boltzmann distribution contribute to the b→c relaxation, gives rise to an exponential B/T dependence as found both by KVS (1981) and Lagendijk et al. (1984)

$$G_{\mathrm{cb}}^{\mathrm{v}} = \exp[2\mu_{\mathrm{B}}B/kT]G_{\mathrm{bc}}^{\mathrm{v}} . \tag{6.103}$$

Comparing with the theoretical result $G_{\mathrm{cb}}^{\mathrm{v}} = 9.7\times10^{-16}\ \mathrm{cm}^3\ \mathrm{s}^{-1}$ of Lagendijk et al. (1984), for $B \simeq 7$ T and $T \simeq 0.71$ K, we calculate an effective cross section for the c→b relaxation of 1.1×10^{-3} Å^2, which is three orders of magnitude smaller than the zero-field spin-exchange cross sections ($\simeq 1$ Å^2, see section 6.2.2). This in turn is at least two orders of magnitude larger than all but the ac→bd spin-exchange cross sections in high field which are suppressed by at least a factor ε^2 (see table 6.13; $\varepsilon^2 \simeq 10^{-5}$ for $B = 10$ T). KVS (1981) were the first to compare the exchange and dipolar relaxation mechanisms between the lower and upper pairs of hyperfine levels as a function of magnetic field. In fig. 6.11 we have redrawn their results using the notation $G\uparrow \equiv G\downarrow \exp(-2\mu_{\mathrm{B}}B/kT)]$ analogous to eq. (6.103). We have no qualitative explanation for the origin of the minimum in the exchange contribution around 10 T.

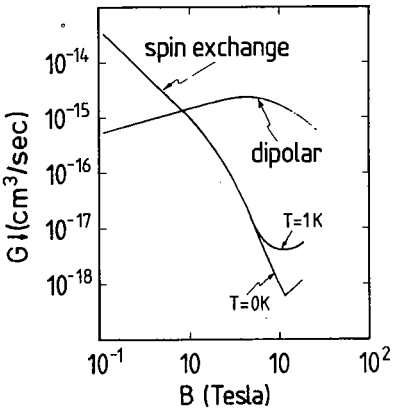

Fig. 6.11. Theoretical results of Kagan et al. (1981), comparing exchange and dipolar depolarization mechanisms. See text for further details.

7. Thermodynamic properties

In the beginning of the 1970s, theoretical evidence of the gaseous nature of H↓ at $T = 0$ K became available. In this section we review the theoretical activities in which the nature of H↓, D↓ and T↓ was established. This involves the calculation of a restricted set of thermodynamic properties. To fully characterize the gas, many thermodynamic properties are of interest. We mention specific heat, compressibilities, pressure, etc., all as a function of temperature, in particular near the critical density for BEC. These properties are conveniently compiled in the recent review by Greytak and Kleppner (1984) to which the reader is referred.

7.1. Quantum theory of corresponding states

An elegant unifying description of the thermodynamic properties of H↓, D↓ and T↓ can be given within the framework of the quantum theory of corresponding states, originally proposed by de Boer (1948) and extended by Nosanow and co-workers to enable a comparison of the various quantum fluids (Nosanow et al. 1975, Miller et al. 1975, 1977, Nosanow 1977b). The theory has been reviewed by de Boer and Bird (1954), and its application to macroscopic quantum systems has been reviewed by Nosanow (1980).

The first application of the theory to the spin-polarized hydrogens is due to Hecht (1959), who calculated critical temperatures. He obtained negative values for both H↓ and D↓ implying the absence of a liquid state,

whereas for T↓ he obtained a value $T_c = 0.95$ K. In 1977 Miller and Nosanow applied the extended version of the corresponding states theory to the hydrogens, using new values for the potential parameters. According to their analysis, D↓ could have a liquid state at $T = 0$ K, possibly under applied pressure. However, H↓ would remain gaseous at all temperatures, including $T = 0$ K, up to pressures of 54 atm (at $T = 0$ K) where it would go directly into the solid state. T↓ would have a liquid ground state. Recently, more accurate calculations by Panoff et al. (1982), to be discussed in the next section, provided theoretical evidence for the existence of a liquid ground state for the deuterium system.

The quantum theory of corresponding states (QTCS) applies to each class of systems, where the potential energy v may be characterized by two parameters, one which sets the energy scale (ε) and the other the length scale (σ). Nosanow and co-workers assumed the potential to be pairwise additive and of Lennard–Jones form, yielding a Hamiltonian given by

$$H = -\frac{\hbar^2}{2m}\sum_i \nabla_i^2 + \sum_{i<j} v(r_{ij}) , \tag{7.1}$$

where

$$v(r_{ij}) = 4\varepsilon[(\sigma/r_{ij})^{12} - (\sigma/r_{ij})^6] \equiv \varepsilon v^*(r_{ij}/\sigma) . \tag{7.2}$$

Here ε is the well-depth and σ is the hard-core diameter, r_i represents the position of atom i and $r_{ij} = |r_i - r_j|$. ∇_i^2 is the Laplacian with respect to r_i. Writing $r_i^* \equiv r_i/\sigma$, eq. (7.1) may be reduced to

$$H = \varepsilon\left[-\tfrac{1}{2}\eta\sum_i \nabla_i^{*2} + \sum_{i<j} v^*(r_{ij}^*)\right] \equiv \varepsilon H^* , \tag{7.3}$$

where ∇_i^* is the Laplacian with respect to the reduced coordinates r_i^* and

$$\eta \equiv \left(\frac{\Lambda^*}{2\pi}\right)^2 \equiv \frac{\hbar^2}{m\varepsilon\sigma^2} \tag{7.4}$$

is a measure of the relative importance of the kinetic energy term in the dimensionless Hamiltonian H^* and Λ^* is the parameter introduced by de Boer.

In table 7.1 we reproduce values for m, ε, σ, η, Λ^* and other useful quantities for various systems of interest (Miller and Nosanow 1977). For the spin-polarized hydrogens they are based on accurate variational calculations of the $^3\Sigma_u^+$ potential (Kolos and Wolniewicz 1974; see section 6.1.3).

Table 7.1

Quantum parameters η for various substances. Also given are the masses Λ^*, coupling constants ε, "core diameters" σ, ε/σ^3, and $N_0\sigma^3$ (from Miller and Nosanow 1977).

Substance	m (amu)[a]	ε/k[b] (K)	σ (Å)	ε/σ^3 (atm)	$N_0\sigma^3$ (cm^3/mol)[c]	η[d]	Λ^*
H↓	1.008	6.46	3.69	17.5	30.2	0.547	4.65
D↓	2.014	6.46	3.69	17.5	30.2	0.274	3.29
^{3}He	3.016	10.22	2.556	83.39	10.06	0.2409	3.08
T↓	3.016	6.46	3.69	17.5	30.2	0.183	2.69
^{4}He	4.003	10.22	2.556	83.39	10.06	0.1815	2.68
H_2	2.016	37.0	2.92	202.5	15.0	0.0763	1.74
D_2	4.028	37.0	2.92	202.5	15.0	0.0382	1.23
Ne	20.18	35.6	2.74	235.8	12.4	0.0085	0.58
Ar	39.95	120.0	3.41	412.3	23.9	0.00088	0.19

[a] 1 amu = 1.66024×10^{-27} kg.
[b] $k = 1.38054 \times 10^{-23}$ J K^{-1}.
[c] $N_0 = 6.02252 \times 10^{23}$ particles/mol.
[d] $\hbar = 1.05430 \times 10^{-34}$ J s.

According to the QTCS, the free energy F of a one-component system may be reduced to a form ($F^* \equiv F/N\varepsilon$; N is the total number of particles in the system) which only depends on the reduced variables for the temperature, $T^* \equiv kT/\varepsilon$, $n^* = \sigma^3 N/V = 1/V^*$ as well as on η and the statistics that apply to the system:

$$F^* = F^*(T^*, V^*, \eta)\,. \tag{7.5}$$

It is also useful to define the reduced pressure $p^* \equiv p\sigma^3/\varepsilon$.

Nosanow and co-workers extended the de Boer theory by interpreting η as an additional thermodynamic variable (besides p^* and T^*). This enabled them to construct phase diagrams in a space spanned by p^*, T^* and η (Nosanow 1977b). To express a change in the free energy F^*, we need to introduce a variable (ϕ^*) which is the thermodynamic conjugate of η (Nosanow et al. 1975)

$$\mathrm{d}F^* = -S^*\,\mathrm{d}T^* - p^*\,\mathrm{d}V^* + \phi^*\,\mathrm{d}\eta\,, \tag{7.6}$$

where

$$\phi^* = (\partial F^*/\partial\eta)_{T^*V^*}\,, \tag{7.7}$$

and the reduced entropy is $S^* = S/Nk$.

Using the powerful framework of statistical mechanics and thermodynamics, the phase diagram in p^*–T^*–η-space can be mapped out. Clearly, η only has physical significance for certain discrete values

(corresponding to real physical systems), but the concept of using η as a continuous thermodynamic variable is useful in obtaining insight into the various phases which are accessible to macroscopic quantum systems. Using Lennard–Jones potentials, the ground-state properties of many-body Bose and Fermi systems as a function of η have been calculated by Nosanow and co-workers and published in a series of papers dealing with the liquid–solid phase transition (Nosanow et al. 1975), liquid–gas phase transition (Miller et al. 1975, 1977) and generalized phase diagrams and critical behavior (Nosanow 1977a,b). Two-dimensional systems were studied by Miller and Nosanow (1978).

Some features of the ground state are immediately clear from eq. (7.3). For small η the system behaves "classically", i.e., the potential energy is dominant and the atoms are located at the equilibrium sites of a crystal lattice. With growing η the kinetic energy becomes increasingly important and beyond a critical value the system melts. If we continue to increase η we reach the point where the system no longer can sustain a many-body bound state and it becomes a quantum gas. However, other features such as the dependence of the results on the statistics of the system are more subtle. For the Fermi-case, due to the Pauli principle the ground-state energy depends markedly on the nuclear spin degeneracy. For D$\downarrow$ this implies a dependence on the occupancy of the various hyperfine states. To distinguish the various cases Miller and Nosanow (1977) introduced the notation D$\downarrow_\nu$, where the index ν refers to the ground-state degeneracy or number of allowed nuclear spin states. In the limit $\nu \to \infty$, keeping n constant, the difference between Fermi and Bose behavior vanishes (Bose limit).

Miller et al. (1975, 1977) calculated the location of the critical point as a function of η, using a variational method to determine the ground-state energy (for more detail on the method see the next section) and found that beyond $\eta_c = 0.33$ (for $\nu = 2$ fermions) and $\eta_c = 0.46$ (for bosons) (see fig. 7.1) the systems are gases at $T^* = 0$. The $\nu = 1$ fermion case was studied by Miller and Nosanow (1977) who found $\eta_c = 0.35$. Comparing the values of η for H$\downarrow$, D$\downarrow$ and T$\downarrow$ (table 7.1) with the relevant values for η_c, we note that at all temperatures H$\downarrow$ should behave as a fluid above its critical point, i.e., it remains a gas down to $T = 0$ K and up to the solidification pressure. T$\downarrow$ is expected to have a liquid ground state. The results for D$\downarrow$ are not unambiguous. D$\downarrow$ could be a liquid or exhibit two coexisting fluid phases. The uncertainty is due to the approximate nature of the theory. Recent Monte Carlo calculations predict D$\downarrow_3$ to be a liquid at $T = 0$ K (Panoff et al. 1982). Such calculations are not available at present for D$\downarrow_1$ and D$\downarrow_2$.

The remarkable phenomenon of two coexisting fluid phases in a one-component system at $T = 0$ K is illustrated in fig. 7.2, reproduced from Miller et al. (1977). Focusing on the curve for $\eta = 0.31$, one notes that at

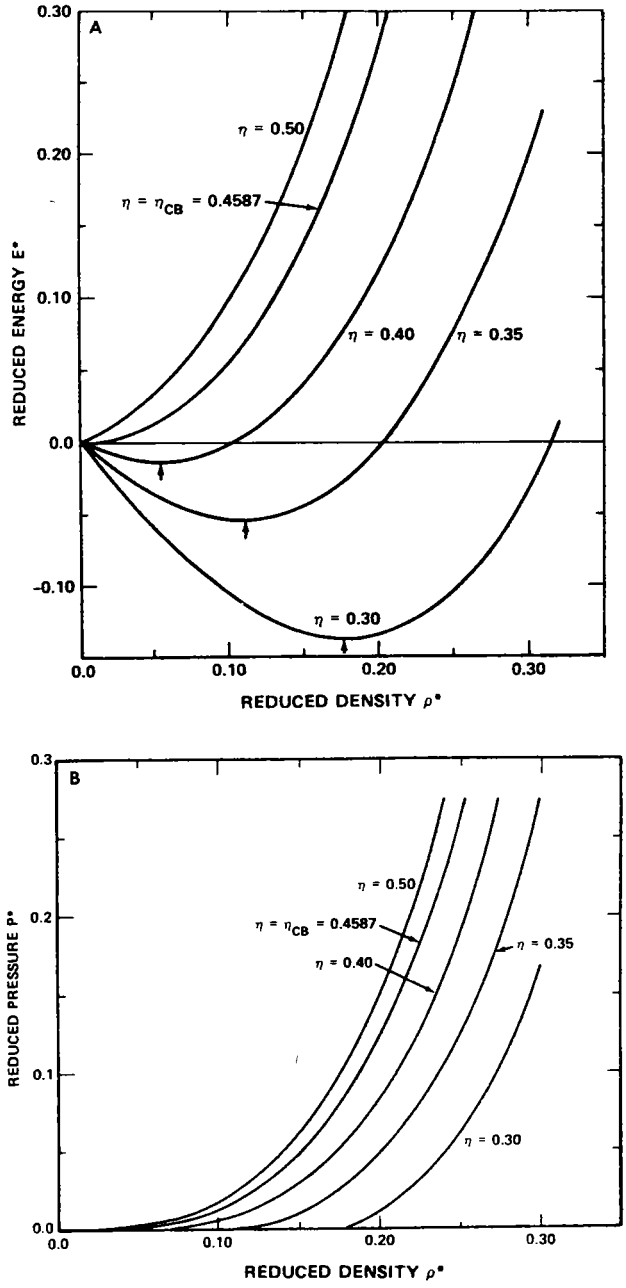

Fig. 7.1. Reduced energy E^* (a) and the corresponding reduced pressure p^* (b) as a function of the reduced density ρ^* (designated n^* in the text) for systems obeying Bose–Einstein statistics. The arrows locate the positions of the energy minimum for each density (from Miller et al. 1977).

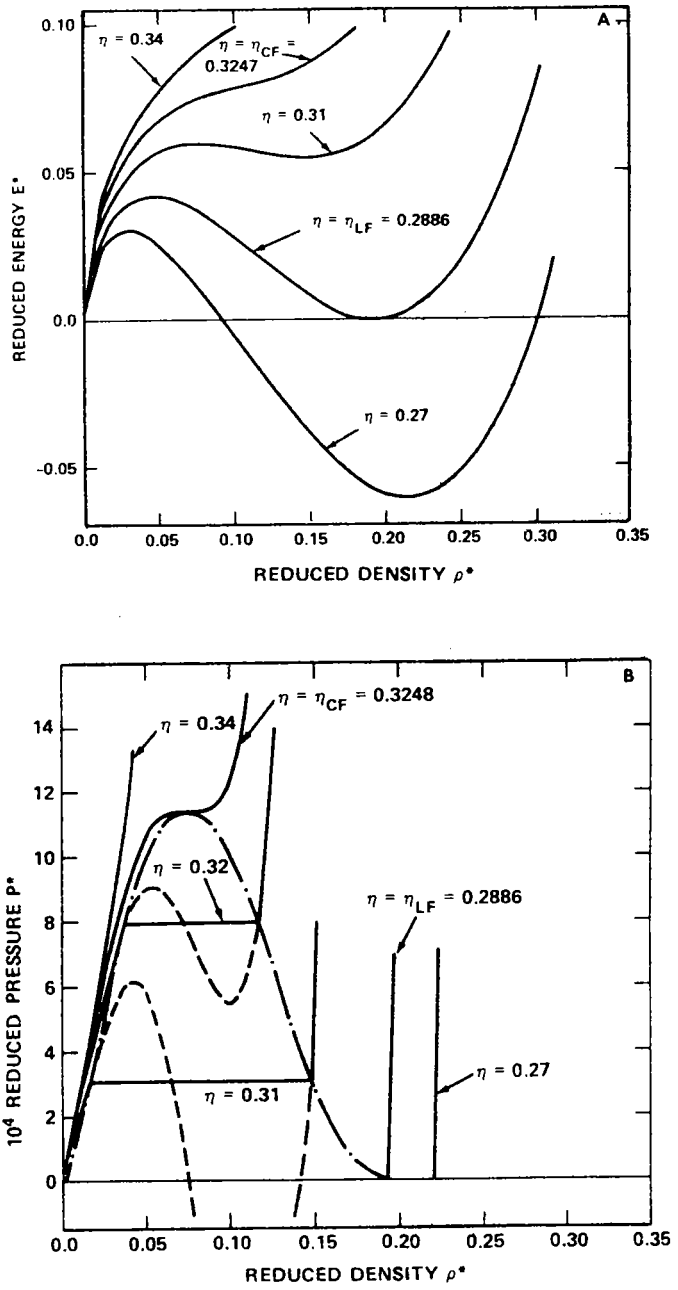

Fig. 7.2. Reduced energy E^* (a) and the corresponding reduced pressure p^* (b) as a function of the reduced density ρ^* (designated n^* in the text) for a system obeying Fermi–Dirac statistics. It is evident that at low densities the statistical repulsion between fermions dominates the total energy (after Miller et al. 1977).

low densities the energy of the system is just proportional to the Fermi energy

$$E_F^* = \tfrac{3}{10}\eta(6\pi^2 n^*/\nu)^{2/3}\,, \tag{7.8}$$

where ν is the spin degeneracy. At higher densities the curve starts to bend over as interactions become important and shows a minimum at $n^* = 0.15$. Beyond a critical density it becomes energetically favorable for the system to phase separate into a low- and a high-density fluid phase. In both phases the pressure and chemical potential are required to be equal. Clearly the phenomenon of coexisting fluid phases does not exist in a Bose system, where both statistics and interactions tend to bring the particles closer together (see fig. 7.1).

Although the QTCS is not decisive as far as the nature of the D↓ ground state is concerned, it leaves little doubt that D↓ may be pressurized into a liquid state. With the aid of fig. 7.3, one finds for the critical point $T_c = 1.29$ K for $D\downarrow_2$, $T_c = 1.68$ K for $D\downarrow_1$, and $T_c = 2.5$ K for T↓. In a recent paper, Hecht (1981) has redone his original calculation (Hecht 1959) of the critical points, based on more recent values for the Lennard–Jones potential parameters and an extrapolation scheme that conserves the

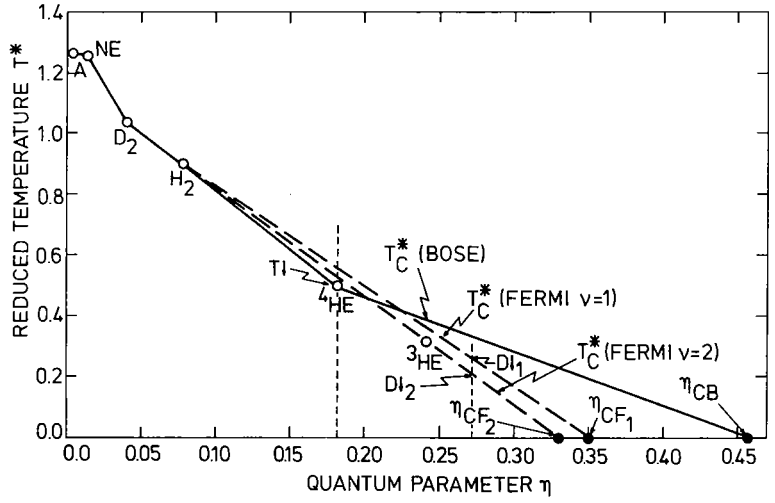

Fig. 7.3. Reduced temperature T^* versus quantum parameter η based on a Lennard–Jones potential. The experimentally available points are indicated by the open circles. The dark circles represent the $T = 0$ K theoretical estimate of η_c for the gas–liquid phase transition. The estimated values for $D\downarrow_1$, $D\downarrow_2$ and T↓ as obtained by interpolation between experimental and theoretical points are indicated by the arrows.

critical ratio $p_c^* V_c^* / T_c^* = 0.3$ as suggested by theory (Nilsen and Hemmer 1969). The results are $T_c = 1.56\,\mathrm{K}$ for D↓, and $T_c = 3.28\,\mathrm{K}$ for T↓. Statistical corrections were neglected, with reference to a paper by Lieb (1967).

To conclude this section on the corresponding-states theory we present estimates of the solidification pressures (p_s). These were obtained using the procedure of Nosanow (1980), based on results of Nosanow et al. (1975) and Nosanow (1977) for the liquid–solid phase transition. In view of the rather speculative nature of these figures we only give the results: $p_s \simeq 54$ atm for H↓, $p_s \simeq 12$ atm for D↓, and $p_s \simeq 5$ atm for T↓.

7.2. Ground-state calculations

After the more general discussion of the spin-polarized hydrogens within the framework of the QTCS, in this section we discuss a number of calculations of the ground-state energy for H↓ and its isotopes. These calculations were intended to yield the "best available" estimate for the nature of the ground state.

The first calculations to provide convincing evidence of the gaseous nature of H↓ down to $T = 0$ K were by Etters and co-workers (Etters 1973, Dugan and Etters 1973, Etters et al. 1975, Danilowicz et al. 1976), who applied the Monte Carlo technique to obtain the energy, pressure and compressibility of the ground state of H↓, $D\downarrow_2$ and T↓ for a variety of densities, ranging between 40 and 200 $\mathrm{cm}^3/\mathrm{mol}$. In 1978, this work was extended to lower densities of order 2×10^4 $\mathrm{cm}^3/\mathrm{mol}$ (Etters et al. 1978). Also the solid, and solid–fluid phase transition were studied by these authors (Danilowicz et al. 1976), but will not be discussed in this review.

Accurate approximate results for the ground-state properties were also obtained by Miller and Nosanow (1977), who applied two different cluster-expansion methods. Apart from improving upon the accuracy of existing theory, this work showed that for D↓ the calculations were not sufficiently accurate to decide upon the nature of the ground state at $T = 0$ K. Relatively clear-cut results were obtained for H↓ (gaseous) and T↓ (liquid).

The required high accuracies for D↓ challenged a number of theorists to apply the most advanced methods of Fermi-fluid theory to decide upon the nature of the $D\downarrow_\nu$ ground state. Clark et al. (1980) and Krotscheck et al. (1981) used the method of correlated basis functions and a Fermi–HNC approximation to calculate the ground-state energy, but this work also lacked the required accuracy. The first results that point convincingly towards the existence of a liquid ground state at zero pressure came from a variational Fermi–Monte Carlo calculation for $D\downarrow_3$. Within statistical

error a negative upper bound was obtained for the energy for a range of densities (Panoff et al. 1982). It is not our aim to give a detailed account of the various calculational techniques employed. For this purpose the reader is referred to reviews by Feenberg (1969), Zabolitzky (1977), Clark (1979) and Clark et al. (1980). In discussing the various results we shall reference the original literature where useful.

The Hamiltonian of a N-body system of atoms interacting pairwise via the triplet potential V_t is given by

$$H = -\frac{\hbar^2}{2m}\sum_i \nabla_i^2 + \sum_{i<j} V_t(r_{ij})\,, \tag{7.9}$$

where r_i represents the position of atom i and $r_{ij} \equiv |\boldsymbol{r}_i - \boldsymbol{r}_j|$. To obtain the ground-state energy per particle one has to calculate the expectation value of the Hamiltonian with respect to the ground state $|\psi\rangle$

$$\langle E\rangle = \frac{1}{N}\,\langle\psi|H|\psi\rangle / \langle\psi|\psi\rangle\,. \tag{7.10}$$

7.2.1. *The boson case*

Both Etters et al. (1975) and Miller and Nosanow (1977) chose a variational wave function of the Jastrow type to approximate the ground state ψ_B of the Bose systems H$\downarrow$ and T$\downarrow$

$$\psi_B = F(r_1, \ldots, r_N) = \prod_{i<j} f(r_{ij})\,. \tag{7.11}$$

This ground state is built up as a product of $\frac{1}{2}N(N-1)$ functions $f(r_{ij})$ describing the correlations of the pair (i, j). Then the ground-state energy per particle for the boson case, $\langle E\rangle_B$, follows from repetitive use of eq. (7.11), the relation

$$\nabla_i F = F\sum_{j\neq i} \nabla_i \ln f(r_{ij})\,, \tag{7.12}$$

and integration by parts (see McMillan 1965)

$$\langle\psi_B|\mathrm{H}|\psi_B\rangle = \sum_{i<j}\int F^2\left[-\frac{\hbar^2}{2m}\,\nabla_i^2 \ln f(r_{ij}) + V_t(r_{ij})\right]\mathrm{d}\tau\,, \tag{7.13}$$

where $\mathrm{d}\tau$ is used to indicate integration over the spatial coordinates of all N particles. Introducing the (Bose) pair-correlation function

$$g_B(r) = \frac{N(N-1)}{n^2}\int \psi_B^2\,\mathrm{d}\boldsymbol{r}_3\cdots\mathrm{d}\boldsymbol{r}_N \Big/ \int \psi_B^2\,\mathrm{d}\tau \tag{7.14}$$

one obtains

$$\langle E \rangle_B = \tfrac{1}{2} n \int g_B(r) \left[-\frac{\hbar^2}{2m} \nabla^2 \ln f(r) + V_t(r) \right] dr . \tag{7.15}$$

We first discuss the approach of Etters et al. (1975), who used a Monte Carlo method on a collection of 32 particles that had proven to be very successful in calculating the properties of the Bose fluid ^{4}He (McMillan 1965). The density of this model system was varied by changing the volume of a cubic box; periodic boundary conditions were used to simulate an infinite system. Originally (Dugan and Etters 1973, Etters et al. 1975), a Morse potential fitted to the $^3\Sigma_u^+$ potential energy curve of Kolos and Wolniewicz (1965) (see section 3) was used

$$V_M(r) = \varepsilon[\exp 2c(1 - r/r_m) - 2 \exp c(1 - r/r_m)] , \tag{7.16}$$

where $r \equiv r_{ij}$, $\varepsilon/k = 6.19$ K, $r_m = 4.1527$ Å is the position of the potential minimum, and $c = 6.0458$ is a dimensionless constant. Equation (7.16) provides a good fit for both the well-region and the short-range part. However, it was pointed out by Stwalley and Nosanow (1976) that for long-range, the Morse potential is incorrect and therefore is not suited for an analysis of the low-density properties. In a later paper, Etters et al. (1978) used the analytic form (3.6), which represents a much better fit to the $^3\Sigma_u^+$ potential of Kolos and Wolniewicz (1974).

Etters et al. (1975, 1978) used a biased random walk procedure to calculate the ground-state energy. This involved the numerical evaluation and averaging of eq. (7.13) for 10^5 configurations. The form of the Jastrow function chosen was

$$f(r) = \exp[-b_1 \exp(-b_2 r)] , \tag{7.17}$$

which represents a WKB solution to the Morse potential, eq. (7.16), at short-range. The Monte Carlo procedure implies random generation of the configurations, which are accepted or rejected by a biasing procedure that conserves the probability distribution $|F(r_1, \ldots, r_N)|^2$. To exploit the variational nature of eq. (7.17) Etters et al. (1975, 1978) minimized the energy for each density. The pressure and compressibility were obtained by taking the appropriate derivatives of the energy with respect to volume.

The results of Etters et al. (1978) for H↓ are reproduced in table 7.2 and shown in fig. 7.4 along with the results of Miller and Nosanow (1977) and the results of the hard-sphere model (Friend and Etters 1980). The monotonic increase of the energy with density points convincingly to the gaseous nature of H↓.

Table 7.2

The Monte Carlo results for the energy E and pressure P versus density. a^3/v is the hard-sphere model expansion parameter, where $a = 6.5$ au and v is the volume per atom. N_0/N is the fractional number of atoms in the condensate.

$10^3 n$ (Å^{-3})	E (K)	$10^3 P$ (kg/cm^2)	$10^2 a^3/v$	N_0/N
3.010	1.902 ± 0.081	1080.0	–	–
2.007	1.105 ± 0.044	431.0	–	–
1.505	0.681 ± 0.027	217.0	–	–
1.204	0.543 ± 0.031	129.0	–	–
0.803	0.326 ± 0.024	46.0	–	–
0.602	0.192 ± 0.014	22.0	2.46	0.764
0.301	0.101 ± 0.012	4.5	1.23	0.833
0.120	0.047 ± 0.007	0.72	0.49	0.895
0.060	0.0165 ± 0.004	0.28	0.25	0.926
0.045	0.0125 ± 0.003	0.065	0.16	0.939
0.030	0.0064 ± 0.002	0.018	0.12	0.047

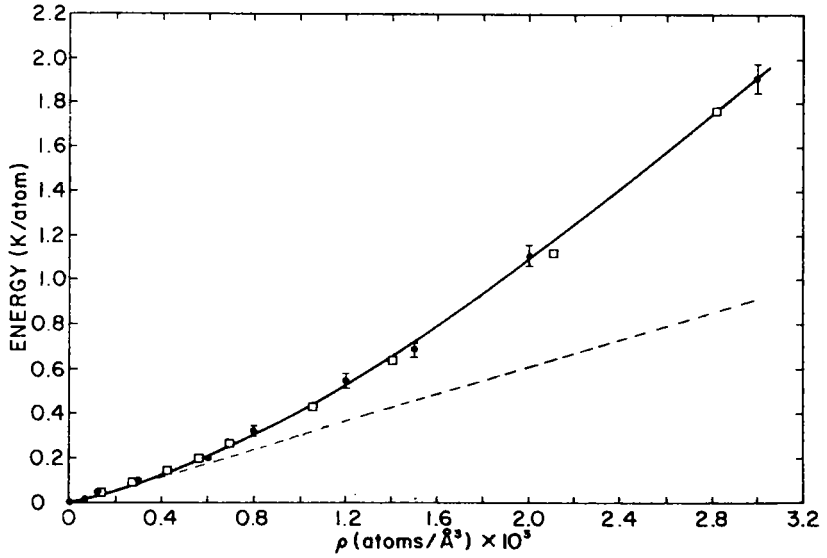

Fig. 7.4. The ground-state energy per H-atom versus density. The dots represent the Monte Carlo results of Etters et al. (1978). The squares are the results of Miller and Nosanow (1977). The dashed line corresponds to the hard-sphere results of Friend and Etters (1980).

In their calculation Miller and Nosanow (1977) tried two potentials, the "exact" $^3\Sigma_u^+$ potential (Kolos and Wolniewicz 1974) and the Lennard–Jones fit to this potential given in table 7.1. The "exact" potential was supplemented for the long-range regime using a polarization expansion determined by Bell (1966)

$$V(r) \sim -c_6 r^{-6} - c_8 r^{-8} - c_{10} r^{-10}, \tag{7.18}$$

where $c_6 = 4.506 \times 10^4$ K Å^6; $c_8 = 2.415 \times 10^5$ K Å^8 and $c_{10} = 1.786 \times 10^6$ K Å^{10}.

The treatment of Miller and Nosanow (1977) was also variational in nature, using a trial wave function of the type eq. (7.11), however, the McMillan form was chosen for $f(r)$:

$$f(r) = \exp\left[-\tfrac{1}{2}(br_m/r)^5 \right], \tag{7.19}$$

where b is a variational constant. Etters et al. (1975) also attempted this form for $f(r)$ in conjunction with a Lennard–Jones potential, but obtained lower energies with eq. (7.17) and the Morse potential.

To calculate the ground-state energy Miller and Nosanow (1977) used two different cluster-expansion methods, which appear to provide a good approximation, in particular in the low-density regime. The methods used are the "BBGKY–KSA" due to Born, Bogoliubov, Green, Kirkwood and Yvon, which includes the Kirkwood superposition approximation (KSA), and the hypernetted chain (HNC) approximation. In fig. 7.4 we only show the BBGKY results, which were found to be slightly lower than the results obtained with the HNC method. The results obtained with the Lennard–Jones potential are also included to provide some perspective of the accuracy of the predictions based on the quantum theory of corresponding states.

7.2.2. The fermion case

For the fermion case the wavefunction has to be antisymmetrical, suggesting a Slater–Jastrow-type trial wavefunction for the ground state

$$\psi_F = F(r_1, \ldots, r_N)\phi(r_1\sigma_1, \ldots, r_N\sigma_N). \tag{7.20}$$

Here F is defined by eq. (7.11), ϕ is a Slater determinant of free fermions

with spin σ_i, and

$$\phi = \det\{\exp(i\boldsymbol{k}_i \cdot \boldsymbol{r}_j)\chi_i(\sigma_j)\} , \tag{7.21}$$

where $\chi_i(\sigma_j)$ is the spin state of the jth particle.

Based on eq. (7.20) various equivalent expressions may be derived for $\langle E\rangle_F$, the ground-state energy per particle for the fermion case. These result from different partial integration schemes for eq. (7.10) (Zabolitzky 1977). We give an expression obtained by use of the Jackson–Feenberg (1961) identity

$$\int \psi^*\nabla^2\psi \, d\tau = \frac{1}{4}\int \{[\psi^*\nabla^2\psi - (\nabla\psi^*)(\nabla\psi)] + [cc]\} \, d\tau . \tag{7.22}$$

Substituting eq. (7.20) and using eq. (7.12) one finds

$$\int \psi_F \nabla_i^2 \psi_F \, d\tau = \frac{1}{2}\sum_{j\neq i}\int F^2|\phi|^2\nabla_i^2 \ln f(r_{ij}) \, d\tau$$

$$+ \int F^2[\phi^*\nabla_i^2\phi - \nabla_i^2|\phi|^2] \, d\tau . \tag{7.23}$$

Introducing the Fermi pair-correlation function,

$$g_F(r) = \frac{N(N-1)}{n^2}\int F^2|\phi|^2 \, d\boldsymbol{r}_3 \cdots d\boldsymbol{r}_N \Big/ \int |\psi_F|^2 \, d\tau , \tag{7.24}$$

one arrives at

$$\langle E\rangle_F = \tfrac{3}{5}(\hbar^2/2m)k_F^2 + \frac{1}{2}n\int g_F(r)[-(\hbar^2/2m)\nabla^2 \ln f(r) + V(r)] \, d\boldsymbol{r}$$

$$+ \frac{1}{N}\int F^2 \sum_i (\hbar^2/2m)\nabla_i^2|\phi|^2 \, d\tau \Big/ \int |\psi_F|^2 \, d\tau . \tag{7.25}$$

The first term is the free-fermion kinetic energy, dominant for $n \to 0$, with k_F the Fermi momentum. The second term is closely analogous to eq. (7.15) but contains, in addition to the dynamical correlations accounted for by $g_B(r)$, also the statistical correlations implicit in $|\phi|^2$. The last term of eq. (7.25) requires evaluation of $\nabla_i^2|\phi|^2$ and represents a kinetic energy correction.

There are various methods to evaluate $\langle E\rangle_F$. A well-known procedure, due to Wu and Feenberg (1962) is to treat the fermions as bosons and to account for the statistical correlations in an approximate way by means of a

cluster expansion. Various methods to generate such a statistical cluster expansion are discussed in the book by Feenberg (1969). This method is expected to work particularly well if the dynamical correlations keep the atoms sufficiently far apart for the statistical repulsion to be small.

The Wu–Feenberg approach was taken by Etters et al. (1975) to study $D\downarrow_2$ in analogy to Schiff and Verlet's (1967) application of the method to liquid ^{3}He. The associated D↓-Bose problem was solved using the same Monte Carlo program that served for the H↓ and T↓ calculations (see foregoing section). Miller and Nosanow (1977) and Miller et al. (1975, 1977) also used a statistical cluster expansion to correct for the statistics, but chose for the BBGKY–KSA and HNC integral equation to approximate $g_B(r)$. In addition to $D\downarrow_2$, Miller and Nosanow (1977) also studied $D\downarrow_1$.

More advanced approximate solutions for eq. (7.25) may be obtained by using the Fermi–hypernetted-chain (FHNC) method in which both dynamical and statistical correlations are treated on equal footing. For a detailed discussion of the method in terms of cluster diagrams the reader is referred to the reviews by Zabolitsky (1977) and Clark (1979). Krotscheck et al. (1981) applied the FHNC-method to $D\downarrow_1$, $D\downarrow_2$ and $D\downarrow_3$, using an "optimized" Jastrow function, obtained by minimizing the energy functional with respect to $\ln f$. The results are shown in fig. 7.5 along with the $D\downarrow_2$ results of Miller and Nosanow (1977) obtained with the McMillan-type Jastrow function given in eq. (7.19) with chosen $b(n)$ to minimize the

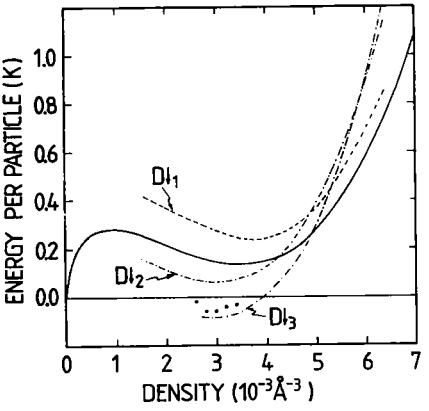

Fig. 7.5. Energy per particle for $D\downarrow_1$, $D\downarrow_2$ and $D\downarrow_3$ as obtained by Krotscheck et al. (1981) using correlated basis functions for $D\downarrow_2$ and $D\downarrow_3$. The result of Miller and Nosanow (1977) is given as a full line; the results of the variational Monte Carlo calculation of Panoff et al. (1982) for $D\downarrow_3$ are indicated by the dots.

energy for each density studied. The results of Etters et al. (1975) were the first available for $D\downarrow$ and stimulated theoretical and experimental work, but are not included in fig. 7.5 since they are no longer considered up-to-date.

Focusing on the FHNC results, one notes that the minimum in the $D\downarrow_3$ energy versus density curve lies below the minima for the $D\downarrow_2$ and the $D\downarrow_1$ results, as one expects intuitively. For detailed considerations and error estimates of the FHNC-method the reader is referred to the original literature (Krotscheck et al. 1981).

The FHNC results substantiated the conclusion, already drawn by Miller and Nosanow (1977), that for $D\downarrow$ the kinetic and potential energies almost cancel each other. Therefore, very accurate calculations are required to decide upon the nature of the ground state. Although the theory presented was not sufficiently accurate to be decisive in this respect, in particular $D\downarrow_3$ is likely to have a liquid ground state. If not, only a very slight applied pressure should suffice to liquify any of the $D\downarrow_\nu$ modifications.

The first convincing result that a liquid ground state of $D\downarrow_3$ exists was obtained by Panoff et al. (1982), using a full Fermi–Monte Carlo evaluation of $\langle E \rangle_F$ for up to 99 particles. The application of this method was made possible by recent advances in high-speed computing facilities. The calculation used the complete antisymmetrized wavefunction (7.21) with an "optimal" choice of $f(r)$ taken from the paper by Krotscheck et al. (1981). The same $f(r)$ was used for all densities. The results are also included in fig. 7.5 and show, within statistical error, a negative minimum, required for a liquid ground state. In view of the "exact" nature of the Monte Carlo evaluation of $\langle E \rangle_F$ these results represent a rigorous upper bound for the energy. Moreover, the interaction potential is also known to high accuracy giving confidence that $D\downarrow_3$ liquifies at sufficiently low temperatures.

8. Many-body static and dynamic magnetic properties

Many of the very new aspects of H, D, and T are due to the magnetic moments associated with the electronic and nuclear spins. The magnetization of the gas has already been generally discussed in section 2.3 and the inhomogeneous density or magnetization due to a magnetic field gradient has been briefly handled in section 5.1.4.1. In this section we consider in greater detail the interaction with a magnetic field, in particular under conditions in which quantum degeneracy is important. We first discuss static properties which display unusual behavior due to the statistics, then dynamical properties or magnetic excitations.

8.1. Static magnetic properties

8.1.1. Noninteracting gases

An intriguing question concerning H↓ is "what happens to the density distribution if the gas Bose condenses?". Since the condensate represents a macroscopic population of the lowest energy state of the gas, one might expect the condensate to accumulate in the highest field regions of an inhomogeneous magnetic field. In order to get some insight into this behavior, Walraven and Silvera (1980) analyzed the problem for a field which varied quadratically with displacement from the field center, such as for a simple solenoid. They made a further (nonphysical) approximation that the field gradient only existed in the z direction so that eqs. (5.1) become

$$B_z(r) = B_0(1 - z^2/z_0^2)\,, \qquad B_\perp = B_\phi = 0\,, \tag{8.1}$$

with $z_0 = 51$ mm, which represents an actual experimental solenoid.

In this case the Schrödinger equation for noninteracting atoms in the $m_s = -\frac{1}{2}$ state becomes

$$\sum_i \left[-\frac{\hbar^2}{2m}\nabla_i^2 + \mu_B B_0 (z_i/z_0)^2 \right] \psi(\boldsymbol{r}_1, \boldsymbol{r}_2, \ldots, \boldsymbol{r}_N) = \varepsilon\psi(\boldsymbol{r}_1, \boldsymbol{r}_2, \ldots, \boldsymbol{r}_N)\,, \tag{8.2}$$

where the energy is measured with respect to the static energy $(-\mu_B B)$ in the field center. This Hamiltonian corresponds to harmonic oscillator motion in the z direction and plane wave motion in the x–y plane. The wavefunction can be factored: $\psi(\boldsymbol{r}_1, \boldsymbol{r}_2, \ldots, \boldsymbol{r}_N) = \psi(\boldsymbol{r}_1)\psi(\boldsymbol{r}_2)\cdots\psi(\boldsymbol{r}_N)$. The single-particle wavefunctions are of the form

$$\psi_{n_z k_\perp}(\boldsymbol{r}) = \phi_{n_z}(z)\exp(i\boldsymbol{k}_\perp \cdot \boldsymbol{r}_\perp)\,, \tag{8.3a}$$

where ϕ_{n_z} is a harmonic oscillator (HO) wavefunction with oscillator energy splitting

$$\hbar\omega_0 = \hbar(2\mu_B B_0/m z_0^2)^{1/2}\,. \tag{8.3b}$$

Here, $\omega_0 \simeq 6.8 \times 10^3$ rad/s for a field of 10 T with $z_0 = 51$ mm. Thus in this field the HO states are very closely spaced and of order 10^8 states are populated for $T \simeq 0.1$ K.

Populations are governed by the Bose distribution function, eq. (1.8),

$N_i = \{\exp[(\varepsilon_i - \mu)/kT] - 1\}^{-1}$ and the density distribution is calculated, using

$$n(r) = \sum_i N_i |\psi_i(r)|^2 . \tag{8.4}$$

Here $\psi_i(r)$ denotes a single-particle eigenstate of eq. (8.2). The density distribution for $T \gg T_c$ shown in fig. 8.1a is Boltzmann-like; a classical approximation is used for $|\psi_i|^2$. Below the critical temperature for BEC the $k_\perp = 0$, ground oscillator state is macroscopically occupied. The width of the HO ground state is approximately 7 μm (fig. 8.1a). The axial density profile for this noninteracting case below T_c is a broad (non-Boltzmann) normal component with a spatially localized, sharp, distinctive peak at the field maximum, representing the condensate fraction.

It is interesting to contrast the Bose and Fermi gases (Silvera and Walraven 1981a), the latter represented by D↓. At $T = 0$ K only the ground oscillator state of the Bose gas is occupied, yielding a sharp density peak around $z = 0$; however, the Fermi gas has a very broad density distribution shown in fig. 8.1b. This is also calculated using eq. (8.4), but with the

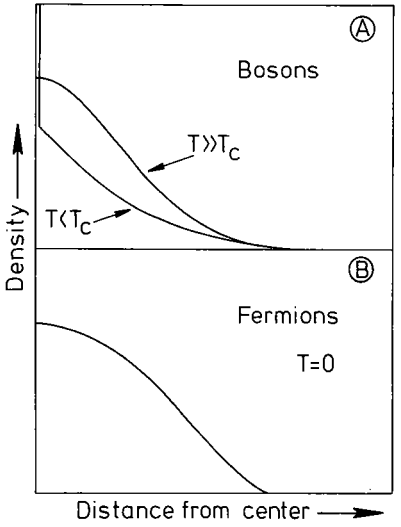

Fig. 8.1. (a) The axial density distribution for noninteracting bosons in an inhomogeneous solenoidal magnetic field above and below T_c, demonstrating the spatial localization of the condensate fraction at the field center. For $T \gg T_c$ the normal fraction can be described by Boltzmann statistics, whereas for $T \leqslant T_c$ it has a characteristic Bose dependence. (b) The $T = 0$ K density distribution for a Fermi gas. At $T = 0$ K the Bose gas density would be represented only by the peak at the center, demonstrating the fundamental differences of the Bose and Fermi gases (after Silvera and Walraven 1981a).

Fermi distribution function $N_i = \{\exp[(\varepsilon_i - \mu)/kT] + 1\}^{-1}$. In this case, each oscillator state is filled up to the Fermi level. The density distribution can be represented by

$$n(z) = n(B_0)[1 - (z/z_F)^2]^{3/2}, \tag{8.5}$$

where z_F defines the boundary of the Fermi surface, $E_F = \frac{1}{2}m\omega_0^2 z_F^2$. The distribution for the degenerate Fermi gas does not differ distinctly from a classical distribution, in contrast with the Bose gas.

8.1.2. The weakly interacting Bose gas

The picture just presented for the ideal Bose gas is quite unrealistic because interactions between particles will prevent the density from building up into a narrow peak. Walraven and Silvera (1980) treated this in the $T = 0$ K case, and showed that the density peak of 7 μm width spread out to several millimeters. This analysis was extended to finite temperatures by Goldman et al. (1981) and Huse and Siggia (1982) using a Hartree–Fock approximation, and Condat and Guyer (1981) who used a Ginzburg–Landau energy functional approach which seems to have some errors, but yields the same general result.

The interaction Hamiltonian is

$$H = \sum_i \left\{ -\frac{\hbar^2}{2m}\nabla_i^2 + U_{ext}(\boldsymbol{r}_i) \right\} + \frac{1}{2}\sum_{i\neq j} V(r_{ij}), \tag{8.6}$$

where U_{ext} represents the interaction with the external magnetic field. $V(\boldsymbol{r}_{ij})$ is taken as the triplet Kolos–Wolniewicz potential. For low energies, $V(\boldsymbol{r}_{ij})$ can be replaced by an effective range potential $v_0\delta(\boldsymbol{r}_{ij})$, for ease of calculations. One approach to the interaction problem is to use scattering theory and a phase-shift analysis. Bosons interact only with even pair angular-momentum states and at low energies (or temperatures) in the $\boldsymbol{k} \to 0$ limit, only s-wave scattering is important. Friend and Etters (1980) have calculated the s-wave scattering length, $a_s = 0.72$ Å, based on the Kolos–Wolniewicz potential. The relation to v_0 is

$$v_0 = \frac{4\pi\hbar^2}{m} a_s . \tag{8.7}$$

The effective range potential can be used in the Hartree–Fock approximation to yield two equations:

$$\left[-\frac{\hbar^2}{2m}\nabla^2 + 2v_0 n_n + 2v_0 n_0 + U_{ext}(\boldsymbol{r}) \right]\phi_k(\boldsymbol{r}) = \varepsilon_k \phi_k(\boldsymbol{r}), \quad \boldsymbol{k} \neq 0, \tag{8.8a}$$

$$\left[-\frac{\hbar^2}{2m}\nabla^2 + 2v_0 n_n + v_0 n_0 + U_{ext}(r)\right]\phi_0(r) = \varepsilon_0\phi_0(r) \,. \tag{8.8b}$$

Here n is the total bulk density and n_n and n_0 are the normal and condensate densities; ε_k and ε_0 are the corresponding single-particle energies. ϕ_0 and ϕ_k are the condensate and normal wavefunctions. The single-particle energies, to first order, are

$$\varepsilon_k = \hbar^2 k_\perp^2/2m + (n_k + \tfrac{1}{2})\hbar\omega_0 + 2v_0 n_0 + 2v_0 n_n$$

and

$$\varepsilon_0 = \tfrac{1}{2}\hbar\omega_0 + 2v_0 n_n + v_0 n_0 \,.$$

Due to identical-particle exchange effects there is an important factor of 2 difference in the interaction energy, which depends on the particle states. If two interacting particles are in the same state then the interaction is $v_0 n$, whereas if they are in different states the term is $2v_0 n$. Thus, interactions between condensate particles are smaller by a factor of two. These equations represent an extension of the Gross–Ginzburg–Pitaevskii theory to finite temperatures with a spatially varying external potential. Note in eq. (8.8b) that the (positive) term $v_0 n_0 \equiv v_0|\phi_0|^2$ makes it energetically unfavorable to have a large, spatially localized, density as in the $v_0 = 0$ noninteracting case.

Gross (1963) and Wu (1961) defined a "healing length" $\xi = (8\pi a_s n)^{-1/2}$ which is the characteristic length for the condensate to spatially adjust to a rapidly varying potential. In the present problem it takes the form $\xi = 2z_{zp}^2/z_{int} = 230\ \text{Å} \times (10^{18}/n)^{1/2}$, with n in cm^{-3}, where the zero-point width is $z_{zp} = (\hbar/2m\omega_0)^{1/2}$ and $z_{int} = (2nv_0/m\omega_0^2)^{1/2}$. Since for the low densities of interest ($n \leqslant 10^{19}/\text{cm}^3$) $\lambda_{th} \ll z_{zp} \ll z_{int}$, the WKB approximation is applicable, so that the effective single-particle potentials can be used in eq. (8.8). Carrying out the usual continuum approximation for N_i, the solutions for the normal and condensate densities are approximately

$$n_n(z) = \lambda_{th}^{-3} g_{3/2} \exp\{[\mu - 2n_n(z)v_0 - 2n_0(z)v_0 - U_{ext}(z)]/kT\} \,, \tag{8.9a}$$

$$n_0(z) = [\mu/v_0 - 2n_n(z) - U_{ext}(z)/v_0]\,\theta[\mu - 2n_n(z)v_0 - U_{ext}(z)] \,, \tag{8.9b}$$

where $\theta[z]$ is the Heaviside unit-step function. Expression (8.9b) expresses the fact that the condensate density adjusts itself so that the interaction

energy balances the energy of the external field. The chemical potential μ is determined in the usual way, by requiring the spatial integral over the condensate and normal densities to be equal to N, the total number of particles. An example of the resulting density profiles for 10^{16} H↓‡ atoms in a tube of cross sectional area 0.01 cm^2 is shown in fig. 8.2 for several temperatures in the neighborhood of T_c. We see that the density does not "diverge" as in the noninteracting case, and is substantially broadened. Nevertheless, the condensate fraction is spatially localized in a distinctive fashion. Since the density profile can in principle be measured by magnetic-resonance techniques, this presents an interesting possible approach to observing BEC.

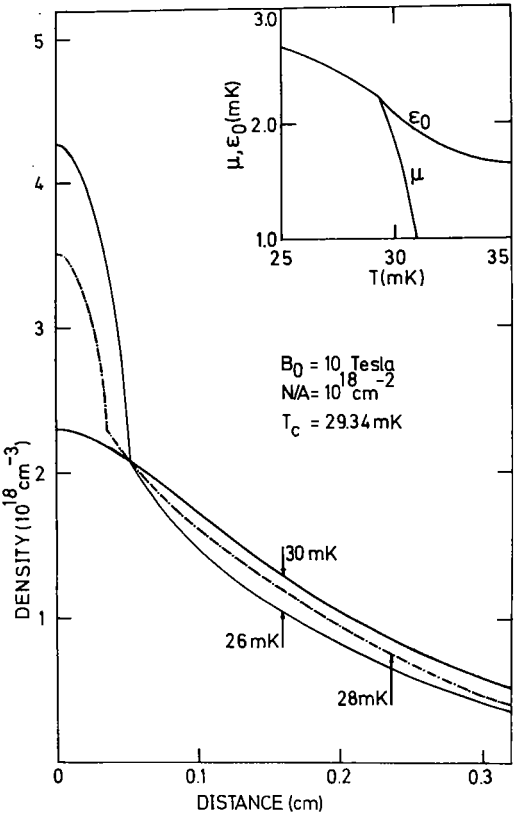

Fig. 8.2. The axial density profile for a gas of interacting H↓‡ in a solenoidal magnetic field in the vicinity of T_c. This demonstrates the broadening of the condensate distribution due to interactions, as compared to fig. 8.1a. The inset shows the behavior of the chemical potential and the ground-state energy ε_0 in the neighborhood of T_c. Below T_c, $\varepsilon_0 = \mu$ (after Goldman et al. 1981).

8.2. Dynamical properties: spin-waves

8.2.1. General

The possible magnetic excitations cover a very broad frequency range, from 10^3–10^{12} Hz. We shall concentrate our attention on hydrogen. Most of the results are applicable to H and D, although D has a richer spectrum since $I = 1$. The excitation spectrum of a degenerate gas of D$\downarrow$ will not be treated.

In a parabolic magnetic field the lowest frequency modes are the axial harmonic-oscillator modes just discussed; these have not been observed. A brief discussion was given by Silvera and Walraven (1981a).

Berlinsky (1977) has considered nuclear and electronic spin-wave excitations in the Bose condensed ($T = 0$ K) state, which range in frequency from 10^9–10^{12} Hz. He found four dispersion relations for excitations from the ground state (a-state) corresponding to the usual spin-independent phonon-like density fluctuation mode for a superfluid and three spin fluctuation modes. These correspond to a coherent nuclear spin-wave (spin-flip) mode, an electron spin-flip mode and an electron–nuclear spin-flip mode. These modes have energy gaps depending on the field, the hyperfine interaction and the exchange.

Berlinsky et al. (1977) investigated the dynamical instability of spin-polarized hydrogen to a spontaneous spin reversal which would lead to recombination. They examined the energy balance between the electronic Zeeman interaction with the external magnetic field and the interaction of a spin with its environment, which favors an antiparallel alignment. Above a critical density, the spin spontaneously reverses, and the system can then decay by recombination. It turned out that the second and third-order recombination processes are so strong that these critical densities can never, in practice, be reached. Kagan and Shlyapnikov (1981) reanalyzed this problem as well as the spin-waves, pointing out that both the singlet and triplet s-wave scattering cross sections must be considered, yielding an even higher critical density for the spontaneous spin-reversal process.

Siggia and Ruckenstein (1980, 1981) considered the hydrodynamics of a two component ($|a\rangle$ and $|b\rangle$) Bose condensate. They showed that the two condensates are coupled and give rise to a spontaneous coherent magnetization perpendicular to the main field.

Recently, nuclear "spin-waves" in H$\downarrow$ have been observed at low densities in the nondegenerate regime. These modes are due to identical-particle effects and involve both diffusion and spin rotation. They are of quite a different nature than the modes first treated by Berlinsky. We shall concentrate on these modes in the remainder of this chapter.

8.2.2. *Nuclear spin-waves in* H↓↕

Spin oscillations or spin-waves have been discussed for dense degenerate liquids such as ^{3}He for some time (see, for example, Leggett and Rice 1968, Leggett 1970). However, Lhuillier and Laloë (1982a, b), Lhuillier (1983) and Bashkin (1981) made the remarkable observation that such effects can also occur in a low-density gas of indistinguishable particles if λ_{th} is somewhat larger than the size of the atom (d). These oscillations find their origin in the "identical-spin rotation effect", a mutual rotation of the spins of two indistinguishable particles about their vector sum due to interference effects when their wave packets of dimension λ_{th} overlap, even for a spin-independent Hamiltonian. The sign of the interference is opposite for bosons and fermions.

^{3}He has nuclear spin $\frac{1}{2}$ and these atoms clearly behave as fermions. The hydrogen atom has both electronic and nuclear spin $\frac{1}{2}$, the spins being weakly coupled by the hyperfine interaction. As long as $\lambda_{th} \geqslant d$ (Pan et al. 1985), the atoms behave as composite bosons and the wavefunction for a pair of H atoms must be symmetric with respect to atomic interchange. Thus, even though the spins are $\frac{1}{2}$, and we focus our attention on the dynamical aspects of the nuclear or electronic spins, separately, the wavefunctions must still be symmetric under interchange of the atoms. Thus the nuclear spin $\frac{1}{2}$ hydrogen atoms are treated as bosons.

Consider two identical spin $\frac{1}{2}$ atoms with spins $\boldsymbol{i}_1$ and $\boldsymbol{i}_2$ in spatially separated states: $\alpha_1|\uparrow\rangle + \beta_1|\downarrow\rangle$ and $\alpha_2|\uparrow\rangle + \beta_2|\downarrow\rangle$. The orientations of the spins in space are determined by the coefficients α and β. If there were no spin interactions or identical-particle exchange effects the particles would scatter off from each other without modification of the spin orientation, i.e., coefficients α and β would be unaffected. However, because of indistinguishability in the overlap region, it is necessary to use properly symmetrized wavefunctions. The proper symmetrization of the orbital wavefunction depends on the spin state of the atoms, hence in general a collision will cause the phase of the α_i and β_i coefficients to shift by different amounts. Since $\alpha_i^2 + \beta_i^2 \equiv 1$ and the total spin $\boldsymbol{I} = \boldsymbol{i}_1 + \boldsymbol{i}_2$ should be conserved, a rotation of $\boldsymbol{i}_1$ and $\boldsymbol{i}_2$ around $\boldsymbol{I}$ is implied. If, say, $\beta_1 = \beta_2 = 0$ so that the spins are parallel, there can be no rotation and if $\beta_1 = \alpha_2 = 0$ so that the spins are antiparallel, the effect vanishes. Since for H↓, $\lambda_{th} = 17.4\ T^{-1/2}$ Å and $d \simeq 3.5$–4 Å, these effects are significant at low temperatures.

For a many-body gas a coherent spin oscillation due to the two-body identical-spin rotation effect can exist if the spins are polarized. Lhuillier and Laloë used a density matrix formalism to find an equation for the ith spatial component of the spin current [see also Johnson (1984) and Freed

(1985), whose treatment we follow]:

$$\boldsymbol{J}_i = \frac{-D_0}{1+\mu^2 P^2}\left[\frac{\partial \boldsymbol{P}}{\partial x_i} - \varepsilon\mu\left(\boldsymbol{P}\times\frac{\partial \boldsymbol{P}}{\partial x_i}\right) + \mu^2\left(\boldsymbol{P}\cdot\frac{\partial \boldsymbol{P}}{\partial x_i}\right)\boldsymbol{P}\right] \tag{8.10}$$

where $\boldsymbol{J}_i$ is the ith component of the spin current (each component is a vector) which describes the flow of the spin polarization $\boldsymbol{P}$. The polarization per atom $\boldsymbol{P}$ is defined by $\boldsymbol{P} = \mathrm{Tr}(\rho\boldsymbol{\sigma})$ where $\boldsymbol{\sigma}$ represents the Pauli spin matrices and ρ is a single-particle density matrix. D_0 is the usual spin diffusion coefficient; $\varepsilon = +1$ for bosons and -1 for fermions, and μ is a temperature-dependent parameter which describes the importance of the identical-spin rotation effect. Lhuillier (1983) gives values of μ for H$\downarrow\downarrow$, D$\downarrow\downarrow$ and ^{3}He$\uparrow\uparrow$ in terms of certain collision integrals. μ diverges as $T^{-1/2}$ in the low-temperature limit, as shown in fig. 8.3. We also show her results for the thermal conductivity of H$\downarrow$ for several values of nuclear polarization in fig. 8.4, and the transverse spin diffusion coefficient as a function of temperature in fig. 8.5.

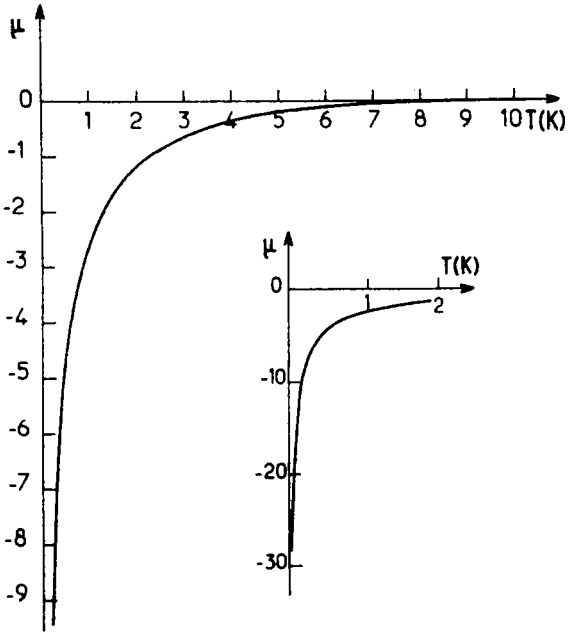

Fig. 8.3. Identical-spin rotation coefficient μ as a function of temperature in H$\downarrow$ (after Lhuillier 1983).

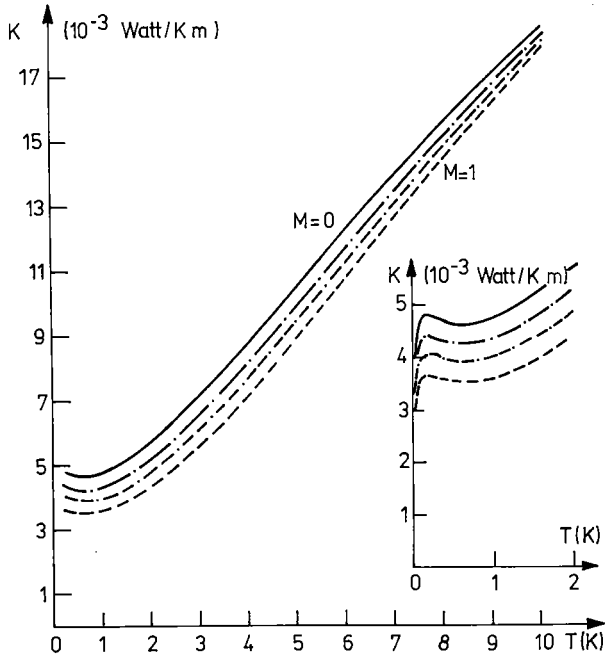

Fig. 8.4. Thermal conductivity in H↓ as a function of temperature for several values of nuclear polarization: $M = 0$, 0.6, 0.8 and 1, in sequential order (after Lhuillier 1983).

The spin polarization $\boldsymbol{P}$ is subject to a continuity equation

$$\frac{\partial \boldsymbol{P}}{\partial t} + \sum_i \frac{\partial}{\partial x_i} \boldsymbol{J}_i = \gamma_n \boldsymbol{P} \times \boldsymbol{B}_0 , \tag{8.11}$$

where $\boldsymbol{B}_0$ is an applied magnetic field and γ_n is the nuclear gyromagnetic ratio. (The spatial gradient is written as a sum over components to avoid a notational difficulty with double vectors.) Combining eqs. (8.10) and (8.11), one finds the nonlinear spin diffusion equation

$$\frac{\partial \boldsymbol{P}}{\partial t} - \gamma_n \boldsymbol{P} \times \boldsymbol{B}_0 = D_0 \sum_i \frac{\partial}{\partial x_i} \left[\frac{1}{1 + \mu^2 P^2} \left\{ \frac{\partial \boldsymbol{P}}{\partial x_i} - \varepsilon\mu \left(\boldsymbol{P} \times \frac{\partial \boldsymbol{P}}{\partial x_i} \right) + \mu^2 \left(\boldsymbol{P} \cdot \frac{\partial \boldsymbol{P}}{\partial x_i} \right) \boldsymbol{P} \right\} \right] . \tag{8.12}$$

This is identical to the Leggett–Rice equation (Leggett 1970) derived for ^{3}He. Leggett showed that the rotation arose from a molecular field type of

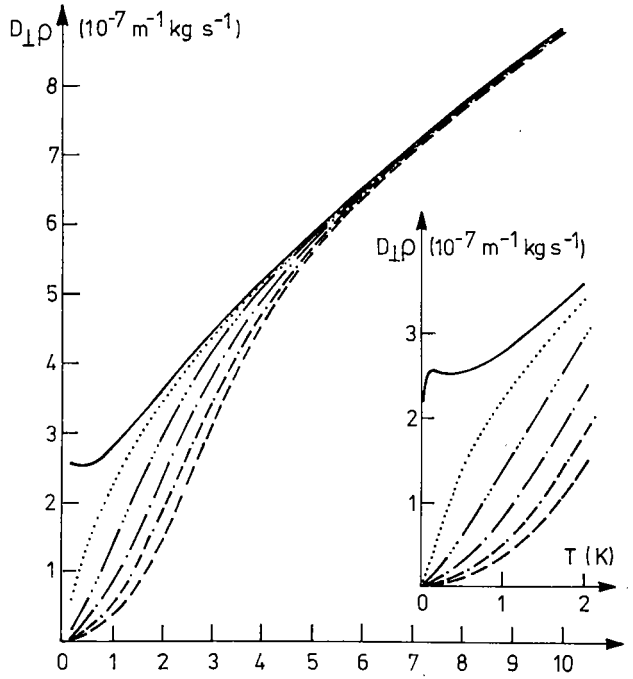

Fig. 8.5. Transverse spin-diffusion coefficient as a function of temperature in H↓ for several values of nuclear polarization. The full curve corresponds to zero polarization (after Lhuillier 1983).

interaction. Lévy and Ruckenstein (1984) have also formulated the dilute-spin problem in a similar formalism using the Hartree–Fock approximation. They found that the identical-spin rotation effect can be cast in terms of a molecular field $\alpha \boldsymbol{P}(\boldsymbol{r}, t)$ where α can be evaluated from scattering considerations, including exchange effects. Since this molecular field is parallel to $\boldsymbol{P}$ it cannot affect the precession rate in eq. (8.11), but it enters into an equation similar to eq. (8.12), which we shall not discuss here.

As we shall now see, eq. (8.12) has oscillatory solutions with frequencies in the neighborhood of the Larmor frequency. If B_0 is uniform, then a long-wavelength rf field can only couple to the uniform precession mode, and the spin-wave modes are not observable by means of a usual dipole field type of pick-up coil. However, a field gradient breaks this symmetry and the modes can then be observed.

In order to obtain insight into eq. (8.12) we take $\langle \boldsymbol{P} \rangle$ along z with a field

gradient $G_x = \delta B_0/\delta x$ in the x direction and linearize the equation to find

$$\frac{\partial P_+}{\partial t} + i\gamma_n \delta B_0 P_+ = \frac{D_0(1 - i\varepsilon\mu P_z)}{1 + \mu^2 P^2} \nabla^2 P_+ , \tag{8.13a}$$

$$\partial P_z/\partial t = D_0 \nabla^2 P_z , \tag{8.13b}$$

where $P_+ = P_x + iP_y$ and $|P_+| \ll |P_z|$. These equations are for the frame rotating at the Larmor frequency. We see that P_z obeys a normal diffusive equation. The transverse polarization P_+ obeys a Schrödinger-like equation where $\gamma_n \delta B_0$ plays the role of the potential energy, $\{D_0 \varepsilon\mu/(1 - \mu^2 P^2)\}\nabla^2 P_+$ the kinetic energy, and $\{iD_0/(1 + \mu^2 P^2)\}\nabla^2 P_+$ is a damping term, which is small for $\mu P \gg 1$. The boundary condition (Lévy and Ruckenstein 1984) $\boldsymbol{n} \cdot \nabla P_+ = 0$ at the surface (with normal $\boldsymbol{n}$) corresponds to $\boldsymbol{J}_+ \cdot \boldsymbol{n} = 0$. If we set the gradient $G_x = 0$, ignore damping and assume a solution of the form $\exp[i(\omega t - qz)]$ we find $P_+ = P_{+0} \cos q_l z$ with $q_l = l\pi/L$, where L is the length of a one-dimensional box and $l = 0, 1, 2, \ldots$. The dispersion relation is $\omega = -D_0 \varepsilon\mu P_z q_l^2/(1 + \mu^2 P^2)$. These modes build up off the Larmor frequency (uniform) mode in frequency space, and as already stated cannot be detected by usual techniques.

With the addition of the gradient term the situation changes. This equation has been studied by Lévy and Ruckenstein and reviewed by Freed (1985). The solutions are Airy functions and the spin-wave frequencies are $\omega_0 \sim 2(\pi q \gamma_n G_x)^{2/3}[D_0 \varepsilon\mu P_z/(1 + \mu^2 P^2)]^{1/3}$.

Spin-waves were observed in H↓↕ by Johnson et al. (1984); their results are shown in fig. 5.19. In fig. 8.6, we show a fit of the theory described above to the experiment, including damping. These experiments used pulsed NMR techniques with small tipping angles. For large tipping angles the linearized equations are no longer applicable. Lévy (1985) has made an extensive analysis of the nonlinear equations and finds several new oscillatory modes.

The experimental coupling to the spin-wave modes by a transverse rf field, $\boldsymbol{b}_t(r)$, results in a measured signal proportional to $\int \boldsymbol{P}_+(r)\boldsymbol{b}_t(r)\,d^3r$. For a field $\boldsymbol{b}_t(r)$, uniform over the sample, coupling exists only to the uniform mode ($q_l = 0$), which is uninteresting. However, due to the gradient field G_x, $P_+(r)$ is nonuniform and the integral is nonzero. Tastevin et al. (1985) have observed spin-waves in gaseous ^{3}He↑ by using a nonuniform field $\boldsymbol{b}_t(r)$ generated by a quadrupole field coil with a similar pickup coil at 45°.

The current discussion has been concerned with nuclear spin-waves. Another possibility is electronic spin-waves. Two ESR experiments (van Yperen et al. 1984, Statt et al. 1985) have been carried out on H↓↕ with no

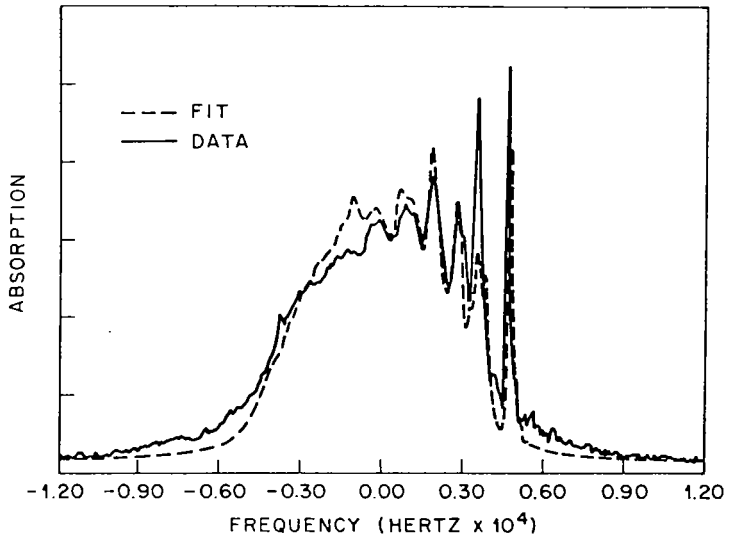

Fig. 8.6. A fit of the linearized spin-wave theory to experiment including damping terms (after Lévy and Ruckenstein 1984).

evidence of spin-waves, however, the experiments were not designed or optimized to observe these effects, although gradient fields were available. Bouchaud and Lhuillier (1985) have recently analyzed spin-waves for the four hyperfine states.

Lhuillier and Laloë (1985) have compared their density-matrix approach to the Hartree–Fock molecular field approach and show that their approach includes additional terms, i.e., it considers both forward and lateral scattering, whereas the molecular field approach has ignored lateral scattering.

9. Many-body effects on the surface

From the preceding chapters, it has become clear that the surface plays a dominant and controlling role in the lifetime, decay, thermal equilibrium and maximum density that can be achieved for a gas of atomic hydrogen. Should one be left with the impression that "the surface is the work of the devil"? To a certain extent we shall see that indeed, were it not for the surface, effects of quantum degeneracy would easily have been observed by now in $H\downarrow$ and $D\downarrow$. On the other hand we shall also see that the surface is "the icing on the cake", responsible for many new and strange phenomena.

9.1. Adsorption isotherms

We first discuss the adsorption isotherms of H↓, the relationship between the surface and gas density at constant temperature. In the introduction, eq. (1.9) and (1.12), for the ideal noninteracting gas, we found

$$n = \frac{\bar{N}_0}{V} + \frac{1}{\lambda_{\rm th}^3}\, g_{3/2} \exp(\mu/kT)\,, \tag{9.1a}$$

$$\sigma = -\frac{1}{\lambda_{\rm th}^2} \ln\{1 - \exp[(\mu_{\rm s} + \varepsilon_{\rm a})/kT]\}\,. \tag{9.1b}$$

Here we have set the degeneracy $g = 1$. In thermodynamic equilibrium the surface chemical potential $\mu_{\rm s}$ is equal to μ, the bulk chemical potential. For this noninteracting picture, when $\mu_{\rm s} = -\varepsilon_{\rm a}$, σ diverges and thus μ is prevented from going to zero, the condition required for Bose–Einstein condensation. Silvera and Goldman (1980) and Edwards and Mantz (1980) realized that interactions between the surface state atoms would resolve this problem of the ideal gas. If the effective interaction between surface H↓ atoms is repulsive, then at high enough density this contribution to the energy will just balance the adsorption energy and $\mu_{\rm s} \to 0$.

The interaction Hamiltonian is similar to eq. (8.6),

$$H = \sum_i \left\{ -\frac{\hbar^2}{2m} \nabla_i^2 + U_{\rm ext}(\boldsymbol{r}) \right\} + \frac{1}{2} \sum_{i \neq j} V(r_{ij})\,. \tag{9.2}$$

For surface atoms $U_{\rm ext} = V_{\rm eff}(z)$ (eq. 4.1 for the adsorption potential); $U_{\rm ext} = 0$ for bulk atoms. We ignore the contribution of any external magnetic fields to $U_{\rm ext}$ as this would contribute an identical energy term for both the bulk and the surface and only give rise to a shift in the zero of energy. $V(\boldsymbol{r}_{ij})$ is taken as the triplet Kolos–Wolniewicz potential for both the bulk and the surface. The effective range form of the interaction, eq. (8.7), is also used here, however, the scattering strength v_0 is in general different for the bulk and surface state atoms.

For the adsorption isotherms we use a Hartree–Fock approximation which yields three equations. Two of these, for the bulk, are identical to eqs. (8.8a, b), however, without the magnetic interaction which is common to bulk and surface.

$$\left[-\frac{\hbar^2}{2m} \nabla^2 + 2v_0 n_{\rm n} + 2v_0 n_0 \right] \phi_{\boldsymbol{k}}(\boldsymbol{r}) = \varepsilon_{\boldsymbol{k}} \phi_{\boldsymbol{k}}(\boldsymbol{r})\,, \quad \boldsymbol{k} \neq 0\,, \tag{9.3a}$$

$$\left[-\frac{\hbar^2}{2m} \nabla^2 + 2v_0 n_{\rm n} + v_0 n_0 \right] \phi_0(\boldsymbol{r}) = \varepsilon_0 \phi_0(\boldsymbol{r})\,, \tag{9.3b}$$

$$\left[-\frac{\hbar^2}{2m} \nabla^2 + 2v_s\sigma + V_{\text{eff}}(z) \right] \phi_{sq}(\boldsymbol{r}) = \varepsilon_{sq}(\boldsymbol{r})\, \phi(\boldsymbol{r}) \,. \tag{9.3c}$$

Here $n = n_n + n_0$ is the total bulk density and n_n and n_0 are the normal condensate densities; the ε's are the corresponding single-particle energies, and v_0 and v_s are the interaction energies in the bulk and on the surface; ϕ_0, ϕ_k and ϕ_{sq} are the condensate, normal and surface wavefunctions. The densities are defined by

$$n_n = \sum_{k\neq 0} N_k |\phi_k(\boldsymbol{r})|^2 \,, \qquad \sigma = \sum_q \sigma_q |\sigma_{sq}(\boldsymbol{r})|^2 \,, \qquad n_0 = N_0 |\phi_0(\boldsymbol{r})|^2 \,.$$

Here $N_0 = \{\exp[(\varepsilon_0 - \mu)/kT] - 1\}^{-1}$ is the number of ground state atoms, $N_k = \{\exp[(\varepsilon_k - \mu)/kT] - 1\}^{-1}$ and $\sigma_q = \{\exp[\varepsilon_{sq} - \mu_s] - 1\}^{-1}$, where μ and μ_s are the bulk and surface chemical potentials. The single-particle energies, to first order, are $\varepsilon_k = (\hbar^2 k^2/2m) + 2v_0 n_0 + 2v_0 n$, $\varepsilon_0 = 2v_0 n_n + v_0 n_0$ and $\varepsilon_{sq} = (\hbar^2 q^2/2m) + 2v_s\sigma - \varepsilon_a$. Note that if two particles are in the same state then the interaction is $v_0 n$, whereas if they are in different states the term is $2v_0 n$. Thus interactions between condensate particles are two times smaller than interactions between normal particles. Bose-condensation is rigorously forbidden in two dimensions (superfluidity is not), so that for surface interactions the factor of two is present for all T. This is explicit when comparing eqs. (9.3b) and (9.3c) where for $T = 0$ K, $n_n = 0$, $n_0 = n$.

Let us now consider the thermodynamic properties. In the interacting Hartree–Fock picture the chemical potential is replaced by

$$\mu \to \mu + 2v_0 n \quad \text{and} \quad \mu_s \to \mu_s + 2v_s\sigma \,, \tag{9.4}$$

in eqs. (9.1). The $T = 0$ K limit is simple and interesting. At equilibrium the chemical potentials for the bulk and surface atoms must be equal: $2v_0 n = -\varepsilon_a + 2v_s\sigma$, or

$$\sigma \equiv \sigma_{\text{sat}} = \frac{\varepsilon_a}{2v_s} + \frac{v_0}{2v_s}\, n \,. \tag{9.5}$$

At $T = 0$ K, as atoms are introduced into the system, they occupy only the surface states until these states are saturated at $\varepsilon_a/2v_s$; they then start populating bulk states. For low densities, $nv_0 \ll \varepsilon_a/2$ and σ_{sat} is essentially constant up to bulk densities of order $10^{20}/\text{cm}^3$ where the second term in eq. (9.5) starts to become important.

The value of v_s was determined by Silvera and Goldman using a two-dimensional hypernetted-chain calculation yielding $v_s = 6.9 \times$

10^{-15} K cm^2 in good agreement with a calculation of Lantto and Nieminen (1980) who found 6.5×10^{-15} K cm^2 by a different method, and another result of 9.7×10^{-14} K cm^2 by Miller and Nosanow (1978) who used a Lennard–Jones potential. These two-dimensional models may be too restrictive as the particles have no freedom to avoid each other in the z-direction. Edwards and Mantz used a less restrictive model in which the wavefunction extended in the z-direction. They found a value $v_s = 5 \times 10^{-15}$ K cm^2. Goldman and Silvera (1981) realized that a factor of two, due to exchange effects amongst identical particles, had been neglected (see eqs. 9.3). Applying this correction to the Edwards–Mantz interaction gives $2v_s = 1 \times 10^{-14}$ K cm^2 or $\sigma_{sat} \simeq \varepsilon_a / 2v_s = 0.96 \times 10^{14}$/cm^2, using a value of 0.96 K for ε_a; the calculated value of v_0 is 0.52×10^{-21} K cm^3.

For finite temperatures the substitution (9.5) is used in eqs. (9.1) which can be solved numerically with $\mu_s = \mu$. The resulting adsorption isotherms are shown in fig. 9.1. At low densities the behavior is well described by eq. (1.7). However, as n_c is approached, the curves flatten out and the critical density for BEC is only achieved after the surface is saturated. This can be

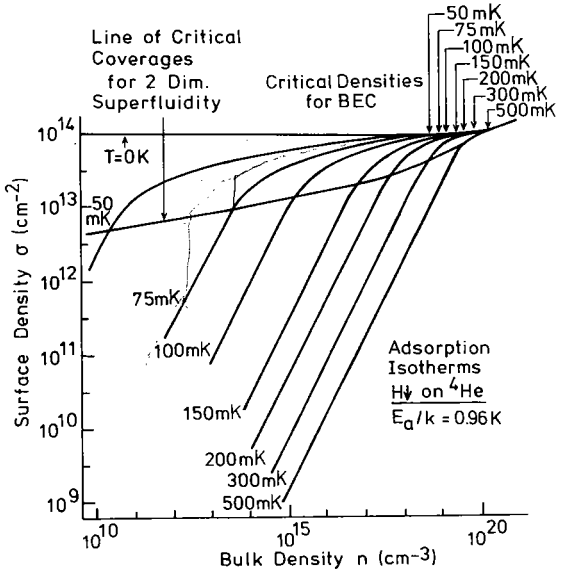

Fig. 9.1. A plot of the adsorption isotherms of H↓↕ with $\varepsilon_a = 0.96$ K and $\sigma_{sat} = 0.96 \times 10^{14}$/cm^2 for various temperatures. The $T = 0$ K isotherm corresponds to BEC for all values of n and intersects the σ-axis at σ_{sat} for $n \to 0$. For each isotherm BEC occurs at the density n corresponding to eq. (1.1) with $g = 1$ and occurs for $\sigma > \sigma_{sat}$. We also show the line for the Kosterlitz–Thouless transition, eq. (9.8). In this case only the σ-axis is meaningful.

understood since one cannot have a macroscopic population of the $k = 0$ bulk state and have yet unfilled surface states, lower in energy. We also note from fig. 9.1 that if the critical density for BEC $n_c \geqslant \varepsilon_a/2v_0$, then the adsorption isotherms are almost classical in behavior. In all cases at BEC $\sigma \geqslant \sigma_{sat}$, which is an extremely important result. The value of σ_{sat} is so large that second- and third-order surface recombination make it extremely difficult to saturate the surface, which is required to achieve BEC in thermodynamic equilibrium.

It is also interesting to study the adsorption isotherms in a regime where the critical density $n_c \gg \varepsilon_a/2v_0$. To do this we maintain the value of v_0 and v_s and reduce the value of ε_a by two orders of magnitude to 9.6 mK. The resulting adsorption isotherms are plotted in fig. 9.2. For a very low temperature isotherm (10 mK) we observe the same behavior as in fig. 9.1. However, for higher temperatures corresponding to higher critical densities, the isotherms cross substantially beyond the $T = 0$ K isotherm and the surface densities increase beyond the value of σ_{sat} for $T = 0$ K (eq. 9.5), before the critical density is achieved. This is a large effect: for $n = n_c$

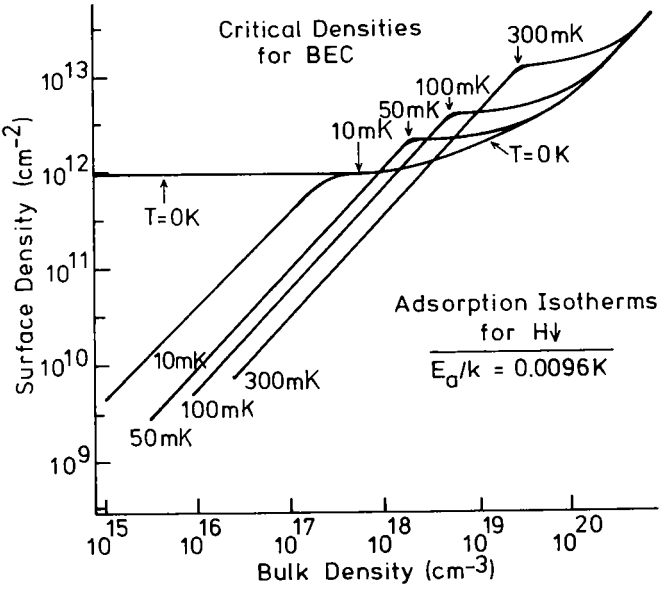

Fig. 9.2. Same as fig. 9.1, but for a fictitious value of ε_a(=0.0096 K), reduced by a factor of 100. In this case we see the effect of the gas phase interaction energy and BEC occurs for surface coverages substantially greater than that of the $T = 0$ K isotherm. Note that the line for two-dimensional superfluidity shown in fig. 9.1 does not appear, as the required values of σ do not exist.

on the 300 mK isotherm, $\sigma = 1.6 \times 10^{13}\,\mathrm{cm}^{-2}$, more than an order of magnitude larger than the zero-temperature saturated density, $\sigma_{sat} = \varepsilon_a/2v_s = 0.96 \times 10^{12}\,\mathrm{cm}^{-2}$. In reality, if ε_a were reduced by two orders of magnitude, this would also reduce v_s since the surface states would be more extended normal to the surface. Note that in this regime, isotherms for different temperatures clearly cross each other; however, the lower temperature isotherm is always at a density above its critical density, n_c, and the higher temperature one is always below its critical density at the crossing.

In summary, for this situation, if a surface existed with such a low value of ε_a, the experimental strategy to minimize surface recombination would be to work at low temperatures so that $\sigma \simeq \varepsilon_a/2v_s$ at n_c.

In eq. (5.13) at BEC for a pure b-state gas, the term

$$K_{bbb}^{eff} = K_{bbb}^{v} + \frac{A}{V}\left[\frac{\sigma_{sat}}{n_c}\right]^3 K_{bbb}^{s} \tag{9.6}$$

is expected to be the dominant loss term, with the surface contribution being larger than that of the bulk. When using ^{3}He surfaces instead of ^{4}He ones, from eq. (9.5), we find that σ_{sat} can be reduced by a factor of $\varepsilon_a^{^3He}/\varepsilon_a^{^4He} \simeq 0.35$ from the calculated value of $\sigma_{sat} \simeq 1 \times 10^{14}/\mathrm{cm}^2$. Thus, the surface recombination rate will be reduced by a factor of 23. The calculated value of σ_{sat} is also a bit pessimistic as it uses the approximation that the total surface energy depends linearly on σ. From Lantto and Nieminen's (1980) calculation of the density dependence of the surface energy, one finds that the interaction energy is increased to about twice that found from the linear extrapolation to densities of order $10^{14}/\mathrm{cm}^2$, so that the expected value for σ_{sat} should be even smaller.

Some of the approximations used in these calculations have been checked by Mello et al. (1983) who performed a QM virial calculation in two- and three-dimensions. They found that the effective range theory is a very good approximation in the region $T < 1$ K and the s-wave scattering theory also gives good results. Their calculation of the temperature dependence of the interactions by means of a virial expansion to correct μ_s does not give a serious change to the results of Silvera and Goldman or Edwards and Mantz. Kagan et al. (1982) have also considered the problem of interactions and dimensionality in quasi two-dimensional situations.

9.2. Two-dimensional superfluidity

In two dimensions for finite temperatures there can be no macroscopic population of the zero-momentum state (Hohenberg 1967), i.e., no

Bose–Einstein condensation. Nevertheless, Edwards and Mantz (1980) pointed out that H↓ may have a Kosterlitz–Thouless transition (Kosterlitz and Thouless 1978) to a two-dimensional superfluid state, such as that already observed in ^{4}He films. The transition occurs at a critical temperature

$$T_c^{2D} = \pi\hbar^2\rho_{sc}/2km^2 , \tag{9.7}$$

where m is the hydrogen mass, k is the Boltzmann constant and ρ_{sc} is the superfluid mass density ($\rho_s = m\sigma$) just below T_c^{2D}. At T_c^{2D}, ρ_s changes discontinuously from zero to ρ_{sc} (Nelson and Kosterlitz 1977). In order to evaluate T_c^{2D} the fraction ρ_{sc}/ρ_s must be determined. Edwards (1982) has estimated $\rho_{sc} \simeq \rho_s$ using results of Saam (1981). Evaluating gives $T_c^{2D} = 0.756(\sigma/1\times10^{14})$ with σ in atoms/cm^2 and T_c^{2D} in K. The line σ versus T_c^{2D} is shown in fig. 9.1. Since high values of σ are difficult to achieve, evidently for values of σ_{sat} in the figure, it is easier to achieve two-dimensional superfluidity than BEC. Superfluidity in two-dimensional films of H↓ has also been theoretically studied by Shevchenko (1982).

9.3. Hydrodynamic modes of two-dimensional H↓

In this section we consider the possibility of detecting H on a surface of helium by studying the hydrodynamic modes of the film. Insight can be obtained by considering the modes of a helium surface, and we first briefly review the litany of theory and experiment.

A free surface of ^{4}He with depth d has capillary or ripplon waves with dispersion relation

$$\omega^2 = \left(gk + \frac{\alpha k^3}{\rho}\right)\tanh(kd) , \tag{9.8}$$

where g is the gravitational acceleration, α the surface tension, k the wave vector and ρ the mass density (Atkins and Rudnick 1977). Such waves which are dominated by the surface tension term for $k \geq 100\,\mathrm{cm}^{-1}$ have been observed experimentally by optical techniques. Andreev and Kompaneets (1972) predicted the existence of a second propagating surface wave which they called surface second-sound. This is an adiabatic wave in the density of ripplons (similar to bulk second-sound in ^{4}He) and could be detected as a temperature wave. This wave has never been observed, and is evidently highly attenuated. They also predicted a propagating adiabatic wave for ^{3}He localized at the ^{4}He surface, which has been observed by thermal detection techniques (Eckardt et al. 1974).

For thin films of a normal fluid which are strongly clamped to the substrate, surface waves cannot propagate due to viscous damping. For superfluid ^{4}He, although the normal component is clamped to the substrate, the superfluid component can oscillate as third-sound waves (Atkins and Rudnick 1977). Since the superfluid carries no entropy, the build-up of superfluid at the wavecrests lowers the temperature there, while the depletion at the troughs raises the temperature. Thus third-sound waves can be detected thermally as well as mechanically due to mass amplitude fluctuations. The dispersion relation for a film of thickness d is

$$\omega = \sqrt{\frac{\pi_s}{\rho} f d}\, k\,, \tag{9.9}$$

where ρ_s is the superfluid density, ρ the total density and f the restoring force exerted by the substrate on the film. If the long-range substrate film potential is $-c/d^3$, then $f = 3c/d^4$. Third-sound has been extensively studied by experimental techniques. In a thin-film mixture of ^{3}He–^{4}He, the two species are believed to phase separate with the ^{3}He on top of the ^{4}He. This system has been studied theoretically and experimentally by Ellis et al. (1981). They found that the normal ^{3}He film loaded the ^{4}He, reducing the third-sound velocity, in agreement with theory. However, there is some controversy here as McQueeny et al. (1984), who have also studied ^{3}He–^{4}He films, believe that a solution model is more appropriate.

With this review of helium surface waves, we are now in a position to discuss the expectations for H↓. The case of H↓ on ^{4}He is quite similar to ^{3}He on ^{4}He. The two systems phase separate with the H↓ on top of the ^{4}He. However, H↓ is a boson (^{3}He a fermion) and is predicted to have a Kosterlitz–Thouless–Nelson superfluid transition. The H↓ is also limited to (sub)monolayer thicknesses. Guyer and Miller (1981, 1982) have studied this problem theoretically. They used a model in which the ^{4}He had a thickness h_4 and the incompressible H↓ a thickness h_1. Both ^{4}He and H↓ were attracted to a substrate by a d^{-3} Van der Waals potential. If both components were superfluid, they found two coupled third-sound modes at each value of k, one corresponding to the ^{4}He, the other to the H↓, both being shifted from their value for a single-component system. If the H↓ is normal, the third-sound velocity of the ^{4}He mode would be shifted by an amount proportional to the H↓ coverage. Thus, third-sound measurements which appear to be within the range of experimental detection by capacitive techniques should enable a direct detection of the surface H↓ coverage, and, according to Guyer and Miller, should give a clear and unequivocal demonstration of superfluidity in H↓. However, Williams (1984) has pointed out that detection of a second propagating mode will

not be unequivocal proof of superfluid H↓, as the second-sound surface mode of Andreev and Kompaneets may not be attenuated for the normal H↓.

Guyer and Saslow (1983) have presented a $T = 0$ K calculation which removes some of the unappealing aspects of the Guyer–Miller model. They introduced a single (or sub) monolayer of H↓ with variable superfluid density σ_s, which is compressible but unlimited in extent in the z-direction, (as compared to an incompressible film of fixed density σ_s with variable thickness h_1). The film was coupled to a rigid substrate, but instead of using a d^{-3} Van der Waals potential they modeled the substrate potential with a short-range (exponential) Morse potential which has an analytical solution. For low coverages the H overlayer is localized several Å away from the surface (see fig. 4.1). For $\sigma \to \sigma_{sat}$ they found the H↓ surface density extended more than 20 Å from the ^{4}He surface as shown in fig. 9.3.

Results of Guyer and Saslow's calculations for the third-sound velocity are shown in fig. 9.4. The velocity increases with coverage and then softens as the film saturates. They ascribe the softening to a weakening of the Van der Waals force on the part of the H↓ density that resides far from the

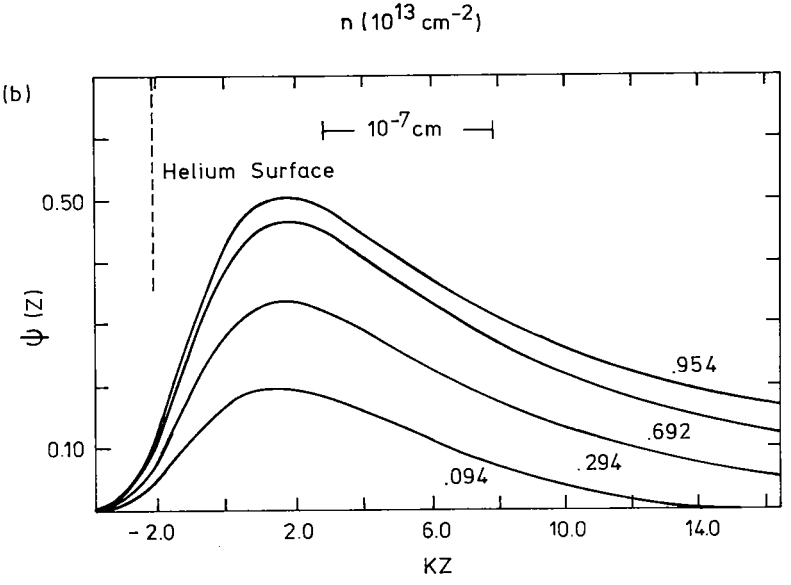

Fig. 9.3. The density distribution of a superfluid film of H↓ on ^{4}He for several values of σ/σ_{sat} (after Guyer and Saslow 1983).

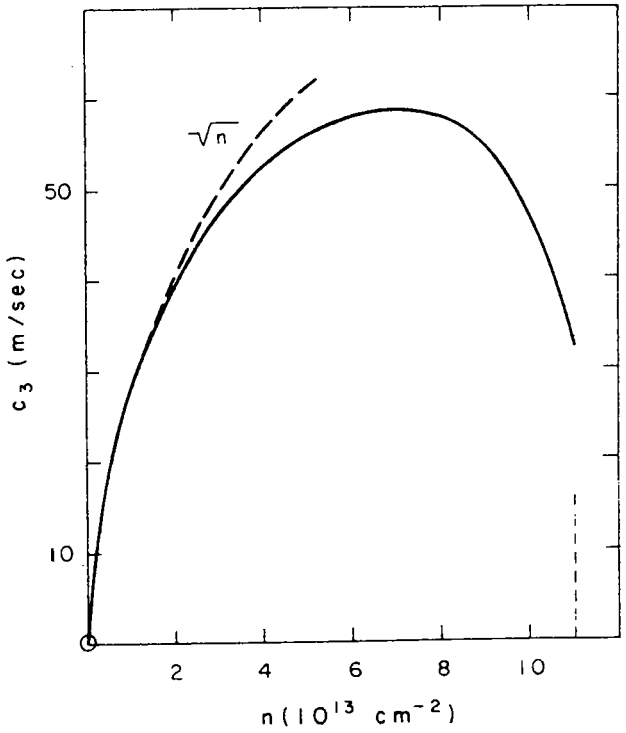

Fig. 9.4. The third-sound velocity as a function of H↓ surface coverage (n) (after Guyer and Saslow 1983).

surface. Although this is reasonable, their calculated, reduced frequency may not be as significant as shown in fig. 9.4 as they replaced the Van der Waals potential with a Morse potential which falls off much faster at large distances.

10. Prospects for spin-polarized hydrogen

With the creation of long-lived gas samples of spin-polarized hydrogen and deuterium, a low-temperature field of study concerning new Boson and Fermion quantum gases has been opened. In this final section we shall discuss some of the challenges facing experimentalists seeking to study these systems in the limit of quantum degeneracy. Our objective is to present possible approaches for achieving these goals and to discuss the formidable problems which are posed. As with any new system the

application of ideas utilizing new properties and techniques can extend into new areas. We shall briefly mention some of these applications, many of which have been discussed in greater detail in the review by Greytak and Kleppner (1984), and then concentrate on quantum fluid aspects.

10.1. Applications

An exciting possible utilization of the techniques developed for stabilizing atomic hydrogen is the construction of a cryogenic hydrogen maser. Currently, the most stable time and frequency source is the room-temperature hydrogen maser (parts in 10^{16} stability over periods of hours). The major intrinsic source of line broadening is spin-exchange scattering. At low temperatures the cross section is reduced by a few orders of magnitude which may translate into a substantial improvement in stability. The increased lifetime in a helium-covered cell may provide higher density and thus power advantages which can be used for increasing the stability. The room-temperature maser is not a primary standard because the frequency depends on the wall shift. The teflon coated walls can slowly become contaminated, giving rise to a small but important variation of the frequency. It is believed that the ^{4}He covered walls of a cryogenic hydrogen maser would overcome this difficulty. Many of these aspects have been analyzed by Berlinsky and Hardy (1981).

Cold sources of H and D in atomic physics can be used to greatly reduce Doppler broadening in precision spectroscopic studies. In high-energy physics nuclear polarized samples can be injected into accelerator beams to study spin-dependent scattering off from polarized targets. In fusion physics spin-polarized $D\downarrow\ddagger$ may be used to enhance the fusion cross section and energy yield in a plasma fusion reactor (Kulsrud et al. 1982). The use of a dense $H\downarrow$ target may simplify experiments for the study of the positron–$H\downarrow$ cross section. Finally, we mention that a gaseous atomic-tritium source may be used for precision measurements of the rest mass of the neutrino in β-decay, with the advantage of having a well-defined atomic final state in the decay process.

10.2. Goals in the study of quantum fluids

The most prominent goal for researchers in atomic hydrogen is to produce hydrogen in a state of Bose–Einstein condensation. For any density below about 10^{21}–$10^{22}/\text{cm}^3$ this would be the first clear experimental example of a weakly interacting Bose gas [see, however, Crooker et al. (1983), who see very similar behavior for thin films of ^{4}He in vicor glass]. A great deal of theory which has never been tested under ideal conditions exists for this

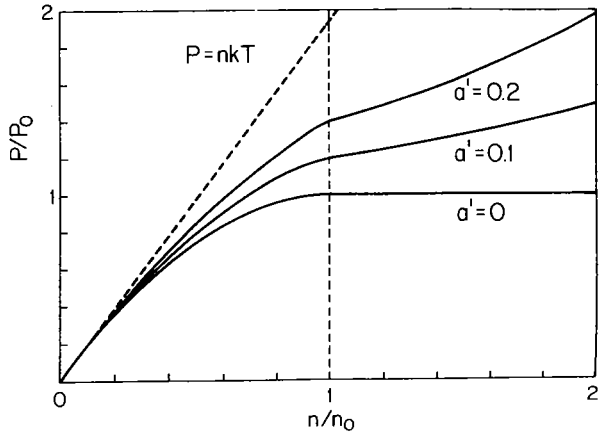

Fig. 10.1. The equation of state for a weakly interacting Bose gas for three values of the interaction strength $a' = n_0 v_0 / kT_c$, where v_0 is given in eq. (8.7). P_0 and n_0 are the pressure and density of the noninteracting gas ($a' = 0$) at the transition (after Greytak and Kleppner 1984).

system [see the review by Greytak and Kleppner (1984) ch. 3, for a summary of these properties]. Clearly, successful achievement of BEC would open the door to studying a remarkable array of predicted properties, including superfluidity in a gas. Moreover, new unexpected phenomena are likely to emerge. Thus, the first and most burning question is "how does one experimentally manipulate a sample to detect the state of BEC?". An obvious technique is to measure the equation of state (EOS) or the compressibility. The characteristic behavior of pressure versus density for an isotherm is shown in fig. 10.1. For the noninteracting gas, p is constant for $n > n_c$, the critical density. Interactions, represented by the parameter a' in the figure, result in an increase of p at n_c, but the curve and its derivative (compressibility) are still quite characteristic of BEC.

It is clear to any reader who has read through this review that techniques are available to measure p, n and T (see section 5.12), and thus the EOS. The problem, however, is to achieve a sufficiently high density or low temperature. The highest density yet achieved (Hess et al. 1984) of $4.5 \times 10^{18}\,\mathrm{cm}^{-3}$ was at $T = 570\,\mathrm{mK}$ ($T_c = 43.5\,\mathrm{mK}$ for this density). The lowest temperatures of study, $T \sim 60$–$70\,\mathrm{mK}$, have been achieved with bulk densities probably in the range of 10^{15}–$10^{16}/\mathrm{cm}^3$ (corresponding to T_c of 159–740 μK). The source of these problems is also clear. At both high and low densities, recombination heats the sample and cell or is sufficiently rapid that a high density cannot be built up. The heating problem can be of two sorts:

(1) the heat load is so high that the temperature of the refrigerator rises, or

(2) the gas sample itself heats up due to thermal gradients and Kapitza resistance so that the gas is not in equilibrium with the cell walls.

10.2.1. Compression of bubbles

The first problem mentioned above can be resolved by using small samples (the bubbles mentioned in section 5.12) so that the total heat load is reduced. Let us analyze the heating problem in a bubble at BEC (Silvera 1985).

We discuss and encounter some of the experimental problems by way of a numerical example. For the sake of clarity we do not parameterize the problem to find an optimum configuration, but rather use a typical situation to demonstrate some of the difficulties that arise. Assume that we seek to attain BEC with a critical temperature, $T_c = 100$ mK, corresponding to $n_c = 1.57 \times 10^{19}/\text{cm}^3$. A bubble of H↓↑ with radius r is created in a vessel of liquid ^{4}He (see section 5.12) at this temperature with $n < n_c$. As the pressure is increased at constant T, the density increases and sweeps through n_c. Thus, we can trace p versus n at constant T to determine the EOS. The H↓↑ sample is under a pressure $p = p_{hyd} + p_{st}$ where p_{hyd} is the hydrostatic pressure due to a column of liquid helium and

$$p_{st} = 2\alpha/r \tag{10.1}$$

is the pressure due to surface tension, $\alpha = 3.78 \times 10^{-4}$ N m^{-1}. For bubbles somewhat smaller than one millimeter in diameter, p_{st} alone can be sufficient to pressurize H↓↑ into BEC. Due to recombination in the bubble, r shrinks and p_{st} increases. From eqs. (1.11) and (10.1) we see that the critical pressure is proportional to $T^{5/2}$ and the critical radius is $r_c = 67.9(100/T_c)^{5/2}$, with T_c in mK and r_c in μm. For the conditions $T_c = 100$ mK and $n_c = 1.57 \times 10^{19}/\text{cm}^3$, $r_c = 67.9$ μm and 2×10^{13} atoms are in the gas phase of the spherical bubble. We establish a bubble having $r > r_c$ and monitor p and n during its decay. We first determine the decay rate. From an analysis of bubble decay (Sprik et al. 1985), one finds that the inverse time constant of the bubble of volume V is

$$\tau^{-1}(V) = -\frac{V}{V} \simeq \left[2\theta_b^v K_{bbb}^v + \left(\frac{A}{V}\right)\left(\frac{\sigma_{sat}}{n_c}\right)^3 2\theta_b^s K_{bbb}^s\right] n^2 . \tag{10.2}$$

All of these terms are known and $\tau^{-1} \simeq (1.79 + 6.84) = 8.63\ \text{s}^{-1}$, or $\tau = 116$ ms, where we have taken $\sigma_{sat} = 5 \times 10^{13}/\text{cm}^2$. The power dissipated is

$-\dot{N}D_0/2$ (D_0 is the dissociation energy) or $-\dot{N} = -\dot{n}V = 1.8 \times 10^{14}\ \mathrm{s}^{-1}$ and $\dot{Q} = 66\ \mu\mathrm{W}$.

We make a few remarks at this time. 66 μW at 100 mK is a heat load which a moderate sized ^{3}He–^{4}He dilution refrigerator can handle. A decay time of 116 ms (time for volume decrease of $\sim 1/e$) is rapid, but a measurement time of 10 ms/point seems possible. We note from the calculation of τ^{-1} that the decay is dominated by the surface term. This is quite unfortunate since otherwise one could use smaller bubbles to reduce this contribution to the heating, as $A = 4\pi r^2$. Larger bubbles with lower T_c have greater heat dissipation due to the larger area (of course we could compress these with p_{hyd} to reduce the area, but as already stated our object is to trace through one example).

Now the most important question is "can the temperature of the bubble be maintained at 100 mK in the presence of the released recombination energy?". First assume that all of the recombination energy is dissipated uniformly in the H↓↕ gas. There are two heating problems:

(1) the thermal gradient across the bubble due to the finite thermal conductivity of the gas, and

(2) a thermal step at the boundary due to the Kapitza resistance.

We first calculate gradients due to thermal conductivity. For a density of $1.57 \times 10^{19}\ \mathrm{cm}^{-3}$, using data from Lhuillier (1983), the collision mean free-path $\lambda_{\mathrm{mfp}} = 3\kappa/(nC_v v) \simeq 0.7\ \mu\mathrm{m}$, where κ is the thermal conductivity and C_v the specific heat. The thermal gradient is $\Delta T = (1/15)(\dot{Q}/V)r^2/\kappa$ (Sprik et al. 1985). Using $\kappa = 3.5 \times 10^{-3}\ \mathrm{W/K\,m}$, we find $\Delta T > 1\ \mathrm{K}$.

Next we consider the Kapitza resistance. Using expression (4.13a) with $\alpha = 0.3$ we find $\dot{Q} = 8.6 \times 10^{-5} \Delta T\ \mathrm{W\,K}^{-1}$, or $\Delta T \approx 750\ \mathrm{mK}$ for $T = 100\ \mathrm{mK}$. With this type of heating the bubble will explode due to the thermal instability observed by Sprik et al. (1983) and Tommila et al. (1984), and studied by Kagan et al. (1984).

The problem is thus the following: the gas develops a large thermal gradient and the heat cannot be conducted out through the He walls fast enough. What can be done to help? Certainly the example used is not an optimum, but the problem is severe enough that major improvements are required. One would be to use ^{3}He surfaces which reduces σ_{sat} by a factor of about 0.35, or the heating due to surface recombination (proportional to σ^3_{sat}) by a factor of 23 (we ignore changes in bubble size for $T_c = 100\ \mathrm{mK}$ due to the reduced value of the surface tension for ^{3}He). This alone would be a major gain. However, the use of ^{3}He–^{4}He mixtures, to create ^{3}He surfaces, introduces another problem since the thermal conductivity of ^{3}He–^{4}He mixtures is a few orders of magnitude lower than that of pure ^{4}He (Rosenbaum et al. 1974) and the ^{3}He–^{4}He itself may develop thermal gradients.

The situation for the bubbles, as stated, may be pessimistic. For example, not all of the recombination energy goes into the gas. As pointed out by Silvera (1984), it may be possible for molecular H_2 formed by recombination to go directly into the liquid and relax there without transferring energy to the gas. In section 6 it was shown that the initial recombination step divides ~70 K of energy (of the 51 967 K available) between the excited molecule (H_2^*) and the spectator atom. The average number of collisons to relax from one state to another of H_2^* may be of order 10^2 (the splittings between levels of H_2^* is large compared to the kinetic energy so that the integrals representing relaxation cross sections will be small due to the oscillations in the wavefunctions). Thus, it might be advantageous to use very small bubbles, even though the density and T_c will be higher.

The purpose of this discussion on bubbles, which ends here, was not to be definitive, but to demonstrate with numerical examples some of the problems facing the experimentalists.

10.2.2. Traps for low-field seekers

Recently Hess (1985) has proposed a scheme for magnetic trapping of hydrogen at 20 mK and cooling to temperatures below 10 μK by "evaporation" to obtain BEC. Although the information available in his abstract is limited, we shall discuss what we believe to be possible advantages and problems.

The great advantage of a trap is that one rids the system of helium walls which catalyze recombination. Unfortunately, it is not possible to create a static magnetic field in charge- and current-free space which has an absolute field maximum. Any maximum of a component is always a saddle-point (Wing 1984). In a standard solenoidal geometry (fig. 5.2) the atoms are compressed in along the axis to the field center; they are forced radially outwards resulting in higher densities at the confining side walls. Maxwell's equations do allow static local magnetic-field minima, with $|\boldsymbol{B}|$ not necessarily zero at the minimum. Since states a and b of fig. 2.1 are high-field seekers, it is not possible to trap H↓ with a static magnetic field. On the other hand, states c and d are low-field seekers so that it is possible to trap H↑ in a field minimum. Pritchard (1983) has discussed magnetic trapping of neutral atoms in such fields.

H↑ is a perfectly acceptable two-component thermodynamic system which can Bose condense. The important questions are "can a trap be filled, can the trapped atoms be cooled, what are the lifetimes for decay to H↓ or H_2, and how are the trapped atoms detected?".

Several methods can be used to produce H↑. c and d-state atoms can be

collected by passing an H atomic beam through a hexapole magnet, which focuses c- and d-state atoms and defocuses a- and b-state atoms. Alternately, a 180° ESR pulse on H↓ in a high magnetic field will convert H↓ to H↑, which is then ejected to low field. Still another technique is to use a field gradient at low temperature which drives H↓ to high fields and H↑ to low fields. Whatever the technique, Hess proposes to thermalize the H↑ on 20 mK walls. The field would then be activated to trap and isolate the atoms from the He walls. The trapped atoms can then be cooled by reducing the trapping gradient so that hot atoms "boil" out of the trap and stick to the He walls. The remaining atoms thermalize by collision and cool to temperatures less than 10 μK, according to Hess. The density required for BEC of a (uniform density) one-component gas at 10 μK is $1.6 \times 10^{13}/\text{cm}^3$. The gas could possibly be studied by NMR or ESR.

The greatest problem in this proposal seems to be the thermalization of the atoms without their sticking to the wall before being trapped. Let us estimate the equilibrium density, n. If the walls have a ^{3}He surface with $\varepsilon_a/k = 0.34$ K, then from eq. (1.7), with $T = 20$ mK, $n = \sigma/30$ with n in cm^{-3} and σ in cm^{-2}. The heating rate is $\dot{Q} = K^s\sigma^2(D_0/2)A$. Using a value of K^s (table 5.1) corresponding to $B = 1$ T and $A = 10\,\text{cm}^2$, we find $\sigma \sim 2 \times 10^{10}/\text{cm}^2$ for $\dot{Q} \simeq 10$ μW, which corresponds to the cooling power of a moderate refrigerator operating at 20 mK. The result is $n = \sigma/30 = 6.7 \times 10^8\ \text{cm}^{-3}$ near the thermalizing walls surrounding the trap. Thus the trap cannot be loaded from a fully thermalized gas. This means that the atoms must have a moderate accommodation coefficient and a very low sticking coefficient, α_s. Jochemsen et al. (1981) measured $\alpha_s = 0.016(5)$ for ^{3}He at $T \simeq 100$ mK. Zimmerman and Berlinsky (1983) calculated $\alpha_s \propto T^{1/2}$, so that at 20 mK, $\alpha_s \simeq 0.007$, or an average of 140 bounces before sticking. The scaling of the sticking coefficient is somewhat questionable, as has been mentioned in section 4, Zimmerman and Berlinsky did not use a long-range potential in their calculation, which may be very important. Measurements by Salonen et al. (1984) indicate that the Kapitza conductance is increasing with decreasing temperature. Since this is an energy moment of α_s, it means that α_s probably also increases with decreasing T. In any event, filling of the trap may be a critical problem.

The final consideration is the lifetime of the sample. By assumption the losses due to escape are acceptable and advantageous in the cooling of the gas. The other mechanisms are:

(1) three-body recombination,
(2) spin-exchange decay, and
(3) electron spin relaxation from c, d to a- and b-states, which are then ejected from the trap by the field gradients.

The first process is negligible. If the field $B \leqslant 500$ G (0.05 T) then c-state

atoms will escape from the trap as their magnetic moment decreases in low field (see fig. 2.1), leaving pure d-state, which trivially has no spin-exchange problem. There are no accurate calculations of magnetic-relaxation rates at low fields, and new decay channels open up, compared to high fields (Kagan et al. 1981). A rough estimate indicates lifetimes of order 1–10 s for electronic relaxation with density $5 \times 10^{13}/\text{cm}^3$.

All told this seems to be a promising proposal although it is replete with uncertainty, the largest being the filling of the trap and the question of the cooling time of atoms in the trap which must be much shorter than the decay time.

10.2.3. Traps for high-field seekers

Although it is not possible to make a static trap for the high field seeking a- and b-state atoms, it is possible to make an ac or dynamic trap. This problem has recently been analyzed by Lovelace et al. (1985). The dynamic magnetic trap takes advantage of a principle used in strong-focussing particle accelerators. Consider a solenoidal field $B_z(r)$ of the form of eq. (5.1). The static forces on a magnetic moment are (ignoring radial components of the field)

$$F_\rho = \mu_B B_0 \rho / z_0^2 , \qquad F_z = -2\mu_B B_0 z / z_0^2 . \tag{10.3}$$

The force in the z-direction is inward and leads to confinement of the a- and b-state atoms, whereas the force in the radial direction is outwards and leads to expulsion. The natural harmonic frequency ω_0 for confined particles is given by eq. (8.3b), $\omega_0 = (2\mu_B B_0 / m z_0^2)^{1/2}$. Clearly, as discussed earlier, this static field is nonconfining. Now, a dynamic trap can be achieved if B_0 is superimposed on a large static field in the z-direction and is modulated at a frequency ω. On alternate phases, the forces in eq. (10.3) are positive and negative since orientation of the magnetic moment in space (or spin state) does not change. It can be shown (Landau and Lifshitz 1976) that at a sufficiently high frequency (in practice, of order kHz or greater), the particles undergo a slow motion corresponding to the natural motion (without the ac field) and a fast ac motion. As a result a particle will oscillate with amplitude ξ at frequency ω about the slowly varying coordinate $\rho_0(t)$ such that the particle has larger displacements from the origin, $|\rho_0| + |\xi|$, during the phase when the force is inward and $|\rho_0| - |\xi|$ when the force is outward. Since the force is proportional to ρ, there is a net inward force. This holds for both F_ρ and F_z so that the particle is confined.

Lovelace et al. (1985) have simulated such traps and find that fields of

order of 1 T at a few kHz are required to trap a gas at a temperature of a few mK. The gas can be cooled by reducing the amplitude of the confining field so that hot atoms can escape and stick to cold walls. Internal viscous heating due to the interaction of the atoms with the ac field puts some limitation on the cooling.

There are some experimental difficulties with the dynamic trap. A very careful design must be made to avoid eddy current heating of the refrigeration system. The most serious problem, again as discussed for the static trap, is to fill the trap with a gas at a temperature of a few mK. The advantage over the static trap is that the atoms are in the two lowest hyperfine states so that the lifetime will not be limited by electronic spin relaxation.

10.2.4. Two-dimensional superfluidity

The final subject that we shall discuss is two-dimensional superfluidity. At this time the most sensitive means of detecting this phenomenon seems to be by a study of third-sound in a pill box shaped resonator such as has been used for studying ^{4}He (Ellis and Hallock 1983). In this case H$\downarrow\ddagger$ would be condensed on a ^{4}He film in such a resonator and the shift of the ^{4}He third-sound mode or new modes due to H$\downarrow\ddagger$ would be sought (see section 9). The signals are estimated to be very small but within the sensitivity of measuring techniques. A large uncertainty is in the stability of the ^{4}He film thickness. Godfried et al. (1985) observed large variations in ^{4}He film thickness during the H$\downarrow$ filling phase of the hydrogen cell. Since the frequency of the ^{4}He third-sound depends on the film thickness, the thickness should be stabilized to parts in 10^5 to 10^6. A second and perhaps more serious problem for observing two-dimensional BEC is that it is probably not possible to fill the pill box with a sufficient density of H$\downarrow\ddagger$ to achieve the required coverages shown in fig. 9.1. In the geometry of Ellis and Hallock the pill box resonator has a hole at the center for filling with the condensable gases. If the hole is too large, the Q of the cavity will be attenuated. Estimates indicate that the steady-state density in the cavity, with flow-in through the hole of limited diameter as a source, and surface recombination as a sink for atoms, is too low to achieve the densities required for two-dimensional superfluidity. Nevertheless, such an experiment at lower coverages may give insight into surface decay processes and allow one to study a large region of the adsorption isotherms of fig. 9.1.

Although the pathway to the study of degenerate phenomena in these quantum systems is filled with uncertainty, the rapid developments and many new ideas which have emerged in the past several years encourages experiments and theorists alike to meet the challenge of nature.

Acknowledgement

We acknowledge and thank many colleagues and students for stimulating discussions which have contributed to this review, but in particular: V.V. Goldman, E. Eliel, H. Godfried, A. Lagendijk, R. Sprik and B. Verhaar. J. Gillaspy and R. van Rooijen helped with the programming of some functions. Hans van Zwol and Erik Salomons aided with the calculation of some of the tables in section 6. IFS acknowledges support from DOE contract number DE FGO2-85-ER-45190; JTMW from the Stichting FOM.

References

Adamson, A.W., 1976, Physical Chemistry of Surfaces, 3rd Ed. (Wiley, New York).
Ahlrichs, R., R. Penco and G. Scoles, 1977, Chem. Phys. **19**, 119.
Ahn, R.M.C., J.P.H.W. van den Eijnde, C.J. Reuver, B.J. Verhaar and I.F. Silvera, 1982, Phys. Rev. **B26**, 452.
Ahn, R.M.C., J.P.H.W. van den Eijnde and B.J. Verhaar, 1983, Phys. Rev. **B27**, 5424.
Allison, A.C., 1972, Phys. Rev. **A5**, 2695.
Alt, E.O., P. Grassberger and W. Sandhas, 1967, Nucl. Phys. **B2**, 167.
Amdur, I., 1935, J. Am. Chem. Soc. **57**, 856.
Amdur, I., 1938, J. Am. Chem. Soc. **60**, 2347.
Amdur, I., and A.L. Robinson, 1933, J. Am. Chem. Soc. **55**, 1395.
Andreev, A.F., and D.A. Kompaneets, 1972, Zh. Eksp. & Teor. Fiz. **61**, 2459 (Sov. Phys.-JETP **34**, 1316).
Atkins, K.R., 1957, Physica **23**, 1143.
Atkins, K.R., and I. Rudnick, 1970, in: Progress in Low Temperature Physics, Vol. VI, ed. C.J. Gorter (North-Holland, Amsterdam) p. 37.
Balling, L.C., R.J. Hanson and F.M. Pipkin, 1964, Phys. Rev. **133**, A607.
Bashkin, E.P., 1981, JETP Lett. **33**, 8.
Bass, A.M., and H.P. Broida, eds, 1960, Formation and Trapping of Free Radicals (Academic Press, New York).
Baym, G., 1969, Lectures on Quantum Mechanics (Benjamin, New York) ch. 18.
Bell, D.A., G.P. Kochanski, L. Pollack, H.F. Hess, D. Kleppner and T.J. Greytak, 1984a, in: Proc. 17th Int. Conf. on Low Temperature Physics LT-17, Karlsruhe, August 15–22, eds U. Eckern, A. Schmid, W. Weber and H. Wühl (North-Holland, Amsterdam) p. 449.
Bell, D.A., G.P. Kochanski, D. Kleppner and T.J. Greytak, 1984b, in: Proc. 17th Int. Conf. on Low Temperature Physics LT-17, Karlsruhe, August 15–22, eds U. Eckern, A. Schmid, W. Weber and H. Wühl (North-Holland, Amsterdam) p. 541.
Bell, R.J., 1966, Proc. Phys. Soc. London **87**, 594.
Berlinsky, A.J., 1977, Phys. Rev. Lett. **39**, 359.
Berlinsky, A.J., 1980, J. Phys. (France) **41**, C7-43.
Berlinsky, A.J., 1981, J. Appl. Phys. **52**, 2309.
Berlinsky, A.J., 1984, private communication.
Berlinsky, A.J., and W.N. Hardy, 1981, in: Proc. 13th Annual Precision Time and Time Interval Applications and Planning Meeting, Washington, DC, NASA Conf. Publ. **2220**, 547.

Berlinsky, A.J., and B. Shizgal, 1980, Can. J. Phys. **58**, 881.
Berlinsky A.J., R.D. Etters, V.V. Goldman and I.F. Silvera, 1977, Phys. Rev. Lett. **39**, 356.
Bishop, D.M., and S. Shih, 1976, J. Chem. Phys. **64**, 162.
Böheim, J., W. Brenig and J. Stutzki, 1982, Z. Phys. **B48**, 43.
Bouchaud, J.P., and C. Lhuillier, 1985, J. Phys. (France) **46**, 1781.
Bredohl, H., and G. Herzberg, 1973, Can J. Phys. **51**, 867.
Brenig, W., 1980, Z. Phys. **B36**, 227.
Buckle, S.J., 1984, J. Phys. (France) **C17**, L633.
Castaing, B., and M. Papoular, 1983, J. Phys. Lett. **44**, L-537.
Clark, J.W., 1979, in: Progress in Particle and Nuclear Physics, Vol. II, ed. D.H. Wilkinson (Pergamon, Oxford) p. 90.
Clark, J.W., E. Krotscheck and R.M. Panoff, 1980, J. Phys. (France) **41**, C7-197.
Cline, R.W., T.J. Greytak, D. Kleppner and D.A. Smith, 1980a, J. Phys. (France) **41**, C7-151.
Cline, R.W., D.A. Smith, T.J. Greytak and D. Kleppner, 1980b, Phys. Rev. Lett. **45**, 2117.
Cline, R.W., T.J. Greytak and D. Kleppner, 1981, Phys. Rev. Lett. **47**, 1195.
Condat, C.A., and R.A. Guyer, 1981, Phys. Rev. **B24**, 2874.
Crampton, S.B., 1980, J. Phys. (France) **41**, C7-249.
Crampton, S.B., T.J. Greytak, D. Kleppner, W.D. Phillips, D.A. Smith and A. Weinrib, 1979, Phys. Rev. Lett. **42**, 1039.
Crampton, S.B., J.J. Krupczak and S.P. Souza, 1982, Phys. Rev. **B25**, 4383.
Crooker, B.C., B. Hébral, E.N. Smith, Y. Takano and J.D. Reppy, 1983, Phys. Rev. Lett. **51**, 666.
da Frota, H.O., M.S. Silva and S.G. Rosa Jr, 1984, J. Phys. **C17**, 1669.
Dabrowski, I., 1984, Can. J. Phys. **62**, 1639.
Danilowicz, R.L., J.V. Dugan and R.D. Etters, 1976, J. Chem. Phys. **65**, 498.
Davison, W.D., and Y.C. Liew, 1972, J. Phys. **B5**, 309.
de Boer, J., 1948, Physica **14**, 139.
de Boer, J., and R. Bird, 1954, in: Molecular Theory of Gases and Liquids, eds J.O. Hirschfelder, C.F. Curtiss and R.B. Bird (Wiley, New York) p. 424.
de Goey, L.P.H., and B.J. Verhaar, 1984, private communication.
de Goey, L.P.H., J.P.J. Driesen, B.J. Verhaar and J.T.M. Walraven, 1984, Phys. Rev. Lett. **53**, 1919.
De Simone, C., and B. Maraviglia, 1979, Chem. Phys. Lett. **60**, 289.
Desaintfuscien, M., and C. Audoin, 1976, Phys. Rev. **A13**, 2070.
Dugan, J.V., and R.D. Etters, 1973, J. Chem. Phys. **59**, 6171.
Eckardt, J.R., D.O. Edwards, P.P. Fatouros, F.M. Gasparini and S.Y. Shen, 1974, Phys. Rev. Lett. **32**, 706.
Edwards, D.O., 1982, Physica **109 + 110B**, 1531.
Edwards, D.O., and P.P. Fatouros, 1978, Phys. Rev. **B17**, 2147.
Edwards, D.O., and I.B. Mantz, 1980, J. Phys. (France) **41**, C7-257.
Edwards, D.O., and W.F. Saam, 1978, in: Progress in Low Temperature Physics, Vol. VIIA, ed. D.F. Brewer (North-Holland, Amsterdam) p. 283.
Ehrenfest, P., and J.R. Oppenheimer, 1931, Phys. Rev. **37**, 333.
Ellis, F.M., and R.B. Hallock, 1983, Rev. Sci. Instr. **54**, 751.
Ellis, F.M., R.B. Hallock, M.D. Miller and R.A. Guyer, 1981, Phys. Rev. Lett. **46**, 1461.
Entel, P., and J. Anlauf, 1981, Z. Phys. **B42**, 191.
Etters, R.D., 1973, Phys. Lett. **42A**, 439.
Etters, R.D., J.V. Dugan and R.W. Palmer, 1975, J. Chem. Phys. **62**, 313.

Etters, R.D., R.L. Danilowicz and R.W. Palmer, 1978, J. Low Temp. Phys. **33**, 305.
Feenberg, E., 1969, Theory of quantum fluids, in: Pure and Applied Physics, Vol. 31, eds H.S.W. Massey and K.A. Brueckner (Academic Press, New York).
Freed, J.H., 1980, J. Chem. Phys. **72**, 1414.
Freed, J.H., 1985, Ann. Phys. (France) **10**, 901.
Friend, D.G., and R.D. Etters, 1980, J. Low Temp. Phys. **39**, 409.
Girardeau, M.D., 1976, Phys. Lett. **59A**, 121.
Girardeau, M.D., 1980, Int. J. Quantum Chem. **17**, 25.
Glöcke, W., 1983, The Quantum Mechanical Few-Body Problem (Springer, Berlin).
Godfried, H.P., E.R. Eliel, J.G. Brisson, J.D. Gillaspy, C. Mallardeau, J.C. Mester and I.F. Silvera, 1985, Phys. Rev. Lett. **55**, 1311.
Goldman, V.V., and I.F. Silvera, 1981, Physica **107B**, 515.
Goldman, V.V., I.F. Silvera and A.J. Leggett, 1981, Phys. Rev. **B24**, 2870.
Greben, J.M., A.W. Thomas and A.J. Berlinsky, 1981, Can. J. Phys. **59**, 945.
Greytak, T.J., 1984, private communication.
Greytak, T.J., and D. Kleppner, 1984, in: New Trends in Atomic Physics, Vol. 2, Les Houches 1982, eds G. Grynberg and R. Stora (North-Holland, Amsterdam) p. 1125.
Gross, E.P., 1963, J. Math. Phys. **4**, 195.
Guyer, R.A., and M.D. Miller, 1979, Phys. Rev. Lett. **42**, 1754.
Guyer, R.A., and M.D. Miller, 1981, Phys. Rev. Lett. **47**, 349.
Guyer, R.A., and M.D. Miller, 1982, Phys. Rev. **B25**, 5749.
Guyer, R.A., and W. Saslow, 1983, Phys. Rev. Lett. **19**, 1765.
Guyer, R.A., M.D. Miller and J. Yaple, 1981, in: Proc. LT-16, Physica **108B**, 941.
Guyer, R.A., M.D. Miller and J. Yaple, 1982, Phys. Rev. **B25**, 4570.
Haftel, M., 1985, private communication.
Hardy, W.N., and L.A. Whitehead, 1981, Rev. Sci. Inst. **52**, 213.
Hardy, W.N., A.J. Berlinsky and L.A. Whitehead, 1979, Phys. Rev. Lett. **42**, 1042.
Hardy, W.N., M. Morrow, R. Jochemsen, B.W. Statt, P.R. Kubik, R.M. Marsolais, A.J. Berlinsky and A. Landesman, 1980a, J. Phys. (France) **41**, C7-157.
Hardy, W.N., M. Morrow, R. Jochemsen, B.W. Statt, P.R. Kubrik, R.M. Marsolais, A.J. Berlinsky and A. Landesman, 1980b, Phys. Rev. Lett. **45**, 453.
Hardy, W.N., M. Morrow, R. Jochemsen and A.J. Berlinsky, 1982, Physica **109+110B**, 1964.
Harriman, J.E., M. Twerdochlib, M.B. Milleur and J.O. Hirschfelder, 1967, Proc. Natl. Acad. Sci. USA **57**, 1558.
Hecht, C.E., 1959, Physica **25**, 1159.
Hecht, C.E., 1981, Phys. Rev. **B23**, 3547.
Hellwig, H., R.F.C. Vessot, M. Levine, P.W. Zitzewitz, H.E. Peters, D.W. Allen and J. Glaze, 1970, IEEE Trans. Instrum. Meas. **IM-19**, 200.
Hepburn, J., G. Scoles and R. Penco, 1975, Chem. Phys. Lett. **36**, 451.
Herzberg, G., 1970, J. Mol. Spectrosc. **33**, 147.
Herzberg, G., and L.L. Howe, 1959, Can. J. Phys. **37**, 636.
Hess, H., 1985, Bull. Am. Phys. Soc. **30**, 854.
Hess, H.F., D.A. Bell, G.P. Kochanski, R.W. Cline, D. Kleppner and T.J. Greytak, 1983, Phys. Rev. Lett. **51**, 483.
Hess, H.F., D.A. Bell, G.P. Kochanski, D. Kleppner and T.J. Greytak, 1984, Phys. Rev. Lett. **52**, 1520.
Hess, R., 1971, Ph.D. Thesis (University of Stuttgart, Stuttgart) unpublished.
Hohenberg, P.C., 1967, Phys. Rev. **158**, 383.
Huang, K., 1963, Statistical Mechanics (Wiley, New York).

Huse, D.A., and E.D. Siggia, 1982, J. Low Temp. Phys. **46**, 137.
Jackson, H.W., and E. Feenberg, 1961, Ann. Phys. (USA) **15**, 266.
Jochemsen, R., and A.J. Berlinsky, 1982, Can. J. Phys. **60**, 252.
Jochemsen, R., M. Morrow, A.J. Berlinsky and W.N. Hardy, 1981, Phys. Rev. Lett. **47**, 852.
Jochemsen, R., M. Morrow, A.J. Berlinsky and W.N. Hardy, 1982, Physica **109+110B**, 2108.
Johnson, B.R., 1984, Ph.D. Thesis (Cornell University) unpublished.
Johnson, B.R., J.S. Denker, N. Bigelow, L.P. Lévy, J.H. Freed and D.M. Lee, 1984, Phys. Rev. Lett. **52**, 1508.
Jones Jr, J.T., M.H. Johnson, H.L. Meyer, S. Katz and R.S. Wright, 1958, publication U-216 (Aeronutronic Systems Inc., a subsidiary of Ford Motor Company).
Kagan, Yu., and G.V. Shlyapnikov, 1981, JETP Lett. **34**, 341.
Kagan, Yu., and G.V. Shlyapnikov, 1982, Phys. Lett. **88A**, 356.
Kagan, Yu., and G.V. Shlyapnikov, 1983, Phys. Lett. **95A**, 309.
Kagan, Yu., I.A. Vartanyantz and G.V. Shlyapnikov, 1981, Sov. Phys.-JETP **54**, 590.
Kagan, Yu., G.V. Shlyapnikov, I.A. Vartanyantz and N.A. Glukhov, 1982, JETP Lett. **35**, 477.
Kagan, Yu., G.V. Shlyapnikov and I.A. Vartanyantz, 1984, Phys. Lett. **101A**, 27.
Kagan, Yu., G.V. Shlyapnikov and N.A. Glukhov, 1985, JETP Lett. **41**, 238.
Kleppner, D., and T.J. Greytak, 1983, in: Proc. 5th Int. Conf. on High Energy Spin Physics, Brookhaven, ed. G.M. Bunce, Am. Inst. Phys. Conf. Proc. **95**, 546.
Kleppner, D., H.M. Goldenberg and N.F. Ramsey, 1962, Phys. Rev. **126**, 603.
Kolos, W., and L. Wolniewicz, 1965, J. Chem. Phys. **43**, 2429.
Kolos, W., and L. Wolniewicz, 1968, J. Chem. Phys. **49**, 404.
Kolos, W., and L. Wolniewicz, 1974, Chem. Phys. Lett. **24**, 457.
Kolos, W., and L. Wolniewicz, 1975, J. Mol. Spectrosc. **54**, 303.
Kosterlitz, J.M., and D.J. Thouless, 1978, in: Progress in Low Temperature Physics, Vol. VIIB, ed. D.F. Brewer (North-Holland, Amsterdam) p. 371.
Krotscheck, E., R.A. Smith, J.W. Clark and R.M. Panoff, 1981, Phys. Rev. **B24**, 6383.
Kulsrud, R.M., H.P. Furth, E.J. Valeo and M. Goldhaber, 1982, Phys. Rev. Lett. **49**, 1248.
Kumar, P., 1981, Physica **108B**, 939.
Kürten, K.E., and M.L. Ristig, 1985, Phys. Rev. **B31**, 1346.
Lagendijk, A., 1982, Phys. Rev. **B25**, 2054.
Lagendijk, A., G. van Yperen and J.T.M. Walraven, 1984, J. Phys. Lett. (France) **45**, L-929.
Lamb, W.E., and R.C. Retherford, 1950, Phys. Rev. **79**, 549.
Landau, L.D., and E.M. Lifshitz, 1976, Mechanics (Pergamon Press, New York) p. 93.
Lantto, L.J., and R.M. Nieminen, 1980, J. Phys. (France) **41**, C7-49.
Lee, T.D., K. Huang and C.N. Yang, 1957, Phys. Rev. **106**, 1135, and references therein.
Leggett, A.J., 1970, J. Phys. **C3**, 448.
Leggett, A.J., 1980, J. Phys. (France) **41**, C7-19.
Leggett, A.J., and M.J. Rice, 1968, Phys. Rev. Lett. **20**, 586.
LeRoy, R.J., 1971, J. Chem. Phys. **54**, 5433.
LeRoy, R.J., and M.G. Barwell, 1975, Can. J. Phys. **53**, 1983.
LeRoy, R.J., and R.B. Bernstein, 1971, J. Chem. Phys. **54**, 5114.
Lévy, L.P., 1985, Phys. Rev. **B31**, 7077.
Lévy, L.P., and A.E. Ruckenstein, 1984, Phys. Rev. Lett. **52**, 1512.
Lhuillier, C., 1983, J. Phys. (France) **44**, 1.
Lhuillier, C., and F. Laloë, 1980, J. Phys. (France) **41**, C7-51.

Lhuillier, C., and F. Laloë, 1982a, J. Phys. (France) **43**, 197.
Lhuillier, C., and F. Laloë, 1982b, J. Phys. (France) **43**, 225.
Lhuillier, C., and F. Laloë, 1985, Phys. Rev. Lett. **54**, 1207 (comment).
Lieb, E.H., 1967, J. Math. Phys. **8**, 43.
London, F., 1938, Phys. Rev. **54**, 947; Nature **141**, 663.
Lovelace, R.V.E., C. Mehanian, T.J. Tommila and D.M. Lee, 1985, Nature **318**, 30.
Mantz, I.B., and D.O. Edwards, 1979, Phys. Rev. **B20**, 4518.
Mathur, B.S., S.B. Crampton, D. Kleppner and N.F. Ramsey, 1967, Phys. Rev. **158**, 14.
Matthey, A.P.M., J.T.M. Walraven and I.F. Silvera, 1981, Phys. Rev. Lett. **46**, 668.
Matthey, A.P.M., J.T.M. Walraven and I.F. Silvera, 1984, unpublished.
Mayer, R., and G. Seidel, 1985, Phys. Rev. **B31**, 4199.
Mayer, R., A. Ridner and G. Seidel, 1981, Physica **108B**, 937.
McMillan, W.L., 1965, Phys. Rev. **138A**, 442.
McQueeney, D., G. Agnolet and J.D. Reppy, 1984, Phys. Rev. Lett. **52**, 1325.
Mello, E.V.L., J.J. Rehr and O.E. Vilches, 1983, Phys. Rev. **B28**, 3759.
Messiah, A., 1970, Quantum Mechanics (North-Holland, Amsterdam).
Miller, M.D., 1976, Phys. Rev. **B14**, 3937.
Miller, M.D., 1978, Phys. Rev. **B18**, 4730.
Miller, M.D., 1980, Ann. Phys. (USA) **127**, 367.
Miller, M.D., and L.H. Nosanow, 1977, Phys. Rev. **B15**, 4376.
Miller, M.D., and L.H. Nosanow, 1978, J. Low Temp. Phys. **32**, 145.
Miller, M.D., L.H. Nosanow and L.J. Parish, 1975, Phys. Rev. Lett. **35**, 581.
Miller, M.D., L.H. Nosanow and L.J. Parish, 1977, Phys. Rev. **B15**, 214.
Milleur, M.B., L.A. Curtiss, M. Twerdochlib and J.O. Hirschfelder, 1968, J. Chem. Phys. **48**, 4261.
Misha, W.A., 1972, J. Chem. Phys. **57**, 2184.
Mitchell, D.N., and R.J. LeRoy, 1977, J. Chem. Phys. **67**, 1042.
Morrow, M., and A.J. Berlinsky, 1983, Can. J. Phys. **61**, 1042.
Morrow, M., R. Jochemsen, A.J. Berlinsky and W.N. Hardy, 1981, Phys. Rev. Lett. **46**, 195; erratum **47**, 455.
Nelson, D.R., and J.M. Kosterlitz, 1977, Phys. Rev. Lett. **39**, 1201.
Niinikoski, T.O., 1981, in: Proc. Intern. Symp. on High-Energy Physics with Polarized Beams and Polarized Targets, Lausanne, EXS 38 (Birkhäuser, Basle and Stuttgart) p. 191.
Niinikoski, T.O., S. Pentilä, J.M. Rieubland and A. Rijllart, 1984, in: Polarized Proton Ion Sources, eds G. Roy and P. Schnor, Am. Inst. Phys. Conf. Proc. **117**, 139.
Nilsen, T.S., and P.C. Hemmer, 1969, J. Stat. Phys. **1**, 175.
Nosanow, L.H., 1977a, in: Quantum Fluids and Solids, eds S.B. Trickey, E.D. Adams and J.W. Dufty (Plenum, New York) p. 279.
Nosanow, L.H., 1977b, J. Low Temp. Phys. **26**, 613.
Nosanow, L.H., 1980, J. Phys. (France) **41**, C7-1.
Nosanow, L.H., L.J. Parish and F.J. Pinsky, 1975, Phys. Rev. **B11**, 191.
Pan, J., J. Yuan, D.H. Feng and C. Wu, 1985, preprint.
Pandharipande, V.R., J.G. Zabolitsky, S.C. Pieper, R.B. Wiringa and U. Helmbrecht, 1983, Phys. Rev. Lett. **50**, 1676.
Panoff, R.M., J.W. Clark, M.A. Lee, K.E. Schmidt, M.H. Kalos and G.V. Chester, 1982, Phys. Rev. Lett. **48**, 1675.
Papoular, M., 1983, J. Low Temp. Phys. **50**, 253.
Papoular, M., B. Collaudin and J.B. Robert, 1984, J. Phys. (France) **45**, 1571.
Petit, P., M. Desaintfuscien and C. Audoin, 1980, Metrologia **16**, 7.
Pinard, M., and F. Laloë, 1980a, J. Phys. (France) **41**, 769.

Pinard, M., and F. Laloë, 1980b, J. Phys. (France) **41**, 799.
Pritchard, D.E., 1983, Phys. Rev. Lett. **51**, 1336.
Ramsey, N.F., 1956, Molecular Beams (Oxford Press, Oxford).
Ray, S., 1975, Phys. Rev. **12A**, 2031.
Reynolds, M.W., I. Shinkoda, W.N. Hardy, A.J. Berlinsky, F. Bridges and B.W. Statt, 1985, Phys. Rev. **B31**, 7503.
Roberts, R.E., R.B. Bernstein and C.F. Curtiss, 1969, J. Chem. Phys. **50**, 5163.
Rosenbaum, R.L., J. Landau and Y. Eckstein, 1974, J. Low Temp. Phys. **16**, 131.
Ruckenstein, A.E., and E.D. Siggia, 1982, Phys. Rev. **B25**, 6031.
Saam, W.F., 1981, Phys. Rev. **B23**, 1485.
Salonen, K., S. Jaakkola, M. Karhunen, E. Tjukanov and T. Tommila, 1984, in: Proc. 17th Int. Conf. on Low Temperature Physics LT-17, Karlsruhe, August 15–22, eds U. Eckern, A. Schmid, W. Weber and H. Wühl (North-Holland, Amsterdam) p. 543.
Salonen, K.T., I.F. Silvera, J.T.M. Walraven and G.H. van Yperen, 1982, Phys. Rev. **B25**, 6002.
Schiff, D., and L. Verlet, 1967, Phys. Rev. **160**, 208.
Schmid, E.W., and H. Ziegelman, 1974, The Quantum Mechanical Three-Body Problem (Vieweg, Braunschweig).
Shevchenko, S.I., 1982, Fiz. Nizk. Temp. **8**, 453 (Sov. J. Low Temp. Phys. **8**, 221).
Siggia, E.D., and A.E. Ruckenstein, 1980, Phys. Rev. Lett. **44**, 1423.
Siggia, E.D., and A.E. Ruckenstein, 1981, Phys. Rev. **B23**, 3580.
Silvera, I.F., 1979, Finnish Winter School, Lammi, Finland, unpublished.
Silvera, I.F., 1980, Rev. Mod. Phys. **52**, 393.
Silvera, I.F., 1982, Physica **109 + 110B**, 1499.
Silvera, I.F., 1984, Phys. Rev. **B29**, 3899.
Silvera, I.F., 1985, in: Proc. 6th General Conference of the European Physical Society, Prague, August 1984, eds J. Janta and J. Pantoflicek (Polygraphia np, Prague) p. 114.
Silvera, I.F., and H.P. Godfried, 1984, unpublished results.
Silvera, I.F., and V.V. Goldman, 1980, Phys. Rev. Lett. **45**, 915.
Silvera, I.F., and J.T.M. Walraven, 1979, Phys. Lett. **74A**, 193.
Silvera, I.F., and J.T.M. Walraven, 1980a, Phys. Rev. Lett. **44**, 164.
Silvera, I.F., and J.T.M. Walraven, 1980b, Phys. Rev. Lett. **45**, 1268.
Silvera, I.F., and J.T.M. Walraven, 1980c, J. Phys. (France) **41**, C7-137.
Silvera, I.F., and J.T.M. Walraven, 1981a, J. Appl. Phys. **52**, 2304.
Silvera, I.F., and J.T.M. Walraven, 1981b, in: Recent Developments in Condensed Matter Physics, Vol. I, ed. J.T. Devreese (Plenum Press, New York) p. 29.
Sprik, R., J.T.M. Walraven, G.H. van Yperen and I.F. Silvera, 1982, Phys. Rev. Lett. **49**, 153.
Sprik, R., J.T.M. Walraven and I.F. Silvera, 1983, Phys. Rev. Lett. **51**, 479; erratum **51**, 942.
Sprik, R., J.T.M. Walraven and I.F. Silvera, 1985, Phys. Rev. **B32**, 5668.
Statt, B.W., 1982, Phys. Rev. **B25**, 6035.
Statt, B.W., 1984, Ph.D. Thesis, University of British Columbia, unpublished.
Statt, B.W., and A.J. Berlinsky, 1980, Phys. Rev. Lett. **45**, 2105.
Statt, B.W., and W.N. Hardy, 1981, private communication.
Statt, B.W., A.J. Berlinsky and W.N. Hardy, 1985, Phys. Rev. **B31**, 3169.
Stwalley, W.C., 1970, Chem. Phys. Lett. **6**, 241.
Stwalley, W.C., 1976, Phys. Rev. Lett. **37**, 1628.
Stwalley, W.C., 1982, Chem. Phys. Lett. **88**, 404.
Stwalley, W.C., and L.H. Nosanow, 1976, Phys. Rev. Lett. **36**, 910.
Tastevin, G., P.J. Nacher, M. Leduc and F. Laloë, 1985, J. Phys. (France) **6**, 249.

Thomas, A.W., ed., 1977, Modern Three-Hadron Physics (Springer, Berlin).
Tommila, T., S. Jaakkola, M. Krusius, K. Salonen and E. Tjukanov, 1984a, in: Proc. 17th Int. Conf. on Low Temperature Physics LT-17, Karlsruhe, August 15–22, eds U. Eckern, A. Schmid, W. Weber and H. Wühl (North-Holland, Amsterdam) p. 453.
Tommila, T., S. Jaakkola, M. Krusius, K. Salonen and E. Tjukanov, 1984b, in: Proc. 17th Int. Conf. on Low Temperature Physics LT-17, Karlsruhe, August 15–22, eds U. Eckern, A. Schmid, W. Weber and H. Wühl (North-Holland, Amsterdam) p. 545.
Uang, Y.H., and W.C. Stwalley, 1980a, J. Phys. (France) **41**, C7-33.
Uang, Y.H., and W.C. Stwalley, 1980b, Phys. Rev. Lett. **45**, 627.
Uang, Y.H., R.F. Ferrante and W.C. Stwalley, 1981, J. Chem. Phys. **74**, 6256.
van den Eijnde, J.P.H.W., 1984, Ph.D. Thesis (Technical University Eindhoven, Eindhoven).
van den Eijnde, J.P.H.W., C.J. Reuver and B.J. Verhaar, 1983, Phys. Rev. **B28**, 6309.
van Yperen, G.H., A.P.M. Matthey, J.T.M. Walraven and I.F. Silvera, 1981, Phys. Rev. Lett. **47**, 800.
van Yperen, G.H., I.F. Silvera, J.T.M. Walraven, J. Berkhout and J.G. Brisson, 1983, Phys. Rev. Lett. **50**, 53.
van Yperen, G.H., J.T.M. Walraven and I.F. Silvera, 1984, Phys. Rev. **B30**, 2386.
Verhaar, B.J., 1985, private communication.
Verhaar, B.J., J.P.H.W. van den Eijnde, M.A.J. Voermans and M.M.J. Schaffrath, 1984, J. Phys. **A17**, 595.
Verhaar, B.J., L.P.H. de Goey, J.P.H.W. van den Eijnde and E.J.D. Vredenbregt, 1985, Phys. Rev. **A32**, 1424.
Waech, Th.G., and R.B. Bernstein, 1967, J. Chem. Phys. **46**, 4905.
Walraven, J.T.M., 1982, Ph.D. Thesis (University of Amsterdam) unpublished.
Walraven, J.T.M., 1984a, Proc. LT-17, Physica **126B + C**, 176.
Walraven, J.T.M., 1984b, in: Atomic Physics 9, eds R. Van Dyck Jr and E.N. Fortson (World Scientific, Singapore) p. 187.
Walraven, J.T.M., and I.F. Silvera, 1980, Phys. Rev. Lett. **44**, 168.
Walraven, J.T.M., and I.F. Silvera, 1982, Rev. Sci. Inst. **53**, 1167.
Walraven, J.T.M., E.R. Eliel and I.F. Silvera, 1978, Phys. Lett. **66A**, 247.
Walraven, J.T.M., I.F. Silvera and A.P.M. Matthey, 1980, Phys. Rev. Lett. **45**, 449.
Williams, G.A., 1984, Phys. Rev. Lett. **52**, 1567.
Wilson, B.J., and P. Kumar, 1983, Phys. Rev. **B27**, 3076.
Wimmett, T.F., 1953, Phys. Rev. **91**, 499A.
Wineland, D.J., and N.F. Ramsey, 1972, Phys. Rev. **A5**, 821.
Wing, W.H., 1984, Prog. Quantum Elect. **8**, 181.
Winkler, P.F., D. Kleppner, T. Myint and F.G. Walther, 1972, Phys. Rev. **A5**, 83.
Wise, H., and B.J. Wood, 1967, in: Advances in Atomic and Molecular Physics, Vol. 3, eds D.R. Bates and I. Esteman (Academic Press, New York) p. 291.
Wolniewicz, L., 1983, J. Chem. Phys. **78**, 6173.
Wood, W.W., 1960, in: Physics of Simple Liquids, eds H.N.V. Temperley, J.S. Rowlingoon and G.S. Rushbrooke (North-Holland, Amsterdam).
Wu, F.Y., and E. Feenberg, 1962, Phys. Rev. **128**, 943.
Wu, T.T., 1961, J. Math. Phys. **2**, 105.
Yurke, B., J.S. Denker, B.R. Johnson, N. Bigelow, L.P. Lévy, D.M. Lee and J.H. Freed, 1983, Phys. Rev. Lett. **50**, 1137.
Zabolitsky, J.G., 1977, Phys. Rev. **A16**, 1258.
Zimmerman, D.S., 1982, M.Sc. Thesis (University of British Columbia, Vancouver) unpublished.
Zimmerman, D.S., and A.J. Berlinsky, 1983, Can. J. Phys. **61**, 508.